DISSERTATION

SPINAL CORD AND MENINGEAL MECHANICS: VISCOELASTIC CHARACTERIZATION AND COMPUTATIONAL MODELING

Submitted by

Nicole Lauren Ramo

School of Biomedical Engineering

In partial fulfillment of the requirements

For the Degree of Doctor of Philosophy

Colorado State University

Fort Collins, Colorado

Fall 2018

Doctoral Committee:

Advisor: Christian M. Puttlitz
Co-advisor: Kevin L. Troyer

Paul Heyliger
Susan James

ABSTRACT

SPINAL CORD AND MENINGEAL MECHANICS: VISCOELASTIC CHARACTERIZATION AND COMPUTATIONAL MODELING

Suffering a spinal cord injury (SCI) can be physically, emotionally, and financially devastating. With the complex loading environment typically seen in SCI events, finite element (FE) computational models provide an important economical and ethical option for investigating the mechanical etiology of SCI, evaluating prevention techniques, and assessing clinical treatments. To this end, numerous research groups have developed FE models of the spinal cord using various degrees of material and structural sophistication. However, the level of model complexity that is necessary to achieve accurate predictions of SCI has not been explicitly investigated as few studies have reported applicable tissue behavior.

What are reported in the literature as "spinal cord mechanical properties" are most commonly based on *ex-vivo* tests of the spinal-cord-pia-arachnoid construct (SCPC). The pia and arachnoid maters are fibrous meningeal tissues that closely envelope the spinal cord, and together are referred to as the pia-arachnoid-complex (PAC). Currently available data demonstrate the PAC's importance in the overall SCPC stiffness and shape restoration following compression. However, only one previous study has reported mechanical properties of isolated spinal PAC, and therefore, conclusions about its contribution to SCPC mechanics are largely unknown. Additionally, it has been shown that SCPC material properties begin to degrade within 90 minutes of death. Considering the experimental difficulties and ethical concerns associated with

in-vivo mechanical testing of the SCPC, determining the relationship between *in-vivo* and *ex-vivo* viscoelastic properties would allow researchers to more accurately analyze existing *ex-vivo* data.

Therefore, the overarching goal of this work is to address the current gaps in knowledge regarding spinal cord and meningeal tissue mechanics and incorporate the developed material models into a FE model. Comparisons of *ex-vivo* and *in-vivo* porcine SCPC non-linear viscoelastic behavior revealed significantly different acute behaviors where the *ex-vivo* condition exhibited a higher stress response but also relaxed quicker and to a greater extent than the *in-vivo* condition. Although it only made up less than 6% of the ovine SCPC volume, the PAC was found to significantly affect the non-linear viscoelastic behavior of the SCPC which supports the conclusion that it plays an important protective mechanical role. Examining the fitting and predictive accuracy of linear, quasi-linear, and non-linear viscoelastic formulations to SCPC, cord, and PAC stress-strain data, non-linear formulations are recommended to model the SCPC and cord response to arbitrary loading conditions while the QLV is recommended for the PAC.

This work provides researchers with novel insights into the complex mechanical behavior of the spinal cord and PAC. The experimental results represent an important addition to the limited literature on *in-vivo* versus *ex-vivo* neural tissue viscoelastic properties; they are also the first to quantify the non-linear elastic behavior of spinal PAC and the non-linear viscoelastic properties of the isolated spinal cord. Finally, the computational portion of this work provides a detailed report of the effects of viscoelastic formulation complexity on FE model prediction accuracy and computational time allowing researchers interested in modeling SCI to make informed decisions about the balance of accuracy and efficiency necessary for their specific modeling efforts.

TABLE OF CONTENTS

ABSTRACT ii

CHAPTER 1: BACKGROUND 1
1.1 Significance 1
1.2 Spinal Column Structural Anatomy 2
1.2.1 Human Cervical Spine 2
1.2.2 Ovine Cervical Spine 4
1.2.3 Porcine Lumbar Spine 6
1.3 Spinal Cord Injury Mechanisms and Modeling 6
1.3.1 Human Injuries 6
1.3.2 Large Animal Experimental Models of SCI 8
1.3.3 Computational Models of SCI 11
1.4 Relevant Tissue Material Properties 15
1.4.1 Isolated Spinal Gray Matter and White Matter 15
1.4.2 Isolated Pia Mater, Arachnoid Mater, and PAC 18
1.4.3 Spinal-Cord-Pia-Arachnoid Construct (SCPC) 24
1.4.4 Spinal Dura Mater 30
1.5 Viscoelastic Model Formulations 31
1.5.1 General Features of Viscoelasticity 32
1.5.2 Linear Viscoelasticity (LV) 33
1.5.3 Quasi-Linear Viscoelasticity (QLV) 35
1.5.4 Non-linear Viscoelasticity (NLV) 36
1.5.5 Numerical Integration Method 37
1.6 Summary 38
1.7 Specific Aims 39

CHAPTER 2: COMPARISON OF *IN-VIVO* AND *EX-VIVO* VISCOELASTIC BEHAVIOR OF THE SPINAL CORD 42
2.1 Introduction 42
2.2 Materials and Methods 45
2.2.1 Ex-vivo experimentation 45
2.2.2 In-vivo experimentation 46
2.2.3 Mechanical testing 47
2.2.4 Viscoelastic modeling 49
2.3 Results 54
2.3.1 Stress-relaxation response 54
2.3.2 Viscoelastic modeling 58
2.4 Discussion 63
2.4.1 Conclusions 69
2.4.2 Funding and acknowledgements 70

CHAPTER 3: VISCOELASTICITY OF SPINAL CORD AND MENINGEAL TISSUES 71
3.1 Introduction 71
3.2 Materials and Methods 74
3.2.1 SCPC preparation 74
3.2.2 Experimental testing 75
3.2.3 Cord and PAC dissection and testing 77
3.2.4 Data analysis 78
3.2.5 Statistical methods 80
3.3 Results 81
3.3.1 Cyclic stress response 81
3.3.2 Viscoelastic modeling 84
3.4 Discussion 89
3.4.1 Conclusions 95
3.4.2 Funding and acknowledgements 96

CHAPTER 4: COMPARING PREDICTIVE ACCURACY AND COMPUTATIONAL COST FOR VISCOELASTIC MODELING OF SPINAL CORD TISSUES 97
4.1 Introduction 97
4.2 Materials and Methods 99
4.2.1 Experimental testing 99
4.2.2 Viscoelastic modeling 100
4.2.3 Statistical analysis 107
4.3 Results 107
4.3.1 Dynamic cyclic data fits 107
4.3.2 Stress-relaxation predictions 110
4.4 Discussion 122
4.4.1 Recommendations and conclusions 127

CHAPTER 5: CONCLUSION 128
5.1 Summary of Findings 128
5.2 Future Work 130

REFERENCES 132

APPENDIX A: DAMAGE ACCUMULATION MODELING AND RATE DEPENDENCY OF SPINAL DURA MATER 144
A.1 Introduction 144
A.2 Materials and Methods 146
A.2.1 Specimen preparation 146
A.2.2 Mechanical testing 147
A2.2.3 Constitutive modeling 149
A.2.3 Fitting procedure 151
A.3 Results 153
A.4 Discussion 157
A4.1 Conclusions 166
A4.2 Funding and acknowledgements 166

APPENDIX A REFERENCES 167

APPENDIX B: THE DEVELOPMENT AND VALIDATION OF A NUMERICAL INTEGRATION METHOD FOR NON-LINEAR VISCOELASTIC MODELING 172
B.1 Introduction 172
B.2 Materials and Methods 174
B.2.1 Model development 174
B.2.2 Model validation 179
B.3 Results 180
B.3.1 Stress-relaxation 180
B.3.2 Dynamic cyclic 184
B.4 Discussion 187
APPENDIX B REFERENCES 189

APPENDIX C: SUPPLEMENTAL FIGURES FOR CHAPTER 4 192

CHAPTER 1: BACKGROUND

1.1 Significance

The annual incidence rate of spinal cord injury (SCI) in the United States has been estimated to be between 43 and 71 per million – representing approximately 20,000 new injuries each year [1,2]. Despite the relatively low incidence rate, SCI can have very serious and lasting consequences. Of the 20,000 new injuries per year, up to 30% prove fatal before they can be treated at a hospital. Those who survive are often faced with significant neurological, psychological, and financial hardships related to their injury. Unlike many other debilitating conditions, SCI primarily affect young people, with up to 70% of the patients living with an SCI between 15 and 35 years of age [1–3]. While it is impossible to measure the personal cost of lost independence, satisfaction, and lifestyle, over $7 billion is spent annually in the United States on direct costs such as hospitalizations, medications, rehabilitation, and equipment related to SCI. With the addition of $2.5 billion in indirect costs from lost productivity, the total annual cost to society due to SCI is approximately $9.5 billion [4–6].

This significant societal impact has motivated much research on the cause, prevention, and treatment of SCI over the past fifty years. As the initiation of the vast majority these injuries is a mechanical insult to the spinal column [1,2], a requisite first step in understanding how damage occurs is characterization of the behavior of the tissues that make up the spinal column, including the spinal cord itself. Despite the work of many research groups around the world, there still exist important unanswered questions regarding the properties of the spinal cord and meningeal

tissues. This current work aims to address a number of these questions through experimental and computational modeling methodologies.

1.2 Spinal Column Structural Anatomy

Since the majority of SCI occur at the cervical level and these injuries result in the highest rates of mortality and morbidity [2,3,7], the cervical spine is the focus of this work. The following sections describe the structure of the human and ovine cervical spines. Since a subset of the experimental data was collected from the lumbar spine of a pig, the porcine lumbar spine is also discussed briefly. The biological and anatomical similarities between the human, sheep, and pig spines support the use of ovine and porcine models to study spinal mechanics and injury.

1.2.1 Human Cervical Spine

The bony structure of the human cervical spine is composed of the seven vertebrae of the neck that run from the base of the skull to the height of the shoulders (Fig. 1.1A). The shape and articulating surfaces of the cervical vertebrae allow for a larger range of motion than that of the thoracic and lumbar spinal levels [8]. As shown in Fig. 1.1B, the spinal cord is situated in the canal created by the posterior processes of the vertebrae. At the cervical level, this canal is approximately 25 mm in the transverse direction and 16 mm in the anterior-posterior direction [9]. The human cervical spinal cord is also oval in shape with a larger transverse diameter (11.5 – 13.5 mm) than anterior-posterior diameter (6 – 8.3 mm) based on *in-vivo* imaging [10,11] and *ex-vivo* cadaveric measurements [12,13]. The cord itself is composed of a central region of gray matter surrounded by white matter (as detailed in Section 1.4.1) [14–16]. Between each pair of adjacent vertebrae, nerve roots from the spinal cord exit the spinal canal through foramina, which are held

open by the height of the intervertebral disc (Fig. 1.1). These nerve roots extend beyond the spinal region to innervate various regions of the upper body as a part of the peripheral nervous system.

The entire central nervous system (brain and spinal cord) is surrounded by three connective tissue meningeal layers: the dura mater, the arachnoid mater, and the pia mater, as shown in Fig. 1.1B and 1.1C. The dura mater is the outermost and strongest of the three meninges, and has been reported to be 80 – 350 μm thick in the human spine [17–19]. It is separated from the perimeter surface of the spinal canal by the epidural space, which is typically occupied by adipose tissue. The arachnoid mater is separated from the inner surface of the dura mater by the relatively thin subdural space. The arachnoid mater, often described as a delicate spider-web like structure, connects to the underlying pia mater through trabecular extensions within the subarachnoid space. The subarachnoid space is also occupied by cerebrospinal fluid and vasculature. The pia mater is the innermost of the meninges and closely envelopes the spinal cord. The thickness of the pia mater in humans has been reported to be 60 μm at the optic nerve [20] and 200 μm at the thoracic and lumbar regions [21]. Detailed descriptions of the structure and properties of the tissues that make up the spinal cord and meningeal layers can be found in Section 1.4.

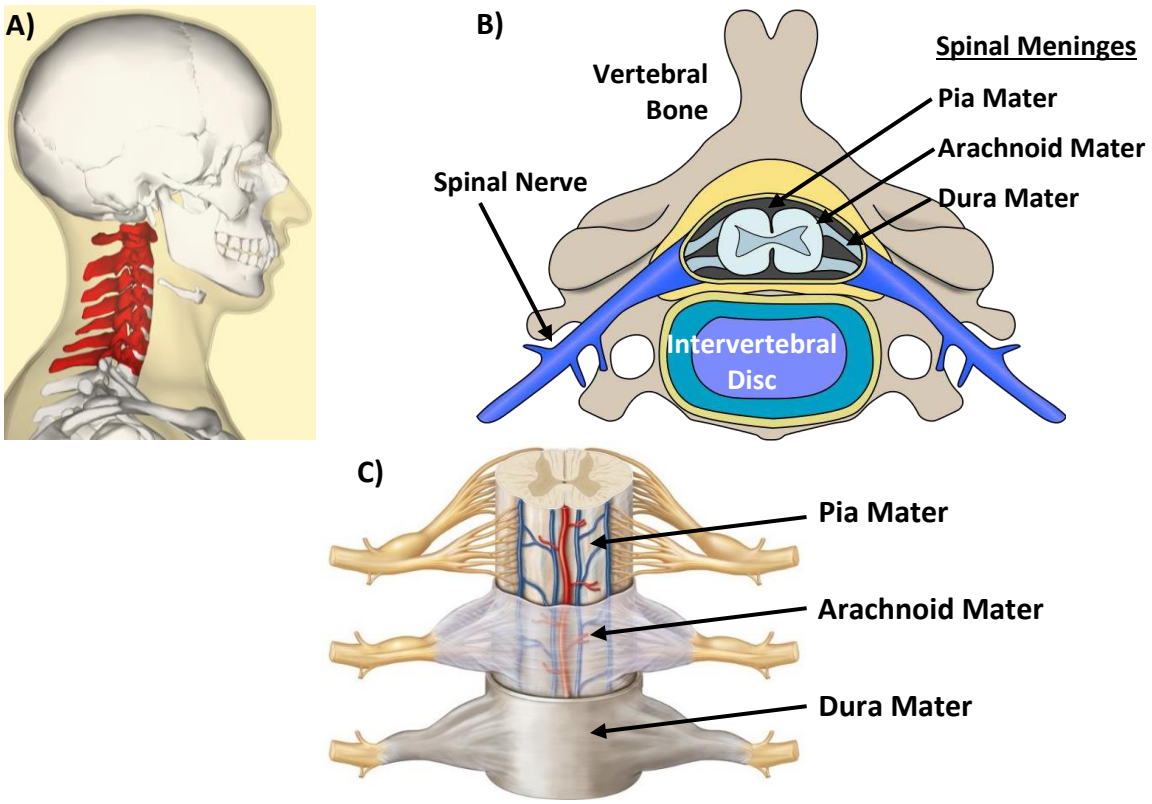

Figure 1.1: A) Sagittal view of the human cervical spine [BodyParts3D, licensed under CC Attribution-Share Alike 2.1 Japan]; B) Axial view of single human cervical vertebra [Debivort, licensed under CC Attribution-Share Alike 3.0 Unported]; C) Spinal meningeal layers [Adapted from [16] with permission of McGraw-Hill Education]

1.2.2 Ovine Cervical Spine

Due to ethical and logistical complications related to human central nervous system research, animal models are often used to study spinal cord and meningeal tissue properties and SCI. While rat or mouse models are the most common [7,22–27], anatomical and physiological differences between the rodent and human spine often result in poor translation of research results [28–30]. Therefore, many groups have begun to use large-animal models (e.g., cat, dog, pig, sheep, cow, and non-human primate) that more closely approximate the human spine. Due to our research group's close relationship with the Preclinical Surgical Research Laboratory at Colorado State University which provided access to both expert knowledge and fresh samples, the ovine (sheep) model was primarily utilized in this work.

Similar to the human cervical spine, the bony structure of the ovine cervical spine consists of seven vertebrae that connect the base of the skull to the thoracic spinal region [9,31,32] (Fig. 1.2A). Although the shape of the cervical vertebrae differ between humans and sheep, their structure and function is remarkably similar [9,32]. As shown in Fig. 1.2B, the canal occupied by the spinal cord is more circular than in humans, with an average diameter of 13 – 16 mm [9,32]. However, the dimensions of the ovine spinal cord itself are similar to that of humans (transverse diameter: 10.33 – 11.67 mm; dorsal-ventral diameter: 7.5 – 8 mm [31,33]). The general organization of the central nervous system and the peripheral nervous system is the same as in humans, with nerve roots exiting through intervertebral foramina to innervate other areas of the animal (Fig. 1.2B). Although not studied nearly as extensively as humans, the organization of ovine meningeal tissues and the spaces between each is the same. The thickness of ovine spinal dura at the cervical level has been reported as 350 ± 90μm [34] while the thickness of the ovine pia mater has not been reported previously.

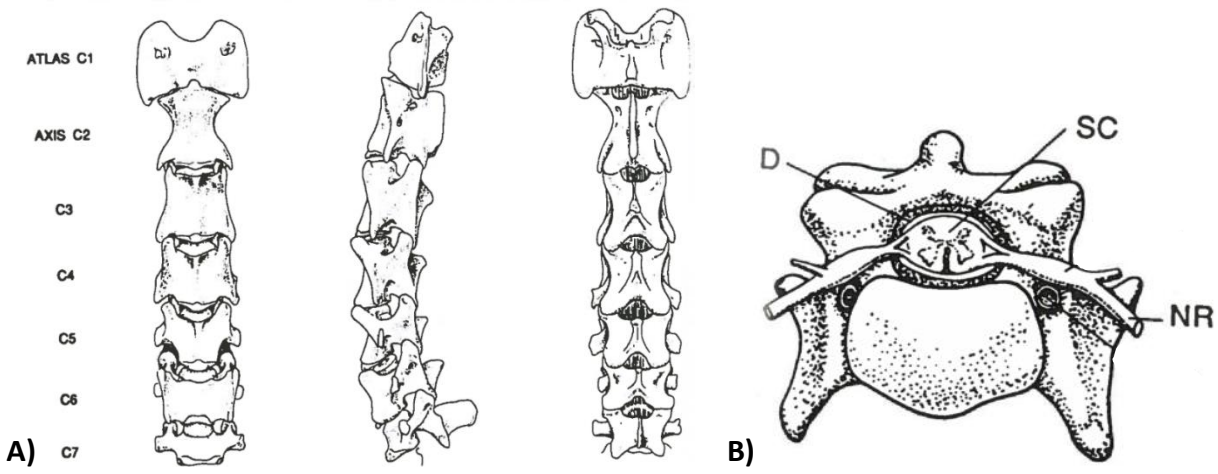

Figure 1.2: A) Anterior, sagittal, and posterior view of the ovine cervical spine; B) Axial view of single ovine cervical vertebra (D: dura mater, SC: spinal cord, NR: nerve root). Reprinted with permission from Cain and Fraser [32].

1.2.3 Porcine Lumbar Spine

Six vertebrae make up the bony structure of the porcine lumbar spine and connect the thoracic spine to the sacrum. Similar to the human cervical and lumbar levels, the porcine lumbar spinal canal is oval in shape with a larger transverse diameter than dorsal-ventral diameter (approximately 15 – 17mm versus 10 – 12mm [35–37]). The porcine spinal cord has been reported as smaller than the human and ovine cervical cord with a transverse diameter of 7 – 7.7mm and a dorsal-ventral diameter of 5.2 – 5.6mm [38–40]. The organization of meninges is the same as for human and ovine spines [41]. The thickness of the porcine dura mater at the lumbar level has not been reported, but at the cervical level it has been measured as 80 ± 10μm [17]. The thickness of the porcine pia mater has also not been reported in the literature.

1.3 Spinal Cord Injury Mechanisms and Modeling

Despite over a century of research, SCI are still not well understood and therefore the best methods for their prevention, diagnosis, and treatment are debated. The following section describes current knowledge and efforts to understand SCI based on clinical observation, animal experimental models, and computational simulation. Taken together, the literature suggests that the different injury mechanisms observed clinically cause different patterns of tissue damage and neurological deficits. The severity of neurological impairment is related to localized cord mechanics, specifically maximum principal strain [23,42–47].

1.3.1 Human Injuries

The pathophysiology of SCI can be characterized as a primary mechanical injury to the spinal column followed by a biochemical and cellular response [2,48]. The primary injury is typically

caused by high-velocity dynamic events such as traffic accidents, falls, violence, or sport or recreational activities (which together account for 75 – 90% of all cases) [1–3,7,42,49]. The specific clinical mechanism of these injuries can generally be classified as contusion/compression, dislocation/transection, distraction, or any combination thereof [2,7,43,44,48,50].

Contusion injuries are the result of transient transverse compressive forces on the spinal cord. These types of injuries may be due to vertebral burst fractures where bone fragments are propelled into the spinal canal and impact the cord [43,46,48,51,52]. Compressive injuries are the result of more prolonged compressive forces and can be caused by herniated or ruptured intervertebral discs or vertebral fracture [2,48,50]. Combined contusion-compression injuries, where an initial impact is followed by persistent compression, are the most common [2,38,44,48,53]. Dislocation injuries occur when the cord is subjected to shear forces caused by relative nonphysiologically motion of adjacent vertebrae, often due to fracture and/or damage to the intervertebral disc [2,43,46,50,54] as shown in Fig. 1.3. Depending on the severity of the dislocation and the presence of bone fragments in the canal, partial or complete transection of the spinal cord at the affected level is possible, although rare [2,7].

While the injury mechanisms discussed above can typically be observed using standard clinical radiography or computed tomography (CT) procedures, distraction injuries are much more difficult to diagnose without magnetic resonance imaging (MRI) [2,24,55,56]. It is thought that SCI without radiographic abnormality (SCIWORA) are distraction injuries [2,48,49,56,57]. Distraction or whiplash injuries at the cervical level are caused by over extension or flexion of the neck, resulting in damage to spinal ligaments and tensile forces on the spinal cord [7,23,24,26,46,48,50,55,56,58].

This type of injury is common in motor vehicle accidents, where there is sudden acceleration or deceleration of the head relative to the torso [24,42,55,59].

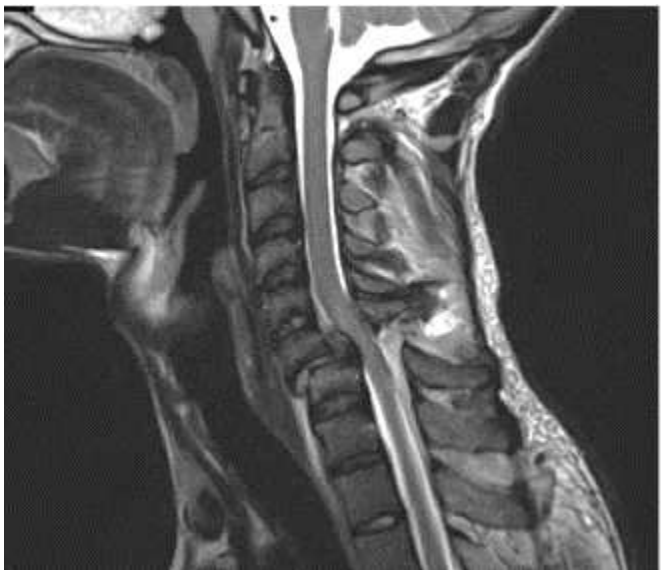

Figure 1.3: Mid-sagittal MR image showing dislocation SCI at the C6/C7 level. Reprinted with permission from Theodotou et al [54].

1.3.2 Large Animal Experimental Models of SCI

Inducing SCI in *in-vivo* animal models has allowed researchers to explore the connections between global loading conditions and local injury patterns and neurological deficit. Such methods typically involve anesthetizing the animal, surgically removing the posterior elements of the vertebrae to expose the dura mater, transecting a portion of the dura mater, and using mechanical means to create an injury to the exposed SCPC. The first such animal model was developed over a century ago when Allen published the preliminary results of a weight-drop contusion model for dogs in 1911 [60]. As they are relatively inexpensive and readily available, rats and mice have been the focus of the majority of SCI modeling efforts with numerous publications describing methods of creating reproducible and controlled transection, contusion, compression, distraction, and dislocation SCI [7,23,26,44,50,61]. However, concerns about differences

in anatomy and physiology between rodents and humans have led other research groups to adopt larger animal SCI models that may better approximate human injuries [7,39,62–66].

Non-human primate models provide the most direct correlation to humans [32,63,65], but the costs and risks associated with their care preclude them as an option for many researchers [39,67,68]. In a recent survey of over 300 researchers and clinicians in the SCI-field, over half of respondents felt the rodent model was insufficient (with 31% feeling strongly so) while 65% agreed that treatment effectiveness in non-primate large animal models was necessary before human clinical trials. Interestingly, less than half of respondents thought effectiveness in primate models was necessary before human trials [28]. Accordingly, many research groups have chosen other large animals such as the pig, sheep, cat, dog, and cow to study spinal mechanics and model SCI [7,9,71,32,39,53,62,64,66,69,70]. For example, the International Collaboration on Repair Discoveries (ICORD) group at the University of British Columbia has published extensively on the use of a miniature pig model to study the functional, histological, and biochemical effects of SCI. As shown in Fig. 1.4, this model uses a weight-drop impactor instrumented with a load cell to create contusion-compression SCI at the porcine thoracolumbar level [39,40,62,64,72,73].

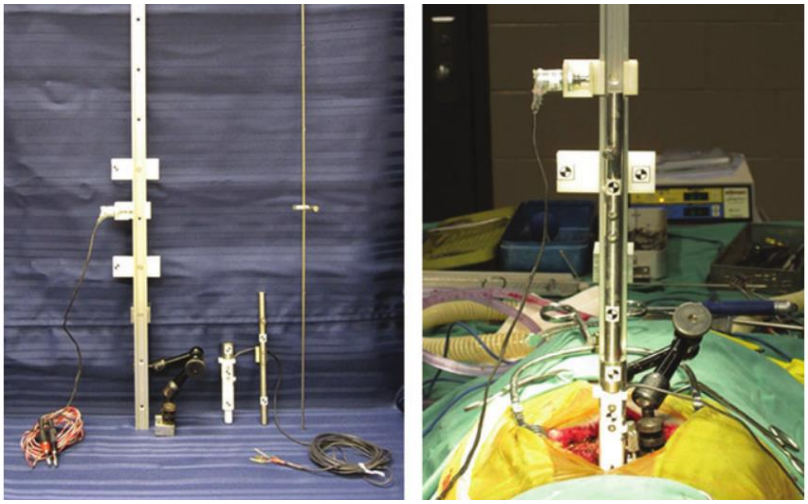

Figure 1.4: Custom weight-drop system used by the ICORD group to create contusion-compression SCI in a porcine animal model. Reprinted with permission from Lee et al. [39]

The anatomical and vascular similarities between the sheep and human spine [9,32,33,66] has motivated the use of ovine models in *in-vivo* studies of spinal cord blood flow [74]; cerebrospinal fluid (CSF) flow [75,76]; spinal nerve development and injury [33,77]; intervertebral disc morphology [9]; and most frequently, spinal surgery techniques [9,78–82]. Although less common than porcine models, ovine SCI models have also been utilized since the 1970s [53,66,78,83–87]. Wilson et al. developed an ovine SCI model that utilized a weight-drop technique (similar to that of the ICORD group) to create a repeatable moderate contusion injury to the thoracic spinal cord; behavioral and electrophysiological tests were used to confirm the extent of injury over time [66,86].

While published rodent models are capable of creating SCI by each of the three injury mechanisms (contusion/compression, dislocation, distraction), the majority of large animal models published to date use a drop-weight method to create contusion or contusion-compression SCI. Specifically, several rat distraction SCI models have been published in the last fifteen years [23,26,50,61], but this important injury mechanism has yet to be consistently modeled in a large animal. In light of the fact that distraction injuries are more difficult to diagnose [2,24,55,56] it is critically important for researchers to elucidate the relationships between tensile loading conditions, injury patterns, and neurological deficit in order to best inform clinicians. To the author's knowledge, only two research groups have attempted to address this by publishing the results of *in-vivo* distraction injuries in a large animal model [58,69,88,89]. In the early 1980's, Hung et al. introduced an *in-vivo* "elongation" model in which a segment of lumbar cat SCPC was stretched between 1.1 to 1.5 times its original length [88]. Similar to other reports of large animal SCI models, there were inconsistent initial motor and sensory deficiencies [7,39,66], but all normal

function was recovered within 4 weeks [88]. Hung et al. not only presented the feasibility of creating a distraction SCI in a large animal model, but also characterized the *in-vivo* mechanical properties of the spinal cord [88,90,91]. Such efforts are important for informing future SCI modeling endeavors. Detailed information on the mechanical properties of spinal tissues is provided in Section 1.4.

1.3.3 Computational Models of SCI

While *in-vivo* animal SCI models can provide data linking global loading conditions to injury patterns and neurological deficit, computational models of the spine can provide insight into how these global loading conditions lead to a localized mechanical response of the affected tissues. Unlike *in-vivo* animal modeling, finite element (FE) computational modeling allows researchers to conduct very controlled SCI simulations and relate global loading conditions to internal tissue stress and strain distributions [24,42–44,52]. Therefore, FE modeling is an important economical and ethical way of informing the design of *in-vivo* animal experiments and directly studying the mechanical etiology of SCI.

FE models are composed of meshed geometries or volumes to which material properties are assigned. The sophistication of the geometric and material model can be scaled depending on the desired level of FE model complexity, with a trade-off between computational cost and consistency with the particular physical condition being modeled. Specific simulation conditions, such as boundary constraints and loading scenarios, are then applied to the model; the FE model is considered "validated/verified" if the resultant model predictions agree with experimental results.

As large animal models require significantly greater financial and logistical resources than rodent models, many researchers attempt to optimize the design of large animal SCI experiments prior to utilization. Optimization techniques can take the form of scaled-down tests on rodent models, preliminary tests on synthetic surrogate materials, and/or FE modeling [43,67]. As exemplified in Sparrey et al. [67], effective use of FE modeling to simulate the intended injury mechanism can determine the sensitivity of various tissue response measures (e.g., displacement, stress, energy, etc.) to experimental variables (e.g., impactor alignment and velocity). Such modeling efforts allow researchers to identify specific combinations of experimental input parameters that are expected to result in the intended level of neurological damage, thereby reducing the number of actual animals needed to develop a standardized large animal SCI model [63,67].

While FE modeling can be used to improve *in-vivo* SCI animal models, it is more often used directly to gain insight into the mechanical aspects of SCI [24,42,43]. FE models are particularly useful in studying complex human injury scenarios that are difficult to recreate or measure using *in-vivo* animal models (e.g., the very rapid distraction seen in motor vehicle accidents). However, it is important to note that the predictive value of a FE model for a given application is dependent on the chosen geometry, material models, and validation method [45,59,92–94]. For the case of spinal FE modeling, the geometry may be based on medical imaging data (e.g., MRI or CT) [44,45,52,67], cadaveric measurements [42,43], published anatomical descriptions [51,59,92], or any combination thereof [24,46]. The spinal cord itself is typically modeled as one homogenous material [43,51,52,67,92] or as a construct of gray and white matter regions [24,42,44–46,59,93]. The pia mater meningeal layer or PAC is frequently excluded from FE models [24,42–46,51,52,67,92]. Inclusion of other spinal components (e.g., vertebrae, intervertebral discs, spinal ligaments, dura mater, CSF, etc.)

depends on the SCI condition being modeled. For example, as most *in-vivo* animal SCI models involve localized removal of the dura mater and direct insult to the exposed SCPC, FE simulations would typically not include the dura mater. Some of the most geometrically inclusive FE models for studying SCI are those developed by Russell et al. [44] and Khuyagbaatar et al. [46] The human cervical FE model recently published by Khuyagbaatar et al. is shown in Fig. 1.5. FE models that are geometrically relevant to this dissertation include that of Sparrey at al. [93] and Ichihara, Kato, and Taguchi et al. [57,94–98] which include only the gray matter, white matter, and PAC/pia mater as shown in Fig. 1.6.

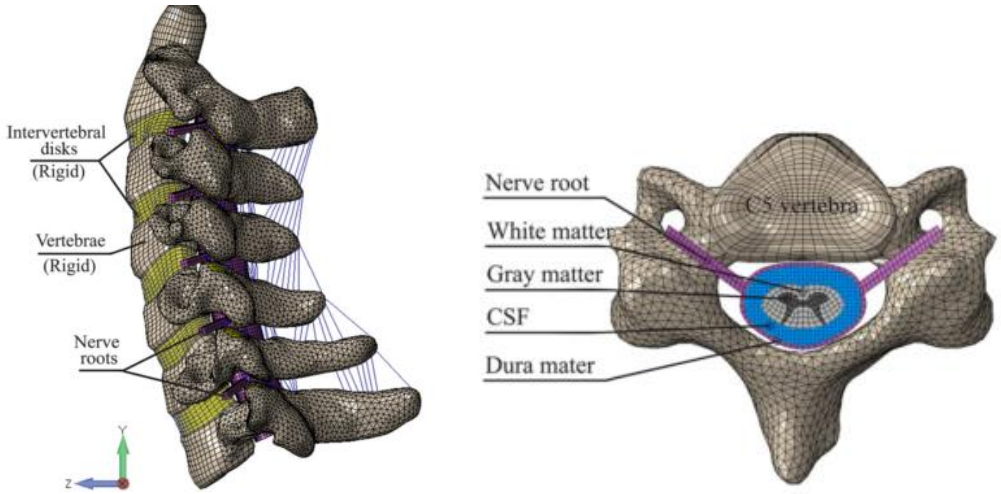

Figure 1.5: A) Sagittal view of a relatively geometrically inclusive human cervical spine FE model; B) Axial view of single vertebral level of same FE model. Reprinted with permission from Khuyagbaatar et al. [46]

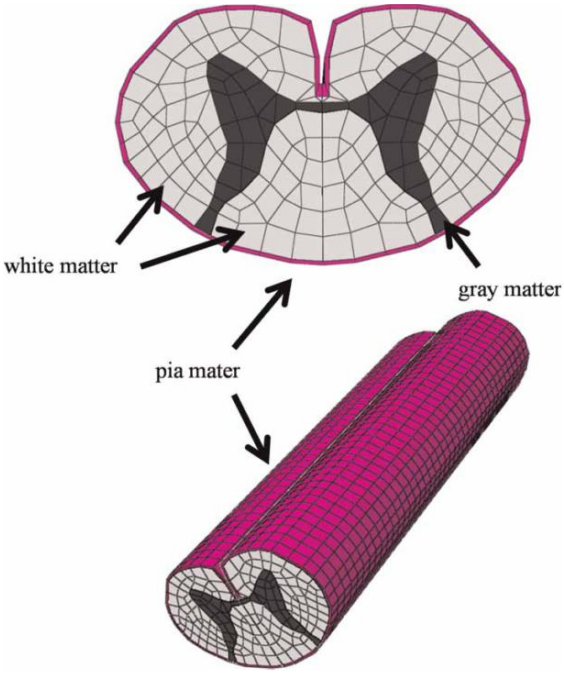

Figure 1.6: FE model of the SCPC including the gray and white matter of the spinal cord and the pia mater. Reprinted with permission from Nishida et al. [98]

When spinal or meningeal tissues are included in a FE model, the material behavior assigned to them may vary from linearly elastic [24,42,95–98,43,46,51,52,57,92–94] to hyperelastic [46,51,59,67,92,93] to viscoelastic [44,45,57,94,97], or some combination thereof. While the spinal cord (or white matter and gray matter) is usually modeled with more sophisticated behavior, the dura and PAC, when included, are usually assigned isotropic linearly elastic properties [46,51,57,92–94,97]. The choice of material model is dependent not only on the desired level of model complexity, but also on the availability of experimental data applicable to the condition being modeled. Section 1.4 describes previous work on characterizing the various aspects of the *in-vivo* and *ex-vivo* spinal tissue behavior.

1.4 Relevant Tissue Material Properties

Knowledge of the material properties of spinal and meningeal tissues under various loading conditions is required in order to make valid conclusions about SCI based on the clinical observation, experimental animal modeling, and computational simulation work discussed in Section 1.3. Accordingly, numerous studies have focused on characterizing the structure and mechanical properties of the SCPC, isolated cord, and dura mater using histological, *ex-vivo*, and *in-vivo* techniques. Unfortunately, the PAC has received less attention. This section describes the composition and structure of each of the spinal and meningeal tissues (cord gray matter, cord white matter, pia mater, arachnoid mater, and dura mater) and material models that have been used to describe their mechanical behavior.

1.4.1 Isolated Spinal Gray Matter and White Matter

Composition and Structure: The spinal cord itself is composed of a butterfly-shaped region of gray matter surrounded by a periphery of white matter; the cross-sectional area of the spinal cord as well as the ratio of gray to white matter varies with spinal level [11,14,99]. The cross-sectional morphology of the spinal cord is also characterized by the central canal (a small CSF-filled cavity through the center), the shallow posterior median sulcus, and the deeper anterior median fissure [14,15] (Fig. 1.7). The gray matter region of the spinal cord contains neuronal cell bodies and certain types of support (glial) cells, while the white matter region contains mainly myelinated axons [15,99–101]. While most areas of the gray matter do not display a cellular organizational pattern, the axons of the white matter form longitudinally aligned tracts [100–108]. In general, the anterior (or ventral) portion of the spinal cord is responsible for motor control of skeletal muscle while the posterior (or dorsal) portion is responsible for processing and relaying sensory

information [14,15,99]. This distribution of function helps explain why different injury mechanisms, which load distinct regions of the cord, can cause different neurological symptoms.

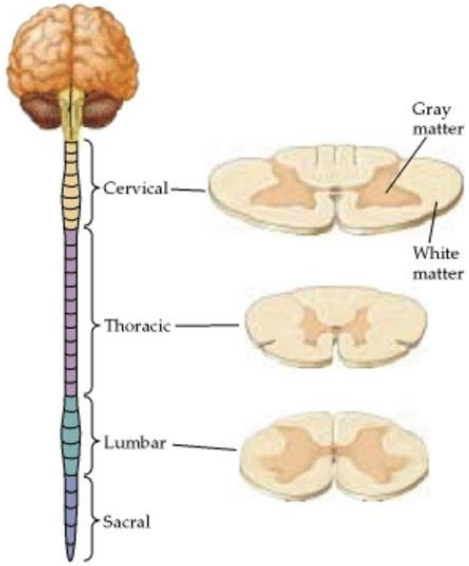

Figure 1.7: The cross-sectional area and ratio of white to gray matter in the human spinal cord varies with spinal level. Reprinted from [99] with permission from Oxford University Press, USA

Mechanical Behavior: Obtaining the mechanical properties of neurological tissues, including those of the brain and spinal cord related to studies of SCI, is difficult for many reasons: *in-vivo* methods can be logistically and ethically challenging; their low stiffness makes harvesting and experimentally testing *ex-vivo* samples complicated; and their properties degrade relatively quickly following death [109–111]. While most reports on the effect of time post-mortem on neurological tissue structure and mechanical properties show no significant changes within the first 3 – 6 hours [101,110–112], some researchers suggest much shorter testing time frames [113,114]. Further, the behavior of neurological tissues has been shown to depend on numerous experimental parameters including load modality (e.g., compression, tension, or shear), strain-rate, preconditioning protocol, and donor age. However, these effects have been studied almost

exclusively in brain tissue and the relative influence of each effect remains controversial [101,113,115,116].

Since it requires dissection of the spinal cord, only *ex-vivo* mechanical tests of isolated spinal gray and white matter have been reported. Samples have been tested using a pipette aspiration method [114], in tension using a traditional materials testing system [94,95], and in indentation and tension using atomic force microscopy [100]. White matter samples have also been tested in unconfined compression [113]. Although both tissues have been shown to exhibit hyper-viscoelastic behavior (or non-linear elastic time-dependence) [94,100,113,114], linear elastic moduli are typically reported and used as inputs for FE models [95,114]. The above studies reported conflicting relationships between isolated gray and white matter properties. Ozawa et al. [114] and Ichihara et al. [94,95] both used a combined experimental and FE modeling approach (in which the material properties assigned to the tissues in the FE model were adjusted until the predictions matched experimental values), but the studies reported different results. Ozawa et al. reported both tissues have an elastic modulus of approximately 3.5kPa, while Ichihara et al. reported a much stiffer response for both tissues, with a higher modulus for gray matter than white matter when 5% – 35% strain is applied to the tissues. These discrepancies may be due to differences in testing method and range of applied strain analyzed [94,95,114]. Atomic force microscopy has also reported a stiffer response for spinal gray matter than white matter at the cellular level [100]. While Ozawa reported no significant effect of testing direction (transverse, coronal, or sagittal) [114], atomic force microscopy has showed spinal white matter to be transversely anisotropic [100], which may reflect the alignment of axons into longitudinal tracts.

In perhaps the most in-depth analysis of isolated white matter mechanical properties, Sparrey et al. reported the effects of strain-rate, preload, and peak strain on peak stress and hyperelastic fitted parameters in unconfined compression [113]. It was found that experimental variability was partially influenced by time post-mortem and sample aspect ratio (i.e., diameter/height), but not the use of a preload. Despite experimental variability, the peak stress was shown to increase with increasing strain-rate (across the range of 0.005/sec – 5.0/sec) and the use of a preload. The two fitted parameters of the Ogden hyperelastic model were also influenced by strain-rate, the use of a preload, and the peak strain. Finally, the study also reported the optimized coefficients of a quasi-linear viscoelastic model of the tissue [113]. A different viscoelastic formulation for white matter and gray matter was reported by Ichihara et al. to characterize the tensile response [94].

1.4.2 Isolated Pia Mater, Arachnoid Mater, and PAC

Composition and Structure: As discussed briefly in Section 1.2.1, the pia mater is the innermost of the meninges and closely follows the surface of the spinal cord. The thin membrane is composed mainly of type I and type III (reticular) collagen fibers embedded in an amorphous matrix with some elastin fibers present [21,117–119]. While some studies have described it as a two-layer structure, the composition and organization of each layer is debated [21,118]. Using various microscopy techniques, spinal pia has been characterized as a loose connective tissue with no dominant fiber orientation [21,117]. However, a recent polarized light microscopy study of the rat pia mater found three longitudinally aligned bundles of collagen and reticular fibers [119]. Although considered by some to be distinct from the pia mater, denticulate ligaments run along each lateral surface of the pia mater at the cervical and thoracic levels. Described as dense longitudinally-aligned collagenous strips, the denticulate ligaments tether the pia mater and

underlying spinal cord to the dura mater through 21 pairs of small triangular extensions which provide lateral stability [119–122].

At the cranial level, a network of small trabeculae separate the arachnoid and pia maters, creating the subarachnoid space that contains CSF and vasculature; this network of collagen and elastin fibers creates a web-like appearance which gives rise to the name "arachnoid" matter [15,20,21,99,122,123]. While this trabecular network is thought to not be as extensive at the spinal level, it serves the same purpose. In the human spine, two main arteries (the anterior spinal artery in the anterior median fissure and posterior spinal artery the posterior median sulcus) traverse the subarachnoid space to supply the spinal cord. The ovine spine features a similar ventral spinal artery, but may have one main or two smaller equally spaced dorsal arteries [32,78]. In addition to the longitudinal alignment of axons in the spinal cord white matter and collagen in the denticulate ligaments, these major blood vessels may also contribute to the anisotropic behavior of the SCPC.

An analysis of the ultrastructure of the leptomeninges at the spinal level shows that at there is pia and arachnoid cell overlap within the trabeculae and denticulate ligament extensions, with collagen fibers extending continuously from one tissue to the next [21,122]. This intimacy between the two tissues often results in them being referred to together either as the leptomeninges or the pia-arachnoid complex (PAC) [21,122,124,125].

Mechanical Behavior: Due to challenges in collecting and mechanically testing such thin tissues (reported as approximately 200 μm for human spinal samples [21], 24 μm for bovine cranial

samples [124], 130 μm for porcine spinal samples [59], and 12 μm for rabbit spinal samples [118]), reports on the properties of isolated leptomeninges are rare. This paucity of information is compounded by the fact that poorly described dissection techniques may result in the mechanical behavior of the PAC being attributed to the pia mater alone. Due to differences in the relative size of subdural and subarachnoid spaces between cranial and spinal meninges, such identifications may depend on the source of sample [15,126]. To the author's knowledge only two groups have previously published the results of mechanical tests performed on what is identified as isolated spinal pia [59,117]. It should be noted that since the PAC is collagen-based, there is less concern of rapid post-mortem degradation (as compared to neurological tissues), but testing temperature and humidity are still influential [59,117,124,125].

In 1978, Tunturi reported "the pia mater [of the dog thoracic spine] and its loose connective tissue were easily stripped from the cord after a longitudinal incision" but did not mention the arachnoid mater. This previous study tested samples of the tissue isolated in incremental longitudinal elongation and only reported its qualitative elastic behavior until failure at approximately 30% strain [117]. In 2006, Kimpara et al. included the results of "a series of tensile experiments using porcine [cervical] pia mater" but gave no detail on the collection of samples beyond that it was carefully peeled away from the spinal cord. Figure 1.8 indicates the three anatomical collection sites of the 20 mm by 1 mm samples that were tensioned-to-failure at strain-rates of 0.005, 0.05, or 0.5/sec. The resulting stress-strain curves were fit to a linear model determine the elastic modulus for each of the 9 combinations of site and strain-rate. For all three sites, the average elastic modulus increased with strain-rate although no statistical analysis was performed to determine the significance of these increases. Differences between sites were

determined to be due to inclusion of the denticulate ligament or holes from exiting nerve roots in the test samples. Kimpara et al. went on to use 39.3MPa as the modulus for the pia mater and 63.9MPa as the modulus for the denticulate ligament in their FE model. Similar to the results reported by Tunturi, the tissue was found to fail at approximately 35% strain [59].

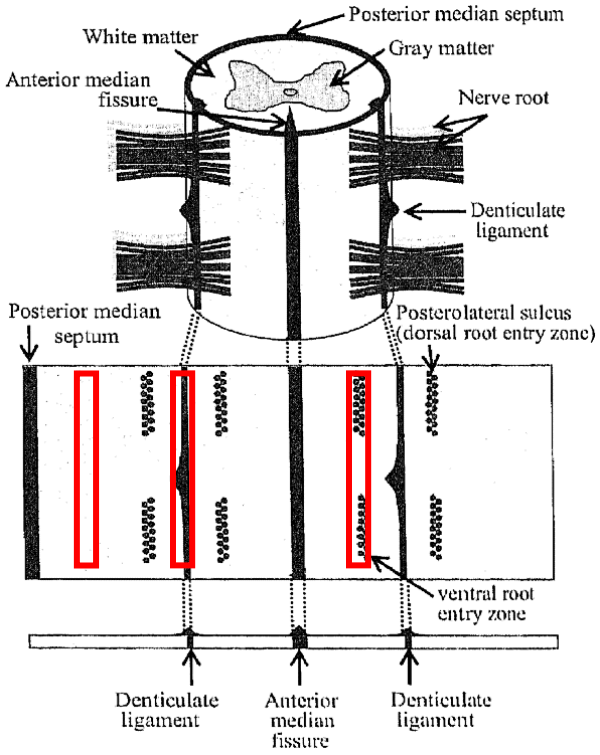

Figure 1.8: Kimpara et al. tested porcine spinal pia mater from three sites (identified by the red boxes) in tension-to-failure at one of three strain-rates. Reprinted with permission from Kimpara et al. [59]

In contrast to the scarcity of information on spinal PAC, Jin et al. has published numerous reports of the mechanical behavior and associated material models of bovine cranial PAC [123–127]. Aimedieu et al. also published preliminary results of tensile experiments on bovine cranial pia mater, but only reported bi-linear tissue stiffness as cross-sectional area measurements were not obtained [128]. Interestingly, both groups reported similar specimen preparation techniques but differed in the nomenclature used to describe the tissue collected (PAC versus pia mater). This

preparation technique involved removing the skull (which is assumed to also remove the dura mater), laying a sheet of paper or polyethylene on the exposed brain surface, cutting around this sheet into the brain, harvesting this construct from the cranial cavity, and carefully removing the brain tissue from the opposite surface following immersion in saline [123–125,128].

Unlike the Aimedieu study, Jin et al. utilized a histological procedure to measure the thickness of the PAC (reported as 23.6 ± 5.8μm [124,125]), which allowed for *post-hoc* calculation of engineering stress. Jin et al. also reported a bi-linear behavior for the cranial PAC under tension as shown in Fig. 1.9, with an average initiation of failure at approximately 26% strain [124]. Tests at 0.05, 0.5, 5, and 100/sec strain-rates showed the tangent modulus of both linear regions and the ultimate stress to be strain-rate dependent above 0.5/sec. The elastic moduli of the high-strain linear region were approximately 7 MPa, 8 MPa, 11 MPa, and 40 MPa, for each of the respective strain-rates. Tests in two orthogonal directions (coronal and sagittal) revealed no significant effect of sample orientation [124] which supports the contention that cranial PAC has no dominant in-plane fiber alignment. Jin et al. went on to develop material models to represent the transversely isotropic viscoelastic behavior of the bovine cranial PAC in tension, normal traction, and shear [123,125–127].

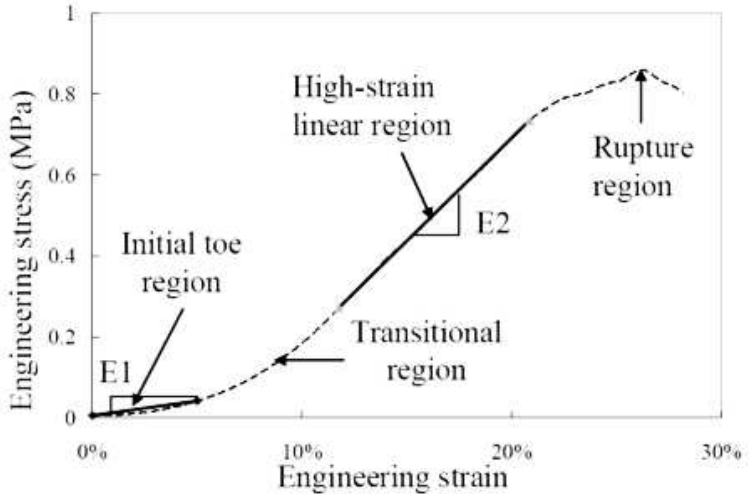

Figure 1.9: Jin et al. reported a non-linear relationship between stress and strain for cranial PAC under uniaxial tension-to-failure; the two elastic moduli (E1 and E2 shown above) were found to be strain-rate dependent over 0.5/sec. Reprinted with permission from Jin et al. [124]

Another experimental approach, which avoids testing the PAC itself, is to infer its mechanical properties by removing its contribution to SCPC behavior [105,118]. In this method, the results of mechanical tests on the spinal cord with the native PAC intact (i.e., on the SCPC) are compared to those obtained when the PAC is cut [105] or completely removed [118]. Mazuchowski and Thibault reported a 16-fold decrease in elastic modulus under longitudinal tension once three circular incisions were made through the pia mater [105]. Ozawa et al. measured the incremental transverse elongation of spinal cord segments with and without the pia mater and determined a 3-fold difference in elastic moduli. By histologically measuring the tissue thickness (reported as 12 ± 3μm) and representing the composite SCPC as a Voigt mechanical model, the elastic moduli of the pia mater was calculated as 2.3MPa (460 times that of the cord with the membrane removed). Ozawa also demonstrated a significant decrease in transverse compressive stiffness and recovery of cross-sectional shape following removal of the pia mater [105,118]. As with other studies, no mention of the arachnoid mater was made so it is unclear if the initial tests included both intact

leptomeninges or just the pia mater. However, the results from these studies demonstrate that the leptomeninges play an important role in the mechanical behavior of the SCPC.

1.4.3 Spinal-Cord-Pia-Arachnoid Construct (SCPC)

Composition and Structure: The majority of "spinal cord" mechanical properties reported in the literature are obtained from tests of constructs containing the neural tissues of the cord itself and the intact pia (and likely arachnoid) mater. Detailed descriptions of the composition and structure of each component is discussed above in Section 1.4.1 and Section 1.4.2. As previously stated, the pia mater closely envelops the spinal cord which makes its removal without damaging the underlying cord tissue difficult. As most publications do not mention the meninges beyond indicating the removal of the dura mater, it is typically assumed that the arachnoid mater is either removed as a part of the dura mater or does not sufficiently influence the measured mechanical properties to warrant inclusion in the experimental description. Unless explicitly stated, the following mechanical properties are assumed to be that of the spinal cord with intact pia and arachnoid maters (SCPC), but void of the dura mater.

Mechanical Behavior: In contrast to the relatively limited number of publications on the mechanical behavior of isolated spinal white matter, gray matter, and PAC, the SCPC has been studied under various loading conditions by numerous researchers. It should be noted that since the SCPC includes the spinal neural tissue, experimental parameters such as loading modality (e.g., compression, tension, or shear), strain-rate, preconditioning protocol, and time post-mortem are all expected to influence the resulting behavior to some degree.

Compressive SCPC Properties: Although many animal models involve transverse compression of the SCPC in order to create contusion or contusion-compression SCI, the only mechanical parameters typically recorded are those related to the creation of consistent injuries (e.g., time, force, and displacement). Since the primary goal of such animal modeling is to study the resulting pathology and evaluate possible therapeutic interventions (as opposed to the determination of specific mechanical properties), resulting mechanical data or tissue material models are rarely reported [101,129,130]. However, the force-displacement data that is reported is sometimes used to validate FE models [42,43,45,93]. In 1982, Hung et al. reported the non-linear stress-strain behavior of the *in-vivo* feline SCPC under gradually applied (quasi-static) transverse compression [70]. Although only reported for one animal, the compressive elastic moduli was constant at approximately 2kPa up to 10% strain before increasing to approximately 15kPa at 30% strain [70]. In contrast to the quasi-static loading rate used by Hung et al., Fradet et al. tested *ex-vivo* porcine SCPC sections in transverse compression at strain-rates of 0.5/sec, 5/sec, and 50/sec [38]. Based on ramp-to-damage tests, the strains at which damage occurred (73%, 68%, and 64%, respectively) and linear elastic moduli (5.5Pa, 8.4Pa, and 9.4Pa, respectively) were both strain-rate dependent. The results of cyclic tests performed at the same strain-rates showed the SCPC viscous response was also rate-dependent [38].

Tensile SCPC Properties: Tensile testing of the SCPC is much more common than compression. In 1978 and 1980, Tunturi provided initial evidence of the viscoelastic nature of the construct by providing the stress-strain and stress-relaxation behavior of the *ex-vivo* canine SCPC under incrementally applied tension [101,117,131]. As discussed briefly in Section 1.3.2, Hung et al. and Chang et al. measured the *in-vivo* stress-strain [69,88,90] and/or stress-relaxation [91] response of feline

[88,90,91] and canine [69] SCPC under tension. In these *in-vivo* studies, the dura mater was cut open at the level of testing, the CSF was drained, and rings were glued onto the exposed SCPC surface which interfaced with the materials testing stand (Fig. 1.10) [69,88,90,91]. At the relatively low strain-rates tested (0.0003/sec – 0.003/sec), the SCPC displayed a linear stress-strain behavior up to 5% strain, with an elastic modulus (0.25 MPa – 0.4 MPa) dependent on strain history and strain magnitude (Fig. 1.11) [69,88,90,91,101]. This viscoelastic behavior was explicitly examined by Chang et al. by measuring the stress-relaxation response of the feline SCPC under various strain-magnitudes and strain-rates [91]. Chang et al. reported linear viscoelastic behavior (i.e., strain-independent relaxation) for strains below 1%, but a non-linear viscoelastic (i.e., strain-dependent relaxation) behavior at higher strains [91]. Section 1.5 contains a comparison of viscoelastic formulations and their assumptions.

It should be noted that the linear stress-strain response reported by Hung et al. and Chang et al. *in-vivo* (Fig. 1.11) has not been observed *ex-vivo* by any other research group. It has been suggested that the lack of toe region in the *in-vivo* data may be due to a pre-strain that holds the axons and collagen fibers at a less crimped configuration [101].

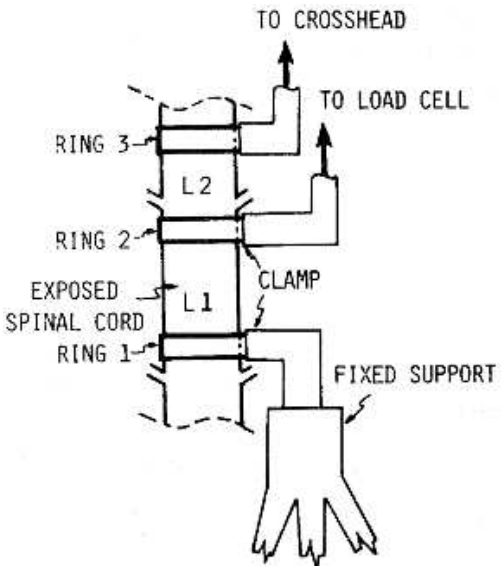

Figure 1.10: Schematic of the *in-vivo* experimental setup of Hung and Chang et al. which was used for viscoelastic characterization of the feline SCPC. Reprinted with permission from Hung and Chang [69]

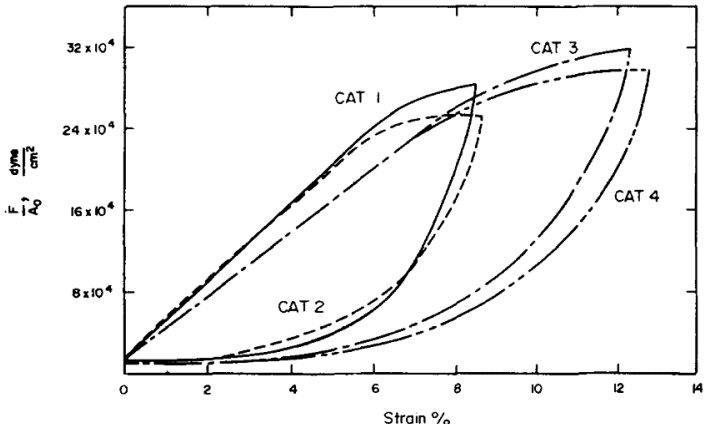

Figure 1.11: Hung and Chang et al. found the *in-vivo* behavior of the feline SCPC to be history dependent as evident in the distinct loading and unloading curves. Reprinted with permission from Hung et al. [90]

More recently, the tensile behavior of the SCPC has been investigated at higher strain-rates *ex-vivo*. Mazuchowski and Thibault reported that the neo-Hookean elastic modulus of human SCPC is insensitive to strain-rates spanning 0.2/sec – 10/sec, with an average value of 1.4MPa. It should be noted that the tests were performed up to 48 hours after death which has been reported to confound observed mechanical properties [105]. Oakland et al. reported the elastic modulus of

the bovine SCPC increased from 1.2MPa within 3 hours post-mortem to almost 2MPa at 72 hours post-mortem under identical loading conditions (0.24/sec strain-rate) [109]. Unlike Mazuchowski and Thibault, Bilston et al. [108], Fiford et al. [25], and Clarke et al. [22] have reported an increase in elastic modulus with increasing strain-rate for human, adult rat, and neonate rat SCPC, respectively (Fig. 1.12). Fiford et al. also reported that the stress-relaxation data could not be adequately represented by quasi-linear viscoelastic formulations and a fully non-linear viscoelastic model (in which the degree of relaxation depends on strain-magnitude) was necessary [25].

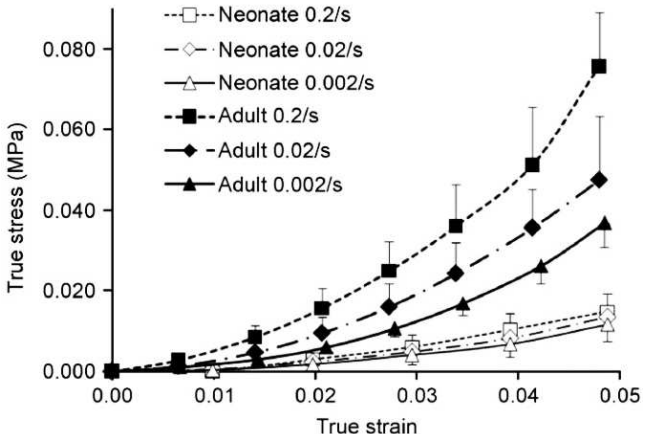

Figure 1.12: The strain-rate dependent non-linear stress-strain behavior of *ex-vivo* neonate and adult rat SCPC samples tested under tension at strain rates between 0.002 – 0.2/sec. Reprinted with permission from Clarke et al. [22]

In 2014, Shetye et al. presented the results of stress-relaxation tests of fresh porcine SCPC samples. The samples were tested in stress-relaxation to 1% – 5% strain at a strain-rate of 0.1/sec [132]. As shown in Fig. 1.13, the amount of relaxation was highly dependent on the magnitude of applied strain explicitly demonstrating the (fully) non-linear viscoelastic behavior of the SCPC [132].

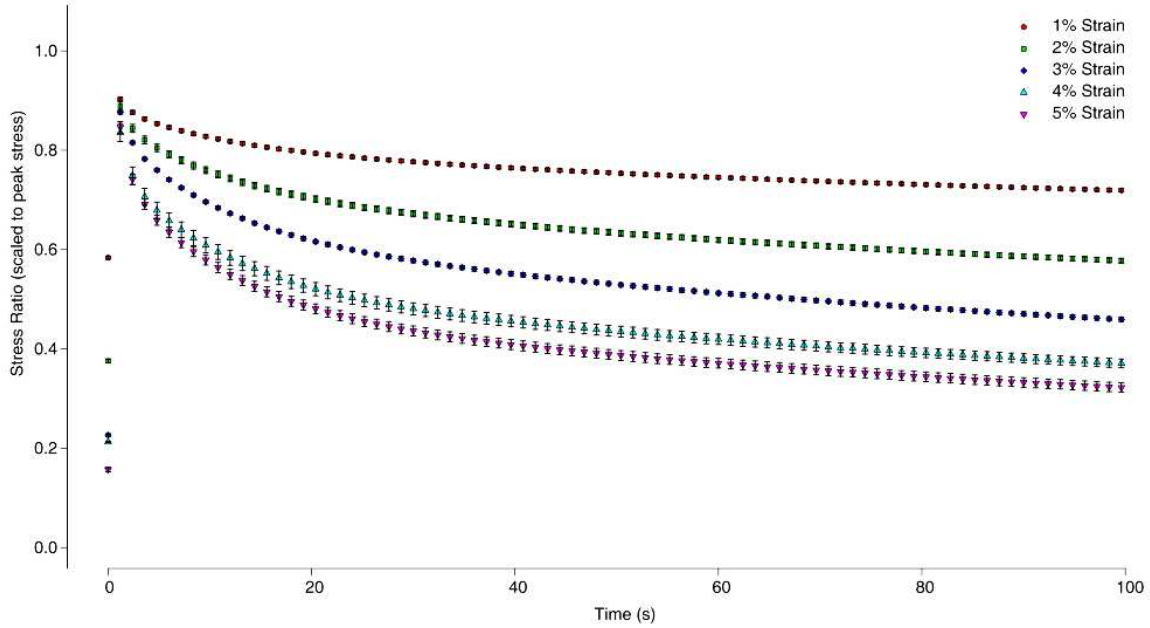

Figure 1.13: The normalized stress-relaxation response of the *ex-vivo* porcine SCPC demonstrates the strain-dependent relaxation behavior. Reprinted with permission from Shetye et al. [132]

While the previously mentioned studies investigated the response of the SCPC to longitudinal (i.e., axial) tension, Ozawa et al. reported transverse tensile properties. This study reported a non-linear stress response of the *ex-vivo* rabbit SCPC to incrementally applied transverse tension with an average elastic modulus of 16kPa [118]. Comparing this modulus to those obtained from longitudinal tensile tests supports the assumption of SCPC transverse isotropy, with a much stiffer response in the direction of white matter axon and PAC fiber alignment.

In-vivo vs. Ex-vivo Mechanical Properties: To the author's knowledge only two previous publications have attempted to directly compare the SCPC *in-vivo* response with that exhibited *ex-vivo*. It has been postulated that changes in blood perfusion, hydration, and temperature may all affect the measured mechanical properties of the SCPC [69,101]. Hung et al. compared the *in-vivo* tensile modulus to the *in-situ* modulus measured one hour after induced cardiac arrest and

reported a 22% increase [69]. The report went on to show that this *in-situ* modulus increased 14-fold when the SCPC was removed from the body and not hydrated for one hour [69]. Chang et al. explored changes in the stress-relaxation behavior of the feline SCPC following death. Despite the hydration and temperature being maintained *in-situ*, the elastic modulus and relaxation response was significantly affected by time post-mortem (Fig. 1.14) [91]. While this study demonstrated important differences between *in-vivo* and *ex-vivo* viscoelastic behavior, it did not quantify how these differences manifest in fitted viscoelastic models.

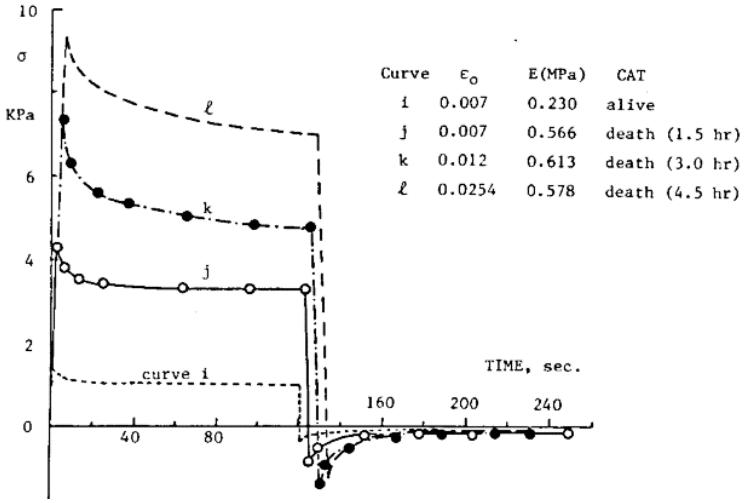

Figure 1.14: A comparison of the *in-vivo* stress-relaxation behavior of the feline SCPC to that obtained *in-situ* 1.5, 3, and 4.5 hours after death. Reprinted with permission from Chang et al. [91]

1.4.4 Spinal Dura Mater

Composition and Structure: The dura mater is the outermost of the meninges, separated from the arachnoid mater and vertebral canal surface by the subdural and epidural spaces, respectively. Although thicker, the dura mater has a similar composition to that of the pia mater – collagen fibers embedded in an amorphous matrix with some elastin fibers [133,134]. Various microscopy studies of human and animal dura mater have described it as a layered dense connective tissue

with a predominately longitudinal fiber alignment, although the degree of alignment is somewhat debated [17,133–136]. The dura is connected to the underlying meninges and spinal cord through extensions of the denticulate ligaments as discussed in Section 1.4.2.

Mechanical Behavior: Experimental and FE simulations of vertebral burst fractures have shown that the dura mater functions to shield the underlying tissues from excessive mechanical loads and reduce cord deformation during traumatic loading scenarios [52,137,138]. Given this functional importance, multiple research groups have characterized the dura's mechanical properties under various loading conditions including uniaxial tension at various strain rates [27,52,135], uniaxial tension in the longitudinal and circumferential directions [17,133,135], and quasi-static biaxial tension [34]. Taken together, these studies demonstrate that the dura mater exhibits an anisotropic viscoelastic response with a stiffness up to 100 times that of the spinal cord in tension. However, unlike other viscoelastic soft tissues, it has been reported that the dura's mechanical response is not rate-dependent at relatively low strain rates (i.e. 0.01/sec to 1/sec) [135]. As damage to the dura mater has important implications for SCI, our research group recently investigated the strain-dependent accumulation of sub-failure damage in spinal dura mater during longitudinal tension. This work has been published as a Research Paper in the ASME Journal of Engineering and Science in Medical Diagnostics and Therapy (DOI: 10.1115/1.4038261) and is included as Appendix A.

1.5 Viscoelastic Model Formulations

As discussed above, many of the investigations of spinal and meningeal tissue mechanical properties only report a tangent elastic modulus calculated as the slope of the stress-strain curve.

While such moduli may be accurate in predicting the behavior of the tissues exposed to very slow (i.e., quasi-static) strain-rates and relatively small strain magnitudes, there is explicit evidence in the literature demonstrating that these tissues display time-dependent behavior. Therefore, many groups have utilized viscoelastic formulations, which describe the time-dependent relationship between stress and strain, in order to better model the tissue response under the dynamic conditions applicable to SCI [22]. The following section introduces the types of viscoelastic theory often used to model the response of biological tissues (linear, quasi-linear, and non-linear viscoelasticity) and present the specific formulations that were utilized in this dissertation.

1.5.1 General Features of Viscoelasticity

Creep, stress-relaxation, hysteresis, and strain-rate dependent stiffness are characteristic phenomena which demonstrate the viscoelasticity of a material under study. Creep characterizes the increase in strain over time when a material is subjected to a constant stress. In a sense, stress-relaxation is the opposite behavior as it describes the decay of stress over time when a material is subjected to a constant strain (e.g., Fig. 1.13 and Fig. 1.14). While creep testing has only been performed on samples of isolated white and gray matter using atomic force microscopy [100], stress-relaxation of isolated white matter [94,113], isolated gray matter [94], dura mater [27,134], and the SCPC [22,25,91,108,131,132,139] have been reported in the literature. Hysteresis describes the dissipation of energy during cyclic loading and is manifested as distinct loading and unloading stress-strain curves (e.g., Fig. 1.11). This phenomenon has been reported for isolated white and gray matter [114] and the SCPC [69,88,90,91]. Strain-rate dependent stiffness describes the observed increase in material stiffness when loaded at higher rates (e.g., Fig. 1.12). This behavior

has been reported for isolated white matter [94,113], isolated gray matter [94], pia mater [59], dura mater [27,140], and the SCPC [22,25,38,91,108,131].

1.5.2 Linear Viscoelasticity (LV)

Since the current stress state of a viscoelastic material depends on loading history, it is necessary to define a general function that can describe the behavior under any arbitrary strain input. Such a strain input can be described by a series of discrete Heaviside-step-function changes in strain:

$$\varepsilon(t) = \sum_{i=1}^{r} \Delta\varepsilon_i H(t - \tau_i) \tag{1.1}$$

where $\Delta\varepsilon_i$ is the change in strain magnitude for the i^{th} (of a total of r) discrete strain steps which occurs at time τ_i, t is the current time, and $H(t - \tau_i)$ is the Heaviside step function. The Boltzman superposition principle can then be imposed to describe the summed effect of these strain steps on the stress response [141]:

$$\sigma(t) = \sum_{i=1}^{r} \Delta\varepsilon_i E(t - \tau_i) H(t - \tau_i) \tag{1.2}$$

where $E(t)$ is the continuous time-dependent relaxation modulus and is often modeled by the discrete Prony series:

$$E(t) = E_\infty + \sum_{i=1}^{N} E_i \, e^{-t/\tau_i} \tag{1.3}$$

where E_∞ represents the long-term equilibrium behavior, E_i is the Prony coefficient corresponding to time constant τ_i, and N defines the finite number of exponential Prony terms in the series. As the number of strain steps (r) goes to infinity, the sum converges to the hereditary integral:

$$\sigma(t) = \int_0^t E(t-\tau)H(t-\tau)\, d\varepsilon(\tau) \qquad (1.4)$$

where τ is a time variable of integration representing the history effect [141]. For $t > 0$, $H(t-\tau) = 1$ since the Heaviside function is equal to unity at any value above zero. Therefore, the stress in a linearly viscoelastic material exposed to any differentiable strain history is given by [141]:

$$\sigma(t) = \int_0^t E(t-\tau)\frac{d\varepsilon(\tau)}{d\tau}\, d\tau \qquad (1.5)$$

Linear viscoelastic (LV) models have been used previously to describe the tensile response of *ex-vivo* dura mater [27] and the *in-vivo* SCPC [91]. LV assumes a linear relationship between stress and strain at any given time (i.e., both the elastic and viscous aspects of the material behave in a linear fashion). If this assumption is valid, two main conditions will be met during stress-relaxation: 1) to satisfy the assumption of linear elastic behavior, the peak stress must vary linearly with applied strain; 2) to satisfy the assumption of linear viscous behavior, the relaxation modulus must be independent of applied strain. Figure 1.15 shows the stress-relaxation response of a LV material subjected to a range of ramp-and-hold strain inputs.

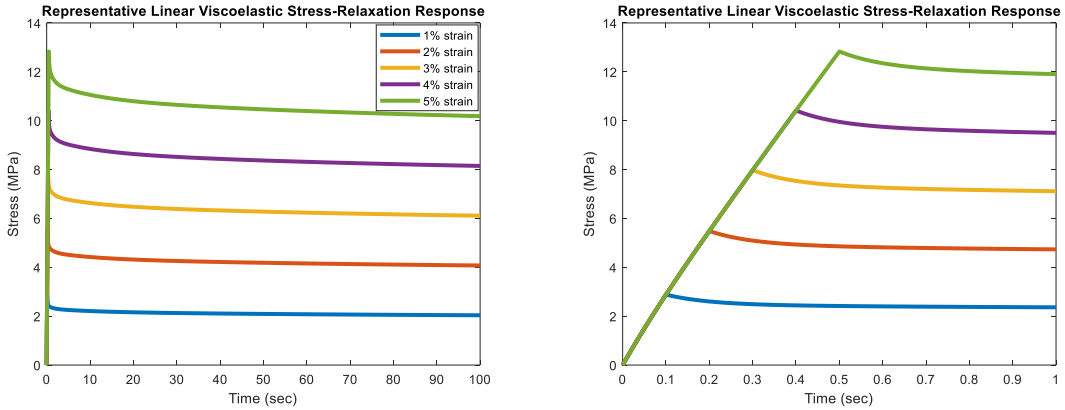

Figure 1.15: During stress-relaxation, the peak stress of a linearly viscoelastic material increases linearly with strain magnitude while the relaxation behavior does not depend on strain magnitude (right panel displays the first second of the stress response only)

However, as previously discussed in Section 1.4.3, the behavior of the SCPC violates both of the above assumptions. Although isolated PAC has not previously been examined in stress-relaxation, it is expected that (like other soft collagen-based tissues) it would also violate the above assumptions. Therefore, it is expected that constitutive models that are able to incorporate nonlinearity in the elastic response (quasi-linear viscoelasticity) or both the elastic and viscous responses (non-linear viscoelasticity) would better predict the transient behavior of the spinal tissues under study.

1.5.3 Quasi-Linear Viscoelasticity (QLV)

Compared to linear viscoelasticity, QLV formulations relax the linear elastic response constraint allowing for the incorporation of elastic nonlinearity (hyperelastic behavior). Therefore, the QLV stress response is dependent on both time and strain via the separable convolution of the linear viscous and non-linear elastic response [142]:

$$\sigma[\varepsilon(t), t] = \int_0^t G(t-\tau)\frac{\partial \sigma^e(\varepsilon)}{\partial \varepsilon}\frac{\partial \varepsilon(\tau)}{\partial \tau}d\tau \qquad (1.6)$$

where the reduced relaxation function $G(t)$ represents the linear (i.e., independent of strain) viscous behavior and $\sigma^e(\varepsilon)$ represents the non-linear elastic behavior. For the case of QLV, the relaxation modulus was represented by the following Prony series:

$$G(t) = G_\infty + \sum_{i=1}^{N} G_i e^{-t/\tau_i} \quad (1.7)$$

subjected to the constraint:

$$G_1 + G_2 + G_3 + \cdots G_N = 1 \quad (1.8)$$

QLV is a popular choice for researchers working with soft biological tissues since it allows for separate characterizations of the elastic and viscous behaviors. QLV formulations have previously been applied in studies of spinal white matter [113,143] and SCPC [108] mechanics.

1.5.4 Non-linear Viscoelasticity (NLV)

While QLV relaxes the restriction on the elastic aspect of a viscoelastic material, a linear behavior is still assumed for the viscous component. Therefore, such models are unable to capture the strain-dependent relaxation behavior (e.g., Fig. 1.13 for the porcine SCPC). As shown in Fig. 1.16, non-linear (or fully non-linear) viscoelasticity models non-linearity in both the elastic and viscous response. As the elastic and viscous behaviors of the SCPC have been shown to be strain-dependent, many research groups have developed and applied non-linear viscoelastic (NLV) formulations to their experimental data [22,25,91,132,139]. Unlike QLV, the relaxation function for NLV is modeled as a non-separable convolution integral:

$$\sigma[\varepsilon(t), t] = \int_0^t E[\varepsilon(\tau), t-\tau] \frac{d\varepsilon(\tau)}{d\tau} d\tau \quad (1.9)$$

where the relaxation modulus $E[\varepsilon(t), t]$ is now dependent on both time and strain and is responsible for describing both elastic and viscous nonlinearities. As with the LV and QLV

formulations, τ is a time variable of integration representing the history effect while t is the current time. For the case of NLV, the relaxation modulus is approximated by the following Prony series:

$$E[\varepsilon(t), t] = E_{\infty}(\varepsilon) + \sum_{i=1}^{N} E_i(\varepsilon) e^{-t/\tau_i} \qquad (1.10)$$

where the Prony weights (E_{∞} and E_i) are functions of strain.

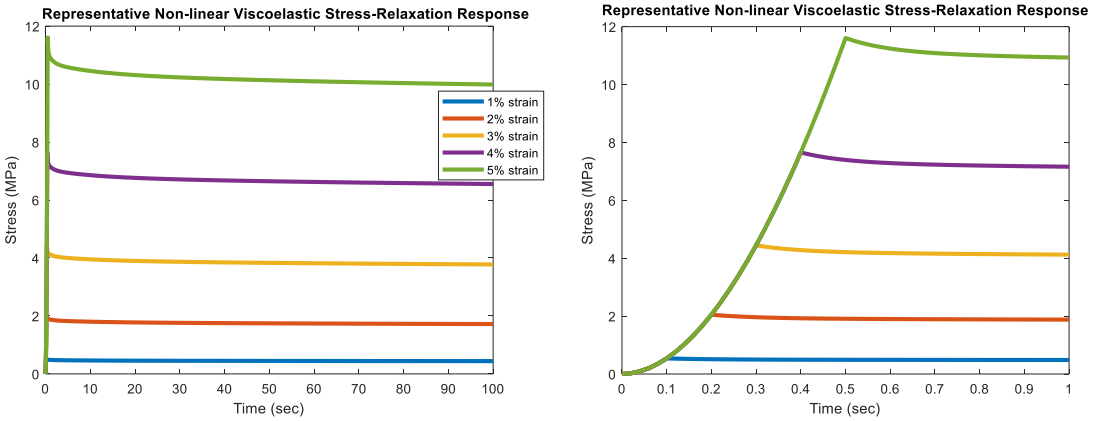

Figure 1.16: During stress-relaxation, the peak stress of a non-linearly viscoelastic material increases disproportionally with strain magnitude and the relaxation behavior depends on strain magnitude (right panel displays the first second of the stress response only)

1.5.5 Numerical Integration Method

The specific numerical integration approach (i.e., the *direct fit method*) utilized in this dissertation leverages the unique properties of the Prony series to approximate the relaxation moduli in Eq. (1.5), Eq. (1.6), and Eq. (1.9) to enable efficient calculation of the current stress from a state variable defined in the previous step. The development and validation of this methodology has been published as a Research Article in PLoS One (DOI: 10.1371/journal.pone.0190137) and is included as Appendix B.

1.6 Summary

Despite over a century of research, the prevention and treatment of spinal cord injuries (SCI continue to represent significant challenges. The complexity of the events that lead to SCI has prompted many researchers to study its mechanical etiology. Experimental and computational modeling have contributed significantly to the current understanding of the correlations between global injury mechanisms, local tissue response, and resulting neurological damage. Computational finite element (FE) models in particular allow researchers to simulate injuries that are difficult to study via experimentation using animal models or diagnose clinically (e.g., distraction or whiplash injuries) and also facilitate predictions of internal tissue stress and strain.

Appropriate use of such FE models, however, requires knowledge of the geometry and material behavior of the tissues involved. While the literature shows that the "spinal cord" is a construct of neural and meningeal tissues which exhibits non-linear viscoelastic behavior, geometric and material simplifications are frequently employed in the development of FE models. Despite evidence of its importance to both the tensile and compressive response of the construct, exclusion of the spinal pia-arachnoid-complex (PAC) is one of the most common geometric simplifications. Since the development, experimental characterization, and computational implementation of fully non-linear viscoelastic formulations are complicated and computationally expensive, material model simplifications are also common. Further, since the material properties of neural tissues have been shown to differ between *in-vivo* and *ex-vivo* conditions, even the use the non-linear viscoelastic models developed from *ex-vivo* data may not accurately reflect the behavior related to SCI.

Without quantifying the effects of the simplifications described above, FE model users are unable to make fully informed decisions about the level of complexity required to accurately simulate the mechanistic underpinnings of SCI. Therefore, the overarching goals of this dissertation are to quantify the relationship between *in-vivo* and *ex-vivo* viscoelastic properties, to delineate the mechanical contribution of the PAC to the global SCPC behavior, and to elucidate the effects of material model simplification on FE model predictions.

1.7 Specific Aims

In order to achieve the aforementioned goals, the following specific aims were proposed:

Specific Aim 1: Characterize the relationship between *in-vivo* and *ex-vivo* SCPC non-linear viscoelastic behavior.

> Previously collected data from stress-relaxation tests of porcine lumbar SCPC samples were fit to a fully non-linear viscoelastic formulation using a novel numerical integration approach. One data set was obtained from freshly excised samples (the *ex-vivo* set), while the other data set was collected from live animals under general anesthesia (the *in-vivo* set). The ability of the viscoelastic formulation to model SCPC behavior of each set was assessed by quantifying its ability to predict independently observed dynamic cyclic behavior (i.e., data excluded from initial fitting). The stress-relaxation response and resulting fitted parameters of each data set were compared to determine the extent to which *ex-vivo* and *in-vivo* SCPC viscoelastic properties differ. The results represent an important addition to the limited literature comparing *in-vivo* to *ex-vivo* SCPC viscoelastic properties.

Specific Aim 2: Determine the contribution of the PAC to the non-linear viscoelastic behavior of SCPC.

The non-linear viscoelastic properties of the *ex-vivo* ovine cervical SCPC, isolated cord, and PAC were determined using the same formulation utilized in Specific Aim 1. Freshly excised SCPC samples were subjected to a stress-relaxation and dynamic cyclic testing protocol within four hours of euthanasia. The PAC was then carefully removed from the construct and the same series of tests were performed on the isolated components. As in Specific Aim 1, independent data from each tissue were used to assess each model's predictive capability. The cyclic stress response and fitted parameters of each data set were compared to determine differences in mechanical behavior. The results were the first to quantify the non-linear mechanical behavior of spinal PAC and the first to characterize the non-linear viscoelastic properties of the isolated spinal cord.

Specific Aim 3: Interrogate the effects of viscoelastic material model sophistication on numerical and finite-element model prediction accuracy.

The data collected in Specific Aim 2 were fit to linear, quasi-linear, and non-linear viscoelastic formulations using the same numerical integration approach to determine differences in fitting ability. As in the two previous aims, these developed material models were then used to predict independent data to determine differences in predictive ability. These predictions were performed both analytically and using a FE model of each sample condition's average geometry. By comparing the computational run times and predictive accuracy of the difference viscoelastic formulations, the results provided

detailed knowledge of the trade-offs between efficiency and accuracy in modeling the behavior of the tissues.

CHAPTER 2: COMPARISON OF *IN-VIVO* AND *EX-VIVO* VISCOELASTIC BEHAVIOR OF THE SPINAL CORD[1]

2.1 Introduction

Traumatic spinal cord injury (SCI) represents a significant health challenge with approximately 20,000 new injuries occurring every year in the United States alone [1,2]. Over $7 billion is spent annually in the United States on direct costs related to SCI, including hospitalizations, medications, rehabilitation, and equipment. With the addition of $2.5 billion in indirect costs from lost productivity, the total annual financial burden of SCI is estimated to be approximately $9.5 billion [4–6]. This substantial financial impact has motivated extensive research efforts with respect to the causes, prevention, and treatment of SCI over the past fifty years. As traumatic SCI is caused by a sudden mechanical injury to the spinal column [1,2], computational models of the spine represent a powerful method for studying the effect of global loading conditions on the localized mechanics of individual spinal tissues. Finite element (FE) computational modeling allows researchers to conduct very controlled SCI simulations and examine the resultant internal tissue deformation and stress distribution [24,42–44,52]. FE models are particularly useful in studying complex human injury scenarios that are difficult to recreate and/or measure using *in-vivo* animal models (e.g., very rapid distraction seen in motor vehicle accidents). However, the predictive accuracy of a FE model for any given application is dependent on the chosen geometry, material models, and validation method [45,59,92–94].

[1] This chapter has been published as a Full Length Research Article in Acta Biomaterialia (DOI: 10.1016/j.actbio.2017.12.024). All content has been adapted with permission from Elsevier.

The choice of material model is dependent not only on the desired level of model complexity, but also on the availability of experimental data applicable to the condition being modeled. Experimentally characterizing the mechanical properties of individual neurological tissues (including those of the brain and spinal cord) is difficult for many reasons: *in-vivo* methods can be logistically and ethically challenging, their relatively low stiffness makes harvesting and physically testing *ex-vivo* samples complicated, and their properties degrade relatively quickly post-mortem [109–111]. While most reports on the effect of time post-mortem on neurological tissue structure and mechanical properties show that no significant changes occur within the first 3–6 h [101,110–112], other data suggest tissue degradation may occur over shorter periods of time [113,114]. Further, the behavior of neurological tissues has been shown to depend on numerous experimental parameters, including deformation modality (e.g., compression, tension, shear), testing direction (e.g., axial or transverse), strain-rate, preconditioning protocol, and donor age. However, these effects have been studied almost exclusively in brain tissue and the relative contribution of each effect remains controversial [101,113,115,116].

Even with use of animal models, significant financial and logistical challenges have resulted in a paucity of information in the literature regarding the *in-vivo* viscoelastic mechanical behavior of spinal tissues, including that of the spinal cord with intact pia mater and arachnoid mater. This three-part construct is commonly referred to as the ‘‘spinal cord” [22,25,69,108,109,132], but for specificity we will refer to this assembly as the ‘‘spinal cord and pia-arachnoid complex” (SCPC). Researchers that have collected *in-vivo* mechanical data from SCPC samples often used relatively low strain-rates, making the applicability of these studies to investigations of the typical traumatic spinal cord injury questionable [69,70,88,90,91]. *Ex-vivo* experimental procedures

have attempted to control temperature and humidity to best recapitulate the *in-vivo* environment, but the lack of blood perfusion and degradation over time postmortem complicate such efforts.

To the authors' knowledge, only two previous studies have directly compared the *in-vivo* and *ex-vivo* SCPC response under similar testing conditions. Hung et al. compared the *in-vivo* tensile modulus to the *in-situ* modulus in a canine model. Despite the same hydration conditions, a 22% increase in elastic modulus was reported one hour after induced cardiac arrest [69]. The report went on to show that this *in-situ* modulus increased 15-fold when the SCPC was removed and not hydrated for one hour [69]. Chang et al. explored changes in the stress-relaxation behavior of the feline SCPC following death. Even though SCPC hydration and temperature were maintained *in-situ*, the elastic modulus and extent of relaxation significantly increased with increased time postmortem [91]. While these studies elucidated important differences between *in-vivo* and *ex-vivo* mechanical properties, neither explicitly demonstrated how to extrapolate *in-vivo* properties from their *ex-vivo* experiments.

Due to the lack of a robust comparison between *in-vivo* and *ex-vivo* mechanical properties, researchers are often forced to assume simplified material properties based on the relatively low strain-rate *in-vivo* stress-strain and stress-relaxation curves or those properties based on *ex-vivo* viscoelastic testing protocols. Without knowledge of the specific viscoelastic changes that manifest *ex-vivo*, the extent to which these assumptions accurately reflect *in-vivo* SCI is unknown. An initial step towards understanding the implications of such assumptions in FE modeling of SCI is to quantify the viscoelastic changes that manifest *ex-vivo* under non-injurious conditions. Therefore, the goal of this study was to determine the relationship between *in-vivo*

and *ex-vivo* large animal SCPC viscoelastic behavior. This study fit previously published *ex-vivo* data [132], which demonstrated the non-linear viscoelastic behavior of the SCPC, and newly collected *in-vivo* data to a nonlinear viscoelastic model using a numerical integration approach. This work represents the first report of *in-vivo* non-linear viscoelastic behavior of the porcine model and the first comparison of *in-vivo* and *ex-vivo* SCPC non-linear viscoelastic behavior.

2.2 Materials and Methods

2.2.1 Ex-vivo experimentation

The details of *ex-vivo* experimental setup can be found in Shetye et al. [132], but is presented briefly herein. Six fresh thoracolumbar SCPC sections (100–150 mm in length) were harvested from six-month old female Yucatan pigs. Small sections of PCV tubing were attached to either end of the SCPC using commercial grade cyanoacrylate glue to create a construct that was approximately 60 mm in length. This construct was loaded into the two metal clamps of a custom-built horizontal uniaxial testing stand, with one clamp rigidly attached to a high resolution linear actuator (0.15625 µm step length, T-LLS105, Zaber Technologies, BC, Canada) and the other clamp attached to a stationary 44.5 N capacity load cell (Model 31, Senotec, Honeywell, Columbus, OH). Samples were immersed in a room temperature saline bath during testing to prevent dehydration. Mechanical testing of *ex-vivo* SCPC was initiated within 60 minutes post-mortem to prevent tissue degradation.

2.2.2 In-vivo experimentation

2.2.2.1 Surgical exposure

This study was performed under the approval of the Animal Care Committee of the University of British Columbia (IACUC protocol #: A16-0311). Six-month old, female Yorkshire pigs (body weights ranging from 26.5 to 34.5 kg, n = 6) were anesthetized and underwent open surgical exposure of the thoracolumbar spine. Following surgical exposure, posterior spinal instrumentation was attached to the vertebrae. Specifically, pedicle screws were rigidly attached to the vertebrae that were located adjacent to the testing site. Spinal rods were locked to the pedicle screws and provided horizontal (i.e., parallel to the axis of the SCPC) stabilization for the mechanical testing system that extended out of the surgical site (Fig. 2.1A, B). The posterior vertebral elements and local dura mater were then excised from the region to be tested (Fig. 2.1C).

2.2.2.2 Experimental setup

Consistent with the aforementioned *ex-vivo* work, small sections of PVC tubing were attached with cyanoacrylate glue to either end of the exposed SCPC region to create a sample gauge length of approximately 65 mm (Fig. 2.1C). Although a different clamping system was utilized to grip the PVC tube sections (allowing for better visualization of the surgical site), the overall testing configuration remained the same as the *ex-vivo* experiments. The uniaxial test stand described above, consisting of a high-resolution linear actuator and a stationary load cell, was lowered onto the vertical posts such that its weight was supported by the vertebrae as shown in Figs. 2.1A and B. Visual inspection ensured that the test stand and its rigidly attached clamps

aligned with the midline of the attached PVC tubing before the clamps were locked in place. The SCPC was bathed in surgical saline for the duration of the *in-vivo* experimental testing.

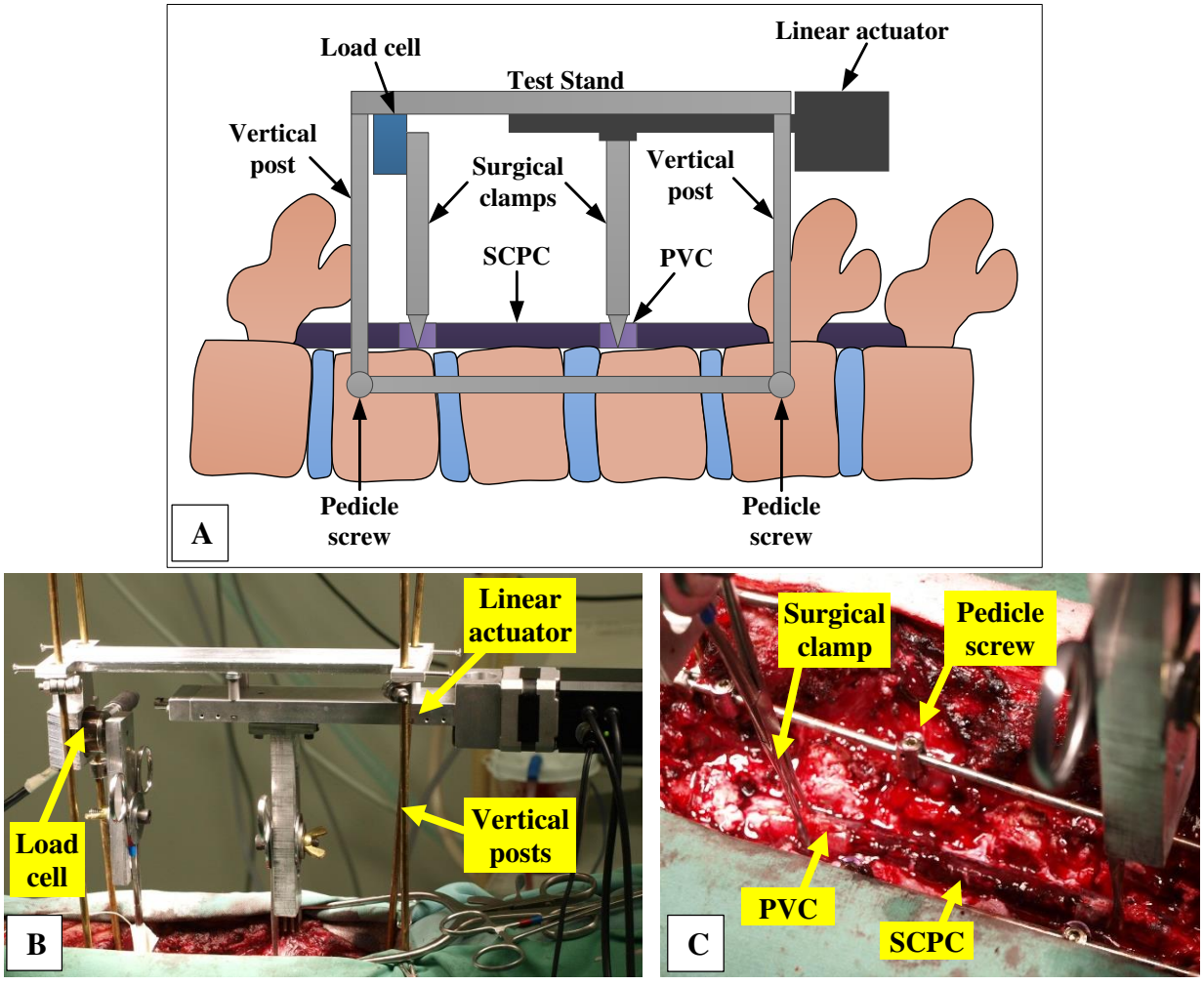

Figure 2.1: Experimental setup for *in-vivo* SCPC tensile testing. (A) Schematic of experimental setup showing pedicle screws, horizontal spinal rods, and vertical posts that provided a rigid support for the test stand. (B) Inverted uniaxial test stand was aligned with the SCPC and locked to vertical posts. (C) Local removal of posterior elements and dura mater allowed for attachment of PVC tubing and gripping by surgical clamps.

2.2.3 Mechanical testing

Nearly identical testing procedures were used for the *ex-vivo* and *in-vivo* experiments. Preconditioning to the highest strain magnitude to be tested was performed to create a consistent strain history as recommended by Cheng et al. [144] and Clark et al. [22]. For the *ex-vivo* samples,

100 cycles to 5% engineering strain at 1 Hz were applied, while the *in-vivo* samples were preconditioned for 50 cycles to 3% engineering strain at 1 Hz. The test protocol for *ex-vivo* samples included 5 stress-relaxation tests (1%, 2%, 3%, 4%, and 5% engineering strain) and 1 dynamic cyclic test (2% engineering strain at 1 Hz), while that for the *in-vivo* samples included 4 stress-relaxation tests (1%, 2%, 2.5%, and 3% engineering strain) and 1 dynamic cyclic test (2% engineering strain at 1 Hz). For both *ex-vivo* and *in-vivo* stress-relaxation tests, the ramping rate was kept constant at 6 mm/s (representing a strain rate of approximately 0.1/sec) and the relaxation time was 100 s. The order of the tests was randomized for each sample to minimize any order effects. The tissue was allowed to recover unloaded for 1000 s between each test. Prior to the start of each test, a 0.5 N preload was used to establish the gauge length for that test. A custom LabVIEW (National Instruments, Austin, TX) code was used to control the actuator and simultaneously collect resultant force data at 100 Hz from the load cell. The initial gauge length and associated input displacement necessary to obtain the required global strain level was manually recorded.

Post-hoc analysis of preliminary data from the *in-vivo* animals revealed that the external ventilation created breathing artifacts in the recorded force data. Therefore, ventilation was paused during the first and last 7 s of the *in-vivo* tests.

After testing was complete, and the animal euthanized for the *in-vivo* case, the mid-substance of the SCPC sample was cut into 4 sections and imaged with a 10MP digital camera. The cross-sectional area of each SCPC section was measured using ImageJ (National Institutes of Health, Bethesda, MD), and the average of the four measurements was used for *post-hoc* engineering

stress calculations for each sample. Strain data were calculated using the actuator displacements relative to the measured sample gauge lengths, and therefore, reflected the desired global strain magnitude.

2.2.4 Viscoelastic modeling

2.2.4.1 Model formulation

Our group has previously published data demonstrating the non-linear viscoelasticity of the *ex-vivo* SCPC [132], and the results of fitting this data to a non-linear viscoelastic formulation using the Comprehensive Viscoelastic Characterization (CVC) method [132,145–147]. The CVC method corrects for finite ramp times during stress-relaxation experiments and determines the strain-dependence of each Prony weight *post-hoc* by plotting the fitted Prony weights as a function of strain [132]. The formulation presented below represents a new characterization technique (called the *direct fit method*) that allows for direct determination of the strain-dependence of fitted Prony weights using a numerical integration approach that avoids the need to store the stress value at every previous time point of the analysis. Below we provide an abbreviated derivation of the novel features of the *direct fit method* with additional details on the derivation of the formulation provided in [148].

Uniaxial non-linear viscoelastic material behavior may be represented by the hereditary (or convolution) integral [149–151]:

$$\sigma[\varepsilon(t), t] = \int_0^t E[\varepsilon(\tau), t-\tau] \frac{d\varepsilon(\tau)}{d\tau} d\tau, \qquad (2.1)$$

where σ is stress, ε is strain, t is time, τ is a time variable of integration representing the history effect, and $E(t, \varepsilon)$ is the material's relaxation modulus that describes the non-linear time

dependent relationship between stress and strain. The continuous relaxation spectrum is approximated by the discrete spectrum Prony series:

$$E[\varepsilon(t), t] = E_\infty(\varepsilon) + \sum_{i=1}^{N} E_i(\varepsilon) e^{-t/\tau_i}, \tag{2.2}$$

where $E_i(\varepsilon)$ is the strain-dependent Prony weight corresponding to time constant τ_i, $E_\infty(\varepsilon)$ represents the long-term strain-dependent modulus, and N defines the finite number of exponential Prony terms. Combining Eq. (2.1) and Eq. (2.2) yields the following definition for stress at the current time, t:

$$\begin{aligned} \sigma[\varepsilon(t), t] &= \int_0^t \left\{ E_\infty(\varepsilon) + \sum_{i=1}^{N} E_i(\varepsilon) e^{-(t-\tau)/\tau_i} \right\} \frac{d\varepsilon(\tau)}{d\tau} d\tau \\ &= E_\infty(\varepsilon) * \varepsilon(t) + \int_0^t \left\{ \sum_{i=1}^{N} E_i(\varepsilon) e^{-(t-\tau)/\tau_i} \right\} \frac{d\varepsilon(\tau)}{d\tau} d\tau. \end{aligned} \tag{2.3}$$

We now introduce a history state variable that is used to recursively update the stress at each incremental time step; the history state variable at the current time t is defined as:

$$h_i[\varepsilon(t), t] = \int_0^t \left\{ E_i(\varepsilon) e^{-(t-\tau)/\tau_i} \right\} \frac{d\varepsilon(\tau)}{d\tau} d\tau, \tag{2.4}$$

such that Eq. (2.3) can be recast as:

$$\sigma[\varepsilon(t), t] = E_\infty(\varepsilon) * \varepsilon(t) + \sum_{i=1}^{N} h_i[\varepsilon(t), t]. \tag{2.5}$$

The stress at the next time step, $t + \Delta t$, is given as:

$$\sigma[\varepsilon(t + \Delta t), t + \Delta t] = E_\infty(\varepsilon) * \varepsilon(t + \Delta t) + \sum_{i=1}^{N} h_i[\varepsilon(t + \Delta t), t + \Delta t], \tag{2.6}$$

where the updated history variable is:

$$h_i[\varepsilon(t+\Delta t), t+\Delta t] = \int_0^{t+\Delta t} \left\{ E_i(\varepsilon) e^{-(t+\Delta t-\tau)/\tau_i} \right\} \frac{d\varepsilon(\tau)}{d\tau} d\tau. \tag{2.7}$$

Equation (2.7) can be expanded by use of the summation rule for definite integrals and inputted into Eq. (2.6) to yield the following expression for the stress at the next time step:

$$\begin{aligned} &\sigma[\varepsilon(t+\Delta t), t+\Delta t] \\ &\quad = \sum_{i=1}^{N} \int_0^{t} \left\{ E_i(\varepsilon) e^{-(t+\Delta t-\tau)/\tau_i} \right\} \frac{d\varepsilon(\tau)}{d\tau} d\tau \\ &\quad + \sum_{i=1}^{N} \int_t^{t+\Delta t} \left\{ E_i(\varepsilon) e^{-(t+\Delta t-\tau)/\tau_i} \right\} \frac{d\varepsilon(\tau)}{d\tau} d\tau \\ &\quad + E_\infty(\varepsilon) * \varepsilon(t+\Delta t), \end{aligned} \tag{2.8}$$

where the first integral term represents the effect of the past loading events, the second integral term represents the effect of the current loading event, and the final term represents the effect of the material's long-term (equilibrium) response. Application of the product law of exponentials, the 2nd mean-value theorem of integrals, and the central difference rule, yields the following expression for Eq. (2.6):

$$\begin{aligned} &\sigma[\varepsilon(t+\Delta t), t+\Delta t] \\ &\quad = E_\infty(\varepsilon) * \varepsilon(t+\Delta t) \\ &\quad + \sum_{i=1}^{N} \left\{ h_i[\varepsilon(t), t] * e^{-\Delta t/\tau_i} + \frac{E_i(\varepsilon) * \left(1 - e^{-\Delta t/\tau_i}\right)}{\left(\Delta t/\tau_i\right)} \Delta\varepsilon \right\}. \end{aligned} \tag{2.9}$$

Using the incremental notation $f_{n+1} = f_n + \Delta f_n$, where f is an incremental variable, f_n is the variable value at the preceding increment, and Δf_n is the current variable increment, the following incremental formulation for non-linear viscoelasticity is obtained:

$$\sigma_{n+1} = E_{\infty}(\varepsilon) * \varepsilon_{n+1}$$

$$+ \sum_{i=1}^{N} \left\{ h_i[\varepsilon(t), t] * e^{-\Delta t_n/\tau_i} + \frac{E_i(\varepsilon) * \left(1 - e^{-\Delta t_n/\tau_i}\right)}{\left(\Delta t_n/\tau_i\right)} \Delta\varepsilon_{n+1} \right\}. \qquad (2.10)$$

It should be noted that evaluating Eq. (2.9) or Eq. (2.10) at the current time step requires storage of the history state variable, $h_i[\varepsilon(t), t]$, from only the previous time step. Also, unlike the previously developed CVC method [132,145,147], Eq. (2.10) can be used to fit both cyclic and stress-relaxation experimental curves as it can be applied to any arbitrary strain history.

2.2.4.2 Fitting procedure and model assessment

As in our work with the CVC method, a 4-term Prony series was used to approximate the relaxation modulus with each Prony weight represented by a second-order polynomial function of strain:

$$E_i(\varepsilon) = C_1^{\tau_i}\varepsilon + C_2^{\tau_i}\varepsilon^2 \qquad (2.11)$$

$$E_{\infty}(\varepsilon) = C_1^{\infty}\varepsilon + C_2^{\infty}\varepsilon^2 \qquad (2.12)$$

where C_1 and C_2 are coefficients that define the strain dependence of each Prony weight, resulting in a total of 10 fitted coefficients. Decadal time constants ($\tau_1 = 0.1, \tau_2 = 1, \tau_3 = 10, \tau_1 = 100$ s) were also prescribed to capture both the short-term and longer-term aspects of the SCPC behavior. For each sample, simultaneous fits of all stress-relaxation data were performed using MATLAB's (R2014b, Mathworks, Natick, MA) fmincon function, a constrained non-linear minimization algorithm, to obtain the C_1 and C_2 coefficients for each strain-dependent Prony weight [$E_i(\varepsilon)$]. Each Prony weight was constrained to be positive and monotonically increasing in order to satisfy thermodynamic restrictions. As multiple curves were

fit simultaneously, the root mean squared errors (RMSE) for each stress-relaxation curve in the fit were summed, and this sum was minimized in the MATLAB algorithm.

The validity of the fitted coefficients for modeling the nonlinear viscoelastic behavior of the SCPC was determined by predicting the stress response of independent data that were not included in the fits. For both *in-vivo* and *ex-vivo*, the average coefficients obtained from the stress-relaxation fits were used with the average strain history of the cyclic tests to predict the average cyclic stress response. Similar to coefficient validation methods used for the CVC method [132,145,152], the predictive ability of the fitted parameters was assessed via RMSE (a global measure) and percent error (a point-wise measure) between the predicted and averaged experimental curve. These results were compared to the experimental variability of each condition by assessing the RMSE and percent error resulting from a one standard deviation from the average stress response.

2.2.4.3 Statistical methods

Statistical analyses were performed in RStudio (vd1.0.153, RStudio, Inc. Boston, MA; vR-3.4.1) with two- or three-factor repeated measures ANOVAs for assessing differences in the relaxation response data and unpaired t-tests for assessing differences in the fitted coefficients. Model residual plots were used to confirm normality and equal variance. A Tukey p-value adjustment was included for any multiple pairwise tests. The threshold for statistically significant differences was defined as $p < .05$.

2.3 Results

2.3.1 Stress-relaxation response

As shown in Fig. 2.2, both the *ex-vivo* and *in-vivo* stress-relaxation data demonstrated non-linear viscoelastic behavior as evidenced by a significant increase in relaxation with increasing strain magnitude (*ex-vivo*: total relaxation 1% < 2% < 3%, $p < .001$ for all three comparisons; *in-vivo*: total relaxation 1% < 3%, $p < .001$ and 2% < 3%, $p = .001$). Table 2.1 shows the average percent relaxation for each shared strain level at decadal time points (isochrones) after peak stress. The extent of relaxation of the *ex-vivo* samples was greater than the *in-vivo* samples at all strain levels and time points, with all differences being statistically significant except for the initial 0.1 s time point.

Table 2.1: Extent of relaxation (i.e., normalized stress response) for *ex-vivo* and *in-vivo* samples at 4 decadal time points after the peak stress. *Ex-vivo* samples displayed greater relaxation (common letters indicate a significant difference between *ex-vivo* and *in-vivo*), while both conditions displayed increasing relaxation at greater applied strain (common symbols indicate a significant difference between strain levels within the experiment group). Data presented as mean ± standard deviation. {A: $p = .048$; B: $p = .026$; C: $p = .041$; D: $p = .022$; E: $p = .002$; F: $p < .001$ G: $p = .025$; H: $p = .001$; I: $p < .001$; *: $p < .001$ for all three *ex-vivo* comparisons; +: $p < .001$ (*in-vivo* 1% vs. 3%); ^: $p = .001$ (*in-vivo* 2% vs. 3%)}

	***Ex-vivo* 1% strain**	***In-vivo* 1% strain**	***Ex-vivo* 2% strain**	***In-vivo* 2% strain**	***Ex-vivo* 3% strain**	***In-vivo* 3% strain**
0.1 sec	4.6 ± 0.9%	0.7 ± 0.6%	4.3 ± 0.7%	0.8 ± 0.8%	3.8 ± 0.7%	0.8 ± 0.7%
1 sec	10.7 ± 1.4% **A**	3.4 ± 2.8% **A**	13.0 ± 2.8% **D**	4.5 ± 3.8% **D**	13.9 ± 2.6% **G**	5.5 ± 3.5% **G**
10 sec	18.4 ± 4.0% **B**	10.2 ± 5.7% **B**	25.7 ± 7.0% **E**	13.5 ± 7.4% **E**	31.8 ± 5.5% **H**	19.2 ± 6.4% **H**
100 sec	29.0 ± 6.2% **C ***	21.5 ± 11.6% **C +**	42.6 ± 10.4% **F ***	27.1 ± 14.1% **F ^**	54.2 ± 6.3% **I ***	36.3 ± 10.4% **I + ^**

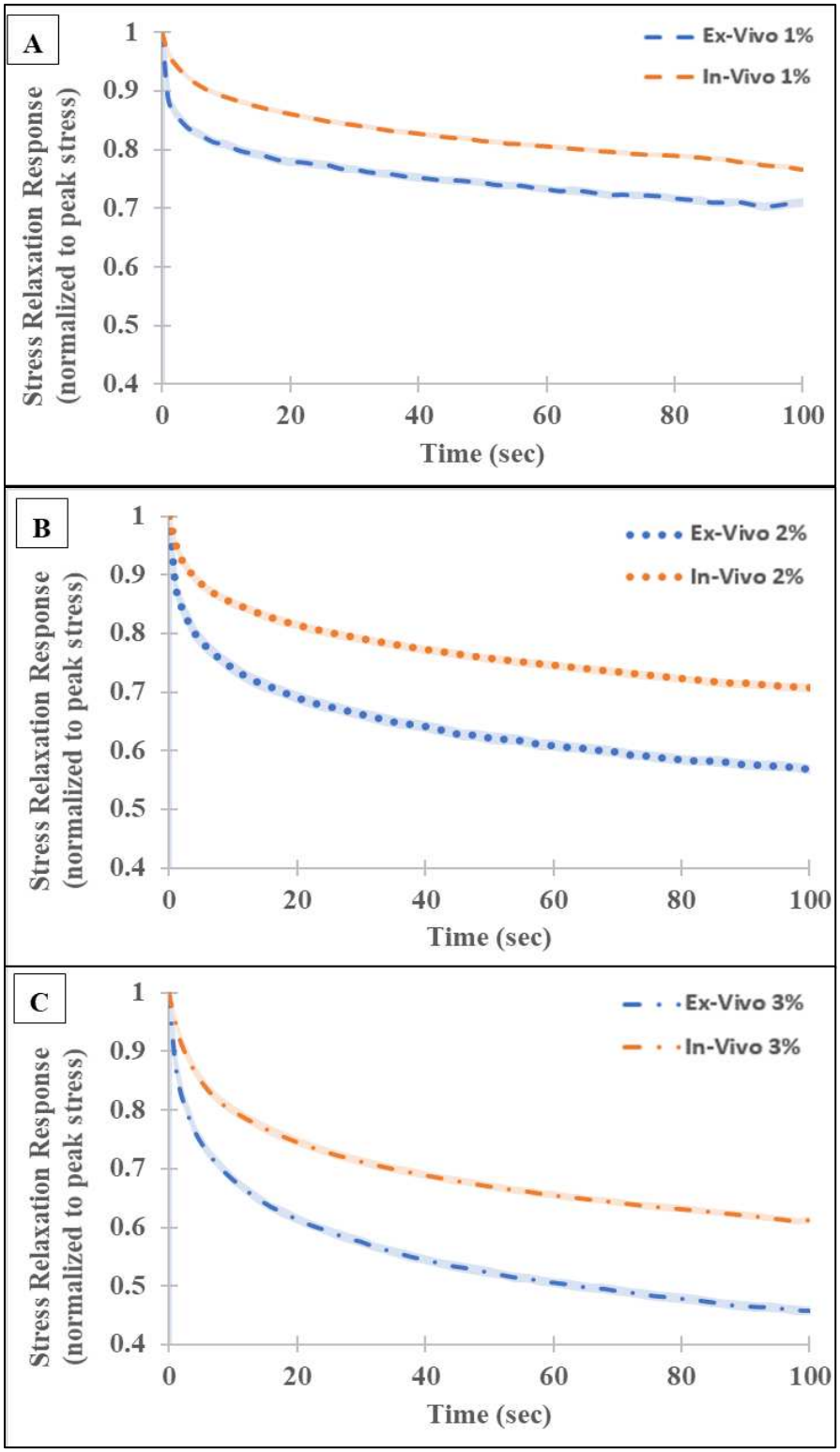

Figure 2.2: Normalized mean stress-relaxation response at (A) 1%, (B) 2%, and (C) 3% applied engineering strain demonstrate strain-dependent relaxation for both *ex-vivo* and *in-vivo* SCPC samples. At all three strain magnitudes, the *ex-vivo* samples experienced greater relaxation. Shaded regions indicate ±1 standard deviation from the mean.

Figure 2.3 displays the isochronal average stress response of the *ex-vivo* and *in-vivo* samples at five decadal time points after peak stress as a function of applied strain. At all isochrones examined during the 2% and 3% tests, the *ex-vivo* samples displayed a significantly stiffer response than the *in-vivo* samples. As expected from Fig. 2.3, the peak stresses measured during the stress-relaxation tests were also significantly higher for the *ex-vivo* samples as compared to the *in-vivo* samples at 2% and 3% strain (2%: 50 ± 10 kPa vs. 24 ± 9 kPa, $p < .001$; 3%: 72 ± 5 kPa vs. 30 ± 10 kPa, $p < .001$).

Linear fits of the isochronal data between the stress responses at the three strain magnitudes demonstrates that the slopes at the initial .01 and 0.1 s time points are significantly greater than that at the 10 s and 100 s time points for both the *ex-vivo* and *in-vivo* samples. These values were also significantly different between *ex-vivo* and *in-vivo* samples. As shown in Fig. 2.4, the rate of increase for the *ex-vivo* samples was significantly greater than that of the *in-vivo* samples at all 5 decadal time points examined.

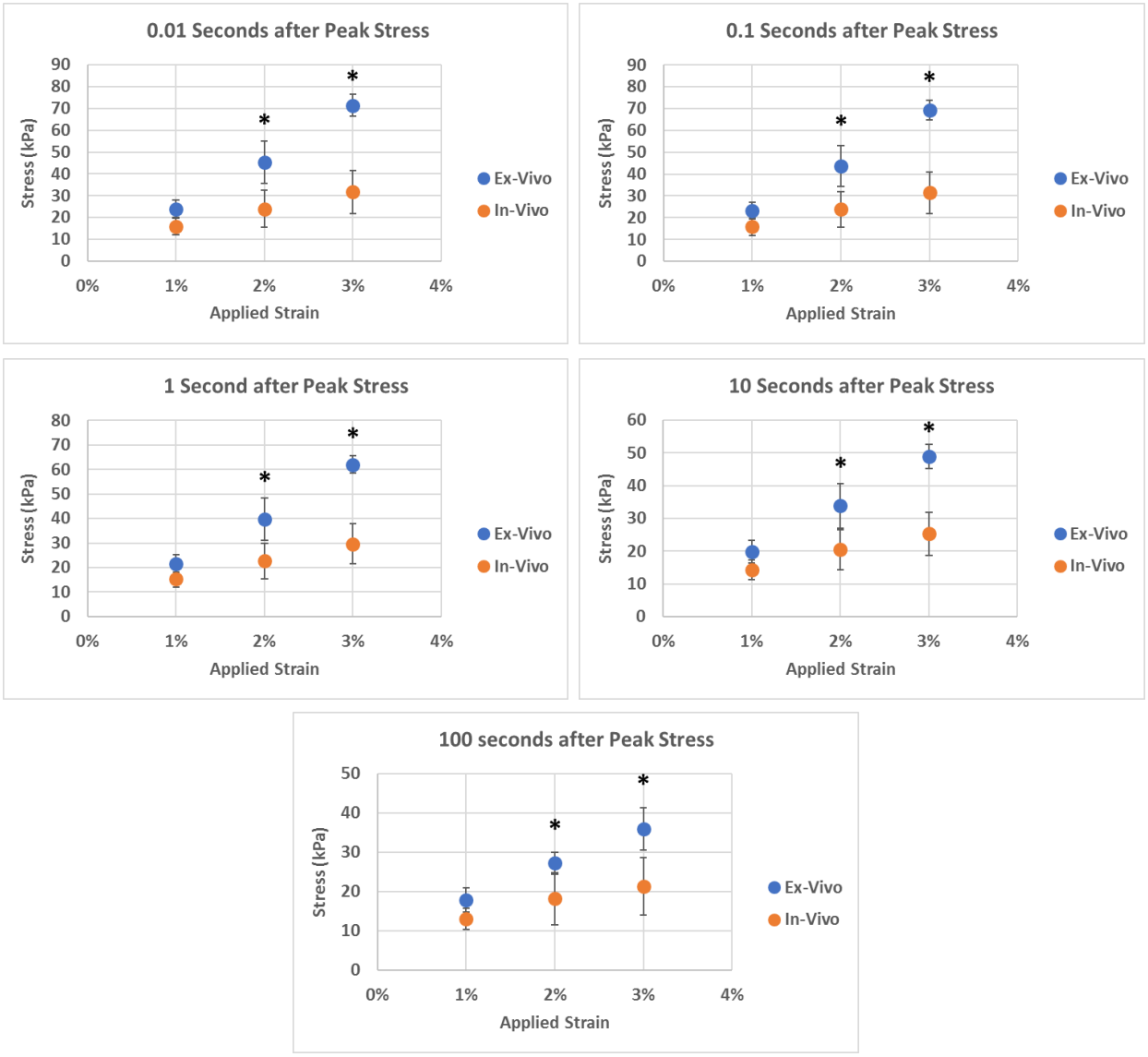

Figure 2.3: Isochronal plots of the stress response for *ex-vivo* and *in-vivo* samples at 5 decadal time points of the shared stress-relaxation tests. The *ex-vivo* samples displayed a stiffer response than the *in-vivo* samples for all isochrones of the 2% and 3% strain tests, while no difference was observed for the 1% test. * indicate a significant difference ($p < .05$) between *ex-vivo* and *in-vivo* stress response. Data presented as mean ± standard deviation at each time point and strain magnitude.

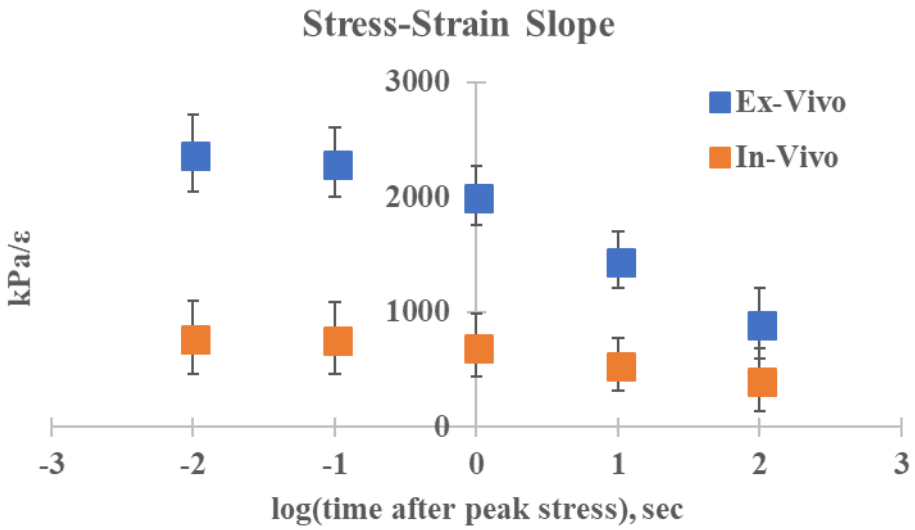

Figure 2.4: Fitted linear slopes of isochrone curves. As expected for a non-linear viscoelastic material, this difference decreases as relaxation time increases. For all 5 isochrones, the *ex-vivo* samples displayed a significantly higher strain dependence compared to the *in-vivo* samples. *Indicate a significant difference ($p < .05$) between *ex-vivo* and *in-vivo* stress-strain fitted slope. Data presented as the slope mean ± standard deviation for each isochronal curve.

2.3.2 Viscoelastic modeling

The new direct fit technique captured the stress-relaxation data well, with an average RMSE across all samples and tests of 5 kPa for the *ex-vivo* samples and 1 kPa for the *in-vivo* samples (approximately 7% and 4% of the average peak stresses, respectively). Figure 2.5 provides representative model fits for each data set. Table 2.2 provides the fitted expressions for each strain dependent Prony weight. Significant differences were found in the $C_2^{\tau_1}$ ($p < .001$), $C_2^{\tau_2}$ ($p = .006$), and $C_2^{\tau_3}$ ($p < .001$) terms; these coefficients are associated with the non-linearity of the relaxation modulus component at $\tau = 0.1$, 1, and 10 s, respectively.

As expected from the larger positive C_2 terms, the *in-vivo* relaxation modulus component is more concave at the shortest time constants (0.1 s and 1 s), while that of the *ex-vivo* condition is approximately linear (Fig. 2.6). At the 10 s time constant, the larger negative C_2 term for the *ex-*

vivo condition produces a more convex relaxation modulus component. Both *ex-vivo* and *in-vivo* curves displayed a convex response at the 100 s time constant and steady-state, with very little difference in overall steady-state response (i.e., E_∞).

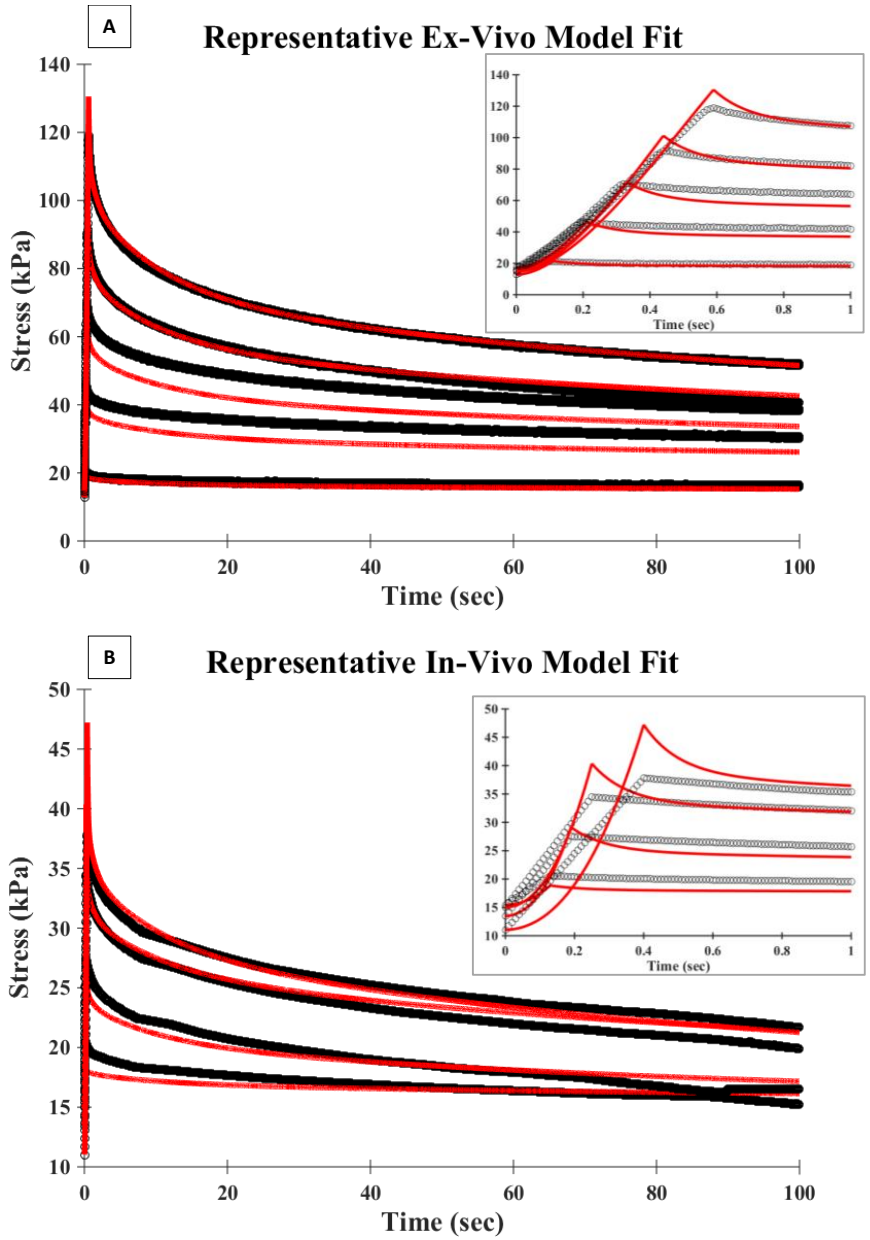

Figure 2.5: Representative non-linear viscoelastic model fits obtained using the direct fit technique for the (A) *ex-vivo* and (B) *in-vivo* stress-relaxation data. Inset plots depict the initial second of the data. In each plot, the experimental data is shown as dark circles while the model fit is a continuous red line. For each SCPC sample, all stress-relaxation data were fit simultaneously resulting in an average RMSE across all samples and tests of 4.87 kPa for *ex-vivo* data and 1.04 kPa for *in-vivo* data.

Table 2.2: Non-linear viscoelastic fitted coefficients from the numerical integration approach for *ex-vivo* and *in-vivo* conditions where $E_i = C_1^{\tau_i}\varepsilon + C_2^{\tau_i}\varepsilon^2$. The C_2 terms at the 0.1, 1, and 10 s time constants, associated with the non-linearity of the relaxation modulus component at that time constant, were significantly different ($p < .05$) between experimental groups.

All units MPa	***Ex-vivo***	***In-vivo***
$C_1^{\tau=0.1}$	67.67 ± 12.97	8.04 ± 14.71
$C_2^{\tau=0.1}$ *	**-173.39 ± 305.35**	**1207.27 ± 396.99**
$C_1^{\tau=1}$	14.83 ± 9.50	0.39 ± 0.94
$C_2^{\tau=1}$ *	**69.05 ± 200.95**	**359.8 ± 112.16**
$C_1^{\tau=10}$	40.93 ± 8.94	8.31 ± 11.83
$C_2^{\tau=10}$ *	**-383.79 ± 98.74**	**75.45 ± 298.23**
$C_1^{\tau=100}$	34.30 ± 5.24	20.11 ± 18.06
$C_2^{\tau=100}$	-399.16 ± 52.66	-159.15 ± 346.55
C_1^{∞}	11.67 ± 7.42	11.54 ± 13.01
C_2^{∞}	-115.71 ± 75.15	-93.57 ± 315.13

The coefficients from the stress-relaxation fits (Table 2.2) were used to predict the *ex-vivo* and *in-vivo* stress response from the average dynamic cyclic strain input (20 cycles to 2% strain at 1 Hz). As shown in Fig. 2.7, the predicted stresses for both cases fell well within one standard deviation of the measured stress. For the *ex-vivo* case, the prediction had an RMSE of 2.6 kPa (approximately 6% of the peak cyclic stress), which was less than the 5.3 kPa experimental variability (i.e., the RMSE of a 1 standard deviation from the mean). The percent error for the prediction was significantly lower than that resulting from experimental variability ($p < .001$). For the *in-vivo* case, the prediction had an RMSE of 2.1 kPa (approximately 8% of the peak stress), which was less than the 3.3 kPa experimental variability. The percent error for the prediction was significantly lower than that resulting from experimental variability ($p < .001$). Analyzing only the initial second of the dynamic cyclic response, the *ex-vivo* prediction had an

RMSE of 5.0 kPa (approximately 12% of the initial cycle peak stress) compared to the 7.1 kPa measure of experimental variability, while the *in-vivo* prediction had an RMSE of 2.9 kPa (approximately 11% of the initial cycle peak stress) compared to the 3.3 kPa experimental variability. The percent error over this initial second was also significantly less than experimental variability for both *ex-vivo* ($p < .001$) and *in-vivo* ($p = .001$) predictions. Comparing the average *ex-vivo* and *in-vivo* dynamic cyclic response, the greater *ex-vivo* stiffness and relaxation seen in the stress-relaxation data was also observed in the cyclic data as a higher stress response and reduction in peak stress from the 1st to the 20th cycle.

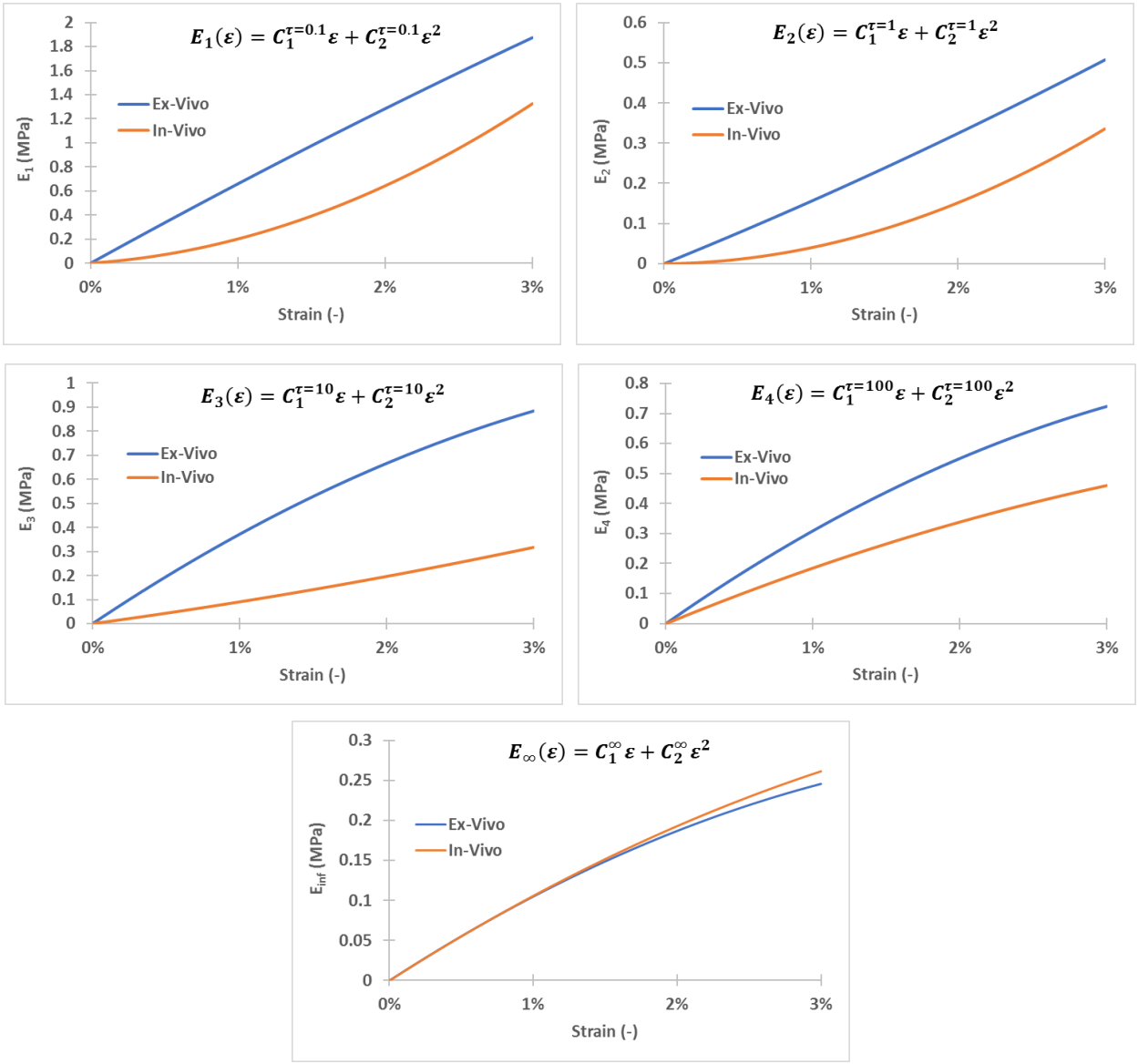

Figure 2.6: Plots of each relaxation modulus component (i.e., Prony series weight) as a function of applied engineering strain. Based on the second-order polynomial used to approximate each modulus component, the C_1 term is associated with the slope of the relaxation modulus component while the C_2 term is associated with the non-linearity. Distinct *ex-vivo* and *in-vivo* profiles can be seen at the lower time constants, while those at τ = 100 and the steady state are more similar in shape.

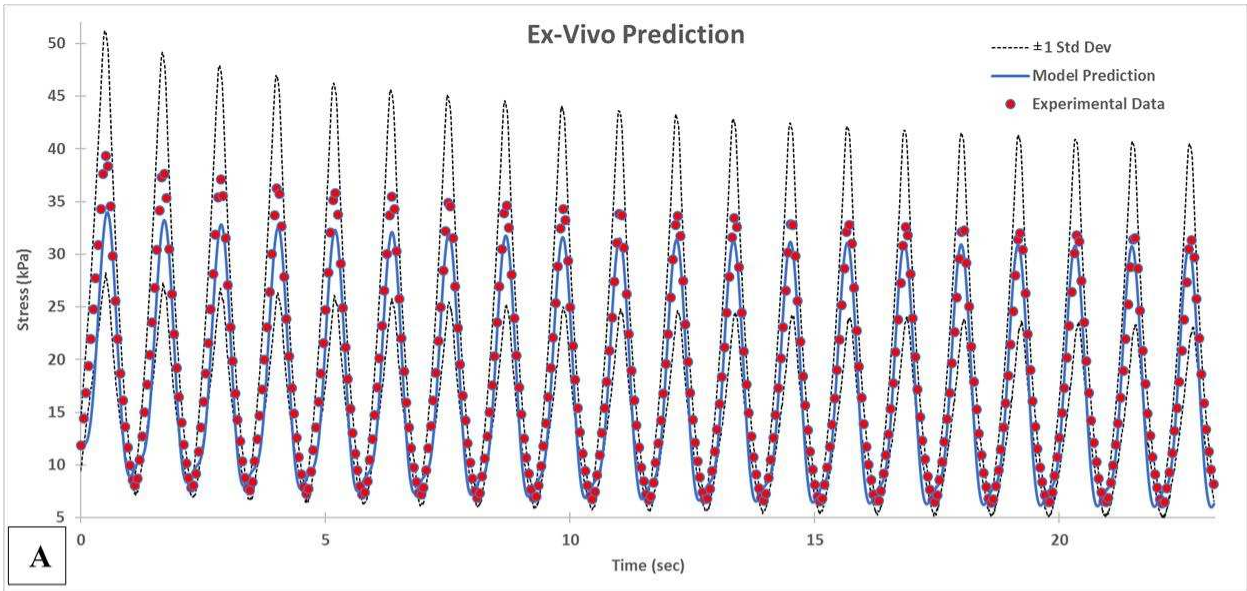

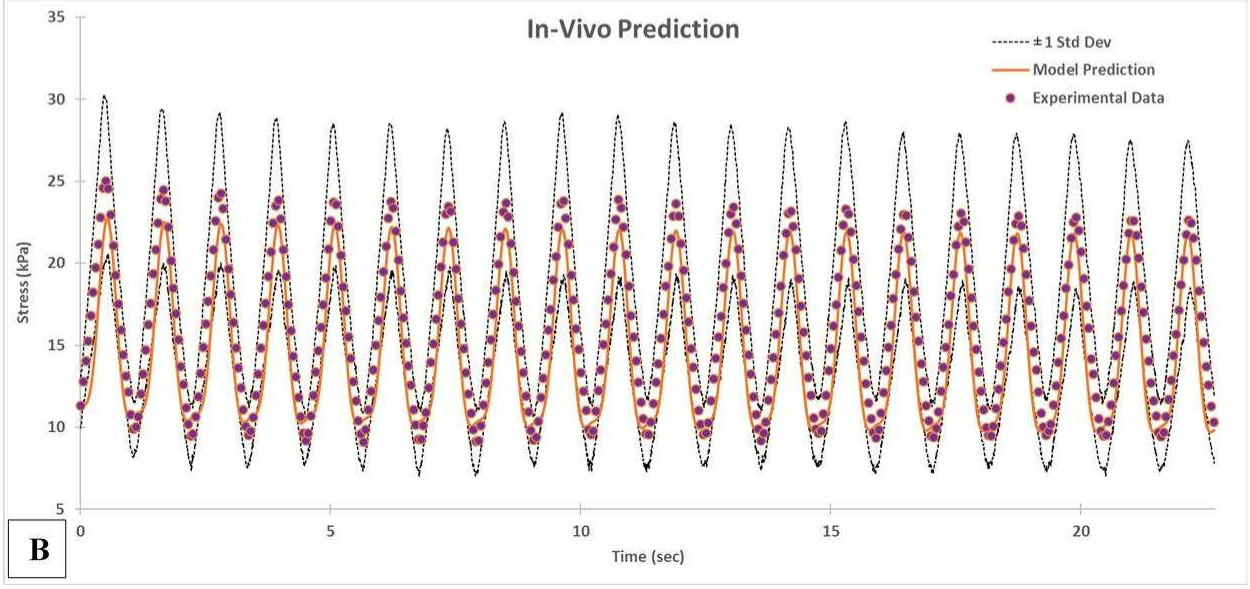

Figure 2.7: Non-linear viscoelastic model predictions of (A) *ex-vivo* and *in-vivo* (B) dynamic cyclic response to a 1 Hz, 2% strain input. Both model predictions fell within ±1 standard deviation from the respective mean experimental response (dashed lines). The frequency of the experimental average has been reduced in these plots to improve visibility of the predicted response.

2.4 Discussion

While it has been recognized that the mechanical behavior of neural tissues is influenced by the absence of blood perfusion, the post-mortem time before testing, and other conditions [101,109–

[111,115], very few studies have quantified these effects on the SCPC *in-vivo* response. Without identifying the viscoelastic changes that occur *ex-vivo*, computational models investigating spinal cord mechanics are often forced to use either the narrowly available data that has been collected *in-vivo* at relatively low strain-rates [69,70,88,90,91], or the viscoelastic models based on *ex-vivo* experimentation [22,25,38,108,132]. To surmount these shortcomings, this study is the first to quantitatively compare the non-linear viscoelastic behavior of the *ex-vivo* and *in-vivo* SCPC as well as provide validated modeling coefficients for both conditions. Consistent with previous *in-vivo* [91] and *ex-vivo* work [132], both conditions displayed nonlinear viscoelastic behavior in stress-relaxation, with greater relaxation observed at higher applied strain magnitudes. Moreover, the *ex-vivo* samples relaxed significantly quicker and to a greater extent than the *in-vivo* samples when subjected to the same strain magnitude. This increase in *ex-vivo* relaxation was also observed by Chang et al. in studies of the feline SCPC before and after death, although the specific alterations with respect to the relaxation behavior was not quantified [91]. Our isochronal data also support this conclusion of unique relaxation behavior as the difference between stress responses is significantly greater for the *ex-vivo* samples at all relaxation times examined. Therefore, the relaxation of the *ex-vivo* samples is more sensitive to increases in applied strain than the *in-vivo* samples. It should be noted that the relationship between the stress response and applied strain for each isochrone is expected to be non-linear for viscoelastic materials. However, in the current study, these relationships had strong linear correlations which may have resulted from: (1) the relatively few datum points (three total) used to fit the isochronal data, and (2) the relatively small applied strain magnitudes (1%, 2%, and 3%). Specifically, previous *ex-vivo* [22,101,108,109] and *in-vivo* [69,90] tensile studies have shown that there is a transition in elastic behavior between 2% and 4% strain; therefore, the SCPC may have been in a linear elastic

region for the current investigation, which allowed for the use of a single linear correlation to describe each isochrone. Other evidence of non-linear viscoelastic behavior is the strongly strain-dependent relaxation behavior and the strongly strain-dependent Prony weights for both *in-vivo* and *ex-vivo* samples.

The isochrones also show that at 2% and 3% strain the *ex-vivo* samples are significantly stiffer than the *in-vivo* samples and undergo a higher stress at all points of the relaxation, including the peak stress. This increase in stiffness is also consistent with data previously reported by Hung et al. in studies of the canine SCPC [69]. The fact that *ex-vivo*, the SCPC displays a stiffer response but experiences greater relaxation has important implications for SCI modeling and treatment. While it is accepted that larger applied strains result in more severe neurological deficits [26,44,50,58,61,69,88,153], the suggested injurious thresholds of 10–14% strain [44,153] do not take into account any time-dependent behavior. The results of this study suggest that the use of *ex-vivo* SCPC experimental data would lead to significant model overpredictions of the stress response in the acute time frame (i.e., at least the first 100 s of the analysis). Further, the use of *ex-vivo* characterization data would over-predict the acute relaxation due to a traumatic event (i.e., applied strain to the SCPC), and therefore, under emphasize the effect of dwell time at the applied strain. *In-vivo* studies have reported a significant effect of distraction or compression duration on neurological injury [26,39,154] suggesting that the severity of neurologic impairment is highly time-dependent. The reduction of *in-vivo* SCPC relaxation, as compared to *ex-vivo*, also supports the current clinical practice of early intervention for SCI; the removal of non-physiological strain (e.g., through anatomic reduction) as soon as safely possible has been shown to have positive effects on patient recovery [155–158].

Figs. 2.4 and 2.6 also emphasize important differences and similarities in the short-term and long-term *ex-vivo* and *in-vivo* response. Figure 2.4 shows that both conditions are most sensitive to increases in applied strain over the initial 1 s of relaxation, although to differing extents as previously discussed. Also supporting the distinct short-term relaxation behavior are the relaxation modulus component plots of Fig. 2.6. While *ex-vivo* and *in-vivo* conditions have similar relaxation responses for τ_4 and almost identical steady-state responses, the relaxation components for τ_1, τ_2, and τ_3 are more divergent. This suggests that for quasi-static analyses of SCPC behavior, the use of *ex-vivo* data may be appropriate, but attempts to accurately model dynamic or injurious scenarios should include *in-vivo* viscoelastic material characterizations.

The presented non-linear viscoelastic modeling methodology efficiently fit both *ex-vivo* and *in-vivo* stress-relaxation responses. Although the RMSE values for the *ex-vivo* fits were greater than that previously reported for CVC method fits of the same data (0.365 kPa [132]), this is expected as the CVC method fits each curve independently while the *direct fit method* fits all response curves for each sample simultaneously. It is believed that coefficients obtained from fits of all available data are more likely to reflect the average behavior of that sample, as indicated by the lower prediction RMSE for the current work compared to the previous CVC prediction (2.6 versus 3.5 kPa). As shown in Fig. 2.7, each nonlinear viscoelastic model presented was validated through predictions of the respective dynamic cyclic response whereas both predictions fell well within the range of experimental variability. It should be noted that the standard deviation values used to quantify cyclic data experimental variability were based on nonnormalized responses. Therefore, the variability of the cyclic data (Fig. 2.7) appears greater than that for the stress-relaxation data in Fig. 2.2 where the data were normalized to the peak stress before average and

standard deviation calculations were made. Although some global relaxation was captured by these predictions (*ex-vivo* prediction: final cycle peak stress 90% of initial peak; *in-vivo* prediction: final cycle peak stress 96% of initial peak), it was less than what was measured experimentally (*ex-vivo*: 79%; *in-vivo*: 90%). While developing a formulation to include an increase in the degree of global relaxation with concomitant cycle number would be one method for further improvement of the presented methodology, from a clinical standpoint, the SCPC is rarely subjected to periodic cycling of this nature and such an enhancement to the viscoelastic formulation used herein would most likely not substantially improve future modeling efforts that seek to investigate spinal cord mechanics and injury. As the goal of this work was to characterize differences in the overall viscoelastic response of the *in-vivo* and *ex-vivo* SCPC, the fitting procedure evenly weighted the data over the 100 s stress-relaxation test. This method ensured adequate fitting of the relaxation behavior and resulted in coefficients that better predicted the overall cyclic behavior than coefficients obtained by weighting the short-term (i.e., ramp-phase) data in each fit. Incorporation of a weighting function to optimize fitting of the short-term response would likely improve short-term predictions, but as indicated below, additional high rate experimentation is necessary to characterize short-term injurious behavior.

There were several limitations to this study. Firstly, the breed of pig utilized in the *in-vivo* experimental work differed than that of the *ex-vivo* work. This change was necessary based on animal availability. Previous studies have reported similar mechanical SCPC properties across several species [25,69,90,101,108,109], and any differences between two breeds of similarly sized pigs is anticipated to be negligible. Secondly, the use of global strain histories based on inputs to the linear actuator assumes instantaneous acceleration for the stress-relaxation tests and perfect

sinusoidal motion for the cyclic test, resulting in a homogeneous strain field across the length of the sample. Localized strain measurements using optical methods or micro-mechanical transducers are nearly intractable in an *in-vivo* testing environment due to blood coagulation and field of view restrictions. These methods are also confounded by mid-substance creep phenomena. As the stress response was a global measure (i.e., the reaction force at the fixed end of the sample normalized to average cross-sectional area), a global strain measure was also utilized. Further, as the same equipment and analyses were used for both the *ex-vivo* and *in-vivo* experimentation, it is unlikely that the use of localized strain measures would substantially change the conclusions drawn from the presented data. Thirdly, the temperature of the *in-vivo* and *ex-vivo* tissues during testing may have been different. The *in-vivo* tissue was submerged in surgical saline and other fluids (e.g., blood and cerebral spinal fluid) that were warmed by body temperature while the *ex-vivo* tissue was submerged in room temperature saline. As a result, the observed difference in tissue viscoelastic behavior may be due (in part) to differences in experimental temperatures. Temperature sensitivity studies of other neural tissues have revealed temperature-dependent responses in shear [159] but not in compression [160]. To the authors' knowledge, the effect of temperature on the tensile viscoelastic behavior of neural tissues has not been reported.

Finally, the strain magnitudes and strain rates examined in the current study are relatively low as compared to those values that are expected to occur during injury [44,153,161,162]. Due to difficulties in consistent gripping of the SCPC, robust tensile experimental data above 5% strain is difficult to obtain. In order to avoid such difficulties and minimize surgical time, the lower range of 1–3% strain was chosen for the *in-vivo* experimentation, and thus, was the limit for our direct

comparison with the *ex-vivo* data. Inclusion of experimental data at higher applied strains would affect the presented fitted coefficients as the strain dependence of each Prony weight is obtained directly from each fit. Indeed, even the exclusion of the 4% and 5% tests from the *ex-vivo* data fits resulted in two significantly different fitted parameters. For this reason, the comparison of stress response (e.g., the isochrones) provides more insight into the quantitative viscoelastic differences between *ex-vivo* and *in-vivo* conditions than comparison of specific fitted coefficients. As the differences were more pronounced with increasing strain, it is expected that these differences would become even more apparent at higher strains. The presented model coefficients accurately predicted the response of each condition to a strain magnitude included in the range of fits (2%), but the use of the presented coefficients to model the response to higher strains may not produce accurate predictions.

2.4.1 Conclusions

In summary, this study is the first to report a detailed quantitative comparison of *ex-vivo* and *in-vivo* viscoelastic SCPC behavior. *Ex-vivo* and *in-vivo* stress-relaxation data from the same animal model demonstrate that each condition exhibits distinct non-linear viscoelasticity at relatively low strain magnitudes (1–3%). The stress-relaxation data of each sample were fit to a non-linear viscoelastic model using a novel numerical integration approach. The resulting average coefficients were validated based on their ability to predict the respective dynamic cyclic response within experimental variability (±1 standard deviation). The significant differences between *ex-vivo* and *in-vivo* behavior underscores the necessity of *in-vivo* data collection to enable the development of more accurate material models which are applicable to studies of SCI.

Future work will also include application of the presented model to mechanical tests of *ex-vivo* SCPC, pia and arachnoid meningeal layer, and isolated cord parenchyma.

2.4.2 Funding and acknowledgements

This work was supported by the National Institutes of Health [grant number EB012048], the Monfort Family Excellence Fund, and the International Collaboration on Repair Discoveries Distinguished Visiting Scholar Program.

The veterinarian and animal-care staff at the UBC Center of Comparative Medicine are also recognized for their tremendous dedication and skill with the animals. Finally, the authors would like to thank Dr. Ann Hess of the Franklin A. Graybill Statistical Laboratory for her assistance on statistical analysis.

CHAPTER 3: VISCOELASTICITY OF SPINAL CORD AND MENINGEAL TISSUES[2]

3.1 Introduction

Traumatic spinal cord injury (SCI) is typically initiated by high-velocity, dynamic events such as traffic accidents, falls, violence, or sport/recreation injuries [1–3,7,42,49]. Due to the complex loading environments which occur during SCI, it is difficult to accurately model human injury and/or measure local tissue mechanical forces using *in-vivo* animal surrogates. In contrast, computational models provide an efficient, economical, and ethical method for investigating SCI mechanical etiology, prevention techniques, and clinical treatments. As tissue deformation and stress have been shown to correlate with injury severity and neurological impairment [23,42–47], finite element (FE) computational modeling allows researchers to conduct very controlled SCI simulations and predict the resultant internal tissue response (and associated injury severity) under various conditions [24,42–44,52]. However, it is important to highlight that the predictive value of an FE model is dependent on the implementation of accurate geometric and material models [45,59,92–94].

In the majority of FE models of the spine, the spinal cord itself is typically modeled as one homogenous material [43,51,52,67,92] or as a construct of gray and white matter regions [24,42,44–46,59,93], while explicit modeling of the innermost meningeal layers (the pia and arachnoid maters) is frequently neglected [24,42–46,51,52,67,92]. The material models assigned to the various spinal cord components vary in complexity from linearly elastic [24,42,95–98,43,46,51,52,57,92–94] to hyperelastic

[2] This chapter has been published as a Full Length Research Article in Acta Biomaterialia (DOI: 10.1016/j.actbio.2018.05.045). All content has been adapted with permission from Elsevier.

[46,51,59,67,92,93] to viscoelastic [44,45,57,94,97], or some combination thereof. The material models utilized to represent the homogenous spinal cord are often developed using experimental data collected from spinal cord samples with at least the pia mater intact [25,45,69,70,90,108]. However, as most published experimental procedures do not include detailed descriptions of dissection techniques beyond removal of the dura mater, it is difficult to determine if the arachnoid mater is also present (and contributing) to the reported results. These results are often reported as the mechanical properties of the gestalt ‘‘spinal cord”. For specificity in this work, the three-part construct of the neural and connective tissues will be referred to as the spinal-cord pia-arachnoid construct (SCPC), with the spinal cord parenchyma referred to as the cord, and the construct of the innermost meninges as the pia-arachnoid complex (PAC).

As shown by the experimental results of Ozawa et al. [118] and Mazuchowski and Thibault [105], the presence of the PAC significantly effects the mechanical response of the SCPC. Specifically, comparisons of the response before and after PAC removal show a significant decrease in the compressive [118] and tensile stiffness [105], as well as shape recovery after compression [118]. However, to the authors' knowledge, only one study has reported quantitative mechanical properties of isolated spinal PAC [59]. Unfortunately, little detail was provided with respect to the dissection of samples and only a strain-rate dependent linear elastic modulus was reported.

While some groups have included a distinct pia mater in their computational models [57,93–98,143], the lack of appropriate mechanical properties in the literature constrains the predictive fidelity of explicitly modeling this tissue. For example, in a parametric FE study of the effect of material properties on the magnitude and distribution of stress and strain in the cord cross-section,

Sparrey et al. concluded that ‘‘pia mater characteristics had limited (<4% change) effects on outcomes” [93]. However, the pia mater was modeled as a linearly elastic membrane with the tangent modulus varied from 600 kPa to 3 MPa [93]. While this range includes the modulus reported by Ozawa et al. [118], it does not include the higher stiffness values reported by Kimpara et al. for spinal pia mater [59] and by Jin et al. for cranial pia mater [127]. Indeed, a subsequent study by Sparrey which implemented the 40 MPa linear elastic modulus reported by Kimpara et al. concluded distinct modeling of the pia mater was necessary to match experimental measurements and tissue damage [143]. However, since the experimental results of Kimpara et al. and Jin et al. suggest the pia mater is a viscoelastic material, tangent moduli may not be adequate to describe its behavior under dynamic conditions. Jin et al. has published numerous studies of the viscoelastic response of cranial PAC under a variety of loading conditions [123–125,127,163], but due to differences in ultrastructure [21,122,164,165], application of these properties to spinal PAC is questionable.

Therefore, the goal of this study was to compare the viscoelastic behavior of the isolated PAC, the isolated cord, and the SCPC to determine the mechanical contribution of each component. A novel numerical integration approach [139,148] was used to develop non-linear viscoelastic material models for each of the three tissues. Each material model was then validated through predictions of an independent (i.e., not included in the original model fits) data set. The results presented herein represent the first known published account to: (1) describe the nonlinear behavior of spinal PAC; (2) characterize the viscoelastic properties of the isolated cord; and (3) publish validated non-linear viscoelastic material models for the PAC and cord. These findings will

allow researchers interested in modeling spinal cord injuries to make informed decisions about the balance of accuracy and complexity necessary for their specific modeling endeavors.

3.2 Materials and Methods

3.2.1 SCPC preparation

Eight cervical spines (C0–C7) were collected from skeletally mature (greater than 4 years old) ewes immediately following euthanasia for unrelated research studies. The spinal-cord meningeal complex, including the dura mater, was carefully removed from the spinal canal through gross dissection, use of an oscillating saw, and transection of nerve roots. As the dura mater is relatively loose at the cranial aspect (where it was previously connected to the cranial dura mater), surgical scissors were used to create a longitudinal cranial-to-caudal cut in the dura mater. Transection of denticulate ligament extensions and exiting nerve roots allowed for *en-bloc* removal of the dura mater. Before trimming the nerve roots, the surrounding PAC tissue was gently pushed back toward the SCPC surface. Vasculature and cerebral spinal fluid evident in samples collected using the above technique confirm the arachnoid mater remained intact during removal of the dura mater (Fig. 3.1A) [20,21,122,123,164,165]. After discarding any SCPC section containing visible damage, a single length of approximately 60 mm was selected for experimental testing. Two or three of these sections were typically collected from each cervical spine, but due to the time constraints associated with *ex-vivo* neural tissue experimentation [101,109–112], only one section per animal was tested. Small sections of PVC tubing (approximately 10 mm in length) were attached to each end of the SCPC section using commercial grade cyanoacrylate adhesive (Loctite Gel Control, Henkel Corporation, Rocky Hill, CT; Fig. 3.1B). Throughout the preparation process, phosphate-buffered saline spray was used to maintain tissue hydration.

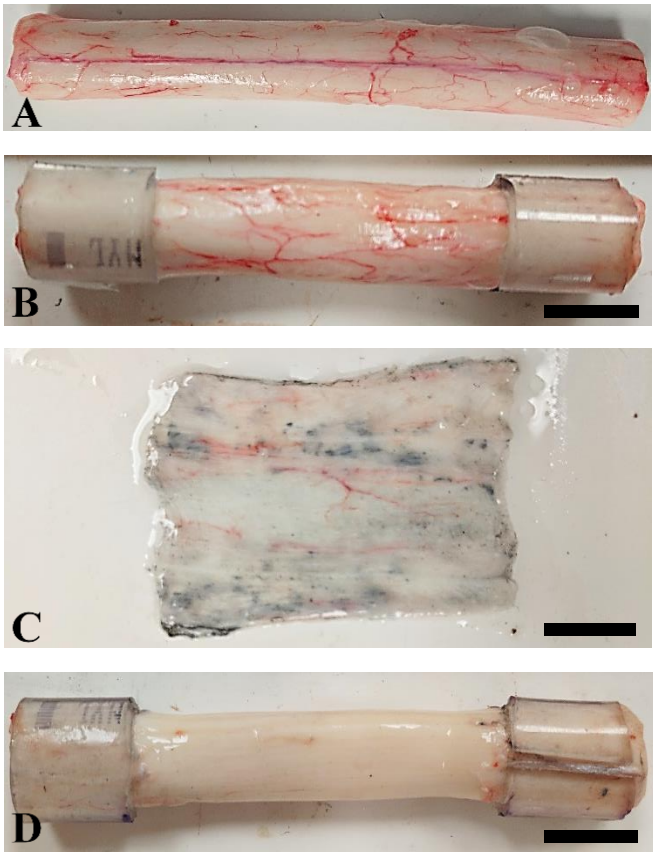

Figure 3.1: A) Fresh ovine SCPC section with small bubble of cerebrospinal fluid near right end, B) SCPC-PVC construct prepared for longitudinal tension testing, C) Sheet of isolated PAC removed from SCPC surface, the black areas are from graphite powder on opposite face of the translucent tissue, D) isolated cord devoid of PAC ready for longitudinal tension testing. All scale bars = 10 mm.

3.2.2 Experimental testing

The SCPC section was loaded into a uniaxial test stand (Fig. 3.2A) consisting of sand-paper lined metal clamps, a high-resolution linear actuator (0.15625 µm step length, model: T-LLS105, Zaber Technologies, BC, Canada), and a 44.5 N capacity load cell (Model 31, Sensotec, Honeywell, Columbus, OH) [139]. A 4.2MP camera (Grasshopper3, Point Grey, BC, Canada) was centered above the sample. Graphite powder was applied to the surface of the PVC tubing facing the camera before the first mechanical test was performed to introduce sufficient optical texture and allow for *post-hoc* calculation of displacement via digital image correlation.

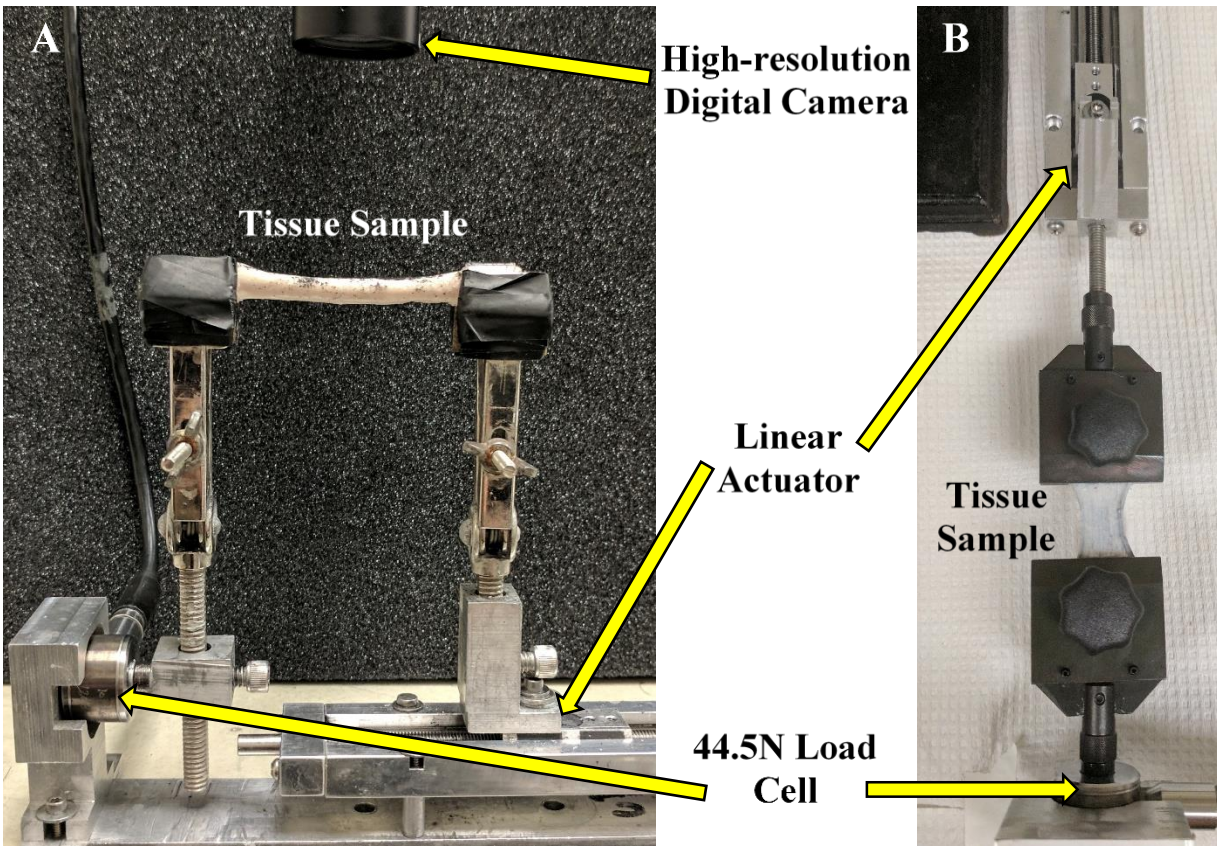

Figure 3.2: The uniaxial test stands used for SCPC, cord (A) and PAC (B) longitudinal tension testing consisted of a grip rigidly attached to a stationary load cell, a second grip rigidly attached to a high-resolution actuator, and a digital camera positioned directly above the tissue sample to enable image-based strain measurements. Apart from the grips, the same equipment was used for all SCPC, cord, and PAC tests.

Following 100 cycles of preconditioning to 5% engineering strain, two stress-relaxation and four dynamic cyclic tests (three 5-cycle tests and one 2-cycle test) were performed. Specifically, the following mechanical tests were performed in a randomized order with a 0.5 N preload (to establish reference length), a minimum of 4 min of unloaded recovery, and hydration between each test: stress-relaxation tests to 3% and 5% strain (6 mm/s ramping rate, 100 s relaxation period); dynamic cyclic tests to 5% strain at target frequencies given by $f_i = {}^{1}/_{2\pi\tau_i}$ where $\tau_i =$ 0.1, 1, 10, and 100 s (approximately 1.6 Hz, 0.16 Hz, 0.016 Hz, and 0.0016 Hz, respectively). The resulting average strain-rates for the dynamic cyclic tests are given by $2f_i\varepsilon = 0.1f_i =$

approximately 16%/sec, 1.6%/sec, 0.16%/sec, and 0.016%/sec. The lowest frequency (i.e., quasi-static) cyclic test consisted of only two cycles to shorten the overall duration of the testing procedure in order to avoid time sensitive neural tissue degradation effects [101,109–112]. Due to equipment limitations and the increase in sample length with relaxation (especially for the isolated cord), the speed required to reach the highest target frequency was occasionally unobtainable; for these cases, the maximum speed of the actuator was used. During each test, the reaction force was collected from the load cell at 100 Hz while series of images were collected from the camera at a frequency scaled to the speed of the test (between 1 and 45 frames per second). A custom LabVIEW code controlled the actuator and synchronized data collection.

3.2.3 Cord and PAC dissection and testing

Following the completion of the six mechanical tests of the SCPC, it was removed from the test stand and washed free of graphite powder using saline. Under a lighted magnifying loop, a shallow incision was made adjacent to the anterior median fissure near one of the PVC tubing sections. Small surgical scissors extended this incision to the opposite PVC tubing section, creating a longitudinal opening in the PAC. The PAC was then removed from the circumference of the SCPC in an incremental fashion by carefully lifting the edge away from the cord surface and separating it at this interface; the ends of the PAC were cut as close to the PVC tubing edges as possible. The resulting PAC sheet (Fig. 3.1C) was covered with saline soaked gauze and stored in an airtight container while the isolated cord sample (Fig. 3.1D) was mechanically tested using the same test stand and procedure outlined for the SCPC above. Following the completion of cord mechanical tests, thin cross-sectional slices taken near the mid-substance of the sample were imaged using the high-resolution camera for *post-hoc* cross-sectional area measurements

and subsequent stress calculations. All mechanical tests of neural tissue (i.e., that of the SCPC and cord conditions) were performed within 5 h of animal sacrifice. The configuration of the uniaxial test stand was then modified with the metal clamps replaced with thin film grips (FC-40, Imada, Northbrook, IL) for PAC testing (Fig. 3.2B).

Apart from a lower preload (0.25 N versus 0.5 N), the same testing procedure described above was applied to the PAC sample. Following the completion of PAC testing, images of the sample in the testing configuration and with the grips turned perpendicular to the camera were collected for *post-hoc* width and thickness measurements, respectively.

3.2.4 Data analysis

ImageJ (v1.48, National Institutes of Health) was used to perform dimensional measurements for PAC cross-sectional area calculations and direct cord cross-sectional area measurements; these areas were used to convert respective measured force data to engineering stress. The sum of the cord and PAC cross-sectional areas represented the cross-sectional area of the SCPC for stress calculations. The series of images collected during each experimental test were converted to strain data using a MATLAB-based digital image correlation program [166]. For every image, the relative displacement of each end of the sample (averaged over an approximately 200 mm^2 area) was normalized to the gauge length of the initial test image. Application of this analysis procedure to images of a surrogate material translated through the camera field of view demonstrated an error of less than 0.06% strain. Since the collection rate of the force and image data differed, a smoothing-spline was used to obtain the interpolated global strain at each time of recorded stress.

For each of the three tissues, the initial cycle of the resulting stress-strain curves of the four dynamic cyclic tests were simultaneously fit to the non-linear viscoelastic convolution integral (Eq. (3.1)) using a novel characterization technique (the *direct fit method*) that is detailed in previous publications [139,148]. Briefly, this technique allows for the direct determination of the strain-dependence of the discrete Prony series used to approximate the relaxation modulus (Eq. (3.2)) and avoids the need to store the stress $[\sigma(\varepsilon, t)]$ at all previous time points through use of a history state variable $[h_i[\varepsilon(t), t]$, Eq. (3.4)] that is recursively updated at every time step:

$$\sigma[\varepsilon(t), t] = \int_0^t E[\varepsilon(\tau), t-\tau] \frac{d\varepsilon(\tau)}{d\tau} d\tau, \tag{3.1}$$

where the viscoelastic kernel function, $E[\varepsilon(\tau), t]$, is represented as the Prony series

$$E[\varepsilon(\tau), t] = E_\infty(\varepsilon) + \sum_{i=1}^{4} E_i(\varepsilon) e^{-t/\tau_i}. \tag{3.2}$$

Using the *direct fit method*, the current stress is defined as

$$\begin{aligned} &\sigma[\varepsilon(t+\Delta t), t+\Delta t] \\ &\quad = E_\infty(\varepsilon)\varepsilon(t+\Delta t) \\ &\quad + \sum_{i=1}^{4} \left\{ h_i[\varepsilon(t), t] e^{-\Delta t/\tau_i} + \frac{E_i(\varepsilon)\left(1 - e^{-\Delta t/\tau_i}\right)}{\left(\Delta t/\tau_i\right)} \Delta\varepsilon \right\}, \end{aligned} \tag{3.3}$$

with

$$h_i[\varepsilon(t), t] = \int_0^t \left\{ E_i(\varepsilon) e^{-(t-\tau)/\tau_i} \right\} \frac{d\varepsilon(\tau)}{d\tau} d\tau, \tag{3.4}$$

where ε is the strain at the current time $(t + \Delta t)$, $E_\infty(\varepsilon)$ is the long-term strain-dependent modulus, and $E_i(\varepsilon)$ is the strain-dependent Prony weight corresponding to the time constant τ_i

(τ_1 = 0.1, τ_2 = 1, τ_3 = 10, and τ_4 = 100 s). Each of the five strain-dependent Prony weights were represented as a second-order polynomial function, resulting in a total of ten fitted coefficients:

$$E(\varepsilon) = C_1\varepsilon + C_2\varepsilon^2 \quad (3.5)$$

MATLAB's (R2014b, Mathworks, Natick, MA) fmincon function, a constrained non-linear minimization algorithm, was used to determine the set of fitted coefficients which resulted in the lowest root mean squared error (RMSE) when summed across the four cyclic curves included in the fit. In order to satisfy thermodynamic requirements, each Prony weight [$E_i(\varepsilon)$] was constrained to be positive and monotonically increasing.

The coefficients obtained from fits of the cyclic data were averaged across like samples to create one non-linear viscoelastic material model for each of the three tissues. In line with previously published validation methods [132,145,152], the ability of these developed models to predict the non-linear viscoelastic behavior of each tissue under independent loading conditions (i.e., those not included in model fits) was assessed. The RMSE and percent error between the averaged 3% and 5% measured stress-relaxation response and the response predicted by the material model were calculated and compared to the degree of experimental variability (defined by the RMSE and percent error resulting from a one standard deviation in mean response).

3.2.5 Statistical methods

SAS Studio (3.71 University Edition, SAS Institute, Cary, NC) was used to perform all statistical analyses. SAS PROC MIXED procedures were used to develop mixed linear models for cyclic peak stress measurements and fitted coefficients with the sample treated as a random effect. A logarithmic transformation was applied to the raw cyclic stress data before the analysis was

performed in order to achieve normality and equal variance (as assessed by model residual plots). A Tukey p-value adjustment was implemented for all subsequent comparisons of least squares means between the SCPC, isolated cord, and isolated PAC values.

Paired t-tests were performed to assess differences in the percent error of the model predictions and the percent error associated with the experimental variability. Statistically significant differences were defined as those resulting in $p < 0.05$.

3.3 Results

In order to mitigate the effects of post-mortem neural tissue degradation [101,109–112], all experimental tests of the SCPC and cord conditions were completed within 5 h of animal sacrifice (SCPC: mean 2.8 h, max 3.5 h; cord: mean 4.5 h, max 5 h). Based on average cross-sectional area measurements, the cord parenchyma represented 94.5% of the total SCPC area (84.22 ± 14.05 mm^2). The PAC's mean circumference and thickness were measured to be 22.24 ± 2.71 mm and 0.20 ± 0.04 mm, respectively, resulting in a mean area of 4.57 ± 1.22 mm^2.

3.3.1 Cyclic stress response

At all four cyclic frequencies tested, the PAC exhibited a significantly greater peak stress than the SCPC, and the SCPC peak stress was significantly greater than the isolated cord (Fig. 3.3). As expected for viscoelastic materials, the peak stress for all conditions increased with increasing test frequency (i.e., strain-rate). For the PAC and isolated cord, the quasi-static test stress was significantly less than that of the two highest frequency tests (1.6 Hz and 0.16 Hz). Additionally for the isolated cord condition, the 0.016 Hz tests was significantly different than the 1.6 Hz and

quasi-static test (Fig. 3.3). The increase in stress with increasing test frequency failed to reach statistical significance for the SCPC condition.

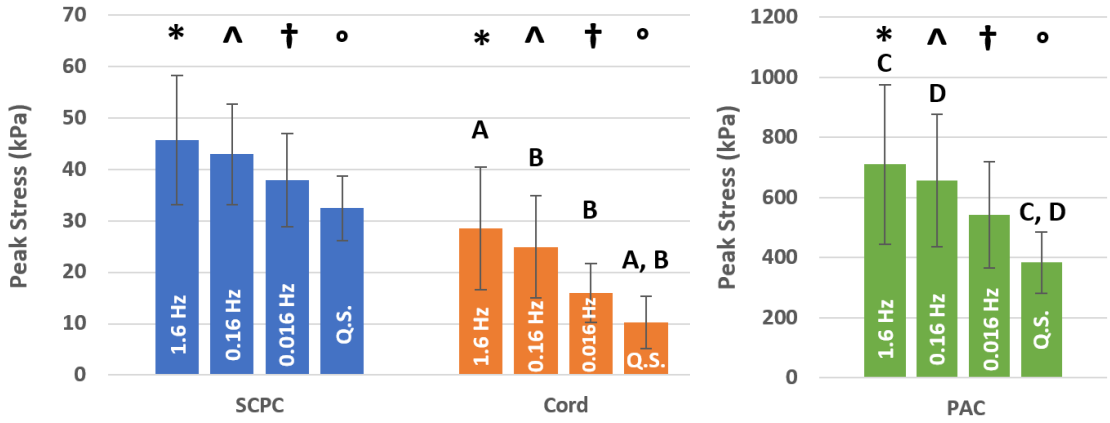

Figure 3.3: The average peak stress of each cyclic test frequency (error bars represent standard deviations); note the larger y-axis scale for the PAC condition. Like symbols indicate significant differences across conditions at the same test frequency whereas PAC > SCPC > cord at all four frequencies tested. Like letters indicate significant differences across frequencies within a condition with significant strain-rate effects found for the isolated cord and PAC but not for the SCPC.

To obtain measures of intra-test relaxation, the peak stresses of each cycle were normalized to that of the first cycle. For the five cycle tests (those conducted at 1.6 Hz, 0.16 Hz, and 0.016 Hz), these data were plotted as a function of cycle number and fit to the power function $y = Ax^b$ (Fig. 3.4). Statistical analysis of the rate (exponential b term) revealed the isolated cord experienced significantly greater cycle-to-cycle relaxation than the SCPC and PAC at all three frequencies. While all conditions displayed decreasing relaxation with increasing test frequency, only the isolated cord 1.6 Hz and 0.016 Hz measurements were found to be statistically different. Consistent with these results, total intra-test (first to final cycle) relaxation was significantly greater for the cord condition than both the SCPC and PAC (Table 3.1). For the two cycle quasi-static test, total intra-test relaxation of the cord (18.5 ± 4.6%) was significantly greater than the

relaxation of the SCPC (7.4 ± 2.9%) but not significantly different than that of the PAC (12.6 ± 5.5%).

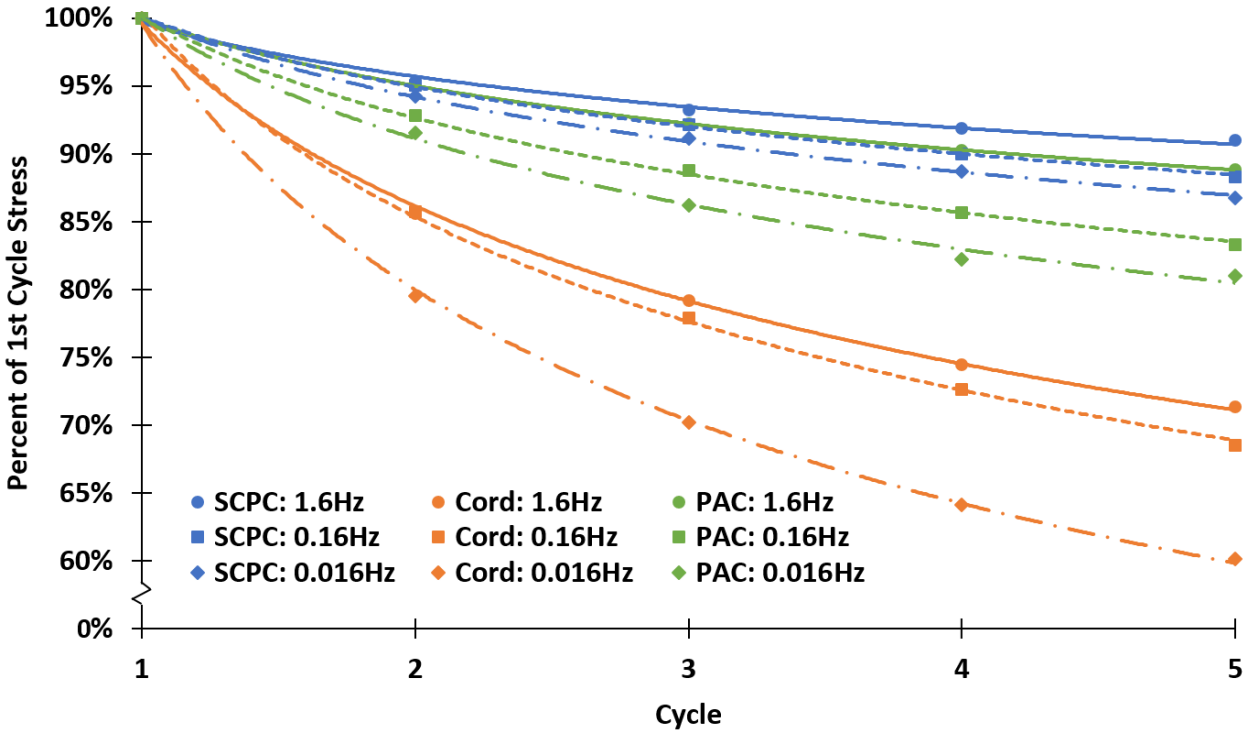

Figure 3.4: Average normalized peak stress per cycle for the three five-cycle tests as well as associated power law fits; standard deviations are not included to allow readability of the plot. At all three test frequencies, the cord condition exhibited significantly greater cycle-to-cycle relaxation than the SCPC and PAC.

Table 3.1: Total intra-test relaxation for the three five-cycle tests. At all three test frequencies, the isolated cord condition experienced significantly greater relaxation than the SCPC and PAC. Data are presented as average ± standard deviation.

Test Frequency	**SCPC**	**Cord**	**PAC**
1.6 Hz	9.0 ± 4.8 %	28.7 ± 8.6 %	11.1 ± 8.6 %
0.16 Hz	11.7 ± 4.7 %	31.5 ± 8.1 %	16.7 ± 10.9 %
0.016 Hz	13.2 ± 4.7 %	39. 9 ± 9.7 %	19.0 ± 10.9 %

3.3.2 Viscoelastic modeling

The *direct fit method* simultaneously fit the cyclic data well, with average RMSE across all samples and test frequencies of 2.44 kPa, 1.75 kPa, and 41.92 kPa for the SCPC, cord, and PAC conditions, respectively. These RMSE values represent approximately 6%, 10%, and 8% of the SCPC, cord, and PAC cyclic peak stresses, respectively. Statistical analysis of the RMSE percentages revealed equivalent fitting ability across all three conditions for the 1.6 Hz, 0.16 Hz, and 0.016 Hz tests, while the relative fitting error for the quasi-static cord curves were significantly higher than those of the SCPC ($p = 0.01$). Representative fits of a single sample in all three conditions are shown in Fig. 3.5. The resulting fitted coefficients for each condition are provided in Table 3.2. Significant differences between the conditions were found for the $C_2^{\tau_1}$, $C_2^{\tau_4}$, and C_2^{∞} fitted coefficients, which describe the quadratic dependence on strain of the relaxation modulus components at $\tau_1 = 0.1$ s, $\tau_4 = 100$ s, and equilibrium. These differences can be seen in plots of each Prony series weight (as defined in Eq. (3.5)) as variations of the convex or concave strain-dependent response at that time constant (Fig. 3.6). At the shortest time constant ($\tau_1 = 0.1$ s), the large positive $C_2^{\tau_1}$ term of the SCPC relaxation modulus component is reflected as a significantly more concave response than the isolated cord and PAC. At the longest time constants ($\tau_4 = 100$ s and equilibrium), the large negative $C_2^{\tau_4}$ terms of the PAC relaxation modulus component represent a significantly more convex response than the isolated cord at both time constants and the SCPC at $\tau_4 = 100$ s.

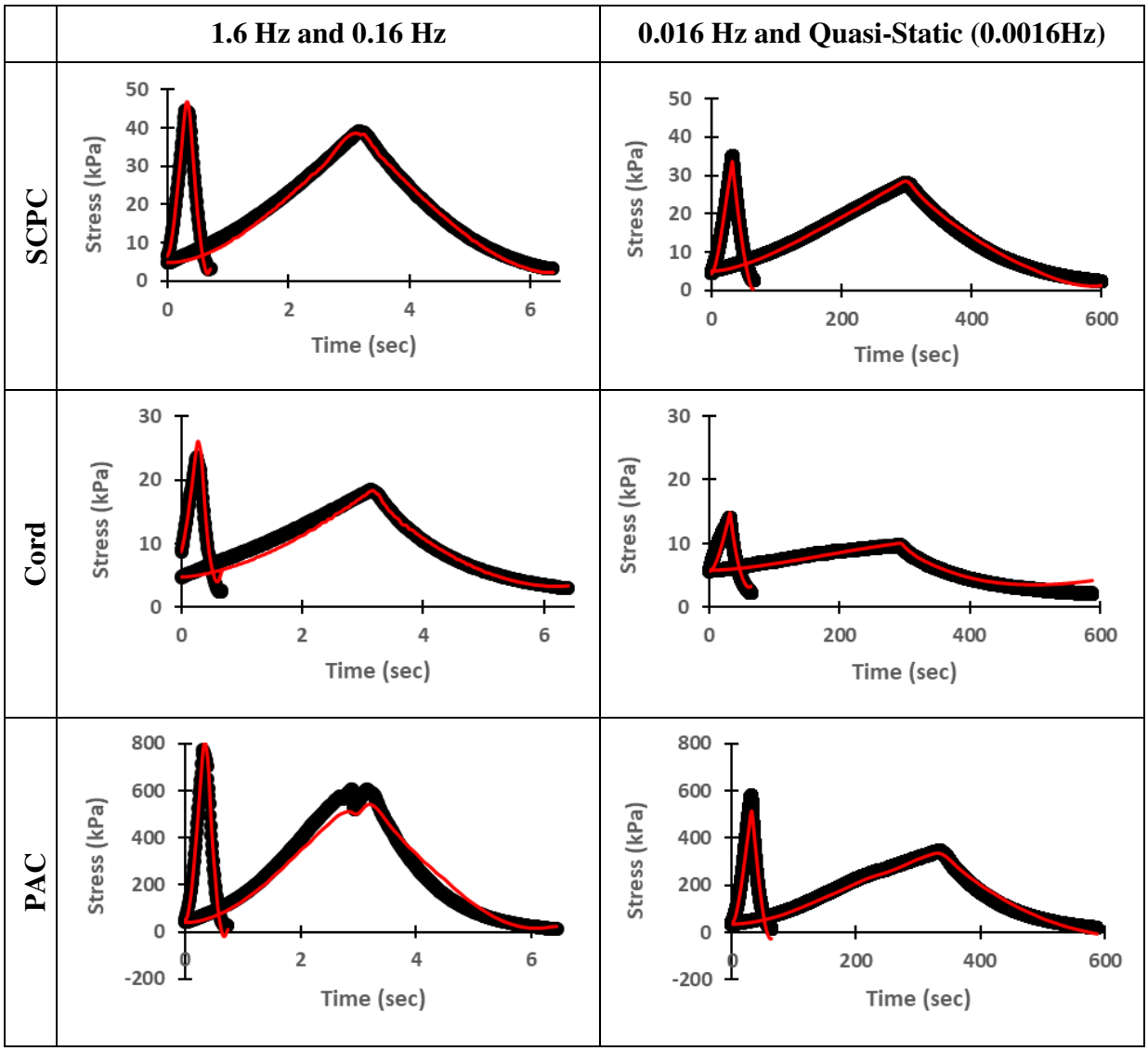

Figure 3.5: Representative non-linear viscoelastic model fits of one sample in all three conditions; although all four cycles of each condition were simultaneously fit, the curves have been separated to enable visibility of the faster tests. The formulation was able to fit the cyclic data well with average RMSE values of approximately 6%, 10%, and 8% of the SCPC, cord, and PAC peak stresses. The reduction in stress seen in the 0.16 Hz PAC test was due to a slight adjustment of the self-aligning grips and was also reflected in the strain data.

Table 3.2: Non-linear viscoelastic model fitted coefficients for all three conditions where $E_i = C_1^{\tau_i}\varepsilon + C_2^{\tau_i}\varepsilon^2$ (Eq. (3.5)). The terms marked with *, which are associated with the non-linearity of the relaxation modulus component at that time-constant, were found to be significantly different between conditions. Data are presented as average ± standard deviation.

(All units MPa)	**SCPC**	**Cord**	**PAC**
$C_1^{\tau_1}$	24.7 ± 13.1	38.9 ± 19.8	219.5 ± 176.1
$C_2^{\tau_1}$ *	**4727.7 ± 3926.2**	**-230.0 ± 352.2**	**755.7 ± 4296.0**
$C_1^{\tau_2}$	21.1 ± 36.0	11.4 ± 9.6	10.0 ± 18.9
$C_2^{\tau_2}$	353.3 ± 979.0	32.6 ± 296.6	821.5 ± 1847.7
$C_1^{\tau_3}$	20.9 ± 32.1	17.2 ± 10.1	82.0 ± 108.9
$C_2^{\tau_3}$	305.9 ± 544.6	-188.6 ± 124.3	1.1 ± 2240.8
$C_1^{\tau_4}$	27.8 ± 23.5	10.4 ± 4.8	212.7 ± 143.4
$C_2^{\tau_4}$ *	**80.9 ± 744.8**	**-108.4 ± 60.2**	**-1868.4 ± 1424.9**
C_1^{∞}	37.1 ± 12.5	1.7 ± 3.9	155.0 ± 45.1
C_2^{∞} *	-592.4 ± 242.0	**-17.3 ± 50.3**	**-1432.1 ± 479.9**

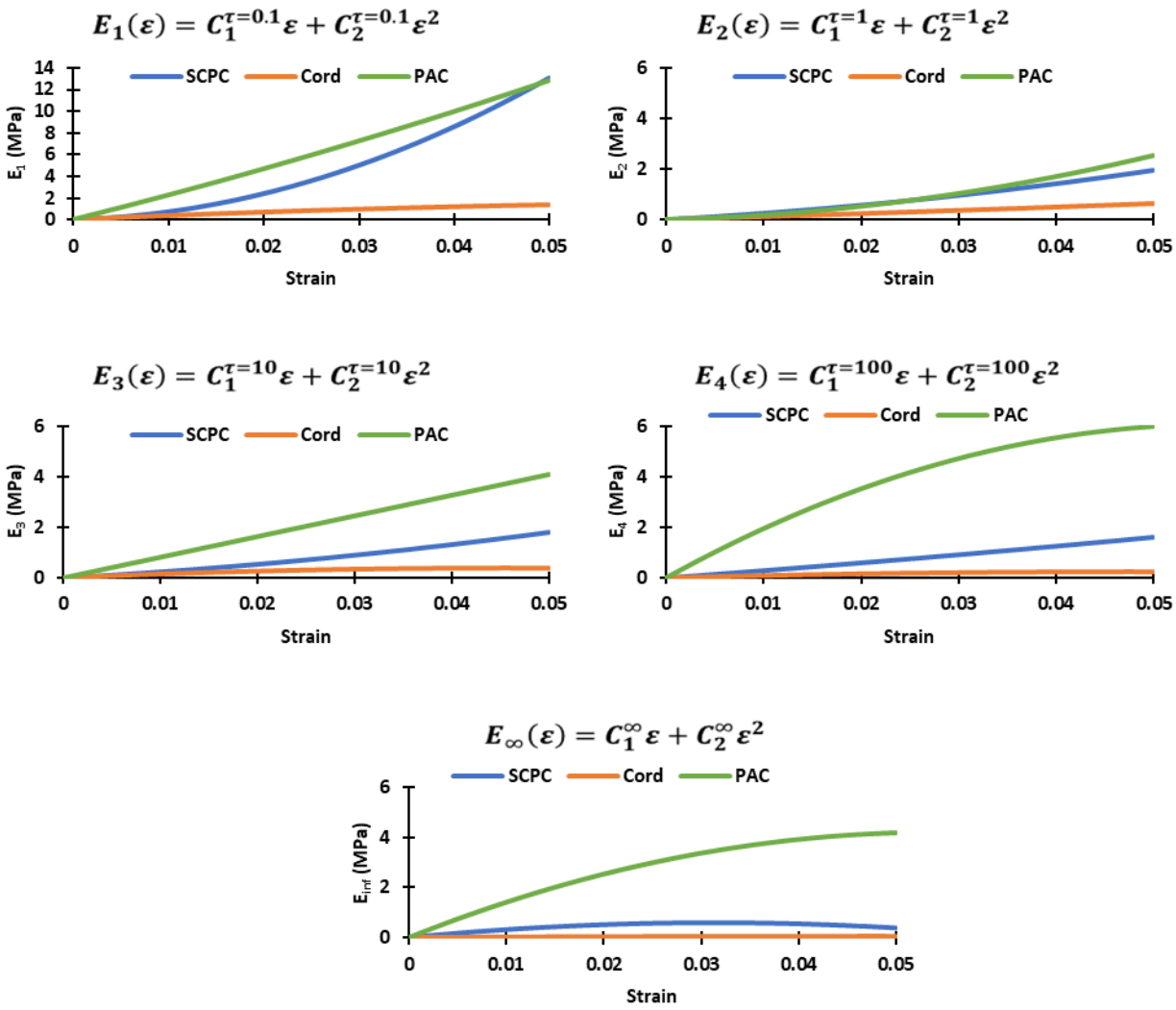

Figure 3.6: Plots of each relaxation modulus component as a function of applied strain given by the second-order polynomial in Eq. (3.5) and the fitted coefficients in Table 3.2; note the larger y-axis scale for the short-term $\tau = 0.1$ s plot.

To validate the resulting material model for each condition, the average measured strain inputs for the independent (i.e., not included in the fitting procedure) 3% and 5% stress-relaxation tests were implemented into Eq. (3.3) with the average fitted coefficients. The measured stress response as well as that predicted by Eq. (3.3) for each condition and strain magnitude are shown in Fig. 3.7. Apart from overpredictions of the acute PAC response, the predictions of all six curves fell within 1 standard deviation of the measured stress. The unweighted RMSE for each prediction was considerably lower than that of experimental variability (i.e., the RMSE resulting

from 1 standard deviation from the mean). For the SCPC, the RMSE of the predictions for the 3% and 5% strain tests were approximately 5% and 2% of the peak stress, respectively, compared to the 15% and 23% experimental variability recorded for these tests. For the cord, the RMSE of the predictions were approximately 3% of the peak stress compared to 20% for the observed experimental variability. Finally, the RMSE of the PAC predictions were approximately 7% of the peak stress compared to 21% experimental variability. The percent error for all six predictions were significantly less than their associated experimental variability ($p < 0.001$ for all). The material models for all three conditions overpredicted the peak stress response. The percent error of these overpredictions varied from 2% for the isolated cord 3% stress-relaxation response to 32% for the PAC 5% stress-relaxation response (the errors for the 3%, 5% stress-relaxation predictions are respectively: SCPC: 6%, 18%; cord: 2%, 7%; PAC: 21%, 32%, respectively). Comparing the average response of each condition, the substantially higher peak stress for the PAC and the greater degree of relaxation for the isolated cord noted in the cyclic data was also evident in the stress-relaxation data.

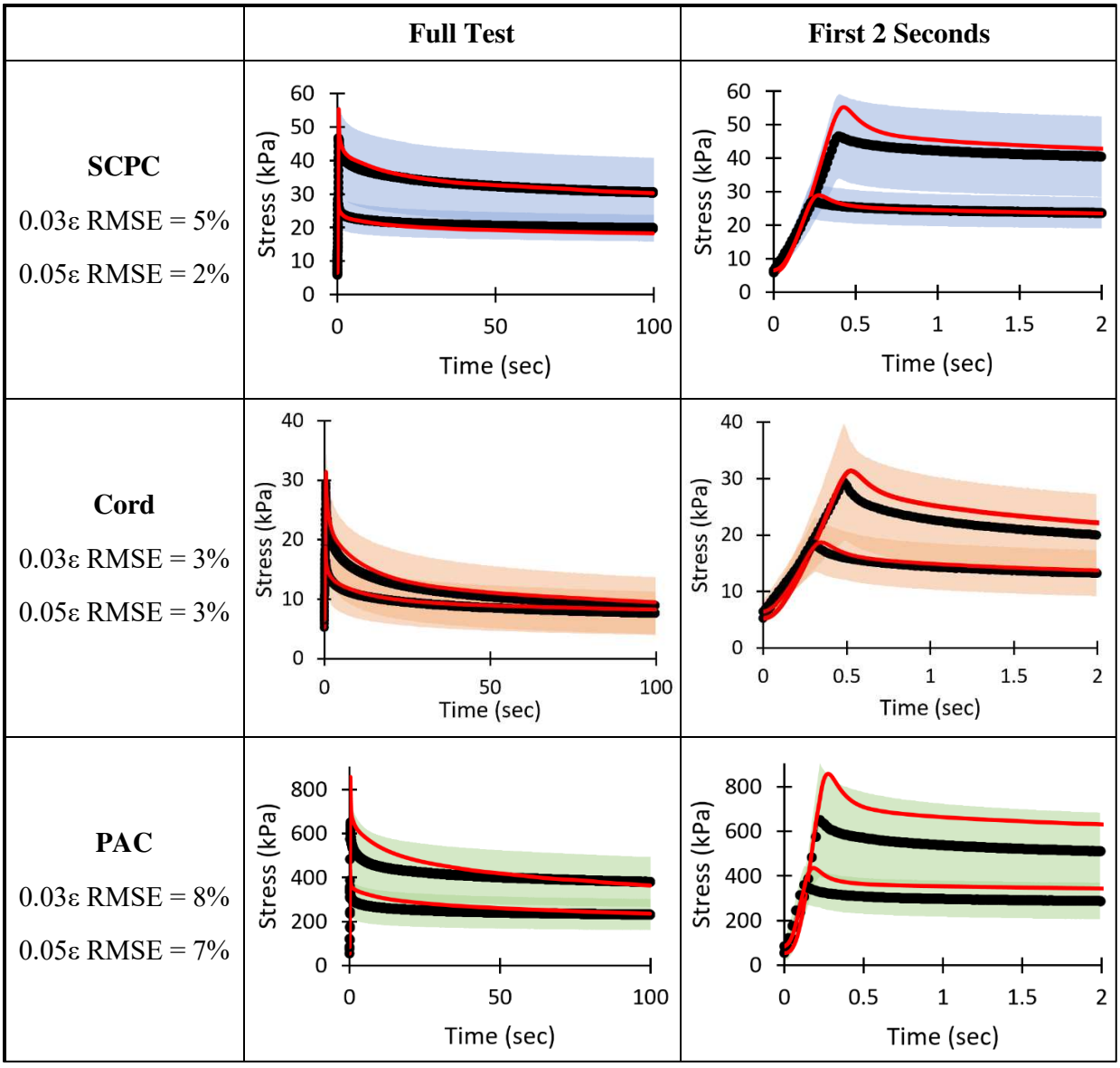

Figure 3.7: The non-linear viscoelastic models developed from fits of cyclic data were able to predict the average stress-relaxation response of each condition to 3% and 5% applied strains; the acute response is shown as a subplot to the right of the complete 100 s test. Apart from an over-prediction of the peak PAC stress response to the 5% applied strain, all predictions fell within ±1 standard deviation of the average response (shaded area).

3.4 Discussion

It is well known that the predictive accuracy of FE computational models is dependent on how accurately the geometries and material properties implemented in the model reflect the native condition being simulated. Many models of the spinal cord do not include explicit geometries for

the innermost meninges, and those which do include what is identified as pia mater often utilize linearly elastic material models to describe its behavior, despite experimental evidence that the tissue is substantially viscoelastic [59,127]. However, with no published viscoelastic models of isolated spinal PAC available, researchers are forced to make these simplifications. The current study fills this critical gap in the literature by providing a validated non-linear viscoelastic model for not only spinal PAC, but also for the isolated cord parenchyma and the SCPC. This study also provides the first quantitative comparison of the viscoelastic behavior of these conditions.

The superior stiffness of the spinal PAC relative to the underlying neural tissue has been reported as early as the work of Tunturi in the 1970's [117]. Although no study has quantitatively compared the mechanical behavior of spinal PAC and isolated cord, comparisons of the SCPC and cord have been published. Mazuchowski and Thibault reported an approximate 15-fold decrease in longitudinal modulus after ''incision of the pia mater" [105]. While the peak stress of the isolated cord was found to be significantly lower than the SCPC in this study, the difference between these two tissues was not nearly as large as has been previously reported (Fig. 3.3). This discrepancy is most likely due to neural tissue degradation over the 48 h between death and the mechanical testing reported by Mazuchowski and Thibault [105]. Relative to fibrous soft tissues (e.g., the PAC), the properties of neural tissues degrade rapidly post-mortem [101,109–112]. The average 2.5-fold (range: 1.6–3.2) difference in SCPC and cord peak stress observed in this study is much closer to that reported by Ozawa et al. for samples tested in transverse tension immediately after animal sacrifice [118].

The two experimental comparison studies discussed above [105,118] report a single elastic modulus for the SCPC and cord. To enable comparison with previous reports of SCPC, cord, and PAC tensile elastic moduli, a linear modulus was estimated from the second half of each 5% stress-relaxation ramp. The estimated SCPC elastic modulus of 2 MPa is in good agreement with other studies of the longitudinal tensile response of the tissue [105,108,109], while the estimated PAC elastic modulus of 17 MPa is within the range reported by Kimpara et al. for tensile tests at a similar strain rate (0.05/sec) [59]. As Kimpara et al. separated the PAC into denticulate ligament (elastic modulus of 31 MPa), posterior median septum (25 MPa), and posterolateral sulcus (11 MPa) sections prior to mechanical tests, it is difficult to directly compare these values to that estimated for the intact PAC. The 0.9 MPa estimated modulus for the cord is consistent with the response of isolated white and gray spinal matter [94,95,114] but is an order of magnitude greater than that reported by Mazuchowski and Thibault for SCPC samples with ‘‘incised pia mater” [105]. As stated above, the very small elastic modulus observed in that study may be due to prolonged post-mortem time prior to mechanical testing.

Examining the relative cycle-to-cycle relaxation behavior, it is clear the PAC significantly reduces SCPC relaxation (Fig. 3.4). It may be expected that the response of the SCPC would display gestalt (i.e., averaged) viscoelastic character relative to its components, as observed for the peak stress response. However, as can be seen in Fig. 3.4 and Table 3.1, the SCPC experiences less relaxation than both the PAC and cord at all test frequencies. This suggests the importance of the interaction between the PAC and cord in the viscous response of the SCPC. In tests of the SCPC, any circumferential pre-tension in the PAC further resists elongation by limiting the mid-substance contraction (i.e., Poisson’s effect). Indeed, a slight opening of the

SCPC was noted when the initial longitudinal incision in the PAC was performed. Because the PAC was tested as a sheet, the contribution of circumferential tension was lost, and therefore, not reflected in the relaxation behavior of the isolated PAC. These results are consistent with the observation of Ozawa et al. that the stiff PAC provides a constraint on the surface of the cord, which prevents changes in circumference. Furthermore, the significant cord relaxation is also in agreement with Ozawa's conclusion that the PAC "produces a large strain energy that is responsible for shape restoration following decompression" [118].

The relaxation modulus component plots in Fig. 3.6 demonstrate the influence of the PAC on the viscoelastic response of the SCPC is most evident in the acute time-frame at higher applied strain magnitudes. At the τ_1 = 0.1 s and τ_2 = 1 s time-constants, the relaxation modulus of the SCPC is in better agreement with the PAC than the isolated cord at almost all applied strain magnitudes. However, at longer time constants, the SCPC appears to transition from a PAC-dominated response to a more PAC-independent (i.e., similar to the isolated cord) response. Based on the relative trajectories of the τ_1 = 0.1 s and τ_2 = 1 s time-constant curves, the divergence of the SCPC and isolated cord short-term behavior increases with increasing applied strain. This suggests the PAC is critical to the SCPC response under injurious loading scenarios which occur on the order of milliseconds to seconds and result in greater applied strains than those utilized in this study.

As shown in Fig. 3.7, the isolated cord model best predicted the associated stress-relaxation response while the PAC model prediction displayed the greatest error, with over-prediction of the short-term stress response at both strain magnitudes. Comparing the average stress-relaxation

response of the cord and PAC conditions, it appears the non-linear viscoelastic formulation utilized in the current work is best suited for modeling a gradual, more consistent, relaxation response, such as that displayed by the isolated cord. The rapid reduction of stress followed by very little further relaxation seen in the PAC response was not as well predicted by its fitted model. While the SCPC experienced less overall relaxation, the reduction in stress was more consist over the 100 s tests as compared to the PAC, which was reflected as better overall predictions. One possible method for improving the predictions of all three conditions would be to utilize different time constants for the relaxation modulus Prony series. Decadal time constants from 0.1 to 100 s were chosen in an attempt to capture both the short-term and long-term response, but it is possible that differences in composition and structure between the three conditions result in different relaxation time distribution spectra [167]. Indeed, the average stress-relaxation responses shown in Fig. 3.7 support the hypothesis of distinct relaxation domains. Based on these results, it is expected that the use of smaller time-constants may facilitate corrections of the acute over-predictions seen in Fig. 3.7.

Overall, it is notable that the use of single cycle stress-strain data from four moderate strain-rate tests were able to predict independent viscoelastic data with less than 8% error. One significant advantage of the presented formulation over previously used characterization methods is the ability to capture non-linear viscoelastic behavior from cyclic tests to a single strain-magnitude as opposed to longer stress-relaxation tests to various strain levels [148]. Multiple cycles were collected at each frequency to enable comparisons of viscous behaviors but fits of the initial cycle only proved to be the more predictive of the stress-relaxation response than fits of the final cycle only or all test cycles. This can be expected as the ramp of the stress-relaxation test is most

similar to the initial cycle which does not experience the intra-test preconditioning of previous cycles. The use of a single initial cycle also promotes testing and fitting efficiency as it negates the need for extensive testing protocols and reduces the computational costs associated with fitting additional stress-strain data.

There are a number of limitations of the presented work which should be noted. Firstly, the strain-magnitudes (3%–5%) and strain-rates (quasi-static to 20%/sec) utilized are well below that expected to occur during SCI [44,153,161,162]. Accordingly, the developed non-linear viscoelastic models are only valid over these conditions and may not produce accurate predictions of the response to injurious scenarios. As the results of this initial study demonstrate the significance of the PAC to the viscoelastic behavior of the spinal cord, additional characterization of the isolated PAC and cord under injurious loads and loading-rates is strongly encouraged. A second limitation is the sequential nature of the characterization protocol; SCPC testing must be completed before isolated cord testing can begin, which precludes randomization of the testing procedure. As previously stated, the timing of neural tissue characterization is critical due to relatively quick post-mortem degradation [101,109–112]. To ensure the differences in SCPC and cord behavior observed were not simply due to differences in time post-mortem, an additional pilot sample was mechanically tested in a shorter time frame. Only a subset of the SCPC tests were performed to enable completion of cord testing within 3 h following animal sacrifice. The peak stresses and normalized relaxation behavior of this sample fell within one standard deviation of those tested within 5 h, suggesting the effects of differing SCPC and cord testing time were minimal. Ideally, *in-vivo* data of all three conditions would be used for comparison as previous data have shown differences between the *ex-vivo* and *in-vivo* SCPC mechanical behavior [69,91,139].

However, removal of the PAC *in-vivo* would not only be extremely experimentally challenging but would also lead to localized neural tissue death due to the vascular function of the tissue.

3.4.1 Conclusions

In conclusion, this work represents an important contribution to the knowledge of spinal and meningeal mechanics as it represents the first study to compare the SCPC, isolated cord, and PAC under the same testing conditions. The results show the spinal cord parenchyma has very little inherent stiffness and is reliant on the PAC for rigidity and recovery from loading, consistent with the limited previous works [105,118]. Despite composing only 5.5% of the SCPC cross-section, the intact PAC significantly influences both its elastic and viscous behavior, especially in the acute time frame, which may have important implications for FE modeling of SCI. The effect of strain-rate, cycle-to-cycle relaxation, and strain-dependence of relaxation modulus components observed for all three conditions add to already compelling evidence of time-dependent SCPC, PAC, and isolated cord behavior [22,25,59,90,94,113,132]. These results emphasize the importance of using viscoelastic material models, such as the validated models presented herein, in FE studies of the spinal cord. Future work will include the development of user subroutines for the implementation of the presented material models into FE software in order to study the effect of structural (e.g., inclusion of an explicit PAC geometry) and material (e.g., non-linear viscoelastic behavior) complexities on resultant cervical spine model predictions.

3.4.2 Funding and acknowledgements

The authors would like to acknowledge Colorado State University's Preclinical Surgical Research Laboratory, especially Kim Lebsock, for their assistance in collection of ovine cervical spines for this study, Nick Meis and Amy Holcomb for their help with data analysis, and Dr. Julia Sharp of Colorado State University's F.A. Graybill Statistical Laboratory for her guidance on statistical modeling. The authors also wish to acknowledge the funding support of the Graduate Teaching Fellowship from the Walter Scott, Jr. College of Engineering at Colorado State University.

CHAPTER 4: COMPARING PREDICTIVE ACCURACY AND COMPUTATIONAL COST FOR VISCOELASTIC MODELING OF SPINAL CORD TISSUES [3]

4.1 Introduction

The significant neurological, psychological, and financial losses associated with spinal cord injuries (SCI) have motivated substantial research efforts on their prevention, cause, and treatment. However, in order to draw valid conclusions from clinical observation, experimental animal modeling, and computational simulation, knowledge of the material properties of the relevant biological tissues is required. Accordingly, a variety of experimental techniques have been employed to examine the mechanical behavior of isolated neural tissues (e.g., gray and white matter of the spinal cord), meningeal tissues (e.g., pia-arachnoid-complex), and combinations thereof. These studies have demonstrated the important viscoelastic nature of the tissues, which is manifested as creep [100], stress-relaxation [22,25,91,94,108,113,131,132,139,168], hysteresis [69,88,90,114], and strain-rate dependent stiffness [22,25,38,59,94,108,113,168] behaviors. As these data have progressively elucidated more advanced knowledge of these temporal material behaviors, the material formulations utilized to model neural tissues have concomitantly increased in sophistication from linear elastic to hyperelastic to viscoelastic. While it is now widely accepted that they exhibit time-dependent behavior, there is limited quantitative information regarding the accuracy and computational resource trade-offs of using linear viscoelastic (LV), quasi-linear viscoelastic (QLV), or (fully) non-linear viscoelastic (NLV) formulations.

[3] This chapter is under review as a fundamental research article to the International Journal for Numerical Methods in Biomedical Engineering.

Reports of tensile testing of the spinal cord with intact leptomeninges (i.e., spinal-cord-pia-arachnoid-construct, SCPC) are relatively common in the literature. Several publications have provided explicit experimental evidence of the NLV nature of the SCPC because its relaxation behavior has been rigorously shown to be dependent on the applied strain magnitude [91,132,139]. Chang et al. has previously reported a transition from LV to NLV behavior around 1% strain for the *in-vivo* feline SCPC [91]. However, QLV formulations remain the default for experimental characterization and computational modeling of the SCPC [44,45,108,143,169]. This discrepancy may be due to the relative ease of model development and implementation in commercial finite element (FE) software packages. In addition, the observed reliance on QLV is also likely due to the lack of information about how the choice of viscoelastic formulation affects resultant model predictions.

Compared to the SCPC, viscoelastic characterization of its isolated components, namely the neural tissue (i.e., cord) and the pia-arachnoid-complex (PAC), is rare. Due to this paucity of data, determining the appropriate level of material model complexity is even more challenging. Samples of isolated spinal neural tissue have been tested in unconfined compression [113] and axial tension [94,168], but the NLV behavior of this tissue has not been explicitly demonstrated to-date. Accordingly, QLV formulations are typically used to characterize and model spinal white matter and gray matter [57,94,97,113,143]. Information on isolated PAC behavior is even more limited; with the exception of one recent publication [168], it has been modeled exclusively as linearly elastic [57,59,93,94,97,98]. Jin et al. has provided evidence of, and material models for, the viscoelastic behavior of cranial PAC [123,163], but it is unknown if differences in cranial and spinal PAC structure prevent a direct translation of results.

To the authors' knowledge, there have been no publications to-date which quantitatively compare the abilities of LV, QLV, and NLV formulations to fit and predict the temporal mechanics of the SCPC, isolated cord, or PAC. Without this information, researchers interested in modeling SCI are unable to make fully informed decisions regarding the balance of accuracy and computational efficiency appropriate for their specific modeling objectives. Therefore, the goal of this work was to critically appraise the trade-offs in predictive accuracy and computational efficiency associated with the use of more sophisticated viscoelastic formulations in fitting dynamic cyclic experimental data and predicting independent stress-relaxation data for all three tissue conditions (SCPC, isolated cord, and PAC).

4.2 Materials and Methods

4.2.1 Experimental testing

Stress-strain data collected from ovine SCPC, isolated cord, and PAC as part of a previous study were used for the current analysis. While the details of the previous study can be found elsewhere [168], the experimental testing technique is briefly described here. Eight ovine cervical spines were collected immediately following animal euthanasia (for unrelated studies). From each spine, a single SCPC sample measuring approximately 60mm in length was extracted and tested in uniaxial tension as detailed below. Following the completion of SCPC testing, the PAC was circumferentially removed from the surface of the construct. The resulting planar sheet of PAC was placed between pieces of saline-soaked gauze and stored in an airtight container while the same mechanical testing procedure was performed on the isolated cord. To minimize the effects of post-mortem neural tissue degradation [101,109–112], all SCPC and isolated cord mechanical tests were completed within 5 hours of animal sacrifice. Following the completion of

isolated cord testing, the uniaxial test stand configuration was modified to allow for the same series of mechanical tests to be performed on the PAC sheet.

The mechanical testing procedure for all three tissue conditions (SCPC, isolated cord, and PAC) consisted of 100 cycles of preconditioning to 5% engineering strain, two stress-relaxation tests, and four dynamic cyclic tests. Experiments were performed in a randomized order with a minimum of 4 minutes of unloaded recovery and hydration between each test. For the stress-relaxation procedures, the samples were strained to 3% and 5% engineering strain at a ramping rate of 6mm/s and allowed to relax for 100 seconds. For the dynamic cyclic procedures, the samples were cycled to 5% engineering strain at four frequencies: 1.6Hz, 0.16Hz, 0.016Hz, and 0.0016Hz. The 1.6Hz, 0.16Hz, and 0.016Hz tests consisted of five cycles, while the lowest frequency (i.e., quasi-static) test consisted of only two cycles to minimize testing time.

4.2.2 Viscoelastic modeling

4.2.2.1 Model fitting

For each sample tissue condition, the dynamic cyclic stress-strain-time data were simultaneously fit to NLV, QLV, and LV formulations using the *direct fit method*. As detailed previously [139,148,168], the *direct fit method* is a viscoelastic characterization technique which leverages the unique properties of the Prony series to avoid storage of the stress at all previous points of the loading history. For each viscoelastic formulation, MATLAB's (R2018a, Mathworks, Natick, MA) fmincon function was used to determine the set of fitted coefficients which minimized the sum of the root mean squared errors (RMSE) across all four frequency curves included in the fit.

The fits were performed using parallel-processing with 2 cores (Intel Core i5-6300U processor) on a laptop computer with 8GB of installed RAM.

4.2.2.2 Model validation

The fitted coefficients for each formulation were averaged across similar tissue conditions to create a total of 9 viscoelastic models, one for each combination of formulation complexity (NLV, QLV, LV) and tissue condition (SCPC, cord, PAC). The ability of these material models, based on fits of dynamic cyclic data, to predict independent viscoelastic behavior was assessed via RMSE and percent error measures between the average experimental stress-relaxation response and that predicted by the material model. This validation procedure was performed in MATLAB by directly applying the average strain histories and fitted coefficients to the same code used for fitting with the time required to perform these calculations recorded.

In order to demonstrate FE implementation of each formulation, this validation procedure was also performed in Abaqus/Explicit (version 2018, Dassault Systemes Simulia Corp., Johnston, RI). The constitutive behavior was defined as VUMAT user subroutines, with a subroutine written for each viscoelastic formulation. For each tissue condition, a single one-dimensional two-node linear-displacement truss element (T3D2) was created and assigned length and cross-sectional area dimensions based on average experimental measurements. A density of 1000 kg/m^3 was utilized for all three tissue conditions [46,92,102,143,170]. One end of the model was pinned in the axial direction while an axial displacement was applied to the other end to match the experimentally measured strain histories. The computational modeling was performed on a

Linux-based workstation with 126GB of installed RAM using the 16 cores of an Intel Xeon E5-2683 v4 processor.

4.2.2.3 Linear Viscoelastic (LV) Formulation

LV models assume a linear relationship between stress and strain at any given time (i.e., the elastic and viscous aspects of a material's behavior are linear). The general uniaxial response of an LV material may be modeled using the hereditary, or convolution, integral given as [149–151]:

$$\sigma(t) = \int_0^t E(t-\tau)\frac{d\varepsilon(\tau)}{d\tau}d\tau. \qquad (4.1)$$

where σ is engineering stress, ε is engineering strain, t is time, τ is a time variable of integration, and $E(t)$ is the LV strain-independent relaxation modulus. All viscoelastic formulations presented herein utilized a 4-term Prony series with fixed decadal time constants to represent the continuous relaxation modulus: $\tau_1 = 0.1$, $\tau_2 = 1$, $\tau_3 = 10$, and $\tau_4 = 100$ seconds. For the case of LV, the relaxation modulus was represented by the following Prony series:

$$E(t) = E_\infty + \sum_{i=1}^{4} E_i e^{-t/\tau_i}, \qquad (4.2)$$

where E_∞ is the steady-state relaxation coefficient and E_i is the Prony coefficient associated with the time constant τ_i. The *direct fit method* [139,148,168] allows for stress after time increment Δt ($\sigma[t+\Delta t]$) to be defined in terms of a history state variable, $h_i(t)$, which is recursively updated at every time step:

$$\sigma(t+\Delta t) = E_\infty \varepsilon(t+\Delta t) + \sum_{i=1}^{4}\left\{(h_i(t))\left(e^{-\Delta t/\tau_i}\right) + E_i\tau_i\left[1-e^{-\Delta t/\tau_i}\right]\left[\frac{\Delta\varepsilon}{\Delta t}\right]\right\}, \quad (4.3)$$

$$h_i(t) = \int_0^t \left\{E_i e^{-(t-\tau)/\tau_i}\right\}\left[\frac{d\varepsilon(\tau)}{d\tau}\right]d\tau. \quad (4.4)$$

Therefore, the LV formulation contained a total of five fitted coefficients (E_1, E_2, E_3, E_4, and E_∞) which were constrained to be positive in the fitting procedure in order to satisfy thermodynamic restrictions.

4.2.2.4 Quasi-linear viscoelastic (QLV) formulation

QLV formulations enable the inclusion of elastic non-linearity by allowing the elastic and viscous aspects of the response to be modeled separately. As proposed by Fung [142], the uniaxial QLV formulation takes the form:

$$\sigma[\varepsilon(t),t] = \int_0^t G(t-\tau)\frac{d\sigma^e(\varepsilon)}{d\varepsilon}\frac{d\varepsilon(\tau)}{d\tau}d\tau, \quad (4.5)$$

where $\sigma^e(\varepsilon)$ represents the instantaneous non-linear elastic (i.e., hyperelastic) behavior and $G(t)$ is the reduced relaxation modulus describing the strain-independent viscous behavior. In this study, the hyperelastic behavior was modeled using the 1-term Ogden constitutive equation [113,171]:

$$\sigma^e(\varepsilon) = \frac{2\mu}{\alpha}\left[(\varepsilon+1)^{\alpha-1} - (\varepsilon+1)^{-\alpha/2-1}\right], \quad (4.6)$$

such that

$$\frac{\sigma^e(\varepsilon)}{d\varepsilon} = \frac{2\mu}{\alpha}\left[(\alpha-1)(\varepsilon+1)^{\alpha-2} + \left(1+\frac{\alpha}{2}\right)(\varepsilon+1)^{-\alpha/2-2}\right], \tag{4.7}$$

where the Ogden fitted parameters μ and α represent the shear modulus and non-linearity, respectively. For the case of QLV, the reduced relaxation modulus, $G(t)$, was modeled using the following Prony series:

$$G(t) = G_\infty + \sum_{i=1}^{4} G_i e^{-t/\tau_i}, \tag{4.8}$$

where G_i is the Prony coefficient associated with the time constant τ_i and G_∞ is the steady-state relaxation coefficient. Equation 4.8 is subject to the constraint

$$G_1 + G_2 + G_3 + G_4 + G_\infty = 1. \tag{4.9}$$

Therefore, the specific QLV formulation used in this study was:

$$\begin{aligned}\sigma[\varepsilon(t),t] = {} & \frac{2\mu}{\alpha}\left[(\alpha-1)(\varepsilon+1)^{\alpha-2} + \left(1+\frac{\alpha}{2}\right)(\varepsilon+1)^{-\alpha/2-2}\right] \\ & * \int_0^t \left\{G_\infty + \sum_{i=1}^{4} G_i e^{-(t-\tau)/\tau_i}\right\} \frac{d\varepsilon(\tau)}{d\tau} d\tau.\end{aligned} \tag{4.10}$$

Following the same *direct fit method* derivation for LV, the current stress and history state variable $[h_i(t)]$ for the QLV formulation were defined as:

$$\sigma[\varepsilon(t+\Delta t), t+\Delta t] = \frac{2\mu}{\alpha}\left[(\alpha-1)(\varepsilon+1)^{\alpha-2} + \left(1+\frac{\alpha}{2}\right)(\varepsilon+1)^{-\alpha/2-2}\right] \\ * \left\{G_\infty \varepsilon(t+\Delta t) + \sum_{i=1}^{4}\left\{(h_i(t))\left(e^{-\Delta t/\tau_i}\right) + G_i\tau_i\left[1-e^{-\Delta t/\tau_i}\right]\left[\frac{\Delta\varepsilon}{\Delta t}\right]\right\}\right\}, \quad (4.11)$$

$$h_i(t) = \int_0^t \left\{G_i e^{-(t-\tau)/\tau_i}\right\}\left[\frac{d\varepsilon(\tau)}{d\tau}\right] d\tau. \quad (4.12)$$

Therefore, the QLV formulation contained a total of seven fitted coefficients (μ, α, G_1, G_2, G_3, G_4, and G_∞) which were constrained to be positive, with the relaxation coefficients also subjected to the constraint given in Eq. (4.9).

4.2.2.5 Non-linear Viscoelastic (NLV) Formulation

NLV models allow for non-linearity in both the elastic and viscous aspects of a material's behavior. Unlike QLV models where these aspects are described by separate functions, the NLV relaxation modulus is a non-separable function of strain and time. The uniaxial response of an NLV material may be represented using a similar equation as that presented for LV [149–151]:

$$\sigma[\varepsilon(t), t] = \int_0^t E[\varepsilon(\tau), t-\tau]\frac{d\varepsilon(\tau)}{d\tau} d\tau, \quad (4.13)$$

where $E(\varepsilon, t)$ is the relaxation modulus that simultaneously describes both elastic and viscous (i.e., time-dependent) non-linearities. For the case of NLV, the Prony series took the following form:

$$E[\varepsilon(t), t] = E_{\infty}(\varepsilon) + \sum_{i=1}^{4} E_i(\varepsilon) e^{-t/\tau_i}, \tag{4.14}$$

where $E_{\infty}(\varepsilon)$ is the steady-state strain-dependent relaxation modulus and $E_i(\varepsilon)$ is the strain-dependent Prony weight associated with the time constant τ_i. Following the same procedure as above, the current stress was defined in terms of a history state variable, $h_i[\varepsilon(t), t]$, which was recursively updated at every time step:

$$\sigma[\varepsilon(t + \Delta t), t + \Delta t] = [E_{\infty}(\varepsilon)][\varepsilon(t + \Delta t)] + \sum_{i=1}^{4} \left\{ (h_i[\varepsilon(t), t]) \left(e^{-\Delta t/\tau_i} \right) + [E_i(\varepsilon)] \tau_i \left[1 - e^{-\Delta t/\tau_i} \right] \left[\frac{\Delta \varepsilon}{\Delta t} \right] \right\}, \tag{4.15}$$

$$h_i[\varepsilon(t), t] = \int_0^t [E_i(\varepsilon)] \left[e^{-(t-\tau)/\tau_i} \right] \left[\frac{d\varepsilon(\tau)}{d\tau} \right] d\tau. \tag{4.16}$$

The strain-dependence of the five Prony series weights [$E_i(\varepsilon)$ and $E_{\infty}(\varepsilon)$] were defined as second-order polynomials:

$$E(\varepsilon) = C_1 \varepsilon + C_2 \varepsilon^2 \tag{4.17}$$

where $C_1^{\tau_i}$ and $C_2^{\tau_i}$ are fitted coefficients defining the linear and quadratic strain dependence of E_i, respectively. Thus, a total of ten fitted coefficients were obtained for the NLV formulation. To satisfy thermodynamic restrictions, each Prony weight function [$E(\varepsilon)$] was constrained to be positive and monotonically increasing over the strain range of the fits.

4.2.3 Statistical analysis

All statistical analyses were performed using JMP statistical software (version 13.0.0, SAS Institute Inc., Cary, NC). To determine differences in formulation fitting ability, linear mixed models with fixed (formulation, cyclic frequency, formulation-frequency interaction) and random (sample, sample-test interaction) effects were used to compare curve fit RMSE values. The same procedure with a single fixed effect was used to determine any differences in fitting time between formulations. To determine differences in fitted coefficients across tissue conditions, linear mixed models with condition, coefficient, and their interaction treated as fixed effects and sample as a random effect were utilized. For the case of the QLV and LV formulations, the fitted coefficients were square root transformed before statistical modeling to improve residual normality and distribution. To statistically compare the ability of each viscoelastic formulation to predict important features of the stress-relaxation response, the predicted peak stress, equilibrium stress (i.e., that at 100 seconds), and percent relaxation of each viscoelastic prediction were compared to that of each experimental sample. One-way repeated measures ANOVAs were then used to compare the absolute errors of each viscoelastic formulation for each tissue condition, strain-magnitude combination. Tukey HSD p-value corrections were used for multiple comparisons.

4.3 Results

4.3.1 Dynamic cyclic data fits

For the SCPC condition, the NLV and QLV formulations fit the data equally well with an average RMSE across all samples and cyclic frequencies of 2.4 kPa (approximately 6% of the average peak stress). However, the RMSE of the LV formulation was significantly larger than

both the NLV ($p < 0.01$) and QLV formulations ($p < 0.01$) and averaged 4.2 kPa. The same pattern was observed for the PAC condition, where the NLV and QLV formulation fits resulted in average RMSE values of approximately 41 kPa (8% of peak stress). The LV formulation fits had an average RMSE of 58 kPa, which was significantly greater than the other two formulations ($p < 0.01$ for both comparisons). For the isolated cord, the QLV formulation fit the cyclic data with a significantly lower RMSE compared to the NLV formulation (1.4 kPa vs. 1.7 kPa, $p = 0.01$), while the LV RMSE (1.6 kPa) was not significantly different than the NLV or QLV RMSE values. The 1.4 kPa RMSE of the QLV formulation represented approximately 9% of the average peak stress of the cord condition. Representative fits of each viscoelastic formulation are provided as supplemental figures C1 – C3 in Appendix C. For all three tissue conditions, the NLV fits required significantly longer computational run times than the QLV and LV fits ($p < 0.01$ for all six comparisons). Across all tissue conditions, LV fits were accomplished within an average of 30-40 seconds, the QLV fits were accomplished within an average of 1-2 minutes, while the NLV fits were accomplished in an average of 1 hour (with a maximum time of 1.7 hours) using two parallel processors.

The average fitted coefficients for the QLV and LV formulations are given in Table 4.1 and Table 4.2, respectively (NLV characterization can be found in [168]). For the QLV formulation, significant differences between tissue conditions were found for the Ogden hyperelastic parameters but not the reduced relaxation modulus coefficients. The fitted shear modulus (μ) was significantly greater for the PAC than the SCPC and cord (both $p < 0.01$). The fitted term representing the non-linearity of the hyperelastic response (α) was found to be greatest for the SCPC ($p < 0.01$ for both PAC and cord comparisons), followed by the cord, which was

significantly greater than the PAC (p = 0.02). For the LV formulation, all relaxation modulus fitted coefficients except E_2 were significantly higher for the PAC than the other two tissue conditions (all comparisons p < 0.01 except E_3 PAC vs. Cord p = 0.02). The steady-state relaxation modulus term, E_∞, of the SCPC was also significantly greater than that of the cord (p = 0.03).

Table 4.1: Fitted coefficients for the QLV formulation where μ, α are the Ogden hyperelastic model parameters as defined in Eq. (4.7) and G_i represent the coefficients of the reduced relaxation modulus as defined in Eq. (4.9). Significant differences between tissue conditions are indicated with * symbols.

(unitless unless noted)	SCPC	Cord	PAC
μ (MPa) *	**0.4 ± 0.2**	**0.3 ± 0.1**	**3.6 ± 1.0**
α *	**54.9 ± 15.2**	**22.9 ± 6.0**	**18.8 ± 12.3**
G_1	0.52 ± 0.06	0.61 ± 0.11	0.44 ± 0.06
G_2	0.09 ± 0.11	0.09 ± 0.10	0.05 ± 0.10
G_3	0.08 ± 0.09	0.20 ± 0.09	0.07 ± 0.11
G_4	0.14 ± 0.07	0.09 ± 0.04	0.23 ± 0.14
G_∞	0.17 ± 0.10	0.01 ± 0.03	0.21 ± 0.09

Table 4.2: Fitted coefficients for the LV formulation where E_i represent the coefficients of the relaxation modulus as defined in Eq. (4.15). Significant differences between tissue conditions are indicated with * symbols.

(All units MPa)	SCPC	Cord	PAC
E_1 *	**0.89 ± 0.32**	**0.64 ± 0.33**	**6.61 ± 2.02**
E_2	0.33 ± 0.32	0.11 ± 0.10	0.93 ± 2.13
E_3 *	**0.16 ± 0.21**	**0.24 ± 0.14**	**1.75 ± 1.67**
E_4 *	**0.39 ± 0.24**	**0.13 ± 0.05**	**3.81 ± 2.38**
E_∞ *	**0.49 ± 0.15**	**0.02 ± 0.07**	**3.46 ± 0.84**

4.3.2 Stress-relaxation predictions

To differentiate acute and long-term predictive accuracy, two RMSE values were calculated between each model prediction and the average stress-relaxation response: (1) the unweighted RMSE of the first two-seconds and (2) the weighted RMSE (wRMSE) of the remaining 98-seconds according to [145,146,172]:

$$w(t_*) = \frac{1}{4}\left(e^{-t_*/\tau_1} + e^{-t_*/\tau_2} + e^{-t_*/\tau_3} + e^{-t_*/\tau_4}\right). \quad (4.18)$$

where t_* is the time relative to the end of the two-second acute phase.

The RMSE values are reported for both the 3% strain and 5% strain predictions obtained from both MATLAB and Abaqus FE modeling in Table 4.3. Figures 4.1 – 4.6 show the acute viscoelastic predictions while supplemental Figs. C4 – C9 (in Appendix C) show predictions of the entire 100-second test.

4.3.2.1 SCPC

Predictions of the acute SCPC response to the 5% applied strain history are shown in Fig. 4.1A, with the associated percent residuals of each prediction shown in Fig. 4.1B. For both MATLAB and FE predictions, the acute response was equally well-predicted by the QLV and NLV formulations, while the LV formulation RMSE values were approximately 1.5 times greater. Examining only the prediction of average peak stress, the QLV formulation over-predicted the average peak stress by approximately 10% and the LV formulation under-predicted the average peak stress by a similar degree. The NLV formulation over-predicted the average peak stress by approximately 17%, however there were no statistically significant differences in the percent

errors of individual sample peak stresses ($p > 0.75$). According to both MATLAB and FE predictions, the long-term response to the 5% applied strain was best predicted by the NLV formulation, followed by the LV formulation and then the QLV formulation. The extent of individual sample relaxation (35 ± 11% of peak stress) was equally well-predicted by the three formulations ($p = 0.20$). Similarly, there was no significant difference between viscoelastic formulations in their ability to predict the final (i.e., equilibrium) stress value of individual samples ($p = 0.47$).

The predictions (and associated normalized residuals) of the acute SCPC response to the 3% applied strain history are shown in Fig. 4.2. In contrast to the 5% applied strain case, the NLV formulation predicted the 3% acute response better than the QLV formulation, which in turn outperformed the LV formulation in both the MATLAB and FE procedures. Examining only the average peak stress predictions, all viscoelastic formulations resulted in over-predictions, with the LV demonstrating significantly greater errors than the other two formulations (MATLAB percent errors: LV > QLV $p = 0.015$, LV > NLV $p = 0.020$; FE percent errors: LV > QLV $p = 0.024$, LV > NLV $p = 0.011$). Also in contrast to the 5% strain case, the long-term response was best predicted in both MATLAB and Abaqus by the LV formulation, followed by the NLV formulation, and then the QLV formulation. However, percent errors in the predictions of relaxation extent (experimental average of 27 ± 4% of peak stress) were significantly greater for the LV formulation, followed by the QLV formulation, and then the NLV formulation ($p < 0.001$ for all comparisons under both prediction methods). As with the 5% strain magnitude, there was no significant difference between viscoelastic formulations in their ability to predict the final (i.e., equilibrium) stress value of individual samples ($p > 0.50$).

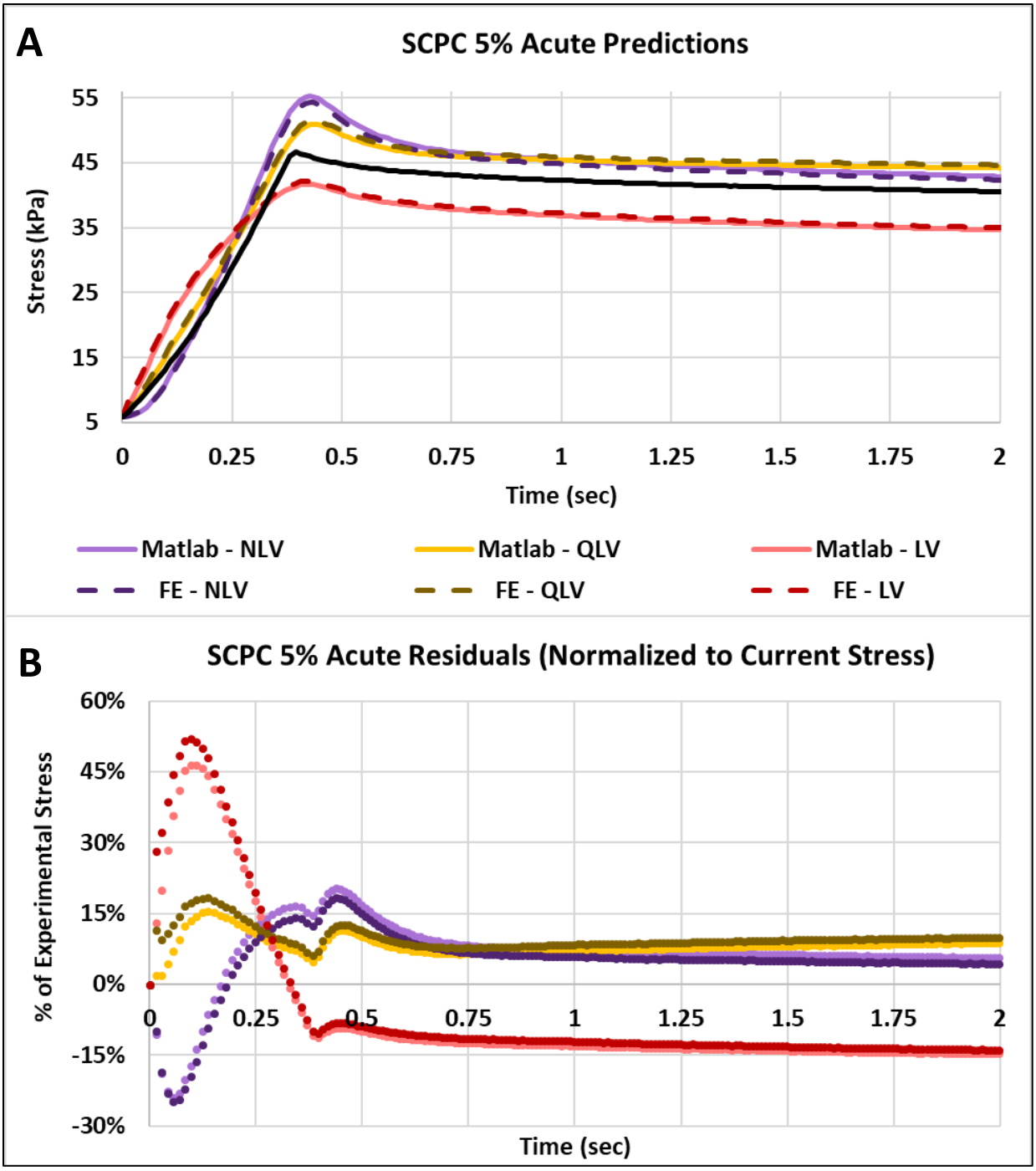

Figure 4.1: Predictions of the acute SCPC response to the 5% applied strain history (A) and the normalized residuals of each prediction (B). Over this range, the RMSE of the NLV and QLV formulations were approximately equivalent while the LV error was greater.

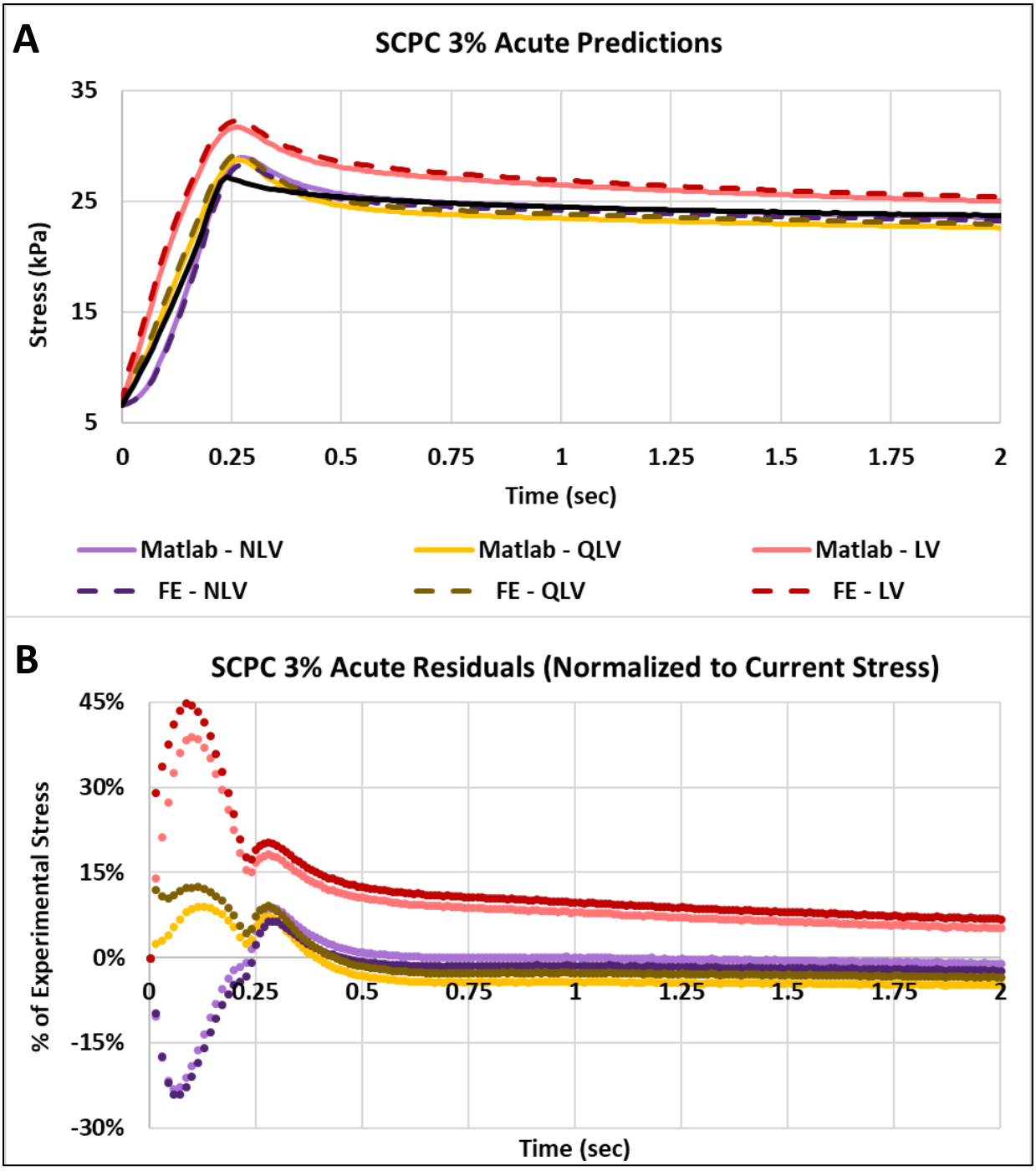

Figure 4.2: Predictions of the acute SCPC response to the 3% applied strain history (A) and the normalized residuals of each prediction (B). Over this range, the RMSE of the NLV formulation prediction was lower than the QLV and LV formulations.

4.3.2.2 Cord

The predictions of the acute stress-relaxation response of the isolated cord to the 5% applied strain are shown in Fig. 4.3. Unlike the SCPC, the acute and long-term cord response was best predicted by the LV formulation, followed by the QLV formulation, and then the NLV formulation. The acute RMSE values for the LV and QLV formulation were similar, but the wRMSE values of the long-term response were approximately 2.5 times greater for the QLV formulation. The average peak stress was best predicted by the QLV formulation, followed by the NLV formulation, and then the LV formulation, but there was no significant difference in the percent errors in individual sample peak stress predictions ($p > 0.096$). There was also no significant difference in the prediction error of individual sample relaxation extent (experimental average 71 ± 7%, $p = 0.81$). The prediction results for the acute and long-term response to the 3% applied strain followed a different pattern than the 5% case (Fig. 4.4). The NLV formulation predicted the acute response best, followed by the QLV formulation, and then the LV formulation. The over-predictions of average peak stress also followed this pattern, although the differences in percent error for individual sample peak stresses was not significant across all viscoelastic formulations ($p > 0.149$). Similarly, the long-term response was best predicted by the NLV formulation, followed by the QLV formulation, and then the LV formulation using both prediction methods, but there was no significant difference in formulation ability to predict individual sample relaxation extent (60 ± 10%, $p = 0.96$). For both strain magnitudes there was no significant difference in individual final stress value prediction errors (5%: $p = 0.09$; 3%: $p = 0.23$).

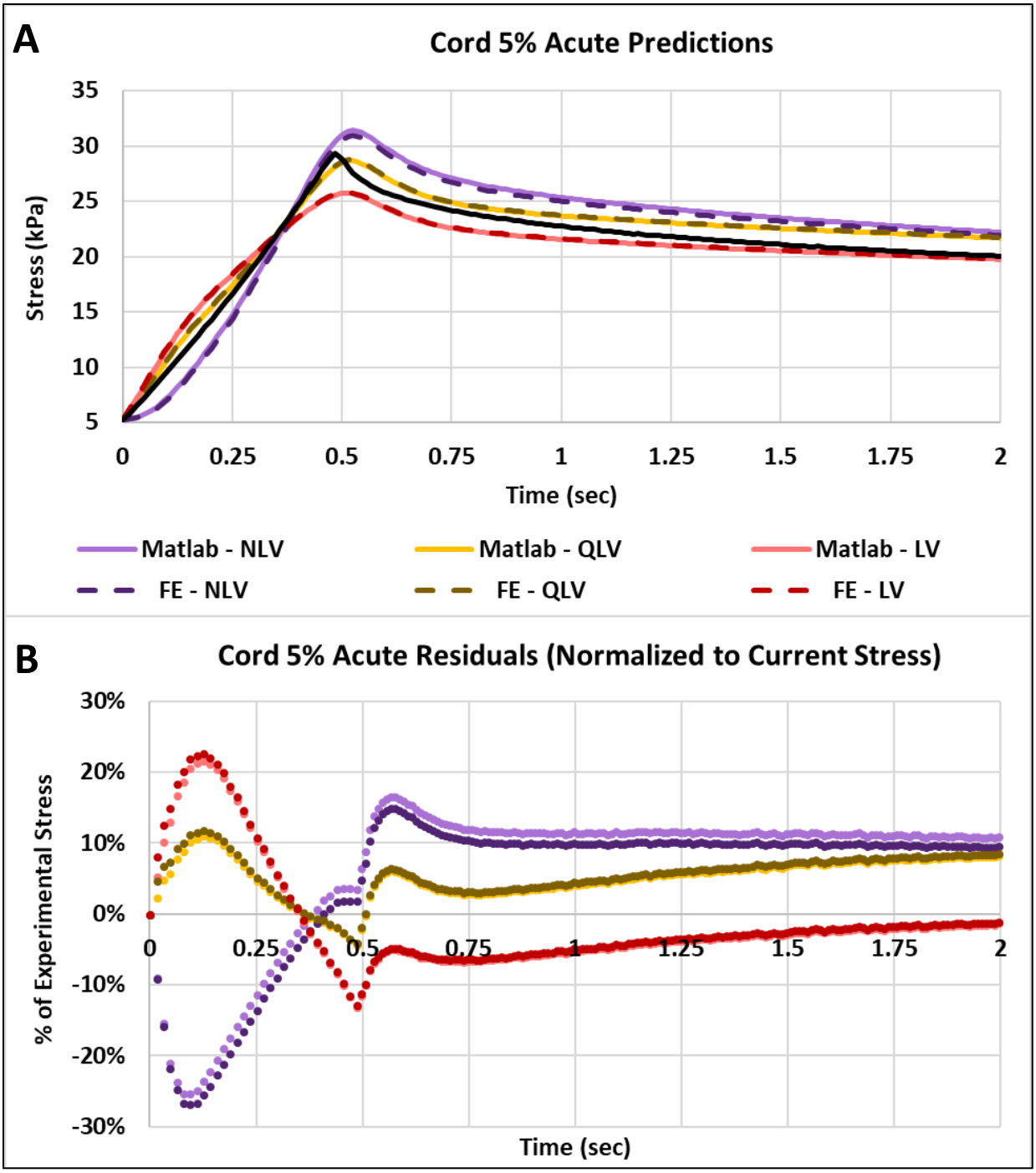

Figure 4.3: Predictions of the acute isolated cord response to the 5% applied strain history (A) and the normalized residuals of each prediction (B). Over this range, the RMSE of the LV formulation prediction was lower than the QLV and NLV formulations.

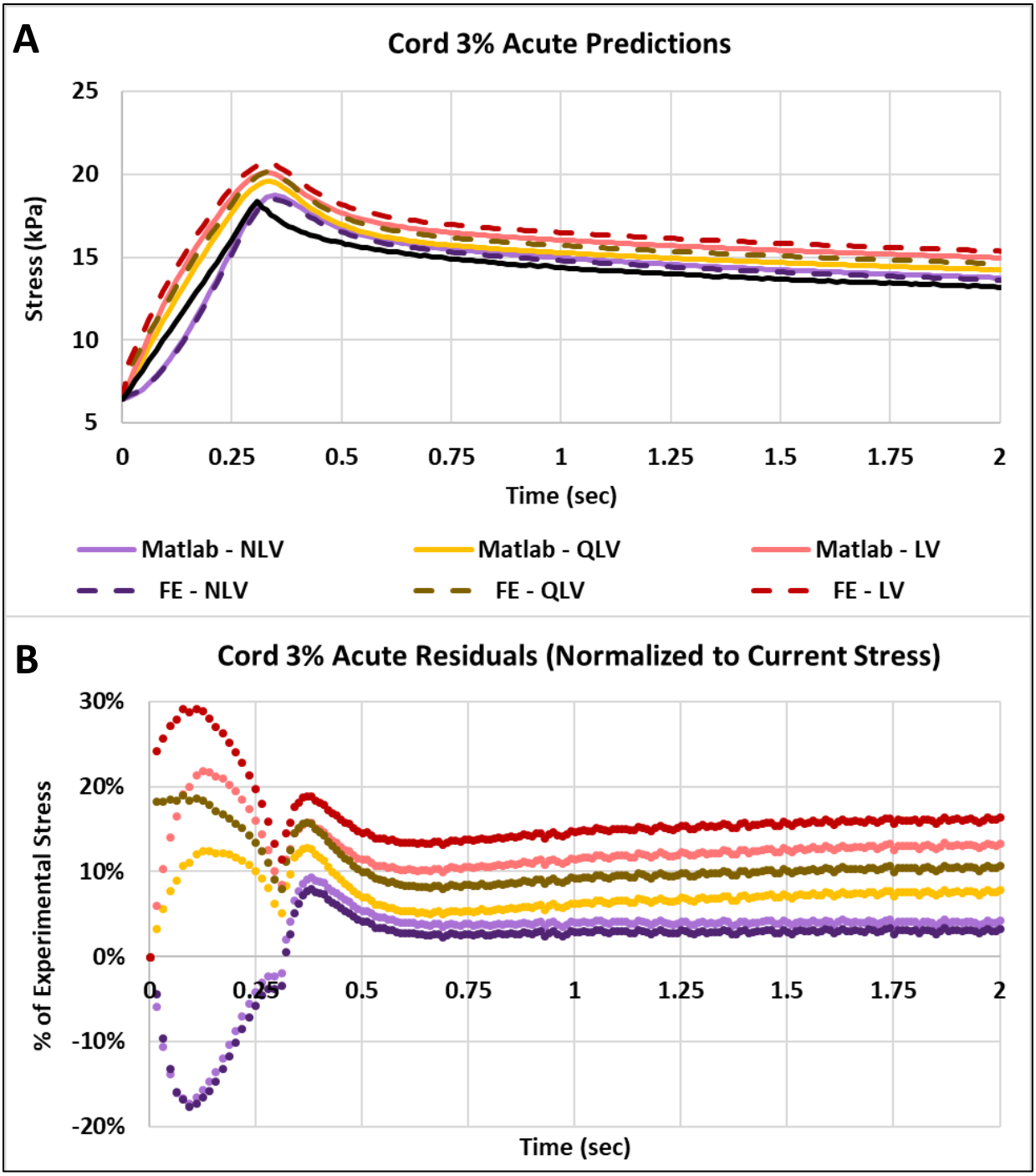

Figure 4.4: Predictions of the acute isolated cord response to the 3% applied strain history (A) and the normalized residuals of each prediction (B). Over this range, the RMSE of the NLV formulation prediction was lower than the QLV and LV formulations.

4.3.2.3 PAC

The predictions of the isolated PAC acute stress-relaxation response to the 5% and 3% applied strain histories are shown in Figs. 4.5 and 4.6, respectively. The 5% average stress-relaxation response was best predicted by the LV formulation, followed by the QLV formulation, and then the NLV formulation according to all measures of predictive accuracy. The predictions of average peak stress followed the same pattern, with over-predictions increasing with increasing model complexity. Analysis of percent errors of individual sample peak stress predictions showed the NLV formulation prediction to be significantly worse than the LV formulation in MATLAB ($p = 0.046$). However, interestingly, when examining the percent errors related to individual sample relaxation, the QLV formulation best predicted the relaxation extent (experimental average 39 ± 13%), followed by the LV formulation, and then the NLV formulation. For the MATLAB predictions, the NLV formulation errors were significantly greater than the other two formulations ($p < 0.001$ for QLV comparison and $p = 0.024$ for LV comparison). For the FE predictions, the QLV formulation errors were significantly less than the other two formulations ($p < 0.001$ for NLV comparison and $p = 0.034$ for LV comparison). The prediction accuracy measures for the 3% applied strain followed a different pattern than the 5% case, with the QLV formulation resulting in the best predictions followed by the NLV formulation, and then the LV formulation using both prediction methods. The average peak stress over-prediction errors for the QLV and NLV formulations were similar, while that of the LV was substantially greater. This finding was also reflected in the percent errors of individual sample peak stresses (MATLAB percent errors: LV > QLV $p = 0.002$, LV > NLV $p = 0.011$; FE percent errors: LV > NLV $p = 0.001$, LV > QLV $p = 0.002$). The NLV formulation was best, followed by the QLV formulation, and then the LV formulation, at matching the total relaxation

observed in experimentally which averaged 36 ± 8%. For both prediction methods, the LV formulation errors were significantly greater than that of the other two formulations (NLV comparison: $p < 0.001$ for both; QLV comparisons: $p < 0.001$ for MATLAB and $p = 0.011$). For the FE predictions, the difference between the QLV and NLV formulation percent errors was also significant ($p = 0.003$). As for the SCPC and isolated cord conditions, there was no significant difference in formulation ability to predict the equilibrium stress value of individual samples (5%: $p = 0.99$; 3%: $p = 0.62$).

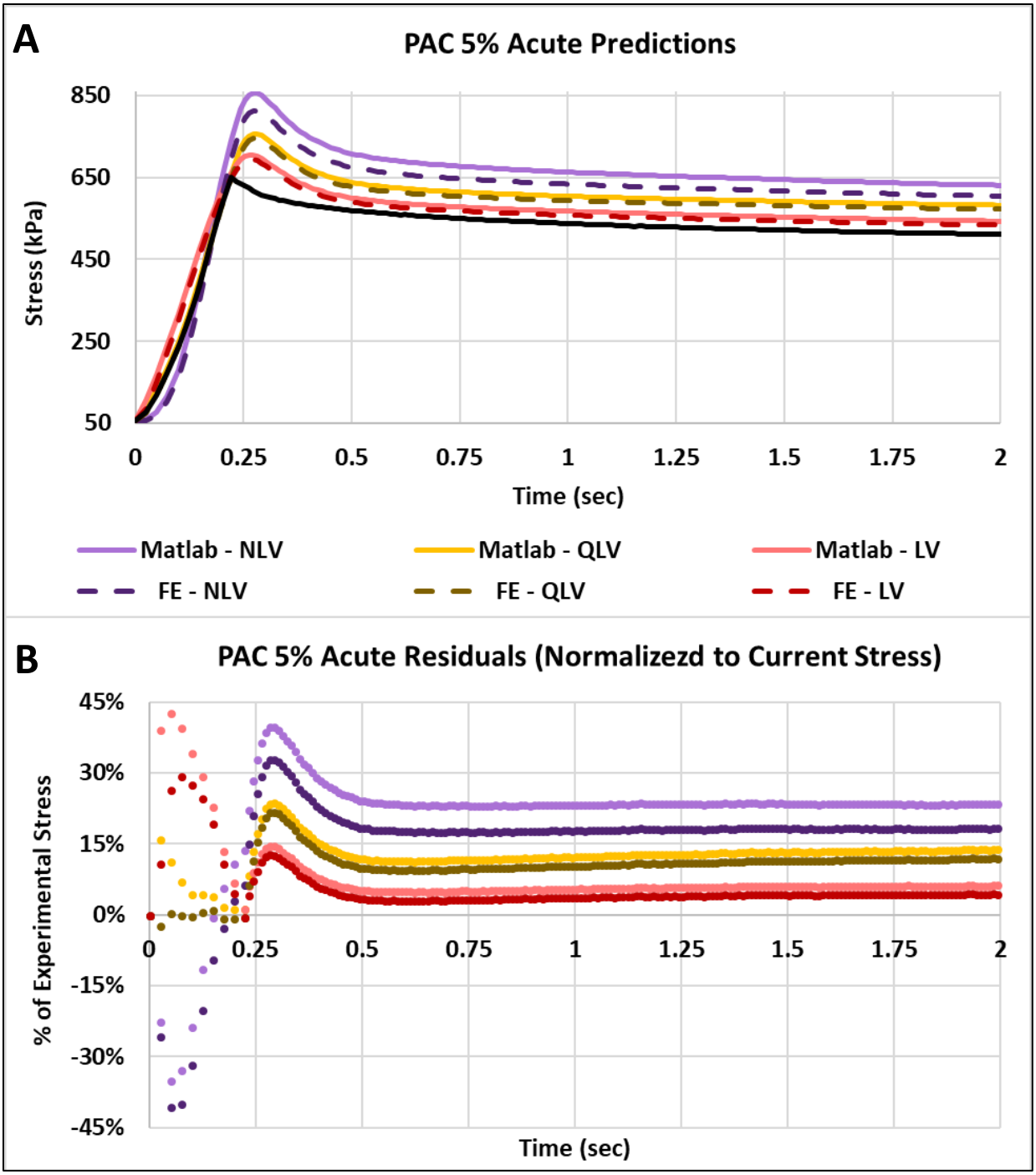

Figure 4.5: Predictions of the acute isolated PAC response to the 5% applied strain history (A) and the normalized residuals of each prediction (B). Over this range, the RMSE of the LV formulation prediction was lower than the QLV and NLV formulations.

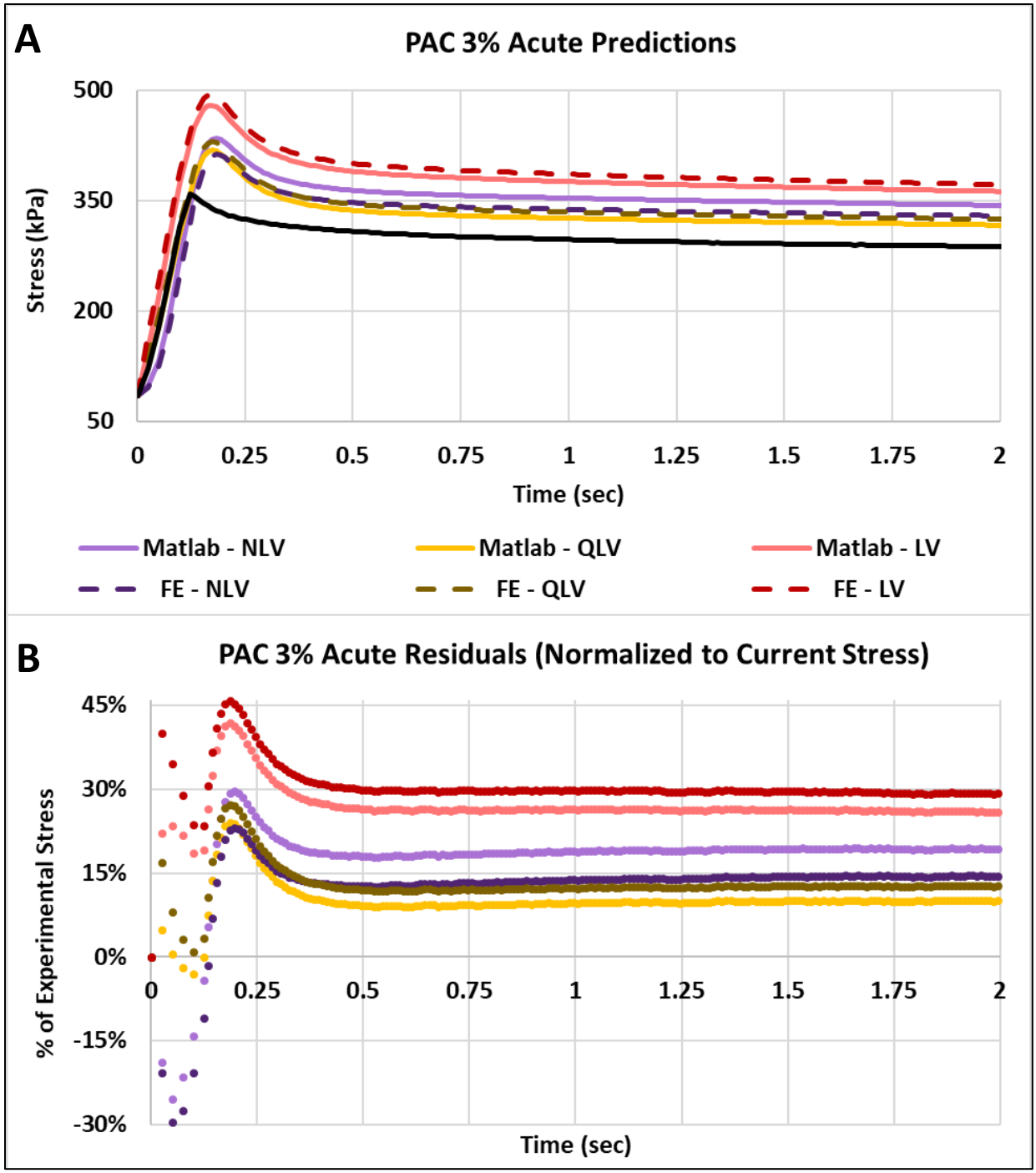

Figure 4.6: Predictions of the acute isolated PAC response to the 3% applied strain history (A) and the normalized residuals of each prediction (B). Over this range, the RMSE of the QLV formulation prediction was lower than the NLV and LV formulations.

4.3.2.4 Computational run times

Predictions of the 3% and 5% stress-relaxation response were preformed simultaneously in MATLAB, but separately in Abaqus. Pooling all three tissue conditions, the time required to compute predictions in MATLAB was greater for the NLV formulation than the QLV formulation (113 milliseconds vs. 87 milliseconds, $p = 0.042$), while the 96-millisecond average duration of LV formulation predictions was not significantly different. As expected, the predictions performed in Abaqus took significantly longer than those in MATLAB ($p < 0.001$ for both strain levels). However, there was no significant difference between formulation prediction time for the 5% stress-relaxation ($p = 0.34$) or 3% stress-relaxation ($p = 0.11$) response in Abaqus when tissue conditions were pooled. There was also no significant difference in the time required for the 5% and 3% stress-relaxation predictions in Abaqus ($p = 0.17$). Across all three tissue conditions and both strain levels, the NLV formulation FE predictions took approximately 4 minutes, the QLV formulation FE predictions took approximately 5 minutes, and the LV formulation FE predictions took 6 minutes.

Table 4.3: Unweighted acute (first 2 seconds only) and weighted long-term (remaining 98 seconds) RMSE values for each viscoelastic formulation prediction. Within each strain magnitude, prediction method (MATLAB or FE), and tissue condition group, the lowest value has been bolded.

(All units kPa)			SCPC		Cord		PAC	
			Acute RMSE	**Long-term wRMSE**	**Acute RMSE**	**Long-term wRMSE**	**Acute RMSE**	**Long-term wRMSE**
5% Strain	**MATLAB**	**NLV**	3.81	**0.30**	2.51	0.30	132.5	16.4
		QLV	**3.33**	1.28	1.25	0.23	72.7	11.9
		LV	5.42	1.03	**1.19**	**0.09**	**38.0**	**6.2**
	FE	**NLV**	**3.23**	**0.24**	2.24	0.26	103.4	12.9
		QLV	3.82	1.35	1.31	0.24	62.8	10.4
		LV	5.16	0.98	**1.17**	**0.09**	**28.5**	**5.8**
3% Strain	**MATLAB**	**NLV**	**0.73**	0.20	**0.75**	**0.10**	58.6	8.6
		QLV	1.05	0.32	1.09	0.12	**33.4**	**4.7**
		LV	2.56	**0.15**	1.81	0.24	82.7	11.3
	FE	**NLV**	**0.77**	0.23	**0.65**	**0.09**	43.7	6.5
		QLV	0.90	0.27	1.53	0.17	**41.4**	**5.9**
		LV	3.01	**0.19**	2.29	0.29	93.1	12.8

4.4 Discussion

Accurate modeling of the mechanical behavior of spinal tissues is critical for understanding the initiation of spinal cord injuries and exploring possible preventative and treatment options through FE analysis. Researchers must evaluate the required degree of accuracy for their specific modeling aims, but these evaluations are subjective as there have been no quantitative comparisons of using LV, QLV, NLV formulations for these tissues. This study addressed this shortcoming by explicitly demonstrating the abilities of the above listed viscoelastic

formulations to fit and predict the stress-strain behavior of the SCPC, the isolated cord, and the PAC. The results of this study will allow researchers to make more objective evaluations of which viscoelastic formulation to implement in their work based on the availability of applicable experimental data, required computational resources, and desired model accuracy.

Within a specific viscoelastic formulation, the significant differences in fitted coefficients reflect differences in tissue condition (SCPC vs. cord vs. PAC) behavior. For the QLV formulation, significant differences in the hyperelastic response of the tissues were found. The PAC was shown to have a significantly greater shear modulus (μ) than the SCPC and isolated cord, which is consistent with other studies of relative tissue stiffness [105,117,118]. Interestingly, the non-linearity (α) of the SCPC was significantly greater than both of its sub-components. This may be due to sliding or interfacial shear deformation in connecting fibers at the interface between the isolated cord and PAC membrane. In the LV formulation, the relaxation modulus coefficients characterize both the elastic and viscous response. Therefore, the significantly greater E_1, E_3, E_4, and E_∞ values for the PAC also reflect its greater stiffness as noted above [105,117,118].

Across all tissue conditions, relative fitting accuracy was not necessarily indicative of relative prediction accuracy, even when fits and predictions occurred at the same strain magnitude. For example, the LV formulation errors for fits of PAC cyclic data were significantly higher than those of the QLV and NLV formulations, but the LV formulation was able to best predict the peak, acute, and long-term 5% stress-relaxation response. Similarly, the cyclic response of the isolated cord was fit best by the QLV formulation, but the acute and long-term 5% stress-relaxation response were predicted best by the LV formulation (Table 4.3). These discrepancies

in fitting and prediction relative accuracies underscore the importance of material model validation through prediction of independent data. Such validation procedures allow for the evaluation of a model's overall utility in characterizing behavior under differing loading protocols.

Comparing the top and bottom sub-tables of Table 4.3, it is clear that the RMSE values for the 5% stress-relaxation predictions and the 3% stress-relaxation predictions follow distinct patterns. These patterns suggest that the choice of viscoelastic formulation for modeling these tissues should depend, in part, on the availability of experimental data at the strain level of interest. For the case of the isolated sub-components (i.e., the PAC and cord), the simplified LV formulation was able to best predict data at the same strain magnitude used to fit the model (5%). However, predictions at a different applied strain magnitude (3%), required a more sophisticated formulation to accurately represent both the acute and long-term response. This necessary increase in model complexity was reflected in the NLV and QLV formulations having the lowest RMSE values for the 3% isolated cord and PAC response, respectively. For both the isolated cord and PAC, the formulation that had the lowest prediction errors at the same strain magnitude as the fitted data, also had the highest prediction errors at the differing strain magnitude. However, the results of the SCPC predictions were more mixed that those of its sub-components. For both the 5% and 3% stress-relaxation cases, the simplified LV formulation had the highest degree of error in predicting the acute SCPC response. The relative long-term predictive accuracy is inverted compared to that of the isolated cord; for the SCPC, the most sophisticated formulation (NLV) best predicted the response at the same strain magnitude as the fitted data,

while the most simplistic formulation (LV) best predicted the response at a differing strain magnitude.

Examining the predictions of individual sample peak stresses, the increase in formulation complexity necessary to accurately predict the 3% stress response was true for all three tissue conditions (Table 4.4 indicates the viscoelastic formulation that resulted in the lowest error for each predictive accuracy measure within a tissue condition and applied strain magnitude). For the PAC, this is reflected in a shift from the LV formulation for the 5% strain magnitude to the QLV or NLV formulation for the 3% case to obtain the best predictions. For the cord, this shift from 5% to 3% is the QLV formulation to the NLV formulation. The change in best formulation for SCPC peak stress predictions from the 5% to 3% strain magnitudes is more subtle, but it still reflects the required increase in complexity from LV or QLV to QLV or NLV.

Table 4.4: Depending on the tissue condition, strain magnitude, and response of interest, the viscoelastic formulation given resulted in the best prediction of stress-relaxation response. Bolded values in the peak stress column indicate a significant difference between at least one other formulation.

Tissue Condition	Strain magnitude relative to fitted data	Peak Stress (% error)	Acute Response (RMSE)	Long-term Response (wRMSE)
SCPC	**Same (5% ε)**	QLV/LV	NLV/QLV	NLV
	Different (3% ε)	**NLV/QLV**	NLV	LV
Cord	**Same (5% ε)**	QLV	LV	LV
	Different (3% ε)	NLV	NLV	NLV
PAC	**Same (5% ε)**	**LV**	LV	LV
	Different (3% ε)	**NLV/QLV**	QLV	QLV

Another consideration for researchers in deciding which viscoelastic formulation to implement is the relative fitting and prediction times. The significant differences in formulation fitting times are most likely due to the relative complexity of the fitting constraints. For the QLV and LV formulations, the fitted coefficients themselves were constrained, with the additional simple linear equality given in Eq. (4.9) for the QLV formulation. In contrast, for the NLV formulation, Eq. (4.17) and its derivative must be evaluated for each Prony weight at every time point to confirm adherence to the constraints. However, after the initial greater computational cost of obtaining the NLV formulation material models, there were no marked difference in the time required for each formulation to predict the stress-relaxation response under both numerical and FE settings. While the difference in NLV and QLV formulation MATLAB prediction duration was statistically significant, the maximum difference of less than 30 milliseconds is not practically relevant.

There are a few limitations within the current work that should be noted. Firstly, the experimental data were all collected at strain-rates and strain-magnitudes lower than that expected to occur during injury [44,153,161,162]. It is possible that under larger strains, the tissues would demonstrate greater elastic non-linearity, which could not be accurately captured by the LV formulations. The second limitation is the unknown effects of computational resource scaling in both fits and FE predictions. As discussed above, the difference in required fitting time was substantial (approximately 1 minute for LV and QLV formulations compared to over 1 hour for the NLV formulation); however, only two parallel processors were utilized in this study. It is expected that with greater computational power, Eq. (4.17) could be evaluated for each Prony weight in parallel, reducing the time needed to verify the NLV constraints. Conversely,

differences in FE prediction time may manifest between formulations if the analysis is extended to multi-element models. Finally, all the presented viscoelastic formulations and material models are for one-dimensional analyses only. Without data on the transverse behavior of each tissue condition or a three-dimensional constitutive equation, all FE modeling was limited to utilizing truss elements. Future work will include development and FE implementation of three-dimensional viscoelastic formulations to address important questions regarding the effect of geometric and material model complexity on stress distributions through the cross-section of the tissues.

4.4.1 Recommendations and conclusions

The results presented herein provide researchers with the necessary evidence to inform their decisions about which viscoelastic formulation to implement when working with specific spinal tissues. The study results also reiterate the need for material model validation, as fitting accuracy was not always correlated with predictive accuracy. As shown in Table 4.4, the choice of viscoelastic formulation for each tissue depends on available experimental data and the response feature of interest. In general, the use of LV or QLV formulations may be justified when experimental data at the strain level of interest is available, although this is not typically the case. The true value of a material model is its ability to determine the expected response of a tissue under arbitrary loading conditions. According to the analysis above, this requires an increase in viscoelastic formulation complexity from LV to QLV (or even LV to NLV for the case of the isolated cord) or from QLV to NLV. Based on the results of this study, the authors will utilize the QLV formulation to characterize PAC behavior and the NLV formulation to characterize the isolated cord and SCPC mechanical behaviors in future modeling efforts.

CHAPTER 5: CONCLUSION

5.1 Summary of Findings

The results of this dissertation represent important contributions to the understanding and modeling of spinal tissue mechanical behavior. The experimental and computational methodologies presented will enable researchers to conduct more thorough characterizations of the tissues involved and make more informed decisions regarding how best to model their respective observed responses.

In this dissertation, post-mortem changes in spinal-cord-pia-arachnoid-construct (SCPC) elastic and viscous behaviors were quantified through comparisons of *in-vivo* and *ex-vivo* stress-strain data. The *ex-vivo* condition was found to exhibit a stiffer response but also experienced greater relaxation than samples tested *in-vivo*. Non-linear viscoelastic modeling of both conditions revealed this divergent behavior to be most significant over the short-term (0.1 – 1 second) response. These results have two important implications for researchers interested in modeling spinal cord injury: (1) explicit evidence of strain-dependent relaxation under both *in-vivo* and *ex-vivo* conditions compels the use of a non-linear viscoelastic formulation to characterize the SCPC response, and (2) the use of non-linear viscoelastic formulations developed from *ex-vivo* experimentation will result in over-predictions of SCPC stress and degree of relaxation.

The contribution of the pia-arachnoid-complex (PAC) to the viscoelastic response of the SCPC was also demonstrated through the implementation of a novel dissection technique. For the first time, experimental data from SCPC was quantitatively compared to that of both of its sub-

components (neural tissue of the isolated cord and the PAC). Despite making up less than 6% of the cross-section, the PAC was shown to significantly influence the elastic and viscous response of the SCPC supporting the conclusion that the PAC plays an important mechanical role in protecting the underlying cord. The non-linear viscoelastic formulations developed for each tissue provides for increased finite element (FE) model geometric and material fidelity which is expected to improve prediction accuracy of internal stress and strain distributions.

Finally, linear (LV), quasi-linear (QLV), and non-linear viscoelastic (NLV) formulations were developed based on our novel *direct fit method* numerical integration approach. The ability of each of these formulations to accurately fit and predict the mechanical behavior of the SCPC, cord, and PAC were quantitatively compared. The presented results allow researchers to identify which viscoelastic formulation would provide the most accurate prediction for each tissue based on existence of experimental data at the strain level of interest and the response feature of interest (e.g., peak stress versus long-term response). Specifically,

- SCPC, experimental data at strain level, peak stress: LV or QLV
- SCPC, experimental data at strain level, acute response: NLV or QLV
- SCPC, experimental data at strain level, long-term response: NLV
- SCPC, no experimental data at strain level, peak stress: NLV or QLV
- SCPC, no experimental data at strain level, acute response: NLV
- SCPC, no experimental data at strain level, long-term response: LV
- Cord, experimental data at strain level, peak stress: QLV
- Cord, experimental data at strain level, acute response: LV
- Cord, experimental data at strain level, long-term response: LV
- Cord, no experimental data at strain level, peak stress: NLV
- Cord, no experimental data at strain level, acute response: NLV
- Cord, no experimental data at strain level, long-term response: NLV
- PAC, experimental data at strain level, peak stress: LV
- PAC, experimental data at strain level, acute response: LV
- PAC, experimental data at strain level, long-term response: LV
- PAC, no experimental data at strain level, peak stress: QLV or NLV
- PAC, no experimental data at strain level, acute response: QLV

- PAC, no experimental data at strain level, long-term response: QLV

The computational run times for the viscoelastic model fits and associated predictions (using both numerical and FE methods) provides additional context for the effect of increased complexity to the NLV formulation.

5.2 Future Work

As indicated in Sections 2.4, 3.4, and 4.4 there are a number of logical extensions to the work presented of this dissertation. This future work can be generally classified as the collection of additional experimental data or the improvement of the presented viscoelastic formulations.

Experimental limitations precluded the collection of mechanical data under conditions applicable to the dynamic events of spinal cord injury. Therefore, future work should include *ex-vivo* analysis of the SCPC, isolated cord, and PAC under applied strains (up to 10%) and strain-rates (up to 2000%/s) indicative of injury. Use of these new data with the viscoelastic characterization techniques described in this dissertation would provide novel insights into damage-induced changes in each tissue's viscoelastic response. Such characterizations would also provide material models that accurately represent the tissue behavior under conditions important to the study of spinal cord injury prevention, diagnosis, and treatment.

As distraction was the injury mechanism of interest, experimental data were collected under uniaxial, longitudinal tension only. However, the same techniques described in this dissertation could be used with transverse compression data to study the more common contusion injury mechanism. As indicated in Section 1.3.2, animal models of contusion injuries are currently

established and may provide the *in-vivo* SCPC data necessary to determine if the post-mortem viscoelastic changes seen in longitudinal tension also manifests in transverse compression. Collection of transverse data would also provide the basis for investigation of the anisotropic behavior of the SCPC, isolated cord, and PAC. *Ex-vivo* transverse compression and transverse tension tests of the SCPC and isolated cord have been reported previously, but biaxial tests of spinal PAC should be performed to determine its anisotropic behavior.

Finally, to enable volumetric representation of the SCPC, cord, and PAC in FE models, the viscoelastic formulations presented in this dissertation should be extended to three-dimensions. This requires not only the collection of data describing the transverse and/or biaxial behavior of each tissue (as described above), but also application of our *direct fit method* numerical integration technique to three-dimensional constitutive equations. Development and FE implementation of three-dimensional viscoelastic formulations would allow researchers to address important questions regarding the effect of geometric and material model complexity on stress and strain distributions through the cross-section of the spinal cord.

REFERENCES

1. Bernhard, M., Gries, A., Kremer, P. & Böttiger, B. W. Spinal cord injury (SCI)--prehospital management. *Resuscitation* **66,** 127–39 (2005).

2. Sekhon, L. H. & Fehlings, M. G. Epidemiology, demographics, and pathophysiology of acute spinal cord injury. *Spine (Phila. Pa. 1976).* **26,** S2-12 (2001).

3. Stover, S. L. & Fine, P. R. The epidemiology and economics of spinal cord injury. *Paraplegia* **25,** 225–228 (1987).

4. Berkowitz, M., O'Leary, P., Kruse, D. & Harvey, C. *Spinal Cord Injury: An Analysis of Medical and Social Costs*. (Demos Medical Publishing, Inc., 1998).

5. DeVivo, M. J. Causes and costs of spinal cord injury in the United States. *Spinal Cord* **35,** 809–13 (1997).

6. French, D. D. *et al.* Health care costs for patients with chronic spinal cord injury in the Veterans Health Administration. *J. Spinal Cord Med.* **30,** 477–481 (2007).

7. Cheriyan, T. *et al.* Spinal cord injury models: a review. *Spinal Cord* 1–8 (2014). doi:10.1038/sc.2014.91

8. White, A. A., Panjabi, M. M. & White. *Clinical Biomechanics of the Spine*. **38,** (Lippincott, 1990).

9. Wilke, H. J., Kettler, A., Wenger, K. H. & Claes, L. E. Anatomy of the sheep spine and its comparison to the human spine. *Anat. Rec.* **247,** 542–55 (1997).

10. Taso, M. *et al.* Construction of an in vivo human spinal cord atlas based on high-resolution MR images at cervical and thoracic levels: preliminary results. *MAGMA* **27,** 257–267 (2014).

11. Fradet, L., Arnoux, P.-J., Ranjeva, J.-P., Petit, Y. & Callot, V. Morphometrics of the entire human spinal cord and spinal canal measured from in vivo high-resolution anatomical magnetic resonance imaging. *Spine (Phila. Pa. 1976).* **39,** E262-9 (2014).

12. Kameyama, T., Hashizume, Y. & Sobue, G. Morphologic features of the normal human cadaveric spinal cord. *Spine* **21,** 1285–1290 (1996).

13. Ko, H.-Y., Park, J. H., Shin, Y. B. & Baek, S. Y. Gross quantitative measurements of spinal cord segments in human. *Spinal Cord* **42,** 35–40 (2004).

14. Nógrádi, A. & Vrbová, G. *Anatomy and Physiology of the Spinal Cord. In: Madame Curie Bioscience Database [Internet]*. (Landes Bioscience, 2013).

15. Martini, F. & Bartholomew, E. *Essentials of Anatomy & Physiology*. (Pearson Education, Inc., 2010).

16. McKinley, M. & O'Loughlin, V. D. *Human Anatomy*. (McGraw-Hill, 2011).

17. Mazgajczyk, E., Ścigała, K., Czyż, M., Jarmundowicz, W. & Będziński, R. Mechanical properties of cervical dura mater. *Acta Bioeng. Biomech.* **14,** 51–8 (2012).

18. Zarzur, E. Mechanical properties of the human lumbar dura mater. *Arq. Neuropsiquiatr.* **54,** 455–60 (1996).

19. Hong, J. Y. *et al.* Analysis of dural sac thickness in human spine - Cadaver study with confocal infrared laser microscope. *Spine J.* **11,** 1121–1127 (2011).

20. Balaratnasingam, C. *et al.* Histomorphometric measurements in human and dog optic nerve and an estimation of optic nerve pressure gradients in human. *Exp. Eye Res.* **89,** 618–628 (2009).

21. Reina, M. A. *et al.* Ultrastructural findings in human spinal pia mater in relation to subarachnoid anesthesia. *Anesth. Analg.* **98,** 1479–85 (2004).

22. Clarke, E. C., Cheng, S. & Bilston, L. E. The mechanical properties of neonatal rat spinal cord in vitro, and comparisons with adult. *J. Biomech.* **42,** 1397–402 (2009).

23. Choo, A. M. *et al.* Contusion, dislocation, and distraction: primary hemorrhage and membrane permeability in distinct mechanisms of spinal cord injury. *J. Neurosurg. Spine* **6,** 255–266 (2007).

24. Scifert, J., Totoribe, K., Goel, V. & Huntzinger, J. Spinal cord mechanics during flexion and extension of the cervical spine: a finite element study. *Pain Physician* **5,** 394–400 (2002).

25. Fiford, R. J. & Bilston, L. E. The mechanical properties of rat spinal cord in vitro. *J. Biomech.* **38,** 1509–15 (2005).

26. Dabney, K. W. *et al.* A model of experimental spinal cord trauma based on computer-controlled intervertebral distraction: Characterization of graded injury. *Spine (Phila. Pa. 1976).* **29,** 2357–2364 (2004).

27. Maikos, J. T., Elias, R. & Shreiber, D. I. Mechanical properties of dura mater from the rat brain and spinal cord. *J. Neurotrauma* **25,** 38–51 (2008).

28. Kwon, B. K., Hillyer, J. & Tetzlaff, W. Translational research in spinal cord injury: a survey of opinion from the SCI community. *J. Neurotrauma* **27,** 21–33 (2010).

29. Tator, C. H. Review of treatment trials in human spinal cord injury: issues, difficulties, and recommendations. *Neurosurgery* **59,** 957-82; discussion 982–7 (2006).

30. Lammertse, D. *et al.* Guidelines for the conduct of clinical trials for spinal cord injury as developed by the ICCP panel: clinical trial design. *Spinal Cord* **45,** 232–42 (2007).

31. Rao, G. S. Anatomical studies on the ovine spinal cord. *Anat. Anz.* **171,** 261–4 (1990).

32. Cain, C. C. & Fraser, R. D. Bony and vascular anatomy of the normal cervical spine in the sheep. *Spine (Phila. Pa. 1976).* **20,** 759–65 (1995).

33. Ghazi, S. R. & Gholami, S. Study on the developmental changes in angulation of spinal nerves, the length of the dorsal roots and spinal nerves in sheep. *Anat. Histol. Embryol.* **26,** 211–5 (1997).

34. Shetye, S. S., Deault, M. M. & Puttlitz, C. M. Biaxial response of ovine spinal cord dura mater. *J. Mech. Behav. Biomed. Mater.* **34,** 146–53 (2014).

35. Dath, R., Ebinesan, A. D., Porter, K. M. & Miles, A. W. Anatomical measurements of porcine lumbar vertebrae. *Clin. Biomech.* **22,** 607–613 (2007).

36. Sheng, S. R., Wang, X. Y., Xu, H. Z., Zhu, G. Q. & Zhou, Y. F. Anatomy of large animal spines and its comparison to the human spine: A systematic review. *Eur. Spine J.* **19,** 46–56 (2010).

37. Busscher, I., Ploegmakers, J. J. W., Verkerke, G. J. & Veldhuizen, A. G. Comparative anatomical dimensions of the complete human and porcine spine. *Eur. Spine J.* **19,** 1104–1114 (2010).

38. Fradet, L., Cliche, F., Petit, Y., Mac-Thiong, J.-M. & Arnoux, P.-J. Strain rate dependent behavior of the porcine spinal cord under transverse dynamic compression. *Proc. Inst. Mech. Eng. Part H J. Eng. Med.* **230,** 858–66 (2016).

39. Lee, J. H. T. *et al.* A novel porcine model of traumatic thoracic spinal cord injury. *J. Neurotrauma* **30,** 142–59 (2013).

40. Jones, C. F., Cripton, P. a. & Kwon, B. K. Gross Morphological Changes of the Spinal Cord Immediately After Surgical Decompression in a Large Animal Model of Traumatic Spinal Cord Injury. *Spine (Phila. Pa. 1976).* **37,** E890–E899 (2012).

41. Moon, S. H., Cha, R., Lee, M., Kim, S. & Soh, K. S. Primo Vascular System in the Subarachnoid Space of the Spinal Cord of a Pig. *JAMS J. Acupunct. Meridian Stud.* **5,** 226–233 (2012).

42. Li, X. F. & Dai, L. Y. Three-dimensional finite element model of the cervical spinal cord: preliminary results of injury mechanism analysis. *Spine (Phila. Pa. 1976).* **34,** 1140–7 (2009).

43. Greaves, C. Y., Gadala, M. S. & Oxland, T. R. A three-dimensional finite element model of the cervical spine with spinal cord: an investigation of three injury mechanisms. *Ann. Biomed. Eng.* **36,** 396–405 (2008).

44. Russell, C. M., Choo, A. M., Tetzlaff, W., Chung, T. E. & Oxland, T. R. Maximum principal strain correlates with spinal cord tissue damage in contusion and dislocation injuries in the rat cervical spine. *J. Neurotrauma* **29,** 1574–85 (2012).

45. Maikos, J. T., Qian, Z., Metaxas, D. & Shreiber, D. I. Finite element analysis of spinal cord injury in the rat. *J. Neurotrauma* **25,** 795–816 (2008).

46. Khuyagbaatar, B., Kim, K., Man Park, W. & Hyuk Kim, Y. Biomechanical Behaviors in Three Types of Spinal Cord Injury Mechanisms. *J. Biomech. Eng.* **138,** 081003 (2016).

47. Lam, C. J., Assinck, P., Liu, J., Tetzlaff, W. & Oxland, T. R. Impact depth and the interaction with impact speed affect the severity of contusion spinal cord injury in rats. *J. Neurotrauma* **31,** 1985–97 (2014).

48. Dumont, R. J. *et al.* Acute spinal cord injury, part I: pathophysiologic mechanisms. *Clin. Neuropharmacol.* **24,** 254–64 (2001).

49. Parizel, P. M. *et al.* Trauma of the spine and spinal cord: Imaging strategies. *Eur. Spine J.* **19,** 8–17 (2010).

50. Choo, A. M.-T. *et al.* Modeling spinal cord contusion, dislocation, and distraction: characterization of vertebral clamps, injury severities, and node of Ranvier deformations. *J. Neurosci. Methods* **181,** 6–17 (2009).

51. Khuyagbaatar, B., Kim, K. & Hyuk Kim, Y. Effect of bone fragment impact velocity on biomechanical parameters related to spinal cord injury: A finite element study. *J. Biomech.* **47,** 2820–2825 (2014).

52. Wilcox, R. K. *et al.* A dynamic investigation of the burst fracture process using a combined experimental and finite element approach. *Eur. Spine J.* **13,** 481–8 (2004).

53. Yeo, J. D., Payne, W., Hinwood, B. & Kidman, A. D. The experimental contusion injury of the spinal cord in sheep. *Paraplegia* **12,** 279–98 (1975).

54. Theodotou, C. B., Ghobrial, G. M., Middleton, A. L., Wang, M. Y. & Levi, A. D. Anterior Reduction and Fusion of Cervical Facet Dislocations. *Neurosurgery* **0,** 1–8 (2018).

55. Silberstein, M. & McLean, K. Non-contiguous spinal injury: clinical and imaging features, and postulated mechanism. *Paraplegia* **32,** 817–823 (1994).

56. Dickerman, R. D., Mittler, M. a, Warshaw, C. & Epstein, J. a. Spinal cord injury in a 14-year-old male secondary to cervical hyperflexion with exercise. *Spinal Cord* **44,** 192–195 (2006).

57. Kato, Y. *et al.* Flexion model simulating spinal cord injury without radiographic abnormality in patients with ossification of the longitudinal ligament: the influence of flexion speed on the cervical spine. *J. Spinal Cord Med.* **32,** 555–559 (2009).

58. Maiman, D. J., Myklebust, J. B., Ho, K. C. & Coats, J. Experimental spinal cord injury produced by axial tension. *J Spinal Disord* **2,** 6–13 (1989).

59. Kimpara, H. *et al.* Investigation of anteroposterior head-neck responses during severe frontal impacts using a brain-spinal cord complex FE model. *Stapp Car Crash J.* **50,** 509–544 (2006).

60. Allen, A. Surgery of Experimental Lesion of Spinal Cord Equivalent to Crush Injury of Fracture Dislocation of Spinal Column. *J. Am. Med. Assoc.* **LVII,** 878–80 (1911).

61. Seifert, J. L., Bell, J. E., Elmer, B. B., Sucato, D. J. & Romero, M. I. Characterization of a novel bidirectional distraction spinal cord injury animal model. *J. Neurosci. Methods* **197,** 97–103 (2011).

62. Jones, C. F., Lee, J. H. T., Kwon, B. K. & Cripton, P. A. Development of a large-animal model to measure dynamic cerebrospinal fluid pressure during spinal cord injury: Laboratory investigation. *J. Neurosurg. Spine* **16,** 624–35 (2012).

63. Salegio, E. A. *et al.* A Unilateral Cervical Spinal Cord Contusion Injury Model in Non-Human Primates (Macaca mulatta). *J. Neurotrauma* **33,** 439–59 (2016).

64. Jones, C. F. *et al.* Cerebrospinal fluid pressures resulting from experimental traumatic spinal cord injuries in a pig model. *J. Biomech. Eng.* **135,** 101005 (2013).

65. Iwanami, A. *et al.* Establishment of graded spinal cord injury model in a nonhuman primate: The common marmoset. *J. Neurosci. Res.* **80,** 172–181 (2005).

66. Wilson, S. *et al.* An ovine model of spinal cord injury. *J. Spinal Cord Med.* 1–16 (2016). doi:10.1080/10790268.2016.1222475

67. Sparrey, C. J. *et al.* Mechanical Design and Analysis of a Unilateral Cervical Spinal Cord Contusion Injury Model in Non-Human Primates. *J. Neurotrauma* **14,** neu.2015.3974 (2016).

68. Mageed, M., Ionita, J. C., Ludewig, E., Brehm, W. & Gerlach, K. Morphometrical analysis of the thoracolumbar dural sac in sheep using computed assisted myelography. *Vet. Comp. Orthop. Traumatol.* **27,** 124–129 (2014).

69. Hung, T. K. & Chang, G. L. Biomechanical and neurological response of the spinal cord of a puppy to uniaxial tension. *J. Biomech. Eng.* **103,** 43–7 (1981).

70. Hung, T. K., Lin, H. S., Bunegin, L. & Albin, M. S. Mechanical and neurological response of cat spinal cord under static loading. *Surg. Neurol.* **17,** 213–7 (1982).

71. Rossignol, S. *et al.* The cat model of spinal injury. *Prog. Brain Res.* **137,** 151–68 (2002).

72. Streijger, F. *et al.* The Effect of Whole-Body Resonance Vibration in a Porcine Model of Spinal Cord Injury. *J Neurotrauma* **921,** 908–921 (2015).

73. Jones, C. F., Newell, R. S., Lee, J. H. T., Cripton, P. A. & Kwon, B. K. The pressure distribution of cerebrospinal fluid responds to residual compression and decompression in an animal model of acute spinal cord injury. *Spine (Phila. Pa. 1976).* **37,** E1422-31 (2012).

74. Hales, J. R., Yeo, J. D., Stabback, S., Fawcett, a a & Kearns, R. Effects of anesthesia and laminectomy on regional spinal cord blood flow in conscious sheep. *J. Neurosurg.* **54,** 620–6 (1981).

75. Stoodley, M. A., Brown, S. A., Brown, C. J. & Jones, N. R. Arterial pulsation-dependent perivascular cerebrospinal fluid flow into the central canal in the sheep spinal cord. *J. Neurosurg.* **86,** 686–93 (1997).

76. Coffey, R. J., Miesel, K. & Billstrom, T. Cerebrospinal fluid pressure measurement in the ovine intrathecal space: a preliminary study towards the diagnosis of intrathecal drug administration catheter dislodgement or occlusion. *Stereotact. Funct. Neurosurg.* **88,** 337–44 (2010).

77. Fullarton, A. C., Myles, L. M., Lenihan, D. V, Hems, T. E. & Glasby, M. A. Obstetric brachial plexus palsy: a comparison of the degree of recovery after repair of a C6 ventral root avulsion in newborn and adult sheep. *Br. J. Plast. Surg.* **54,** 697–704 (2001).

78. Cain, C. M., Langston, P. G., Weston, P. F. & Fraser, R. D. Assessment of spinal cord blood flow and function in sheep after anterolateral cervical interbody fusion in the presence of cord damage. *Spine (Phila. Pa. 1976).* **19,** 511–9 (1994).

79. Benneker, L. M. *et al.* Development of an in vivo experimental model for percutaneous vertebroplasty in sheep. *Vet. Comp. Orthop. Traumatol.* **25,** 173–177 (2012).

80. Elliott-Lewis, E. W., Jolette, J., Ramos, J. & Benzel, E. C. Thermal damage assessment of novel bipolar forceps in a sheep model of spinal surgery. *Neurosurgery* **67,** 166-71; discussion 171–2 (2010).

81. Wang, A. *et al.* Placental mesenchymal stromal cells rescue ambulation in ovine myelomeningocele. *Stem Cells Transl. Med.* **4,** 659–69 (2015).

82. Fransson, B. A., Zhu, Q., Bagley, R. S., Tucker, R. & Oxland, T. R. Biomechanical evaluation of cervical intervertebral plug stabilization in an ovine model. *Vet. Surg.* **36,** 449–457 (2007).

83. Vialle, R., Lacroix, C., Harding, I., Loureiro, M.-C. & Tadié, M. Motor and sensitive axonal regrowth after multiple intercosto-lumbar neurotizations in a sheep model. *Spinal Cord* **48,** 367–74 (2010).

84. Mesquita, R. C. *et al.* Optical monitoring and detection of spinal cord ischemia. *PLoS One* **8,** 1–9 (2013).

85. Böckler, D. *et al.* Spinal Cord Ischemia after Endovascular Repair of the Descending

Thoracic Aorta in a Sheep Model. *Eur. J. Vasc. Endovasc. Surg.* **34,** 461–469 (2007).

86. Safayi, S. *et al.* Treadmill measures of ambulation rates in ovine models of spinal cord injury and neuropathic pain. *J. Med. Eng. Technol.* **40,** 72–79 (2016).

87. Yeo, J. D., Stabback, S. & McKenzie, B. Central necrosis following contusion to the sheep's spinal cord. *Paraplegia* **14,** 276–85 (1977).

88. Hung, T. K., Chang, G. L., Chang, J. L. & Albin, M. S. Stress-strain relationship and neurological sequelae of uniaxial elongation of the spinal cord of cats. *Surg. Neurol.* **15,** 471–476 (1981).

89. Maiman, D. J., Coats, J. & Myklebust, J. B. Cord/Spine Motion in Experimental Spinal Cord Injury. *J. Spinal Disord. Tech.* **2,** (1989).

90. Hung, T. K., Chang, G. L., Lin, H. S., Walter, F. R. & Bunegin, L. Stress-strain relationship of the spinal cord of anesthetized cats. *J. Biomech.* **14,** 269–76 (1981).

91. Chang, G. L., Hung, T. K. & Feng, W. W. An in-vivo measurement and analysis of viscoelastic properties of the spinal cord of cats. *J. Biomech. Eng.* **110,** 115–22 (1988).

92. Persson, C., Summers, J. & Hall, R. M. The importance of fluid-structure interaction in spinal trauma models. *J. Neurotrauma* **28,** 113–125 (2011).

93. Sparrey, C. J., Manley, G. T. & Keaveny, T. M. Effects of white, grey, and pia mater properties on tissue level stresses and strains in the compressed spinal cord. *J. Neurotrauma* **26,** 585–95 (2009).

94. Ichihara, K., Taguchi, T., Sakuramoto, I., Kawano, S. & Kawai, S. Mechanism of the spinal cord injury and the cervical spondylotic myelopathy: new approach based on the mechanical features of the spinal cord white and gray matter. *J. Neurosurg.* **99,** 278–285 (2003).

95. Ichihara, K. *et al.* Gray matter of the bovine cervical spinal cord is mechanically more rigid and fragile than the white matter. *J. Neurotrauma* **18,** 361–367 (2001).

96. Nishida, N. *et al.* Stress analysis of the cervical spinal cord: Impact of the morphology of spinal cord segments on stress. *J. Spinal Cord Med.* **0,** 1–8 (2016).

97. Kato, Y. *et al.* Biomechanical study of cervical flexion myelopathy using a three-dimensional finite element method. *J. Neurosurg. Spine* **8,** 436–41 (2008).

98. Nishida, N., Kato, Y., Imajo, Y., Kawano, S. & Taguchi, T. Biomechanical analysis of cervical spondylotic myelopathy: The influence of dynamic factors and morphometry of the spinal cord. *J. Spinal Cord Med.* **35,** 256–261 (2012).

99. Purves, D. *et al. Neuroscience*. (Sinauer Associates, 2001).

100. Koser, D. E., Moeendarbary, E., Hanne, J., Kuerten, S. & Franze, K. CNS cell distribution and axon orientation determine local spinal cord mechanical properties. *Biophys. J.* **108,** 2137–2147 (2015).

101. Cheng, S., Clarke, E. C. & Bilston, L. E. Rheological properties of the tissues of the central nervous system: A review. *Med. Eng. Phys.* **30,** 1318–1337 (2008).

102. Maikos, J. In Vivo Tissue-Level Thresholds for Spinal Cord Injury. (Rutgers, 2007).

103. Grussu, F., Schneider, T., Zhang, H., Alexander, D. C. & Wheeler-Kingshott, C. A. M. Neurite orientation dispersion and density imaging of the healthy cervical spinal cord in vivo. *Neuroimage* **111,** 590–601 (2015).

104. Pan, Y., Sullivan, D., Shreiber, D. I. & Pelegri, A. A. Finite Element Modeling of CNS White Matter Kinematics: Use of a 3D RVE to Determine Material Properties. *Front. Bioeng. Biotechnol.* **1,** 19 (2013).

105. Mazuchowski, E. L. & Thibault, L. E. Biomechanical properties of the human spinal cord and pia mater. in *ASME Summer Bioengineering Conference* 1205–1206 (2003).

106. Rangwala, N. A., Hackney, D. B., Dai, W. & Alsop, D. C. Diffusion restriction in the human spinal cord characterized in vivo with high b-value STEAM diffusion imaging. *Neuroimage* **82,** 416–425 (2013).

107. Fu, Y., Wang, H., Shi, R. & Cheng, J.-X. Second Harmonic and Sum Frequency Generation Imaging of Fibrous Astroglial Filaments in Ex Vivo Spinal Tissues. *Biophys. J.* **92,** 3251–3259 (2007).

108. Bilston, L. E. & Thibault, L. E. The mechanical properties of the human cervical spinal cord in vitro. *Ann. Biomed. Eng.* **24,** 67–74 (1996).

109. Oakland, R. J., Hall, R. M., Wilcox, R. K. & Barton, D. C. The biomechanical response of spinal cord tissue to uniaxial loading. *Proc. Inst. Mech. Eng. Part H J. Eng. Med.* **220,** 489–92 (2006).

110. Prevost, T. P. *et al.* Dynamic mechanical response of brain tissue in indentation in vivo, in situ and in vitro. *Acta Biomater.* **7,** 4090–101 (2011).

111. Garo, A., Hrapko, M., van Dommelen, J. A. W. & Peters, G. W. M. Towards a reliable characterisation of the mechanical behaviour of brain tissue: The effects of post-mortem time and sample preparation. *Biorheology* **44,** 51–8 (2007).

112. Fountoulakis, M., Hardmeier, R., Höger, H. & Lubec, G. Postmortem changes in the level of brain proteins. *Exp. Neurol.* **167,** 86–94 (2001).

113. Sparrey, C. J. & Keaveny, T. M. Compression behavior of porcine spinal cord white matter. *J. Biomech.* **44,** 1078–82 (2011).

114. Ozawa, H., Matsumoto, T., Ohashi, T., Sato, M. & Kokubun, S. Comparison of spinal cord gray matter and white matter softness: measurement by pipette aspiration method. *J. Neurosurg.* **95,** 221–4 (2001).

115. Gefen, A. & Margulies, S. S. Are in vivo and in situ brain tissues mechanically similar? *J. Biomech.* **37,** 1339–52 (2004).

116. Prange, M. T. & Margulies, S. S. Regional, directional, and age-dependent properties of the brain undergoing large deformation. *J. Biomech. Eng.* **124,** 244–252 (2002).

117. Tunturi, A. R. Elasticity of the spinal cord, pia, and denticulate ligament in the dog. *J. Neurosurg.* **48,** 975–9 (1978).

118. Ozawa, H., Matsumoto, T., Ohashi, T., Sato, M. & Kokubun, S. Mechanical properties and function of the spinal pia mater. *J. Neurosurg. Spine* **1,** 122–7 (2004).

119. Nam, M.-H. *et al.* Discovery of a novel fibrous tissue in the spinal pia mater by polarized light microscopy. *Connect. Tissue Res.* **55,** 147–55 (2014).

120. Ceylan, D. *et al.* The denticulate ligament: anatomical properties, functional and clinical significance. *Acta Neurochir. (Wien).* **154,** 1229–1234 (2012).

121. Tubbs, R. S., Salter, G., Grabb, P. A. & Oakes, W. J. The denticulate ligament: anatomy and functional significance. *J. Neurosurg. Spine* **94,** 271–5 (2001).

122. Nicholas, D. S. & Weller, R. O. The fine anatomy of the human spinal meninges. A light and scanning electron microscopy study. *J. Neurosurg.* **69,** 276–282 (1988).

123. Jin, X., Mao, H., Yang, K. H. & King, A. I. Constitutive modeling of pia-arachnoid complex. *Ann. Biomed. Eng.* **42,** 812–21 (2014).

124. Jin, X. *et al.* Biomechanical response of the bovine pia-arachnoid complex to tensile loading at varying strain-rates. *Stapp Car Crash J.* **50,** 637–49 (2006).

125. Jin, X., Yang, K. H. & King, A. I. Mechanical properties of bovine pia-arachnoid complex in shear. *J. Biomech.* **44,** 467–474 (2011).

126. Ma, C., Jin, X., Zhang, J. & Huang, S. Development of the pia-arachnoid complex finite element model. *2nd Int. Conf. Bioinforma. Biomed. Eng. iCBBE 2008* 1717–1720 (2008). doi:10.1109/ICBBE.2008.757

127. Jin, X. *et al.* Biomechanical response of the bovine pia-arachnoid complex to normal traction loading at varying strain rates. *Stapp Car Crash J.* **51,** 115–26 (2007).

128. Aimedieu, P. & Grebe, R. Tensile strength of cranial pia mater: preliminary results. *J. Neurosurg.* **100,** 111–4 (2004).

129. Kwon, B. K., Oxland, T. R. & Tetzlaff, W. Animal models used in spinal cord

regeneration research. *Spine (Phila. Pa. 1976).* **27,** 1504–1510 (2002).

130. Carlson, G. D. *et al.* Viscoelastic relaxation and regional blood flow response to spinal cord compression and decompression. *Spine (Phila. Pa. 1976).* **22,** 1285–91 (1997).

131. Tunturi, A. R. Viscoelasticity of dog spinal cord. *Physiol. Chem. Phys.* **12,** 373–8 (1980).

132. Shetye, S. S. *et al.* Nonlinear viscoelastic characterization of the porcine spinal cord. *Acta Biomater.* **10,** 792–7 (2014).

133. Runza, M. *et al.* Lumbar dura mater biomechanics: experimental characterization and scanning electron microscopy observations. *Anesth. Analg.* **88,** 1317–21 (1999).

134. Patin, D. J., Eckstein, E. C., Harum, K. & Pallares, V. S. Anatomic and biomechanical properties of human lumbar dura mater. *Anesth. Analg.* **76,** 535–40 (1993).

135. Persson, C., Evans, S., Marsh, R., Summers, J. L. & Hall, R. M. Poisson's ratio and strain rate dependency of the constitutive behavior of spinal dura mater. *Ann. Biomed. Eng.* **38,** 975–83 (2010).

136. Tunturi, A. R. Elasticity of the spinal cord dura in the dog. *J. Neurosurg.* **47,** 391–6 (1977).

137. Jones, C. F., Kroeker, S. G., Cripton, P. A. & Hall, R. M. The effect of cerebrospinal fluid on the biomechanics of spinal cord: an ex vivo bovine model using bovine and physical surrogate spinal cord. *Spine (Phila. Pa. 1976).* **33,** E580-8 (2008).

138. Hall, R. M., Oakland, R. J., Wilcox, R. K. & Barton, D. C. Spinal cord-fragment interactions following burst fracture: an in vitro model. *J. Neurosurg. Spine* **5,** 243–50 (2006).

139. Ramo, N. L. *et al.* Comparison of in vivo and ex vivo viscoelastic behavior of the spinal cord. *Acta Biomater.* **68,** 78–89 (2018).

140. Wilcox, R. K., Bilston, L. E., Barton, D. C. & Hall, R. M. Mathematical model for the viscoelastic properties of dura mater. *J. Orthop. Sci.* **8,** 432–4 (2003).

141. Lakes, R. S. *Viscoelastic Solids*. (CRC Press LLC, 1999).

142. Fung, Y. C. *Strain Strain History Relations of Soft Tissues in Simple Elongation*. (Prentice-Hall, 1972).

143. Jannesar, S., Nadler, B. & Sparrey, C. J. The Transverse Isotropy of Spinal Cord White Matter Under Dynamic Load. *J. Biomech. Eng.* **138,** 091004 (2016).

144. Cheng, S., Clarke, E. C. & Bilston, L. E. The effects of preconditioning strain on measured tissue properties. *J. Biomech.* **42,** 1360–2 (2009).

145. Troyer, K. L., Estep, D. J. & Puttlitz, C. M. Viscoelastic effects during loading play an

integral role in soft tissue mechanics. *Acta Biomater.* **8,** 234–243 (2012).

146. Troyer, K. L. & Puttlitz, C. M. Nonlinear viscoelasticty plays an essential role in the functional behavior of spinal ligaments. *J. Biomech.* **45,** 684–91 (2012).

147. Troyer, K. L., Puttlitz, C. M. & Shetye, S. S. Experimental Characterization and Finite Element Implementation of Soft Tissue Nonlinear Viscoelasticity. *J. Biomech. Eng.* **134,** 114501 (2012).

148. Ramo, N. L., Puttlitz, C. M. & Troyer, K. L. The development and validation of a numerical integration method for non-linear viscoelastic modeling. *PLoS One* **13,** e0190137 (2018).

149. Pipkin, A. C. & Rogers, T. G. A non-linear integral representation for viscoelastic behaviour. *J. Mech. Phys. Solids* **16,** 59–72 (1968).

150. Smart, J. & Williams, J. G. A comparison of single-integral non-linear viscoelasticity theories. *J. Mech. Phys. Solids* **20,** 313–324 (1972).

151. Lakes, R. S. & Vanderby, R. Interrelation of creep and relaxation: a modeling approach for ligaments. *J. Biomech. Eng.* **121,** 612–5 (1999).

152. Troyer, K. L. & Puttlitz, C. M. Human cervical spine ligaments exhibit fully nonlinear viscoelastic behavior. *Acta Biomater.* **7,** 700–9 (2011).

153. Bain, A. C. & Meaney, D. F. Tissue-level thresholds for axonal damage in an experimental model of central nervous system white matter injury. *J. Biomech. Eng.* **122,** 615–622 (2000).

154. Rivlin, A. S. & Tator, C. H. Effect of duration of acute spinal cord compression in a new acute cord injury model in the rat. *Surg. Neurol.* **10,** 38–43 (1978).

155. Fehlings, M. G. *et al.* Early versus delayed decompression for traumatic cervical spinal cord injury: Results of the surgical timing in acute spinal cord injury study (STASCIS). *PLoS One* **7,** (2012).

156. Fehlings, M. G. & Perrin, R. G. The timing of surgical intervention in the treatment of spinal cord injury: a systematic review of recent clinical evidence. *Spine (Phila. Pa. 1976).* **31,** S28–35; discussion S36 (2006).

157. Dvorak, M. F. *et al.* The Influence of Time from Injury to Surgery on Motor Recovery and Length of Hospital Stay in Acute Traumatic Spinal Cord Injury: An Observational Canadian Cohort Study. *J. Neurotrauma* **10,** 1–10 (2015).

158. Wilson, J. R. *et al.* Early versus late surgery for traumatic spinal cord injury: the results of a prospective Canadian cohort study. *Spinal Cord* **50,** 840–3 (2012).

159. Hrapko, M., van Dommelen, J. A. W., Peters, G. W. M. & Wisman, J. S. H. M. The

Influence of Test Conditions on Characterization of the Mechanical Properties of Brain Tissue. *J. Biomech. Eng.* **130,** 0310031-10 (2008).

160. Rashid, B., Destrade, M. & Gilchrist, M. D. Temperature effects on brain tissue in compression. *J. Mech. Behav. Biomed. Mater.* **14,** 113–118 (2012).

161. McKenzie, J. A. & Williams, J. F. The dynamic behaviour of the head and cervical spine during 'whiplash'. *J. Biomech.* **4,** 477–90 (1971).

162. Panjabi, M. M., Cholewicki, J., Nibu, K., Babat, L. B. & Dvorak, J. Simulation of whiplash trauma using whole cervical spine specimens. *Spine (Phila. Pa. 1976).* **23,** 17–24 (1998).

163. Jin, X. Biomechanical Response and Constitutive Modeling of Bovine Pia-Archnoid Complex. (Wayne State University, 2009).

164. Sakka, L., Gabrillargues, J. & Coll, G. Anatomy of the spinal meninges. *Oper. Neurosurg.* **12,** 168–188 (2016).

165. Adeeb, N. *et al.* The pia mater: A comprehensive review of literature. *Child's Nerv. Syst.* **29,** 1803–1810 (2013).

166. Jones, E. M. C., Silberstein, M. N., White, S. R. & Sottos, N. R. In Situ Measurements of Strains in Composite Battery Electrodes during Electrochemical Cycling. *Exp. Mech.* **54,** 971–985 (2014).

167. Xu, B., Li, H. & Zhang, Y. An Experimental and Modeling Study of the Viscoelastic Behavior of Collagen Gel. *J. Biomech. Eng.* **135,** 054501 (2013).

168. Ramo, N. L., Troyer, K. L. & Puttlitz, C. M. Viscoelasticity of Spinal Cord and Meningeal Tissues. *Acta Biomater.* (2018).

169. Fung, Y. C. *Biomechanics: Mechanical Properties of Living Tissues*. (Springer, 1981).

170. Bertram, C. D. Evaluation by fluid/structure-interaction spinal-cord simulation of the effects of subarachnoid-space stenosis on an adjacent syrinx. *J. Biomech. Eng.* **132,** 061009 (2010).

171. Ogden, R. W. Large deformation isotropic elasticity — on the correlation of theory and experiment for incompressible rubberlike solids. *Proc. R. Soc. A* **326,** 565–584 (1972).

172. Lucas, S. R. *et al.* Viscoelastic and failure properties of spine ligament collagen fascicles. *Biomech. Model. Mechanobiol.* **8,** 487–498 (2009).

APPENDIX A: DAMAGE ACCUMULATION MODELING AND RATE DEPENDENCY OF SPINAL DURA MATER[4]

A.1 Introduction

Based on tangent modulus measurements of uniaxial tensile tests on both human and bovine spinal samples [1–4], the dura mater is up to 100 times stiffer than the spinal cord and pia mater tissues that it encases. Accordingly, the dura mater plays an important stability role in the overall behavior of the spinal-cord-meningeal complex (SCM). Together with the cerebrospinal fluid it contains, the dura mater functions to shield the weaker spinal cord from excessive mechanical loads and reduce cord deformation during traumatic loading scenarios such as vertebral burst fracture events [5–7]. Given its functional importance, multiple research groups have characterized the dura's mechanical properties under various loading conditions, including uniaxial tension at various strain rates [7–9], uniaxial tension in the longitudinal and circumferential directions [4,9,10], and quasi-static biaxial tension [11]. Taken together, these studies have demonstrated that the dura mater exhibits a nonlinear viscoelastic response. However, unlike other viscoelastic soft tissues, it has been reported that the dura's mechanical response is not rate dependent at relatively low strain rates (i.e., 0.01–1/s) [9].

The material models developed from the aforementioned studies have provided properties that can be implemented into computational models of the SCM in order to improve our understanding and simulation of spinal cord injuries (SCI). Specifically, due to the complex

[4] This appendix section has been published as a Research Paper in the Journal of Engineering and Science in Medical Diagnostics and Therapy (DOI: 10.1115/1.4038261). All content has been adapted with permission from the American Society of Mechanical Engineers.

loading that often leads to SCI, finite element (FE) models have traditionally been used as a robust means to determine the internal stresses and strains necessary to link the local mechanical environment to resulting tissue damage and/or long-term injury severity. These relationships between internal mechanical parameters and resultant damage are critical to the study, treatment, and prevention of SCI. Numerous research groups have developed FE models of the SCM for investigating the mechanical underpinnings of contusion (during vertebral burst fracture events), distraction, and dislocation events that lead to SCI [7,12–16]. Despite the known functional importance of the dura mater in protecting the spinal cord, most material models found in these FE models use simplifying assumptions of isotropic or anisotropic elasticity [7,14,15]. While such FE models have provided valuable insight into spinal mechanics and internal stress/strain patterns, many researchers in this area have concluded that additional characterization of the components of the SCM is necessary to accurately model the etiology of SCI [14–16], including mechanisms to simulate dynamic tissue damage [16]. Therefore, a thorough description of the material behavior of spinal dura mater, including damage characterization during the sub-failure and failure regimes, is necessary to comprehensively investigate SCI.

One method for incorporating post yield softening behavior of soft tissues into FE models is to implement continuum viscoelastic damage formulae [17–20]. Specifically, a variety of models have been used to describe the failure of vasculature [21–23]; tendon and ligament [24,25]; vaginal [26]; and rectus sheath [27] tissues. However, this technique has not yet been extended to describe the failure behavior of any tissue of the SCM. Therefore, the aim of this study is to characterize the damage accumulation behavior of the spinal dura mater under uniaxial loading. Additionally, while it has been reported that the hyperelastic parameters fitted to dura tension-to-

failure tests are not strain-rate dependent [9], it is unknown whether the parameters used to describe damage accumulation are rate dependent. Therefore, a secondary objective of this study is to compare the damage accumulation process at three different strain rates.

A.2 Materials and Methods

A.2.1 Specimen preparation

Four ovine cervical spines (C2–C7) were collected from animals euthanized at Colorado State University's Surgical Research Laboratory for unrelated studies. Until mechanical testing was performed, spines were wrapped in saline-soaked gauze and stored at -20°C. A single freeze-thaw cycle preservation technique has been shown to not significantly affect the mechanical properties of the dura mater [4,9] and other fibrous soft tissues [28–31]. On the day of testing, the spine was thawed at room temperature and the SCM was carefully removed via gross dissection, transection of the pedicles, and resection of the nerve roots. A longitudinal cranial-to caudal incision was performed on the dura mater and the denticulate ligaments were severed to release the dura from the underlying meninges and cord.

As controversy still exists over the ultrastructural and mechanical differences between longitudinal and circumferential samples of spinal dura [4,7–9], a simple uniaxial tension-to-failure test in the dura's longitudinal direction (i.e., aligned with the long-axis of the SCM) was chosen as the procedure for modeling the damage accumulation in spinal dura. Longitudinal strips measuring 35 mm by 5 mm were cut from the sheet of dura mater, avoiding areas where exiting nerve roots would produce localized effects. This procedure yielded approximately 15 test specimens per spine that were subsequently randomized to one of the three strain rate

groups. In order to keep the tissue adequately hydrated, samples waiting to be tested were placed in a saline bath at room temperature.

A.2.2 Mechanical testing

Uniaxial testing was performed using a custom-built test stand consisting of a 44.5-Newton load cell (model 31, Sensotec, Honeywell, Columbus, OH), a linear actuator with a 0.16 µm resolution (T-LLS105, Zaber Technologies, Vancouver, BC, Canada), two thin film grips (FC-20, IMADA, Northbrook, IL), and a 4.2-megapixel camera (Grasshopper3, Point Grey, Richmond, BC, Canada) positioned directly above the grips (Fig. A1(a)). To prevent slippage at the grip interface, 7.5mm squares of water proof 180 grit sandpaper were attached with a small amount of cyanoacrylate to either end of each dural sample before it was placed in the grips. The sample was then loaded to a 0.5 N preload and digital images were acquired with the grips at 0° (the test orientation) and turned 90° (as shown in Fig. A1(b)). ImageJ (NIH, Bethesda, MD) was used to obtain five thickness measurements from the 90° image (Fig. A1(b)), five width measurements from the 0° image, and one length measurement (also from the 0° image). These measurements were used to determine the mean sample cross-sectional area and original length for *post-hoc* stress and strain rate calculations, respectively. Using displacement control of the linear actuator, each sample was tensioned to failure at 0.01 mm/s, 1 mm/s, or 6 mm/s (representing strain rates of $0.0005 \pm 7.27 \times 10^{-5}$/s, 0.051 ± 0.008/s, and 0.284 ± 0.044/s, respectively). Figures A1(c)–A1(e) show a sample at the preload, just prior to mid-substance failure and just after failure.

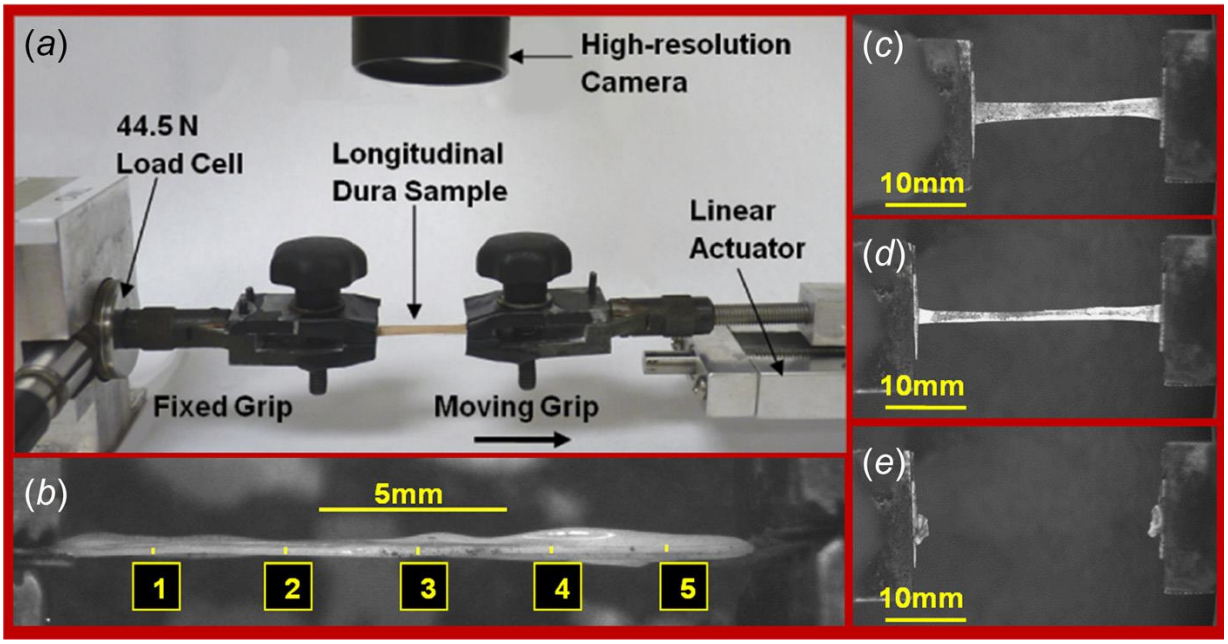

Figure A1: (a) Uniaxial testing apparatus with labeled components; (b) five thickness measurements were made via analysis of images taken with grips turned at a 90° orientation from the testing configuration. A representative tension-to-failure test showing the sample at (c) 0.5 N preload, (d) prior to mid-substance failure, and (e) immediately following mid-substance failure.

In order to follow the damage testing procedure outlined by Martins et al., the dural samples were not preconditioned prior to the pull-to-failure test [27]. Reaction forces were recorded at 1000 Hz for the 1 mm/s and 6 mm/s speeds and at 100 Hz for the quasi-static speed (0.01 mm/s). Images were collected at 45 Hz for all tests (to monitor for grip slip and verify site of failure). Saline irrigation (1 drop per minute) was used to keep samples hydrated during the 0.01 mm/s test; the short duration of the 6 mm/s and 1 mm/s tests (<2 min) precluded the need for intra-test hydration.

Only samples that failed mid-substance with no evidence of slippage were retained for analysis. The final sample sizes for the quasi-static, 1 mm/s, and 6 mm/s loading-rate groups were 14, 21, and 10, respectively. As global stretch measurements are needed for the modeling of failure

behavior, actuator displacement was converted to global stretch using, $\lambda = (L_o + \Delta L)/L_o$ where L_o is the preload length and ΔL is the recorded actuator displacement. Cauchy stress was obtained using $\sigma = \lambda * \left({}^{F}/_{A_0}\right)$, where F is the force (in Newtons) and A_0 is the cross-sectional area (in mm^2). Statistical analysis of dimensional measurements revealed no significant differences between groups, with an overall average initial length of 20.81 ± 3.17 mm, width of 4.29 ± 0.90 mm, and thickness of 0.18 ± 0.04 mm.

A2.2.3 Constitutive modeling

The nonlinear directional damage model for fibrous biological soft tissues first proposed by Calvo et al. [19] and further developed in 2008 [32] and 2012 [27] was used to fit the data in this study. This is an uncoupled directional damage model which defines different damage characteristics for the collagen fibers and the ground substance material (matrix). Assuming that the damage process only affects the isochoric elastic part of the deformation [17], the free-energy density (Ψ) of the continuum damage model can be expressed as follows:

$$\boldsymbol{\psi}\left(\boldsymbol{C}, \boldsymbol{M}, D_m, D_f\right) = \boldsymbol{\psi}_{vol}(J) + (1 - D_m)\overline{\boldsymbol{\psi}}_0^m\left(\overline{\boldsymbol{C}}\right) + (1 - D_f)\overline{\boldsymbol{\psi}}_0^f(\overline{\boldsymbol{C}}, \boldsymbol{M}) \qquad (A11)$$

where $\boldsymbol{M}$ is defined as the tensor product of the fiber direction vector in the undeformed configuration, $\overline{\boldsymbol{C}}$ is the modified right Cauchy–Green tensor (defined by $\overline{\boldsymbol{C}} = \overline{\boldsymbol{F}}^{\boldsymbol{T}}\overline{\boldsymbol{F}}$, where $\overline{\boldsymbol{F}}$ is the product of the deformation gradient tensor, $\boldsymbol{F}$, and the cube root of its determinant, $J^{-\frac{1}{3}}$), and $\overline{\boldsymbol{\psi}}_0^m$ and $\overline{\boldsymbol{\psi}}_0^f$ denote the elastic response of the undamaged matrix and collagen fibers, respectively [18,27]. The terms $(1 - D_m)$ and $(1 - D_f)$ represent the reduction factors for damage as a function of the deformation (stretch) [17]; the damage parameters, D_m and D_f, are normalized [0,1] values related to how the matrix and fibers, respectively, accumulate damage. As proposed

by Simo [17], the evolution of damage parameters are given by a series of piecewise and irreversible functions $D_k(\Xi_t^k)$, with k representing either the matrix (m) or the fibers (f). The interior functions, Ξ_t^k, are defined as time (s) functions.

$$\Xi_s^k = \sqrt{2\bar{\boldsymbol{\psi}}_0^k[\bar{\boldsymbol{C}}(s)]} \tag{A12}$$

The maximum values of Ξ_s^k over the past time history $s \in (-\infty, t)$ are defined as Ξ_t^k.

$$\Xi_t^k = \max_{s\in(-\infty,t)} \sqrt{2\bar{\boldsymbol{\psi}}_0^k[\bar{\boldsymbol{C}}(s)]} \tag{A13}$$

The criterion for damage to occur is given by the following expression [17]:

$$\Phi^k\left(\boldsymbol{C}(t), \Xi_t^k\right) = \sqrt{2\bar{\boldsymbol{\psi}}_0^k[\bar{\boldsymbol{C}}(t)]} - \Xi_t^k \leq 0 \tag{A14}$$

meaning, at any time (t) of the loading procedure, that if the above equality is fulfilled for the matrix or fibers, then damage increases in that component of the tissue. The function describing the evolution of damage $[D_k(\Xi_t^k)]$ is given by

$$D_k\left(\Xi_t^k\right) = \begin{cases} 0, & if\ \ \Xi_t^k < \Xi_{min}^{0_k} \\ \xi^2[1-\beta_k(\xi^2-1)], & if\ \Xi_{min}^{0_k} \leq \Xi_t^k \leq \Xi_{max}^{0_k} \\ 1, & if\ \Xi_t^k > \Xi_{max}^{0_k} \end{cases} \tag{A15}$$

where $\xi = \frac{\Xi_t^k - \Xi_{min}^{0_k}}{\Xi_{max}^{0_k} - \Xi_{min}^{0_k}}$ and is a dimensionless variable, and $\Xi_{min}^{0_k}$ and $\Xi_{max}^{0_k}$ are variables associated with the strain energy at which initial and total damage, respectively, occur during the loading procedure [17,32]. Therefore, the elastic response of the tissue is given by the behavior up to $\Xi_{min}^{0_k}$, while the damage accumulation properties are characterized by the behavior after the $\Xi_{min}^{0_k}$ threshold is passed. Given the irreversible nature of the damage, a constraint is imposed that the damage evolution function $D_k\left(\Xi_t^k\right)$ must be monotonically increasing with Ξ_t^k, $\beta_k \in$

$[-1.0, 1.0]$ [26,32]. The β_k terms are affected by the other fitting parameters and the size of the damage region of the curves [27].

A.2.3 Fitting procedure

The spinal dura was assumed to be incompressible (i.e., $I_3 = J^2 = 1$), which simplifies the free-energy density function given in Eq. (A1) [27].

$$\boldsymbol{\psi} = (1 - D_m)\widehat{\boldsymbol{\psi}}_0^m(\boldsymbol{C}) + (1 - D_f)\widehat{\boldsymbol{\psi}}_0^f(\boldsymbol{C}, \boldsymbol{M}) \tag{A16}$$

For the case of uniaxial tension in the $\mathbf{x}_3$-direction, $\lambda_3 = \lambda$, $\lambda_1 = \lambda_2 = \lambda^{-\frac{1}{2}}$ and $I_4 = \lambda^2$. Therefore, the Cauchy stress tensor is diagonal with $\sigma_{33} = \sigma$ and $\sigma_{11} = \sigma_{22} = 0$. The total strain energy ($\boldsymbol{\psi}$) is the superposition of the strain energies of the isotropic matrix ($\widehat{\boldsymbol{\psi}}_{iso}^m$) and the anisotropic collagen fibers ($\widehat{\boldsymbol{\psi}}_{ani}^f$).

$$\boldsymbol{\psi} = \widehat{\boldsymbol{\psi}}_{iso}^m + \widehat{\boldsymbol{\psi}}_{ani}^f \tag{A17}$$

The isotropic response of the dural matrix was modeled with the exponential strain energy function proposed by Demiray et al. [33], while the anisotropic response of the dural collagen fibers was modeled with the piecewise function proposed by Calvo et al. [26].

$$\widehat{\boldsymbol{\psi}}_{iso}^m = \frac{c_1}{c_2}\{\exp[\frac{c_2}{2}(I_1 - 3)] - 1\} \tag{A18}$$

$$\widehat{\boldsymbol{\psi}}_{ani}^f = \begin{cases} 0, & if\ I_4 < I_{4_0} \\ \frac{c_3}{c_4}\{\exp\left[c_4\left(I_4 - I_{4_0}\right)\right] - c_4\left(I_4 - I_{4_0}\right) - 1\}, & if\ I_{4_0} < I_4 < I_{4_{ref}} \\ c_5\sqrt{I_4 - I_{4_0}} + c_6 \ln\left(I_4 - I_{4_0}\right) + c_7, & if\ I_4 > I_{4_{ref}} \end{cases} \tag{A19}$$

In this formulation, it is assumed that the anisotropic fiber term only contributes to the total strain energy when the fibers are stretched ($I_4 > I_{4_0}$). The terms I_{4_0} and $I_{4_{ref}}$ characterize the location and length of the toe region of the response. In the previous equations, $c_1,\ c_3 > 0$

represent parameters that are analogous to the stiffnesses of the matrix and fibers, respectively, while $c_2,\ c_4 > 0$ are dimensionless parameters that characterize the matrix and fiber nonlinearity, respectively. It should be noted that $c_5,\ c_6,\ c_7$ are not independent as they ensure continuity of the strain field, the stress field, and the derivative of stress [26,27].

Fitting of the experimental data was performed with the fmincon function in MATLAB (version R2012b, The MathWorks, Natick, MA) via constrained nonlinear optimization of c_1, c_2, c_3, c_4, I_{4_0}, $I_{4_{ref}}$, Ξ^m_{min}, Ξ^m_{max}, Ξ^f_{min}, Ξ^f_{max}, β_m, and β_f. In order to facilitate adequate fitting of the failure phase of the curves, which occurred much more rapidly than the ramp phase, the data were resampled to create a balance between the ramp and failure phases. Quality of the fits was assessed by root-mean-square error (RMSE) between the experimental Cauchy stress and stress given by the fitted damage model strain energy function. The results presented are the parameters that resulted in the lowest RMSE for each test.

Large standard deviations were noted for some of the fitted parameters. Accordingly, an outlier analysis was performed on each parameter group according to the method described by Moore and McCabe [34]. Specifically, any datum point more than 1.5 times the interquartile range above the third quartile value or below the first quartile value was identified as an outlier. Tests containing any parameter identified as an outlier were excluded, resulting in final sample sizes of 9, 14, and 7 for the quasi-static, 1 mm/s, and 6 mm/s speed groups, respectively. These reduced data were used to determine statistical differences.

SigmaPlot software (version 13.0, Systat Software, San Jose, CA) was used for all statistical analyses. To determine statistical differences between strain rate groups, Shapiro-Wilk and Brown-Foresythe tests were performed to test for normality and equal variance, respectively. Data that passed both tests were analyzed with a one-way ANOVA and *post-hoc* Student-Newman-Keuls tests. Data that failed either the normality or equal variance test were analyzed with a Kruskal-Wallis one-way ANOVA on ranks and *post-hoc* Dunn's tests. To determine statistical differences between related parameters within a strain rate group (e.g., comparing the stiffness of the matrix, c_1, to that of the fibers, c_3), Shapiro-Wilk tests were performed for normality, followed by paired t-tests. A p-value of 0.05 was selected to define statistical significance.

A.3 Results

All stretch-stress curves demonstrated strong nonlinearity, which is characteristic of hydrated collagen fiber-reinforced soft tissues. The majority of test data displayed a smooth increase in stress up to a maximum value, followed by a rapid decrease to zero. A small subset displayed minor decreases in stress during the ramp phase and/or plateaus in stress during the failure phase (Fig. A2). No significant differences were found between the three strain rate groups with respect to the maximum failure stress ($p = 0.313$) or the stretch at the maximum stress ($p = 0.598$). The data from the two highest speed groups fit the continuum damage model well (Fig. A2), with maximum RMSE values of 0.27 MPa (<1.5% of average maximum stress) and 0.47 MPa (<3% of average maximum stress) for the 6 mm/s and 1 mm/s loading-rate groups, respectively. The RMSE values for the quasi-static strain-rate fits were slightly higher, with a range of RMSE

values from 0.36 to 1.48 MPa. The average RMSE of 0.95 MPa represents approximately 6% of the quasi-static strain-rate group's average maximum stress.

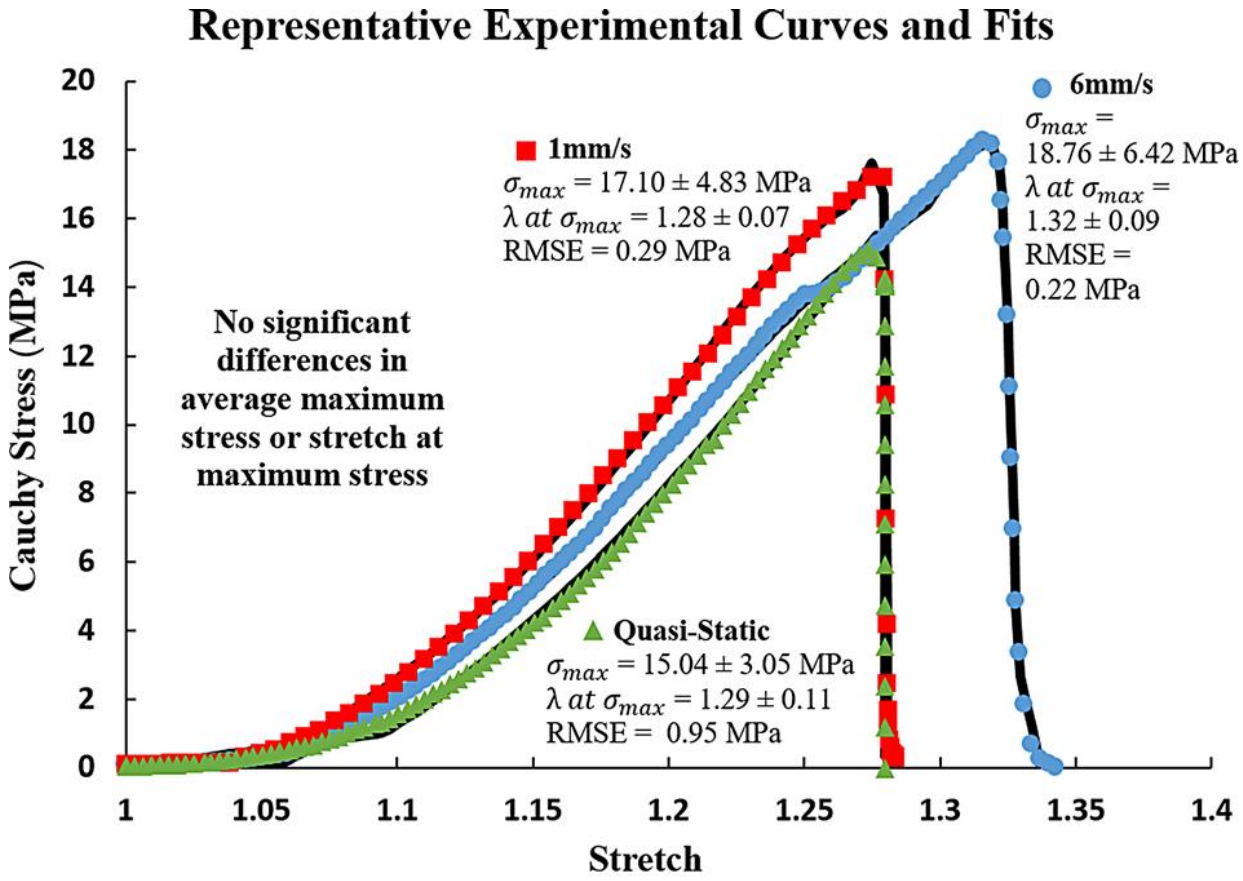

Figure A2: Representative experimental stretch-stress curves (colored symbols) from each strain-rate group demonstrate the elastic nonlinearity which is characteristic of hydrated fibrous soft tissues. The group averages for maximum failure stress, stretch at maximum stress, and the model fit (black curve) RMSE are also given.

The average fitted parameters for the reduced data set (that excluding identified outliers) are shown in Table A1. Statistically significant differences were found between the strain-rate groups for c_3 (stiffness of the fibers), c_4 (nonlinearity of the fibers), Ξ_{min}^{m} (associated with the strain energy at the initiation of matrix damage), Ξ_{max}^{f} (associated with the strain energy at complete fiber damage), and β_f (related to size of the damage region of the fibers). Statistically

significant differences within strain-rate groups were also found between the following parameter pairs: c_1 and c_3 (stiffness of the matrix and fibers, respectively); c_2 and c_4 (nonlinearity of matrix and fibers, respectively); Ξ^m_{min} and Ξ^f_{min} (associated with the strain energy at the initiation of damage in the matrix and fibers, respectively); and Ξ^m_{max} and Ξ^f_{max} (associated with the strain energy at complete matrix damage and fiber damage, respectively).

Table A1: Fitted parameters (average ± std. deviation). Significant differences ($p < 0.05$) between strain-rate groups are denoted with superscripted lower-case letters {**a**: $p < 0.001$; **b**: $p = 0.003$; **c**: $p < 0.001$; **d**: $p = 0.002$; **e**: $p = 0.003$; **f**: $p = 0.006$; **g**: $p = 0.007$; **h**: $p = 0.020$; **i**: $p = 0.008$}. Significant differences ($p < 0.05$) between related parameters within the same strain-rate group are denoted with capital letters {**A**: $p = 0.001$; **B**: $p < 0.001$; **C**: $p = 0.005$; **D**: $p < 0.001$; **E**: $p < 0.001$; **F**: $p = 0.018$; **G**: $p = 0.003$; **H**: $p = 0.019$}.

	Quasi-Static (0.0005 ε/sec)	1mm/s (0.051 ε/sec)	6mm/s (0.284 ε/sec)	P-value of ANOVA
c_1 (MPa)	4.25 ± 2.90	3.95 ± 1.89	**2.69 ± 2.44** [F]	p = 0.301
c_2 (-)	**9.82 ± 5.63** [A]	**15.87 ± 9.05** [D]	**15.46 ± 8.23** [G]	p = 0.196
c_3 (MPa)	**3.10 ± 1.18** [a]	**5.05 ± 2.78** [b]	**29.56 ± 21.86** [a, b, F]	**p < 0.001** *
c_4 (-)	**1.70 ± 0.58** [c, A]	**1.54 ± 0.67** [d, D]	**0.37 ± 0.28** [c, d, G]	**p < 0.001** *
I_{4_0} (-)	1.16 ± 0.10	1.14 ± 0.06	1.17 ± 0.08	p = 0.644
$I_{4_{ref}}$ (-)	1.60 ± 0.29	1.58 ± 0.21	1.63 ± 0.30	p = 0.911
Ξ^m_{min} (MPa$^{1/2}$)	**0.62 ± 0.23** [e, B]	**0.77 ± 0.37** [f]	**1.20 ± 0.25** [e, f]	**p = 0.003** *
Ξ^m_{max} (MPa$^{1/2}$)	**1.10 ± 0.30** [C]	**1.25 ± 0.18** [E]	**1.28 ± 0.23** [H]	p = 0.245
Ξ^f_{min} (MPa$^{1/2}$)	**1.32 ± 0.26** [B]	1.11 ± 0.55	0.72 ± 0.51	p = 0.051
Ξ^f_{max} (MPa$^{1/2}$)	**1.33 ± 0.25** [g, C]	**1.49 ± 0.24** [h, E]	**1.83 ± 0.44** [g, h, H]	**p = 0.008** *
β_m (-)	-0.11 ± 0.47	0.24 ± 0.44	0.27 ± 0.71	p = 0.257
β_f (-)	**-0.40 ± 0.41** [i]	**0.32 ± 0.54** [i]	**-0.10 ± 0.59**	**p = 0.009** *

The average c_3 value of the 6 mm/s loading-rate group was significantly greater than that of quasi-static ($p < 0.001$) and the 1 mm/s ($p = 0.003$) groups, whereas the difference in c_3 between the 1 mm/s and the quasi-static groups was not statistically significant ($p = 0.898$). The c_4 parameter exhibited the opposite pattern; the average c_4 value of the 6 mm/s loading-rate group was significantly less than both the quasi-static ($p < 0.001$) and the 1 mm/s ($p = 0.002$) groups, while the difference between the 1 mm/s and quasi-static groups was not statistically significant ($p = 0.99$). When comparing the stiffness parameters c_1 and c_3 for within strain-rate groups, c_3 was significantly greater than c_1 for the 6 mm/s loading rate ($p = 0.018$). When comparing the nonlinearity parameters c_2 and c_4 within strain-rate groups, c_4 was significantly less than c_2 at all speeds ($p = 0.001$, $p < 0.001$, $p = 0.003$ for the quasi-static group, 1 mm/s loading-rate group, and 6 mm/s loading-rate group, respectively).

The value of Ξ_{min}^{m} (associated with the strain energy at the initiation of damage to the matrix) showed significant differences between the strain rate groups; the 6 mm/s loading-rate Ξ_{min}^{m} was significantly greater than that of both the quasi-static ($p = 0.003$) and 1 mm/s loading-rate ($p = 0.006$) groups. As with other parameters, the difference between the Ξ_{min}^{m} for the quasi-static and 1 mm/s loading-rate groups was not statically significant ($p = 0.278$). The value of Ξ_{max}^{f} (associated with the strain energy at complete fiber damage) followed the same pattern with respect to strain rate; the value for the 6 mm/s loading-rate group was significantly greater than that of both the quasi-static group ($p = 0.007$) and the 1 mm/s group ($p = 0.020$), but the difference between the quasi-static and 1 mm/s groups was not significant ($p = 0.214$). The minimum and maximum Ξ terms within a strain-rate group also showed significant differences. Ξ_{min}^{f} was significantly greater than Ξ_{min}^{m} at the quasi-static rate ($p < 0.001$), while Ξ_{max}^{f} was

significantly greater than Ξ_{max}^{m} at all three rates ($p = 0.005$, $p < 0.001$, $p = 0.019$ for the quasi-static, 1 mm/s loading-rate, and 6 mm/s loading-rate groups, respectively).

The β_f parameter, which describes the size of the damage region for the fibers, was significantly greater for the 1 mm/s loading-rate group than the quasi-static group ($p = 0.008$), but no other significant differences were found for this or the β_m parameter. No significant differences in the I_{4_0} and $I_{4_{ref}}$ parameters, which relate to the nonlinear toe region of the response curve, were found between strain rate groups ($p = 0.644$ for I_{4_0} and $p = 0.911$ for $I_{4_{ref}}$). No other significant differences were found between strain rates groups or related parameters within strain rate groups.

A.4 Discussion

Despite multiple studies in the literature on the tension-to-failure properties of spinal dura mater from both cadaveric and animal sources [4,8–10,35,36], this is the first study to apply a damage constitutive model to the dura and relate the model's parameters to strain-rate effects. These data and damage formulation can be implemented into finite element computational models of the SCM to improve the accuracy of simulations of spinal cord injury scenarios and dynamics.

As the continuum damage model used in this investigation is phenomenological in nature, the results obtained by application of the model (i.e., the damage parameters) are not easily interpreted. However, given the form used to model the anisotropic response of the fibers, $\widehat{\boldsymbol{\psi}}_{ani}^{f}$ (Eq. (A9)), the c_3 term relates to fiber stiffness, while the c_4 term relates to the nonlinearity of the elastic fiber response. The significant differences found between strain-rate groups for c_3 and

c_4, therefore, follow the expectant strain-rate dependent behavior of viscoelastic materials wherein a stiffer and more linearized response is characteristically obtained at higher strain rates [9,37–41]. Persson et al. fit uniaxial tensile tests of bovine dura matter at three strain rates to an Ogden model and reported an increase in G (i.e., stiffness) and a decrease in α (i.e., nonlinearity) with increasing strain rate for longitudinal samples, but the differences failed to reach statistical significance [9]. Our data extended these results by explicitly finding that parameters associated with fiber stiffness and nonlinearity were significantly affected by strain rate.

The lack of significant strain-rate dependence with respect to the stiffness (c_1) and nonlinearity (c_2) of the isotropic matrix, $\widehat{\boldsymbol{\psi}}_{iso}^{m}$ (Eq. (A8)), suggest that the matrix material is less rate-sensitive than the fibers, and that the differences seen in global properties are mainly due to the viscoelastic fiber response. The differences between c_1 (matrix stiffness) and c_3 (fiber stiffness) also support the conclusion that the fibers are primarily responsible for globally observed strain-rate dependency. At 6 mm/s, the stiffness of the fibers was, as expected, significantly higher than that of the matrix. However, at 1 mm/s, this difference was not significant and at the quasi-static loading-rate the stiffness of the fibers approximated that of the matrix. This pattern suggests that at very slow strain rates the matrix and fiber stiffness is nearly equivalent, but any increase in strain rate creates a non-proportionally greater increase in stiffness in the fibers. The significant difference between c_2 (matrix nonlinearity) and c_4 (fiber nonlinearity) was also as expected for a fiber-reinforced composite; while collagen fiber straightening (i.e., uncrimping) does contribute to composite nonlinearity, the majority of composite nonlinearity can usually be attributed to intrinsic properties of the matrix [42–45].

As the other eight fitted parameters are not directly relatable to the tissue's physical properties, it is slightly more difficult to draw conclusions about their significance. The two parameters related to the elastic response of the tissue not discussed earlier, I_{4_0} and $I_{4_{ref}}$, were not significantly different between strain-rate groups. These parameters are associated with the stretch values that define the beginning and end of the curve's toe region. The lack of significance between strain-rate groups show that, despite differences in behavior within the toe region (c_3 and c_4), the location and length of the toe region seems to be unaffected by strain rate. The values obtained for both parameters were similar to those reported in studies applying the same damage model to other soft tissues (rectus sheath: $I_{4_0} = 1.00 - 1.44$ [27]; vaginal tissue: $I_{4_0} = 1.05 - 1.31$, $I_{4_{ref}} = 1.46 - 2.10$ [26]). However, the toe region identified by I_{4_0} and $I_{4_{ref}}$ in the current study comprised a larger portion of the total stretch-stress curve than those found in the aforementioned studies. It is expected that the characteristics of the global toe region would depend not only on the nonlinearity of the matrix and fibers, but also on the distribution, density, and alignment of the fibers. Differences in these tissue-specific properties could account for the differences seen between studies.

The parameters related to the damage response of the tissue (namely, Ξ^m_{min}, Ξ^m_{max}, Ξ^f_{min}, Ξ^f_{max}, β_m, and β_f) also showed significant differences between strain-rate groups and between related parameters within the same strain-rate group. Although the change in Ξ^m_{min} from the quasi-static to the 1 mm/s loading rate was not significant, the increase in Ξ^m_{min} across all three strain rates suggests that the initiation of damage to the matrix may be delayed at higher strain rates. Ξ^f_{min} (related to the initiation of damage to the fibers) showed the opposite trend with respect to strain rate, although none of the differences reached significance; the decrease in Ξ^f_{min} with increasing

strain rate suggests that the fibers incur damage earlier in the loading process at higher strain rates. If a linear relationship between strain rate and the Ξ_{min} terms is assumed (Fig. A3), it is not surprising that the only significant difference between Ξ_{min}^{m} and Ξ_{min}^{f} was observed at the quasi-static loading rate. Interestingly, the slopes of the proposed linear relationships are equal in magnitude (to within two decimal places). According to these data, at relatively low strain rates the matrix incurs damage before the fibers, but at strain rates above 15%/s damage is initiated in the fibers before the matrix.

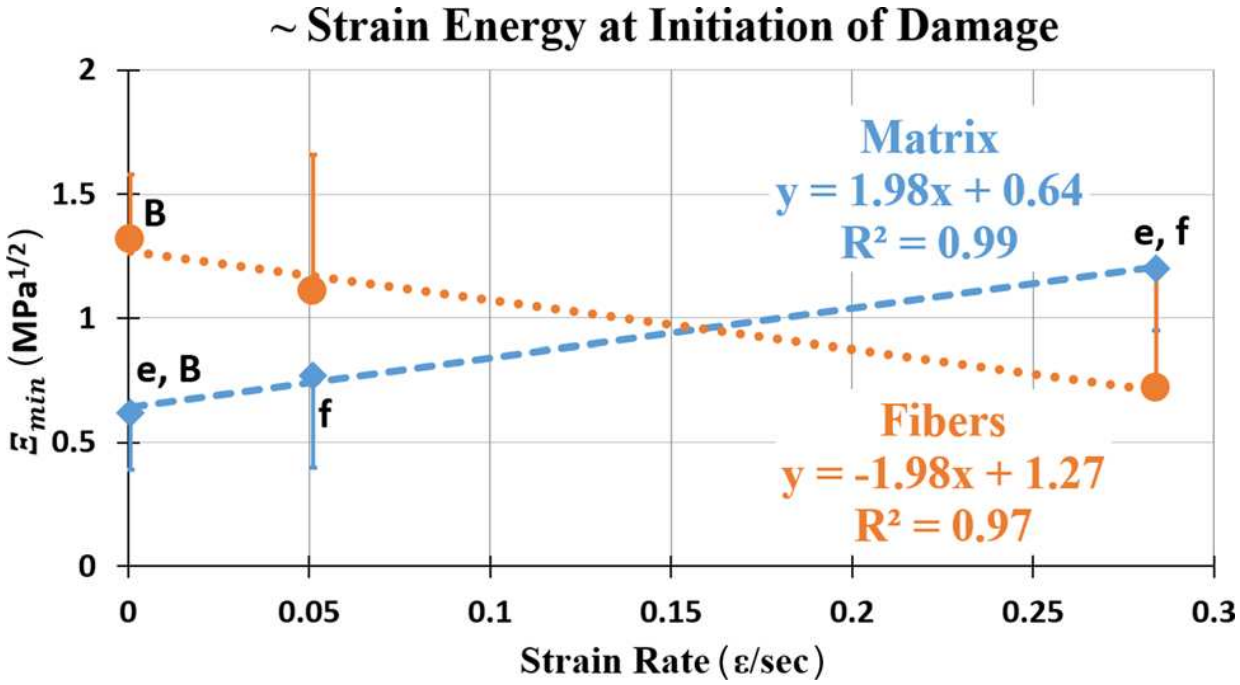

Figure A3: Ξ_{mi}, which is related to the strain energy at which initial damage occurs, appears to follow a linear pattern with respect to strain rate in both the matrix and fibers (R^2 values of 0.99 and 0.97, respectively). While Ξ_{min}^{m} increases with increasing strain rate, Ξ_{min}^{f} decreases at almost the exact same rate. Letters indicate significant differences.

Examining the terms related to complete damage, both Ξ_{max}^{m} and Ξ_{max}^{f} increased with increasing strain rate, but the only differences that reached significance were between the Ξ_{max}^{f} of the 6

mm/s loading-rate group and that of the other two groups. In comparing the fiber and matrix terms, Ξ_{max}^{f} was significantly greater than Ξ_{max}^{m} at all three strain rates; this suggests that the matrix fails before the fibers such that the stress just prior to tissue failure is fully supported by the fibrous component. This pattern was also reported in damage model fits for rectus sheath [27] and vaginal tissue [26]. Figure A4 shows these results in graphical form by plotting the damage parameters D_m and D_f (defined in Eq. (A5) as functions of Ξ_{min}^{m}, Ξ_{max}^{m}, β_m and Ξ_{min}^{f}, Ξ_{max}^{f}, β_f, respectively) at all three strain rates. The initiation of damage relates to the deviation of the damage parameter from zero, while complete damage relates to the maximum value of the damage parameter (typically one). For a minority of the tests, especially those at the quasi-static strain rate, the load did not return completely to zero following mid-substance failure; for these cases, the damage parameter did not reach one and complete damage was taken as the maximum value obtained. In line with the strain-rate-dependent differences found for Ξ_{min}^{m}, the initiation of damage to the matrix occurs at higher stretch levels for the 6 mm/s loading-rate compared to the quasi-static and 1 mm/s loading rates. Also, in line with the strain-rate-dependent differences found for Ξ_{max}^{f}, complete fiber damage occurs at higher stretch levels for the 6 mm/s loading rate compared to the quasi-static and 1 mm/s loading rate.

Examining the difference between the initiation of damage and failure (Ξ_{min} versus Ξ_{max}) also provides insight into the failure process of each component. While there is a relatively large gap in Ξ_{min}^{m} and Ξ_{max}^{m} at the two lower strain rates, this gap is greatly reduced at the 6 mm/s loading rate (from an average of 0.48 MPa^{-1} to 0.08 MPa^{-1}). This can also be seen in Fig. A4. The majority of matrix damage parameter curves at the quasi-static and 1 mm/s loading rate display an exponential shape, while all curves at the 6 mm/s loading rate display very steep slopes. This

suggests that when increasing the loading rate from 1 mm/s to 6 mm/s, the matrix transitions from accumulating damage gradually to experiencing sudden failure with rapid damage accumulation. As for the gap between Ξ_{min}^{f} and Ξ_{max}^{f}, it appears to increase almost linearly as a function of strain rate from 0.01 MPa^{-1} at the quasi-static rate to 1.11 MPa^{-1} at the 6 mm/s (or 0.284/s) rate. In Fig. A4, this is shown as a gradual shift from very steep slopes to a more gradual accumulation of damage. All of the quasi-static D_f curves are nearly vertical lines (representing a brittle-like behavior), whereas almost all of the D_f curves for the 6 mm/s loading-rate group show an exponential shape. This suggests that at higher strain rates the fibers display a more ductile behavior, taking on more energy before failing.

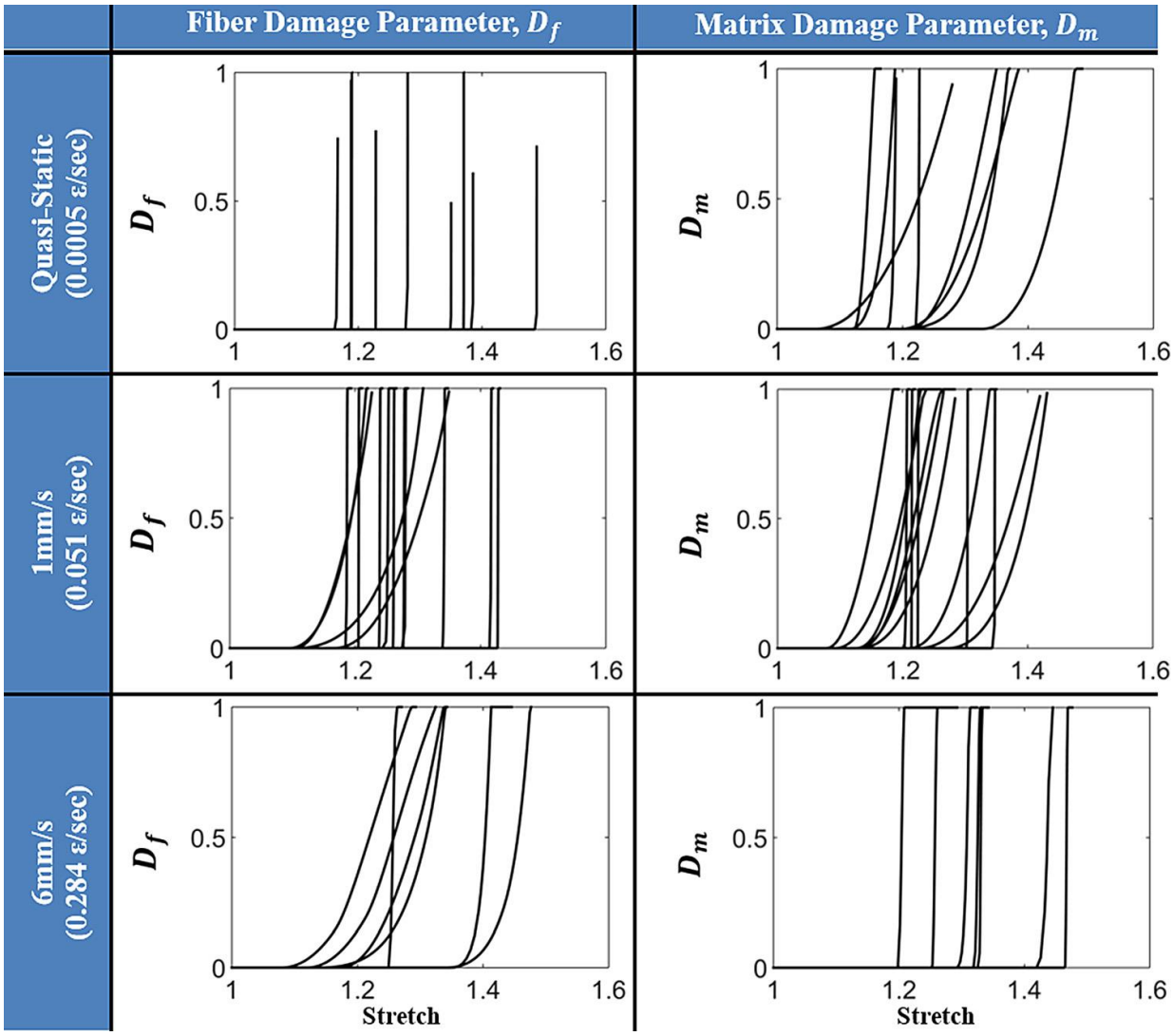

Figure A4: Plots of D_f and D_m [0,1] versus stretch. Damage initiates when the damage parameter deviates from zero and is considered complete when the damage parameter is equal to unity. In a subset of the quasi-static tests, the force did not completely return to zero following mid-substance failure; therefore, for these samples, the damage parameter does not extend all the way to one. Most of the D_m curves approach unity before the D_f curves, indicating that the matrix completely fails prior to fiber failure regardless of strain rate. Variations in damage behavior can be seen as the change in slope between components at the same strain rate or between the same components at different strain rates.

With significant strain-rate effects between the damage behavior of both components at 6 mm/s compared to the other two speeds, these findings may represent a protective mechanism of the dura mater. During normal voluntary neck motion, the spinal tissues are exposed to strain rates

between 0.04 and 0.24/s [1]. The strain rates in this study (0.0005, 0.051, and 0.284/s) were chosen to represent the quasi-static rate, a rate typically experienced during voluntary motion, and a rate slightly above the typical range. At the 0.284/s rate, the initiation of damage to the matrix and the complete damage of the fibers were significantly delayed (occurring later in the loading cycle). This suggests that the tissue is able to support a higher strain energy without failing at higher loading rates. Therefore, in determining if tissue damage has occurred, the rate of loading (not only the maximum load or displacement reached) is significant. This distinction is important for any study of SCM injuries and suggests that computational models that use only static loading and/or static tissue damage properties are not capable of fully capturing the underlying tissue injury mechanisms.

There are limitations to the above work that should be noted. For this initial study, only the longitudinal loading direction was analyzed as it has greater implications for the injury mechanism of interest, i.e., whiplash (or neck hyperflexion). In order to accurately model damage accumulation from circumferential loading, such as from excessive cerebrospinal fluid pressure, the aforementioned study should be repeated using the orthogonal loading direction. Similarly, based on structural and mechanical differences between spinal and cranial dura mater [8], it is unclear if the models developed above would be appropriate for use in cerebral investigations (e.g., models of traumatic brain injury or subdural hematoma). The strain rates utilized, while slightly above those seen in the tissue during normal voluntary motion, are still well below those reported for injurious levels [46–48]. Therefore, it is unknown if the differences seen between 1 mm/s and 6 mm/s can be extrapolated to higher speeds. Also, each group contained a relatively small sample size. It is possible that more significant differences would be

found if additional samples were included in the analysis. Finally, as with most fitting procedures, there can be uncertainties regarding the identification of local versus global minimums and the uniqueness of the fitted results. This is especially true when the number of fitted parameters is relatively high. The application of an outlier analysis allowed for identification of fits that fell outside the typical range, and while this is an accepted practice when working with biological tissues [49–51], the differences identified between parameters may vary if the full data set had been analyzed instead of the reduced data set. However, of the nine statistically significant differences between strain-rate groups (as identified from the reduced data set), six remained significantly different ($p < 0.05$) or trended that way ($p < 0.1$), when the full data set was examined. This suggests that there are indeed differences between the groups that are obscured by one or two relatively large or small fitted coefficients. Again, additional samples could affect the outlier analysis or reduce the number of outliers.

Despite the above limitations, the results presented in the current study encourage additional work with the presented damage constitutive model. Future work will include testing of dura mater at higher strain rates, including those indicative of injury (up to 20/s), to explicitly investigate the role that protective mechanisms may play in dural damage accumulation. The small sample size precluded an analysis of anterior versus posterior differences, but there is evidence to suggest that the anterior dura mater may behave differently than the posterior dura mater [10]. Specifically, since major spinal cord injury scenarios load the anterior and posterior aspects of the dura differently, future work will include a regional comparison of the damage accumulation process. Finally, the damage model will be applied to other tissues of the SCM, including the pia mater and the spinal cord (treating longitudinal axons as fibers).

A4.1 Conclusions

In conclusion, this work is the first to report the application of a constitutive damage model to the dura mater. The results show distinct damage behaviors for the matrix and fiber constituents and that the damage effects vary with applied strain rate. These differences suggest a possible protective mechanism occurring at strain rates above what the tissue experiences during normal voluntary neck motion. Given these findings, it is imperative that the formulation presented herein be implemented into finite element computational models of the SCM in order to improve the accuracy of simulations of spinal cord dynamics and injury/damage scenarios.

A4.2 Funding and acknowledgements

This work was supported in part by the National Institutes of Health [grant number EB012048] and a scholarship from The Force and Motion Foundation.

APPENDIX A REFERENCES

[1] Bilston, L. E., and Thibault, L. E., 1995, "The Mechanical Properties of the Human Cervical Spinal Cord In Vitro," Ann. Biomed. Eng., 24, pp. 67–74.

[2] Mazuchowski, E. L., and Thibault, L. E., 2003, "Biomechanical Properties of the Human Spinal Cord and Pia Mater," Summer Bioengineering Conference, Key Biscayne, FL, June 25-29, Paper No. 1205.

[3] Oakland, R. J., Hall, R. M., Wilcox, R. K., and Barton, D. C., 2006, "The Biomechanical Response of Spinal Cord Tissue to Uniaxial Loading," Proc. Inst. Mech. Eng. H., 220(4), pp. 489–492.

[4] Runza, M., Pietrabissa, R., Mantero, S., Albani, A., Quaglini, V., and Contro, R., 1999, "Lumbar Dura Mater Biomechanics: Experimental Characterization and Scanning Electron Microscopy Observations," Anesth. Analg., 88(6), pp. 1317–1321.

[5] Jones, C. F., Kroeker, S. G., Cripton, P. A., and Hall, R. M., 2008, "The Effect of Cerebrospinal Fluid on the Biomechanics of Spinal Cord: An *Ex-vivo* Bovine Model Using Bovine and Physical Surrogate Spinal Cord," Spine, 33(17), pp. E580–E588.

[6] Hall, R. M., Oakland, R. J., Wilcox, R. K., and Barton, D. C., 2006, "Spinal Cord-Fragment Interactions Following Burst Fracture: An In Vitro Model," J. Neurosurg. Spine, 5(3), pp. 243-250.

[7] Wilcox, R. K., Allen, D. J., Hall, R. M., Limb, D., Barton, D. C., and Dickson, R. A., 2004, "A Dynamic Investigation of the Burst Fracture Process Using a Combined Experimental and Finite Element Approach," Eur. Spine J., 13(6), pp. 481–488.

[8] Maikos, J. T., Elias, R., and Shreiber, D. I., 2008, "Mechanical Properties of Dura Mater From the Rat Brain and Spinal Cord," J. Neurotrauma, 25(1), pp. 38–51.

[9] Persson, C., Evans, S., Marsh, R., Summers, J. L., and Hall, R. M., 2010, "Poisson's Ratio and Strain Rate Dependency of the Constitutive Behavior of Spinal Dura Mater," Ann. Biomed. Eng., 38(3), pp. 975–983.

[10] Mazgajczyk, E., Scigała, K., Czyz, M., Jarmundowicz, W., and Bedzinski, R., 2012, "Mechanical Properties of Cervical Dura Mater," Acta Bioeng. Biomech., 14(1), pp. 51–58.

[11] Shetye, S. S., Deault, M. M., and Puttlitz, C. M., 2014, "Biaxial Response of Ovine Spinal Cord Dura Mater," J. Mech. Behav. Biomed. Mater., 34, pp. 146–153.

[12] Li, X. F., and Dai, L. Y., 2009, "Three-Dimensional Finite Element Model of the Cervical Spinal Cord: Preliminary Results of Injury Mechanism Analysis," Spine, 34(11), pp. 1140–1147.

[13] Sparrey, C. J., Manley, G. T., and Keaveny, T. M., 2009, "Effects of White, Grey, and Pia Mater Properties on Tissue Level Stresses and Strains in the Compressed Spinal Cord," J. Neurotrauma, 26(4), pp. 585–595.

[14] Greaves, C. Y., Gadala, M. S., and Oxland, T. R., 2008, "A Three-Dimensional Finite Element Model of the Cervical Spine With Spinal Cord: An Investigation of Three Injury Mechanisms," Ann. Biomed. Eng., 36(3), pp. 396–405.

[15] Scifert, J., Totoribe, K., Goel, V., and Huntzinger, J., 2002, "Spinal Cord Mechanics During Flexion and Extension of the Cervical Spine: A Finite Element Study," Pain Phys., 5(4), pp. 394–400.

[16] Russell, C. M., Choo, A. M., Tetzlaff, W., Chung, T. E., and Oxland, T. R., 2012, "Maximum Principal Strain Correlates With Spinal Cord Tissue Damage in Contusion and Dislocation Injuries in the Rat Cervical Spine," J. Neurotrauma, 29(8), pp. 1574–1585.

[17] Simo, J. C., 1987, "On a Fully Three-Dimensional Finite-Strain Viscoelastic Damage Model: Formulation and Computational Aspects," Comput. Methods Appl. Mech. Eng., 60(2), pp. 153–173.

[18] Alastrue, V., Rodriguez, J. F., Calvo, B., and Doblare, M., 2007, "Structural Damage Models for Fibrous Biological Soft Tissues," Int. J. Solids Struct., 44(18–19), pp. 5894–5911.

[19] Calvo, B., Pena, E., Martinez, M. A., and Doblare, M., 2007, "An Uncoupled Directional Damage Model for Fibred Biological Soft Tissues: Formulation and Computational Aspects," Int. J. Numer. Methods Eng., 69(10), pp. 2036–2057.

[20] Rodriguez, J. F., Cacho, F., Bea, J. A., and Doblare, M., 2006, "A Stochastic-Structurally Based Three Dimensional Finite-Strain Damage Model for Fibrous Soft Tissue," J. Mech. Phys. Solids, 54(4), pp. 864–886.

[21] Li, D., and Robertson, A. M., 2009, "A Structural Multi-Mechanism Constitutive Equation for Cerebral Arterial Tissue," Int. J. Solids Struct., 46(14–15), pp. 2920–2928.

[22] Gasser, T. C., 2011, "An Irreversible Constitutive Model for Fibrous Soft Biological Tissue: A 3-D Microfiber Approach With Demonstrative Application to Abdominal Aortic Aneurysms," Acta Biomater., 7(6), pp. 2457–2466.

[23] Balzani, D., Schroder, J., and Gross, D., 2006, "Simulation of Discontinuous Damage Incorporating Residual Stresses in Circumferentially Overstretched Atherosclerotic Arteries," Acta Biomater., 2(6), pp. 609–618.

[24] Liao, H., and Belkoff, S. M., 1999, "A Failure Model for Ligaments," J. Biomech., 32(2), pp. 183–188.

[25] De Vita, R., and Slaughter, W. S., 2007, "A Constitutive Law for the Failure Behavior of Medial Collateral Ligaments," Biomech. Model. Mechanobiol., 6(3), pp. 189–197.

[26] Calvo, B., Pena, E., Martins, P., Mascarenhas, T., Doblare, M., Natal Jorge, R.M., and Ferreira, A., 2009, "On Modelling Damage Process in Vaginal Tissue," J. Biomech., 42(5), pp. 642–651.

[27] Martins, P., Pena, E., Natal Jorge, R. M., Santos, A., Santos, L., Mascarenhas, T., and Calvo, B., 2012, "Mechanical Characterization and Constitutive Modelling of the Damage Process in Rectus Sheath," J. Mech. Behav. Biomed. Mater., 8, pp. 111–122.

[28] Woo, S. L. Y., Orlando, C. A., Camp, J. F., and Akeson, W. H., 1986, "Effects of Postmortem Storage by Freezing on Ligament Tensile Behavior," J. Biomech., 19(5), pp. 399–404.

[29] Huang, H., Zhang, J., Sun, K., Zhang, X., and Tian, S., 2011, "Effects of Repetitive Multiple Freeze-Thaw Cycles on the Biomechanical Properties of Human Flexor Digitorum Superficialis and Flexor Pollicis Longus Tendons," Clin. Biomech., 26(4), pp. 419–423.

[30] Suto, K., Urabe, K., Naruse, K., Uchida, K., Matsuura, T., Mikuni-Takagaki, Y., Suto, M., Nemoto, N., Kamiya, K., and Itoman, M., 2012, "Repeated Freeze-Thaw Cycles Reduce the Survival Rate of Osteocytes in Bone-Tendon Constructs Without Affecting the Mechanical Properties of Tendons," Cell Tissue Bank., 13(1), pp. 71–80.

[31] Szarko, M., Muldrew, K., and Bertram, J. E., 2010, "Freeze-Thaw Treatment Effects on the Dynamic Mechanical Properties of Articular Cartilage," BMC Musculoskelet. Disord., 11(1), p. 231.

[32] Pena, E., Calvo, B., Martinez, M. A., and Doblare, M., 2008, "On Finite-Strain Damage of Viscoelastic-Fibred Materials: Application to Soft Biological Tissues," Int. J. Numer. Methods Eng., 74(7), pp. 1198–1218.

[33] Demiray, H., Weizsacker, H. W., Pascale, K., and Erbay, H. A., 1988, "A Stress-Strain Relation for a Rat Abdominal Aorta," J. Biomech., 21(5), pp. 369–374.

[34] Moore, D., and McCabe, G. P., 1998, Introduction to the Practice of Statistics, W. H. Freeman, New York.

[35] Patin, D. J., Eckstein, E. C., Harum, K., and Pallares, V. S., 1993, "Anatomic and Biomechanical Properties of Human Lumbar Dura Mater," Anesth. Analg., 76(3), pp. 535–540.

[36] Zarzur, E., 1996, "Mechanical Properties of the Human Lumbar Dura Mater," Arq. Neuropsiquiatr., 54(3), pp. 455–460.

[37] Rashid, B., Destrade, M., and Gilchrist, M. D., 2014, "Mechanical Characterization of Brain Tissue in Tension at Dynamic Strain Rates," J. Mech. Behav. Biomed. Mater., 33, pp. 43–54.

[38] Fiford, R. J., and Bilston, L. E., 2005, "The Mechanical Properties of Rat Spinal Cord In Vitro," J. Biomech., 38(7), pp. 1509–1515.

[39] Danto, M. I., and Woo, S. L., 1993, "The Mechanical Properties of Skeletally Mature Rabbit Anterior Cruciate Ligament and Patellar Tendon Over a Range of Strain Rates," J. Orthop. Res., 11(1), pp. 58–67.

[40] Pioletti, D. P., Rakotomanana, L. R., and Leyvraz, P. F., 1999, "Strain Rate Effect on the Mechanical Behavior of the Anterior Cruciate Ligament-Bone Complex," Med. Eng. Phys., 21(2), pp. 95–100.

[41] Yamamoto, S., Saito, A., Kabayama, M., Sugimoto, S., Nagasaka, K., Mizuno, K., and Tanaka, E., 2003, "Strain-Rate Dependence of Mechanical Failure Properties of Rabbit MCL and ACL," Summer Bioengineering Conference, Key Biscayne, FL, June 25–29, Paper No. 0109.

[42] Hirsekorn, M., and Grail, G., 2011, "On the Role of Matrix Nonlinearity in Mechanical Modeling of Long-Fiber Reinforced Composites," International Conference on Composite Materials, Jeju, South Korea, Aug. 21–26, Paper No. F10-2-IF0552.

[43] Bocchieri, R. T., and Schapery, R. A., 2000, "Nonlinear Viscoelastic Behavior of Rubber Toughened Carbon and Glass/Epoxy Composites," Time Dependent and Nonlinear Effects in Polymers and Composites, American Society for Testing and Materials, West Conshohocken, PA, pp. 238–265.

[44] Holmes, G. A., Peterson, R. C., Hunston, D. L., McDonough, W. G., and Schutte, C. L., 2000, "The Effect of Nonlinear Viscoelasticity on Interfacial Shear Strength Measurements," Time Dependent and Nonlinear Effects in Polymers and Composites, American Society for Testing and Materials, West Conshohocken, PA, pp. 98–117.

[45] Modniks, J., Joffe, R., and Andersons, J., 2011, "Model of the Mechanical Response of Short Flax Fiber Reinforced Polymer Matrix Composites," Procedia Eng., 10, pp. 2016–2021.

[46] Bilston, L. E., 1994, "The Biomechanics of the Spinal Cord During Traumatic Spinal Cord Injury," Ph.D. dissertation, University of Pennsylvania, Philadelphia, PA.

[47] McKenzie, J. A., and Williams, J. F., 1971, "The Dynamic Behaviour of the Head and Cervical Spine During 'Whiplash'," J. Biomech., 4(6), pp. 477–90.

[48] Panjabi, M. M., Cholewicki, J., Nibu, K., Babat, L. B., and Dvorak, J., 1998, "Simulation of Whiplash Trauma Using Whole Cervical Spine Specimens," Spine, 23(1), pp. 17–24.

[49] Kural, M. H., Cai, M., Tang, D., Gwyther, T., Zheng, J., and Billiar, K. L., 2012, "Planar Biaxial Characterization of Diseased Human Coronary and Carotid Arteries for Computational Modeling," J. Biomech., 45(5), pp. 790–798.

[50] Wagner, H. P., and Humphrey, J. D., 2011, "Differential Passive and Active Biaxial Mechanical Behaviors of Muscular and Elastic Arteries: Basilar Versus Common Carotid," ASME J. Biomech. Eng., 133(5), p. 051009.

[51] Palevski, A., Glaich, I., Portnoy, S., Linder-Ganz, E., and Gefen, A., 2006, “Stress-relaxation of Porcine Gluteus Muscle Subjected to Sudden Transverse Deformation as Related to Pressure Sore Modeling,” ASME J. Biomech. Eng., 128(5), pp. 782–787.

APPENDIX B: THE DEVELOPMENT AND VALIDATION OF A NUMERICAL INTEGRATION METHOD FOR NON-LINEAR VISCOELASTIC MODELING[5]

B.1 Introduction

Viscoelastic theory describes the time-dependent relationship between stress and strain and is commonly used to describe the mechanical behavior of biological tissues. For viscoelastic materials, the current stress state is dependent upon all previous loading events. This history-dependent behavior complicates numerical analyses of viscoelastic materials because the stress at each step throughout the entire loading history must be computed and stored in order to obtain the current stress. For three-dimensional finite element models, computing and storing the stress tensor at each integration point and time step quickly becomes computationally intractable. To simplify numerical analyses for linear and quasi-linear viscoelastic materials, a discrete series of exponentials (such as a Prony series) is often used to approximate the continuous time-dependent relaxation spectrum.

As demonstrated by Puso and Weiss [1] for quasi-linear viscoelasticity (QLV), the unique properties of a discrete relaxation spectrum may allow for the current stress to be computed using only the stress from the previous time step, thereby greatly reducing computational expense. Fung's theory of QLV [2,3] is a popular choice for researchers working with soft tissues due to its relatively straight-forward incorporation of hyperelastic formulations to describe elastic non-linearity. For example, it is widely used to describe the behavior of connective (e.g.,

[5] This appendix section has been published as a Research Article in PLoS ONE (DOI: 10.1371/journal.pone.0190137). All content has been adapted as allowed for creative commons attribution licensing for open access articles.

tendon [1,4] and ligament [1,5-7]) and spinal (e.g., spinal cord [8,9], brain [10], and dura mater [11]) tissues subjected to static and dynamic loading regimes. However, increasing evidence has demonstrated that these tissue types display fully non-linear viscoelasticity [12-17], wherein the non-linear elastic response cannot be separated from the non-linear time-dependent response.

The comprehensive viscoelastic characterization (CVC) method previously developed by our research group has been shown to accurately predict the non-linear viscoelastic cyclic response of both connective and spinal tissues based on fits of stress-relaxation data [13,18,19]. However, this technique is limited in three important ways: (1) it is restricted to fitting only stress-relaxation data, (2) it requires fits of individual stress-relaxation curves at each strain magnitude tested, and (3) it determines the strain-dependent behavior of the tissue *post-hoc* (from a subsequent fit of the strain-dependent behavior of the individual curve fits). To increase modeling flexibility and address each limitation above, the present study develops a novel numerical integration technique (called the *direct fit method*) for fully non-linear viscoelastic modeling. This novel methodology leverages the unique properties of the Prony series to allow the current stress to be computed from a deformation-dependent state variable stored from the preceding time step only. Similar to the formulation developed for QLV theory [1], the following non-linear viscoelastic formulation greatly improves computational tractability by avoiding the need to store the stress at each time step of the analysis. The following sections will present the derivation of our numerical integration technique, demonstrate its implementation using computational methods, and verify its ability to fit non-linear viscoelastic data by recovering a set of known non-linear viscoelastic coefficients. The significant advantage of a fully non-linear

viscoelastic formulation over a linear viscoelastic formulation is also explicitly demonstrated through direct comparison of the fitting results.

B.2 Materials and Methods

B.2.1 Model development

This section outlines the *direct fit* approach for non-linear viscoelastic modeling which calculates the current stress from a state variable stored from the preceding time step only (as opposed to every previous time step). A linear viscoelastic (i.e., strain-independent relaxation behavior) formulation follows the same derivation except where noted.

Uniaxial non-linear viscoelastic material behavior may be represented by the hereditary (or convolution) integral:

$$\sigma[\varepsilon(t), t] = \int_0^t E[\varepsilon(\tau), t-\tau] \frac{d\varepsilon(\tau)}{d\tau} d\tau, \qquad (B2)$$

where σ is stress, ε is strain, t is time, τ is a time variable of integration representing the history effect, and $E(t, \varepsilon)$ is the material relaxation modulus that describes the non-linear time-dependent relationship between stress and strain. The form of the relaxation modulus must be continuous and monotonically decreasing in order to satisfy thermodynamic restrictions [20]. When modeling biological tissues, it is common to approximate the continuous relaxation spectrum $E(t, \varepsilon)$ by a discrete Prony series. For the case of non-linear viscoelasticity, the following strain-dependent Prony series has been shown to successfully capture the strain- and time-dependent behavior of several types of biological tissues [13,18,19,21]:

$$E[\varepsilon(t), t] = E_\infty(\varepsilon) + \sum_{i=1}^{N} E_i(\varepsilon) e^{-t/\tau_i}, \tag{B2}$$

where $E_i(\varepsilon)$ is the strain-dependent Prony weight corresponding to time constant τ_i, $E_\infty(\varepsilon)$ represents the long-term strain-dependent modulus, and N defines the finite number of exponential Prony terms. For linear viscoelasticity, the Prony weights and long-term modulus are replaced with constant (strain independent) coefficients:

$$E(t) = E_\infty + \sum_{i=1}^{N} E_i e^{-t/\tau_i} \tag{B3}$$

In order to satisfy the monotonically decreasing restriction on the relaxation modulus, the non-linear strain-dependent Prony weight functions must be positive and monotonically increasing (or a positive constant for linear viscoelasticity) and the time constants must be positive. Combining Eq. (B1) and Eq. (B2) yields the following definition for stress at the current time t, assuming $\varepsilon(0) = 0$:

$$\begin{aligned}
\sigma[\varepsilon(t), t] &= \int_0^t \left\{ E_\infty(\varepsilon) + \sum_{i=1}^{N} E_i(\varepsilon) e^{-(t-\tau)/\tau_i} \right\} \frac{d\varepsilon(\tau)}{d\tau} d\tau \\
&= \int_0^t E_\infty(\varepsilon) \frac{d\varepsilon(\tau)}{d\tau} d\tau + \int_0^t \left\{ \sum_{i=1}^{N} E_i(\varepsilon) e^{-(t-\tau)/\tau_i} \right\} \frac{d\varepsilon(\tau)}{d\tau} d\tau \\
&= E_\infty(\varepsilon)[\varepsilon(t) - \varepsilon(0)] + \int_0^t \left\{ \sum_{i=1}^{N} E_i(\varepsilon) e^{-(t-\tau)/\tau_i} \right\} \frac{d\varepsilon(\tau)}{d\tau} d\tau \\
&= E_\infty(\varepsilon)\varepsilon(t) + \int_0^t \left\{ \sum_{i=1}^{N} E_i(\varepsilon) e^{-(t-\tau)/\tau_i} \right\} \frac{d\varepsilon(\tau)}{d\tau} d\tau.
\end{aligned} \tag{B4}$$

A strain-dependent history state variable is defined to recursively update the stress at each incremental time step:

$$h_i[\varepsilon(t), t] = \int_0^t \left\{ E_i(\varepsilon) e^{-(t-\tau)/\tau_i} \right\} \frac{d\varepsilon(\tau)}{d\tau} d\tau, \tag{B5}$$

such that Eq. (B4) can be recast as:

$$\sigma[\varepsilon(t), t] = E_\infty(\varepsilon)\varepsilon(t) + \sum_{i=1}^{N} h_i[\varepsilon(t), t]. \tag{B6}$$

The stress at the next time step, $t + \Delta t$, is given as:

$$\sigma[\varepsilon(t+\Delta t), t+\Delta t] = E_\infty(\varepsilon)\varepsilon(t+\Delta t) + \sum_{i=1}^{N} h_i[\varepsilon(t+\Delta t), t+\Delta t], \tag{B7}$$

where the updated history variable is:

$$h_i[\varepsilon(t+\Delta t), t+\Delta t] = \int_0^{t+\Delta t} \left\{ E_i(\varepsilon) e^{-(t+\Delta t-\tau)/\tau_i} \right\} \frac{d\varepsilon(\tau)}{d\tau} d\tau. \tag{B8}$$

Equation (B8) can be expanded by use of the summation rule for definite integrals:

$$\begin{aligned} & h_i[\varepsilon(t+\Delta t), t+\Delta t] \\ & \quad = \int_0^t \left\{ E_i(\varepsilon) e^{-(t+\Delta t-\tau)/\tau_i} \right\} \frac{d\varepsilon(\tau)}{d\tau} d\tau \\ & \quad + \int_t^{t+\Delta t} \left\{ E_i(\varepsilon) e^{-(t+\Delta t-\tau)/\tau_i} \right\} \frac{d\varepsilon(\tau)}{d\tau} d\tau. \end{aligned} \tag{B9}$$

Inputting Eq. (B9) into Eq. (B7) yields the following expression for the stress at the next time step:

$$\begin{aligned} & \sigma[\varepsilon(t+\Delta t), t+\Delta t] \\ & = \sum_{i=1}^{N} \int_0^t \left\{ E_i(\varepsilon) e^{-(t+\Delta t-\tau)/\tau_i} \right\} \frac{d\varepsilon(\tau)}{d\tau} d\tau \\ & + \sum_{i=1}^{N} \int_t^{t+\Delta t} \left\{ E_i(\varepsilon) e^{-(t+\Delta t-\tau)/\tau_i} \right\} \frac{d\varepsilon(\tau)}{d\tau} d\tau \\ & + E_\infty(\varepsilon)\varepsilon(t+\Delta t), \end{aligned} \tag{B10}$$

where the first term represents the history effect (integrated over all previous loading events), the second term represents the effect of the current loading event, and the final term represents the effect of the equilibrium response.

Using the product law of exponentials, the history state variable, $h_i[\varepsilon(t), t]$, could be factored out of the first term of Eq. (B9):

$$\int_0^t \left\{E_i(\varepsilon) e^{-(t+\Delta t-\tau)/\tau_i}\right\} \frac{d\varepsilon(\tau)}{d\tau} d\tau = h_i[\varepsilon(t), t] \left\{ \frac{\int_0^t \left\{E_i(\varepsilon) e^{-(t+\Delta t-\tau)/\tau_i}\right\} \frac{d\varepsilon(\tau)}{d\tau} d\tau}{\int_0^t \left\{E_i(\varepsilon) e^{-(t-\tau)/\tau_i}\right\} \frac{d\varepsilon(\tau)}{d\tau} d\tau} \right\}$$

$$= h_i[\varepsilon(t), t] \left\{ \frac{e^{-t/\tau_i} e^{-\Delta t/\tau_i} \int_0^t \left\{e^{\tau/\tau_i}\right\} \frac{d\varepsilon(\tau)}{d\tau} d\tau}{e^{-t/\tau_i} \int_0^t \left\{e^{\tau/\tau_i}\right\} \frac{d\varepsilon(\tau)}{d\tau} d\tau} \right\} = h_i[\varepsilon(t), t] e^{-\Delta t/\tau_i}. \quad \textit{(B11)}$$

The second mean-value theorem of integrals states that for continuous functions $f(x)$ and $g(x) \geq 0$ over $x \in [a, b]$, there exists $c \in (a, b)$ such that $\int_a^b f(x)g(x)dx = f(c) \int_a^b g(x)dx$. This theorem is imposed on the second term of Eq. (B9) such that:

$$\int_t^{t+\Delta t} \left\{E_i(\varepsilon) e^{-(t+\Delta t-\tau)/\tau_i}\right\} \frac{d\varepsilon(\tau)}{d\tau} d\tau = \frac{d\varepsilon(k)}{d\tau} \int_t^{t+\Delta t} \left\{E_i(\varepsilon) e^{-(t+\Delta t-\tau)/\tau_i}\right\} d\tau, \quad \textit{(B12)}$$

with $k \in (t, t + \Delta t)$. The time steps are assumed to be small enough that the error associated with linear interpolation between sequential strain values is negligible. Accordingly, by the central difference rule:

$$\frac{d\varepsilon(k)}{d\tau} = \frac{\varepsilon(t + \Delta t) - \varepsilon(t)}{t + \Delta t - t} = \frac{\Delta\varepsilon}{\Delta t}. \quad \textit{(B13)}$$

Using Eq. (B13), the second term of Eq. (B9) may be evaluated as:

$$\frac{\Delta\varepsilon}{\Delta t}\int_{t}^{t+\Delta t}\left\{E_i(\varepsilon)e^{-(t+\Delta t-\tau)/\tau_i}\right\}d\tau = \frac{E_i(\varepsilon)\Delta\varepsilon}{\Delta t}\left\{\tau_i\, e^{-(t+\Delta t-\tau)/\tau_i}\Big|_{\tau\in[t,t+\Delta t]}\right\}$$
$$= \frac{E_i(\varepsilon)\tau_i\Delta\varepsilon}{\Delta t}\left(1-e^{-\Delta t/\tau_i}\right). \tag{B14}$$

Therefore, Eq. (B9) may be simplified as:

$$h_i[\varepsilon(t+\Delta t),t+\Delta t] = h_i[\varepsilon(t),t]e^{-\Delta t/\tau_i} + \frac{E_i(\varepsilon)\tau_i\Delta\varepsilon}{\Delta t}\left(1-e^{-\Delta t/\tau_i}\right). \tag{B15}$$

and Eq. (B7) can be recast as:

$$\sigma[\varepsilon(t+\Delta t),t+\Delta t]$$
$$= E_\infty(\varepsilon)\varepsilon(t+\Delta t)$$
$$+\sum_{i=1}^{N}\left\{h_i[\varepsilon(t),t]e^{-\Delta t/\tau_i} + \frac{E_i(\varepsilon)\left(1-e^{-\Delta t/\tau_i}\right)}{\left(\Delta t/\tau_i\right)}\Delta\varepsilon\right\}. \tag{B16}$$

Using the incremental notation $f_{n+1} = f_n + \Delta f_n$, where f is an incremental variable, f_n is the variable value at the preceding increment, and Δf_n is the current variable increment, the following incremental formulation for non-linear viscoelasticity is obtained:

$$\sigma(\varepsilon_{n+1})_{n+1} = E_\infty(\varepsilon)\varepsilon_{n+1}$$
$$+\sum_{i=1}^{N}\left\{h_i[\varepsilon(t),t]e^{-\Delta t_n/\tau_i} + \frac{E_i(\varepsilon)\left(1-e^{-\Delta t_n/\tau_i}\right)}{\left(\Delta t_n/\tau_i\right)}\Delta\varepsilon_{n+1}\right\}. \tag{B17}$$

Following similar mathematical development, the analogous equation for linear viscoelasticity is:

$$\sigma_{n+1} = E_\infty\varepsilon_{n+1} + \sum_{i=1}^{N}\left\{h_i(t)e^{-\Delta t_n/\tau_i} + \frac{E_i\left(1-e^{-\Delta t_n/\tau_i}\right)}{\left(\Delta t_n/\tau_i\right)}\Delta\varepsilon_{n+1}\right\}. \tag{B18}$$

It should be noted that evaluating Eq. (B17) or Eq. (B18) at the current time step requires only the history state variable from the previous time step ($h_i[\varepsilon(t), t]$ for non-linear viscoelasticity and $h_i(t)$ for linear viscoelasticity). Unlike the CVC method previously developed by our group [13,19], the presented formation may be fit to an arbitrary strain history and may be used in a data fitting algorithm to directly determine the non-linear strain-dependence of each Prony weight.

B.2.2 Model validation

The numerical integration technique for our *direct fit method*, and its associated non-linear viscoelastic model, were validated based on its ability to recover coefficients used to create idealized experimental data. These stress-strain data were created by specifying the mathematical formulae and coefficients of the non-linear relaxation modulus ($E[\varepsilon(\tau), t]$), the associated time constants, and the strain magnitude. Values were chosen based on the experimental data provided in Troyer et al. for ovine Achilles tendon [19]. In this previous work, the non-linear viscoelastic relaxation modulus was approximated by a 4-term Prony series, where each strain-dependent Prony weight was described with a two-term polynomial function:

$$E_i(\varepsilon) = C_1^{\tau_i}\varepsilon + C_2^{\tau_i}\varepsilon^2, \qquad \textit{(B19)}$$

$$E_\infty(\varepsilon) = C_1^{\infty}\varepsilon + C_2^{\infty}\varepsilon^2. \qquad \textit{(B20)}$$

The time constants were fixed at decadal values (τ_1 = 0.1 s, τ_2 = 1 s, τ_3 = 10 s, τ_4 = 100 s) in order to adequately capture both the short-term and long-term response of the tissue. The C_1 and C_2 coefficients obtained via the CVC method (Table B1, [19]) were input into Eq. (B17) to create idealized experimental data for two types of viscoelastic experiments: static stress-relaxation and dynamic cyclic tests. The idealized experimental data of each type were then

simultaneously fit, in their entirety, to both the presented non-linear and linear viscoelastic models using MATLAB's (R2014b, Mathworks, Natick, MA) *fmincon* constrained non-linear optimization function. For the non-linear viscoelastic fits, each Prony weight was constrained to be positive and monotonically increasing in order to satisfy thermodynamic restrictions. For the linear viscoelastic fits, the Prony constants were constrained to be positive. Since multiple curves were fit simultaneously, the root mean squared errors (RMSEs) for individual curves in the fit were summed and used to define the objective function minimized by the MATLAB algorithm.

The accuracy of model fits were assessed by computing the RMSE between each idealized experimental stress-strain curve and that predicted by each viscoelastic model. For the nonlinear viscoelastic model, the recovery of input C_1 and C_2 coefficients was assessed by the percent error for each of the 10 coefficients.

B.3 Results

B.3.1 Stress-relaxation

Six idealized stress-relaxation experimental curves were created to match the experimental work by Troyer et al. [19]. Specifically, stress-relaxation experiments at 1%, 2%, 3%, 4%, 5%, and 6% engineering strain at a ramping strain-rate of 0.1/sec with a dwell time of 100 seconds were created using the coefficients in Table B1. An initial guess value of 100 was used for all ten fitted coefficients in the simultaneous fits of the six experimental curves. As shown in Fig. B1, the non-linear viscoelastic model fit the idealized experimental curves very well, including the non-linear stress-strain behavior during the ramping phase, with RMSE values ranging from 1.4 to 12.5 Pa (average RMSE = 5.25 Pa). These RMSE values are approximately six orders of

magnitude less than the peak stress, representing less than 0.003% of the peak stress. On average, there was less than a 0.28% difference between the fitted coefficients and the coefficients used to create the experimental curves (range 0.0001% to 2.18%, Table B1).

Table B1: Input and recovery error of non-linear viscoelastic coefficients. The proposed numerical integration *direct fit* method for non-linear viscoelastic characterization was able to recover input non-linear viscoelastic coefficients using both stress-relaxation and dynamic cyclic stress-strain data with average errors well below 1%.

	Input Coefficients [147] **(MPa)**	**Stress-Relaxation (n=6) Coefficient Recovery Error**	**Dynamic Cyclic (n=3) Coefficient Recovery Error**
$C_1^{\tau = 0.1}$	**901.1**	0.01%	0.003%
$C_2^{\tau = 0.1}$	**8437**	0.05%	0.01%
$C_1^{\tau = 1}$	**343.5**	0.16%	0.01%
$C_2^{\tau = 1}$	**-684.1**	2.18%	0.12%
$C_1^{\tau = 10}$	**331.2**	0.03%	0.01%
$C_2^{\tau = 10}$	**-1201.2**	0.24%	0.08%
$C_1^{\tau = 100}$	**476.5**	0.002%	0.02%
$C_2^{\tau = 100}$	**-363.4**	0.07%	0.90%
C_1^{∞}	**4403.1**	0.0001%	0.001%
C_2^{∞}	**-9959.3**	0.001%	0.01%
Average		**0.28%**	**0.12%**

Contrary to the non-linear viscoelastic model, the linear viscoelastic model was unable to describe the strain-dependent stress-relaxation data. As shown in Fig. B2, the linear model could not capture the non-linear stress-strain behavior during the ramping phase nor the non-linear strain-dependent relaxation response. The RMSE values for the linear model fit were up to six orders of magnitude larger than the values obtained for the non-linear model fit. The RMSE

values for the linear model fit ranged from 0.20 to 2.27 MPa representing an average 80% of the peak stress.

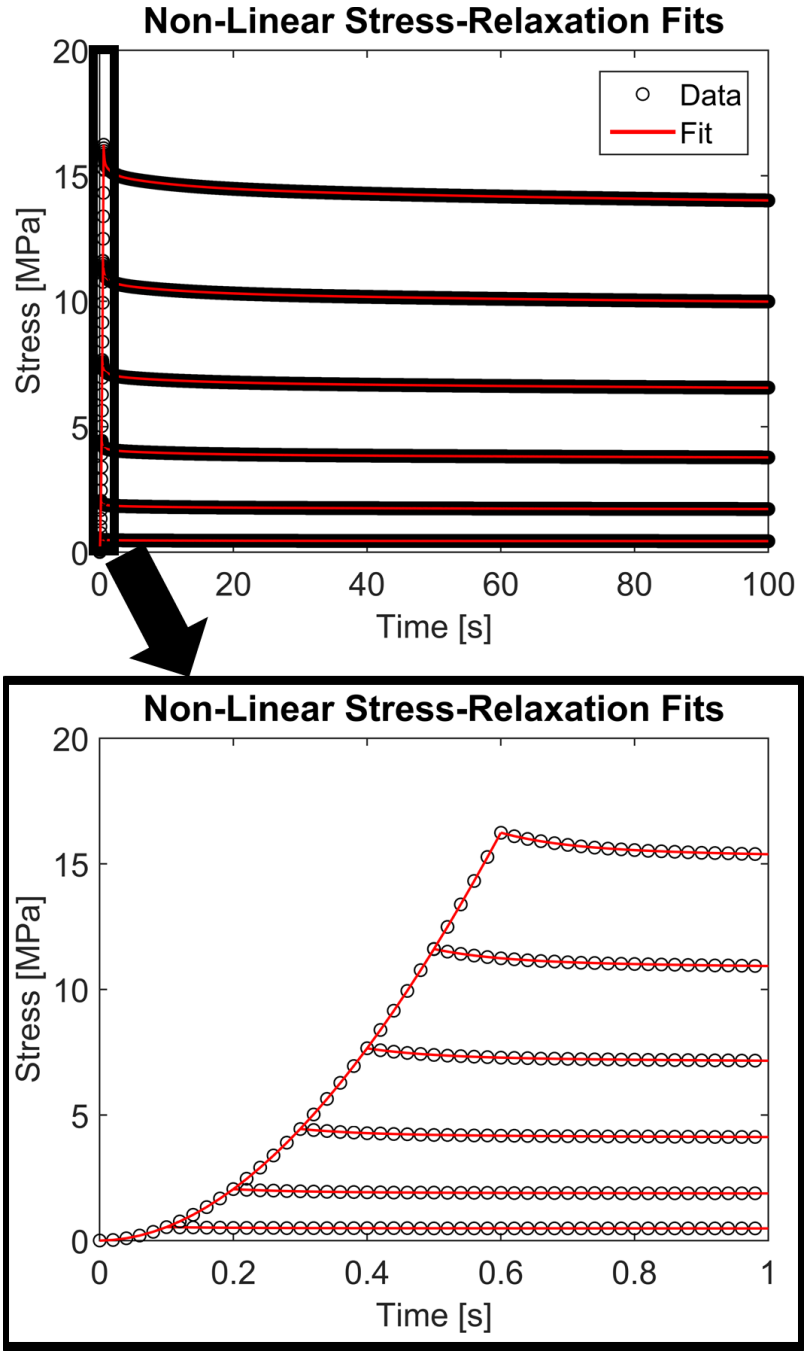

Figure B1: Non-linear stress-relaxation fits. The proposed numerical integration *direct fit method* for non-linear viscoelastic characterization was able to accurately fit the idealized stress-relaxation experimental data, including the non-linear stress-strain behavior during the ramping phase and the strain-dependent relaxation indicative of non-linear viscoelastic behavior.

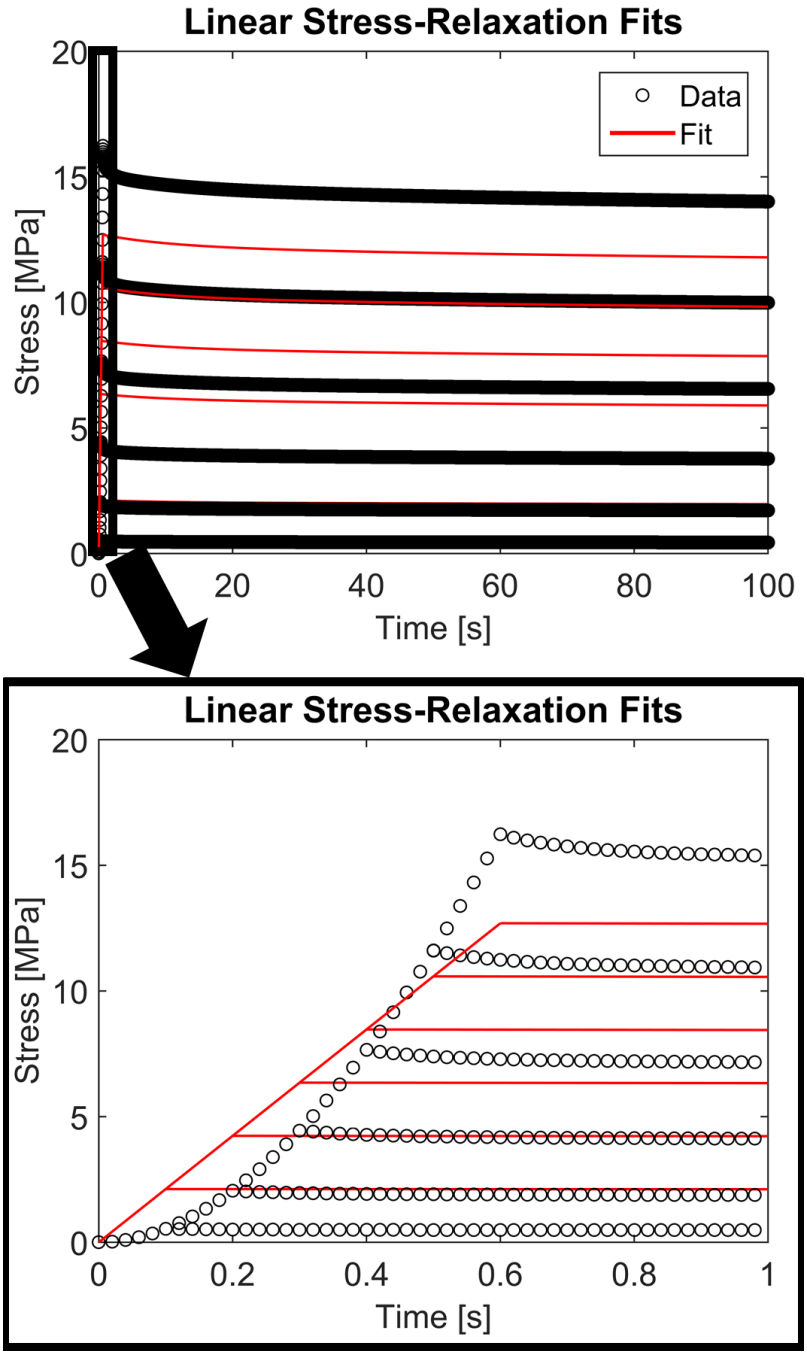

Figure B2: Linear stress-relaxation fits. The linear viscoelastic formulation was not able to capture the idealized strain-dependent stress-relaxation data, resulting in large RMSE values compared to those of the non-linear viscoelastic formulation.

B.3.2 Dynamic cyclic

The ability of the *direct fit method* to recover input coefficients from dynamic cyclic data was also examined. Similar to the stress-relaxation methodology, idealized experimental data were created using the same time constants and relaxation modulus coefficients obtained in Troyer et al. [19] (Table B1). Three idealized experimental dynamic cyclic data curves consisting of 10 cycles to the maximum strain level of interest (6%) at 0.01Hz, 0.1Hz, and 1Hz were created for fitting. As with the stress-relaxation fits, an initial guess of 100 was used for all ten coefficients in the simultaneous fits of the three curves.

The non-linear viscoelastic model also fit the cyclic data very well, with RMSE values (2.75, 2.24, and 1.66 Pa) almost seven orders of magnitude less than the peak stress (Fig. B3). The cyclic fits also exhibited strong coefficient recovery with an average 0.12% difference between the fitted coefficients and the coefficients used to create the idealized experimental curves (range 0.001% to 0.9%, Table B1).

Figure B4 shows the results of fitting the linear viscoelastic model to the same three dynamic cyclic curves. As with the stress-relaxation data, the linear viscoelastic model was unable to capture the strain-dependent viscoelastic response with RMSE values six orders of magnitude larger than those obtained for the non-linear model fit. The linear model resulted in RMSE values of 1.44, 1.47, and 1.65 MPa, which represents approximately 10% of the peak stresses.

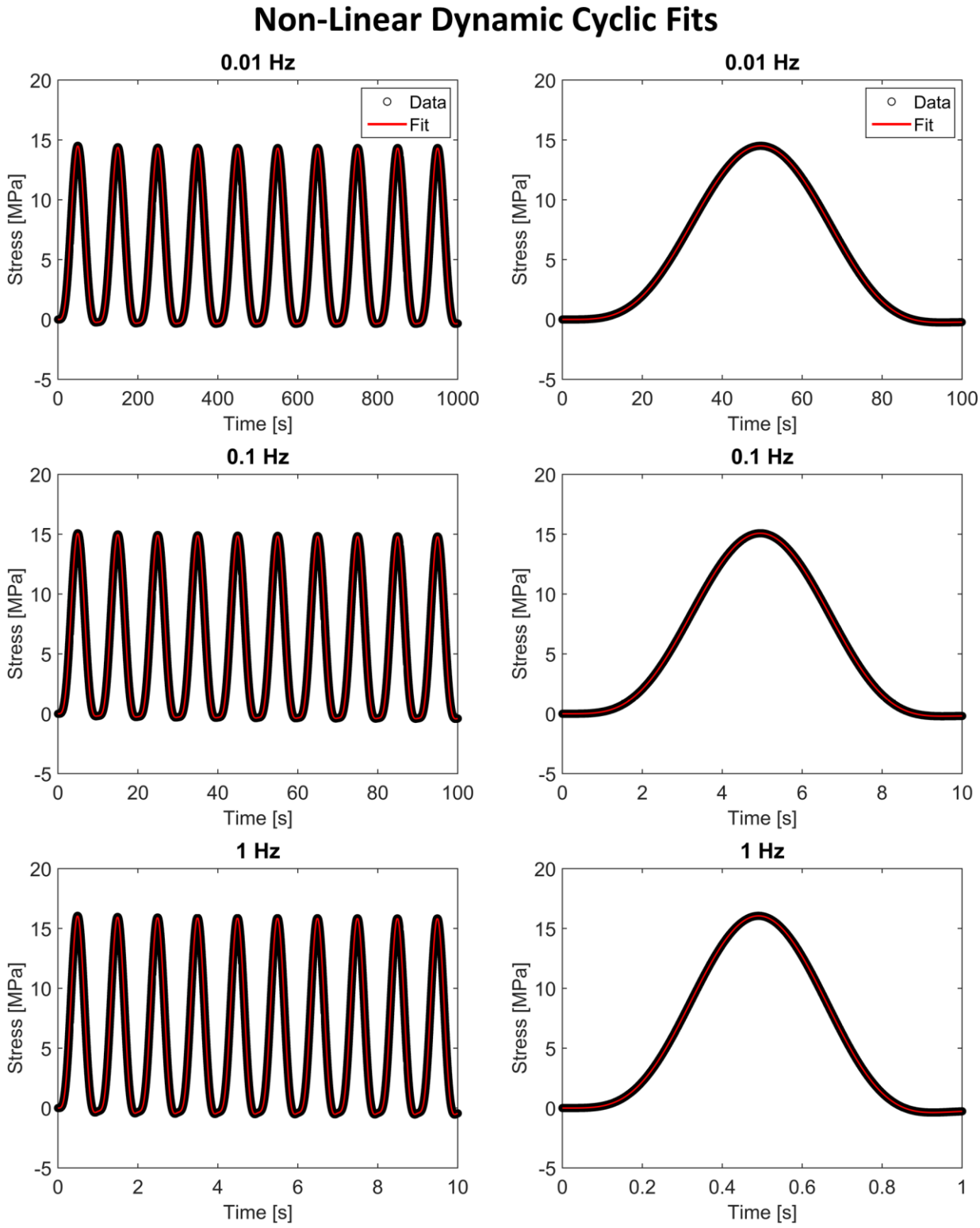

Figure B3: Non-linear dynamic cyclic fits. The proposed *direct fit method* accurately fit the idealized dynamic cyclic response at three frequencies. These curves were fit simultaneously but are plotted separately to improve visualization of the higher frequency fits. Images in the right column show the first cycle of the fit for each frequency.

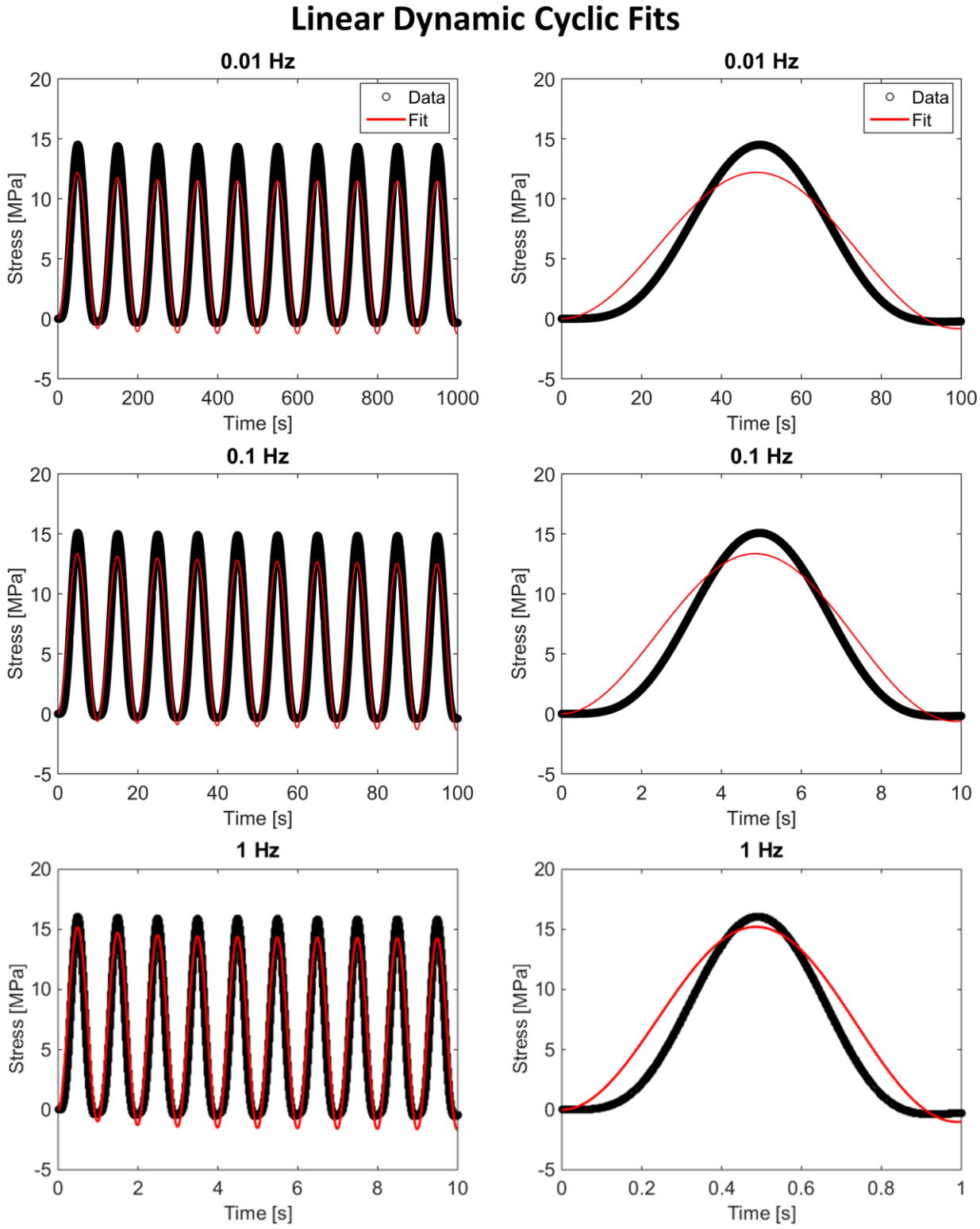

Figure B4: Linear dynamic cyclic fits. The linear viscoelastic formulation was unable to fit the idealized dynamic cyclic response, resulting in very large RMSE values compared to those of the non-linear viscoelastic formulation. These curves were fit simultaneously but are plotted separately to improve visualization of the higher frequency fits. Images in the right column show the first cycle of the fit for each frequency.

B.4 Discussion

With increasing experimental evidence that the mechanical behavior of many biological tissues is not adequately captured by linear and quasi-linear viscoelastic formulations, there is a significant need for computationally tractable fully non-linear viscoelastic modeling methods. The novel *direct fit method* presented herein provides a number of advantages over other non-linear techniques, including that of the CVC method [13,18,19]. Specifically, through the use of a strain-dependent Prony series representation of the relaxation modulus and the product law of exponentials, the *direct fit method* does not require storage of the stress at each time step of the loading history. Instead, the new method recursively updates a strain-dependent history state variable. The new method also permits simultaneous fits of all experimental data from each sample, which is believed to result in a better approximation of the sample's behavior than averaging the results of individual curve fits. In addition, by fitting the data curves in their entirety, the non-linearity is directly determined from the fits themselves instead of *post-hoc* analyses (as with the CVC method). Finally, the *direct fit method* also allows for more experimental flexibility since it may be fit to an arbitrary strain history (e.g., stress-relaxation and cyclical experiments or combinations thereof). While the CVC method is both efficient in its fits and accurate in its predictions [13,19], it is limited to fitting the stress-relaxation response only. Since non-linear viscoelastic characterization based on stress-relaxation data require multiple tests at varying strain magnitudes, this experimental procedure can require significant experimental testing time. For tissues whose mechanical properties demonstrate a relatively quickly post-mortem degradation profile, such as neural tissues [22-24], the ability to fit fewer cyclic experiments for the same predictive accuracy is a very important advantage.

Strong recovery of all ten input coefficients from both stress-relaxation and cyclic experimental data validates the use of the *direct fit method* for non-linear viscoelastic characterization. It is important to note that, on average, the cyclic fits were better at recovering the input coefficients than the stress-relaxation fits. As the strain history is continuously changing over the course of the test, the strain-dependent Prony weights are more sensitive when fitting cyclic data compared to strain-stagnant relaxation data.

While the non-linear viscoelastic model fit the idealized experimental data very well, the linear viscoelastic model performed much worse with RMSE values of up to 200% of the peak stress. The inability of the simplified linear viscoelastic model to fit the idealized experimental data demonstrates the need for fully non-linear viscoelastic models to characterize the mechanical behavior of many biological tissues. As seen in Figs. B2 and B4, the linear formulation of the presented model was unable to capture non-linear elastic or non-linear viscous behavior, both of which are commonly seen in the mechanical response of connective and neural tissues [12-17].

Limitations of the *direct fit method* developed herein include the restriction to uniaxial tension and the use of a simple polynomial model to capture the strain-dependent Prony weights. While uniaxial tension tests are popular experimental methods for characterizing both connective and neural tissues, we plan to extend the method to include descriptions of anisotropic behavior by investigating strain energy-based formulations to describe the strain-dependence of the Prony weights. In future work, we will use the numerical integration *direct fit method* to characterize the viscoelastic behavior of spinal cord and meningeal tissues in order to improve the time-dependent mechanical behavior predictions of spinal cord injury finite element models.

APPENDIX B REFERENCES

1. Puso MA, Weiss JA. Finite element implementation of anisotropic quasi-linear viscoelasticity using a discrete spectrum approximation. J Biomech Eng [Internet]. 1998; 120(1):62-70. Available from: http://link.aip.org/link/?JBY/120/62/1 PMID: 9675682

2. Fung YC. Strain History Relations of Soft Tissues in Simple Elongation. Fung YC, Perrone N, Anliker M, editors. Englewood Cliffs, NJ, NJ: Prentice-Hall; 1972. 181-208

3. Fung YC. Biomechanics: Mechanical Properties of Living Tissues. New York, New York, New York: Springer; 1981.

4. Duenwald SE, Vanderby R, Lakes RS. Viscoelastic relaxation and recovery of tendon. Ann Biomed Eng. 2009; 37(6):1131-40. https://doi.org/10.1007/s10439-009-9687-0 PMID: 19353269

5. Abramowitch SD, Woo SL. An improved method to analyze the stress-relaxation of ligaments following a finite ramp time based on the quasi-linear viscoelastic theory. J Biomech Eng. 2004; 126(1):92-7. PMID: 15171134

6. Weiss J, Gardiner JC. Computational modeling of ligament mechanics. Crit Rev Biomed Eng. 2001; 29(3):303-71. PMID: 11730098

7. Lucas SR, Bass CR, Crandall JR, Kent RW, Shen FH, Salzar RS. Viscoelastic and failure properties of spine ligament collagen fascicles. Biomech Model Mechanobiol. 2009; 8(6):487-98. https://doi.org/10.1007/s10237-009-0152-7 PMID: 19308471

8. Bilston LE, Thibault LE. The mechanical properties of the human cervical spinal cord in vitro. Ann Biomed Eng [Internet]. 1996 [cited 2014 Jul 24]; 24(1):67-74. Available from: http://link.springer.com/article/10.1007/BF02770996 PMID: 8669719

9. Sparrey CJ, Keaveny TM. Compression behavior of porcine spinal cord white matter. J Biomech [Internet]. Elsevier; 2011 Apr 7 [cited 2014 Jul 24]; 44(6):1078-82. Available from: http://www.ncbi.nlm.nih.gov/pubmed/21353225 https://doi.org/10.1016/j.jbiomech.2011.01.035 PMID: 21353225

10. Rashid B, Destrade M, Gilchrist MD. Mechanical characterization of brain tissue in tension at dynamic strain rates. J Mech Behav Biomed Mater [Internet]. Elsevier; 2014 May [cited 2014 Aug 25]; 33:43-54. Available from: http://www.ncbi.nlm.nih.gov/pubmed/23127641 https://doi.org/10.1016/j.jmbbm.2012.07.015 PMID: 23127641

11. Wilcox RK, Bilston LE, Barton DC, Hall RM. Mathematical model for the viscoelastic properties of dura mater. J Orthop Sci [Internet]. 2003 Jan; 8(3):432-4. Available from:

http://www.ncbi.nlm.nih.gov/pubmed/12768491 https://doi.org/10.1007/s10776-003-0644-9 PMID: 12768491

12. Shetye SS, Deault MM, Puttlitz CM. Biaxial response of ovine spinal cord dura mater. J Mech Behav Biomed Mater [Internet]. Elsevier; 2014 Jun [cited 2014 Jul 24]; 34:146-53. Available from: http://www.ncbi.nlm.nih.gov/pubmed/24583806 https://doi.org/10.1016/j.jmbbm.2014.02.014 PMID: 24583806

13. Shetye SS, Troyer KL, Streijger F, Lee JHT, Kwon BK, Cripton P, et al. Nonlinear viscoelastic characterization of the porcine spinal cord. Acta Biomater [Internet]. Acta Materialia Inc.; 2014 Feb [cited 2014 Jul 24]; 10(2):792-7. Available from: http://www.ncbi.nlm.nih.gov/pubmed/24211612 https://doi.org/10.1016/j.actbio.2013.10.038 PMID: 24211612

14. Troyer KL, Puttlitz CM. Human cervical spine ligaments exhibit fully nonlinear viscoelastic behavior. Acta Biomater [Internet]. 2011 Feb [cited 2014 Jul 15]; 7(2):700-9. Available from: http://www.ncbi.nlm.nih.gov/pubmed/20831909 https://doi.org/10.1016/j.actbio.2010.09.003 PMID: 20831909

15. Fiford RJ, Bilston LE. The mechanical properties of rat spinal cord in vitro. J Biomech [Internet]. 2005 Jul [cited 2014 Jul 24]; 38:1509-15. Available from: http://www.ncbi.nlm.nih.gov/pubmed/15922762 https://doi.org/10.1016/j.jbiomech.2004.07.009 PMID: 15922762

16. Russell CM, Choo AM, Tetzlaff W, Chung TE, Oxland TR. Maximum principal strain correlates with spinal cord tissue damage in contusion and dislocation injuries in the rat cervical spine. J Neurotrauma [Internet]. 2012 May 20 [cited 2014 Jul 24]; 29:1574-85. Available from: http://www.ncbi.nlm.nih.gov/pubmed/22320127 https://doi.org/10.1089/neu.2011.2225 PMID: 22320127

17. Jin X, Mao H, Yang KH, King AI. Constitutive modeling of pia-arachnoid complex. Ann Biomed Eng [Internet]. 2014 Apr [cited 2014 Jul 24]; 42(4):812-21. Available from: http://www.ncbi.nlm.nih.gov/pubmed/24322590 https://doi.org/10.1007/s10439-013-0948-6 PMID: 24322590

18. Troyer KL, Estep DJ, Puttlitz CM. Viscoelastic effects during loading play an integral role in soft tissue mechanics. Acta Biomater [Internet]. Acta Materialia Inc.; 2012; 8(1):234-43. Available from: http://dx.doi.org/10.1016/j.actbio.2011.07.035 PMID: 21855664

19. Troyer KL, Puttlitz CM, Shetye SS. Experimental Characterization and Finite Element Implementation of Soft Tissue Nonlinear Viscoelasticity. J Biomech Eng [Internet]. 2012 Oct 11; 134(11):114501. Available from: http://biomechanical.asmedigitalcollection.asme.org/article.aspx?doi=10.1115/1.4007630 PMID: 23387789

20. Christensen RM. Restrictions Upon Viscoelastic Relaxation Functions and Complex Moduli. Trans Soc Rheol [Internet]. 1972 Dec; 16(4):603-14. Available from: http://scitation.aip.org/content/sor/journal/tsor/16/4/10.1122/1.549265

21. Wheatley BB, Morrow DA, Odegard GM, Kaufman KR, Haut Donahue TL. Skeletal muscle tensile strain dependence: Hyperviscoelastic nonlinearity. J Mech Behav Biomed Mater [Internet]. Elsevier; 2016;53:445-54. Available from: http://dx.doi.org/10.1016/j.jmbbm.2015.08.041 PMID: 26409235

22. Garo A, Hrapko M, van Dommelen JAW, Peters GWM. Towards a reliable characterisation of the mechanical behaviour of brain tissue: The effects of post-mortem time and sample preparation. Biorheology [Internet]. 2007; 44(1):51-8. Available from: http://www.ncbi.nlm.nih.gov/pubmed/17502689 PMID: 17502689

23. Prevost TP, Jin G, de Moya MA, Alam HB, Suresh S, Socrate S. Dynamic mechanical response of brain tissue in indentation *in-vivo*, in situ and in vitro. Acta Biomater [Internet]. 2011 Dec [cited 2014 Jul 24]; 7(12):4090-101. Available from: http://www.ncbi.nlm.nih.gov/pubmed/21742064 https://doi.org/10.1016/j.actbio.2011.06.032 PMID: 21742064

24. Oakland RJ, Hall RM, Wilcox RK, Barton DC. The biomechanical response of spinal cord tissue to uniaxial loading. Proc Inst Mech Eng H [Internet]. 2006 May 1 [cited 2014 Jul 24]; 220:489-92. Available from: http://pih.sagepub.com/lookup/doi/10.1243/09544119JEIM135 PMID: 16808065

APPENDIX C: SUPPLEMENTAL FIGURES FOR CHAPTER 4[6]

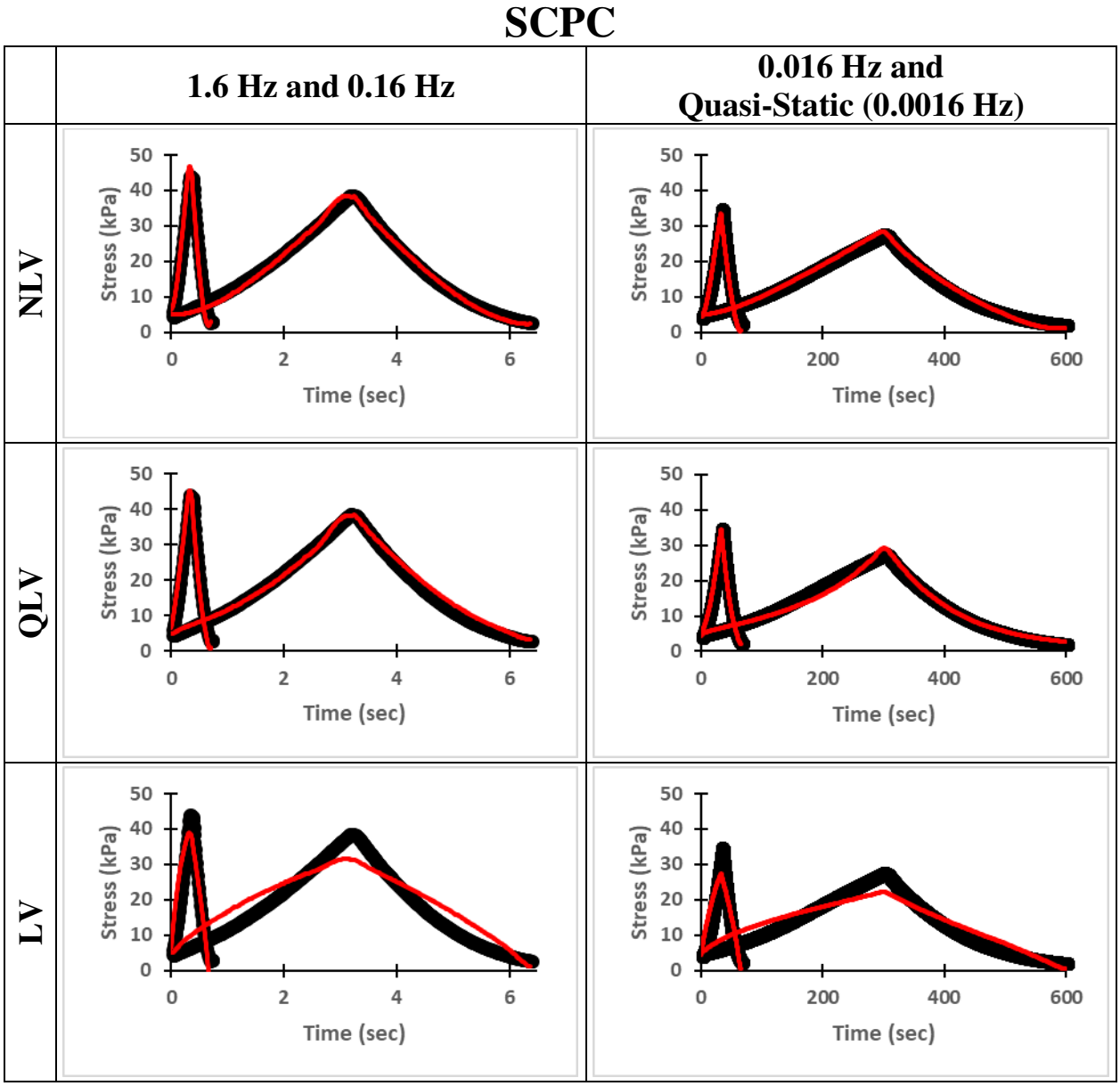

Figure C1: Representative fits of SCPC condition data to all three viscoelastic formulations; for the SCPC condition, the fit RMSE values of the LV formulation were significantly larger than those of the other two formulations. Although all four cycles were fit simultaneously, the curves have been separated to enable visibility of the faster tests.

[6] This appendix section is under review as supplemental information for a fundamental research article to the International Journal for Numerical Methods in Biomedical Engineering.

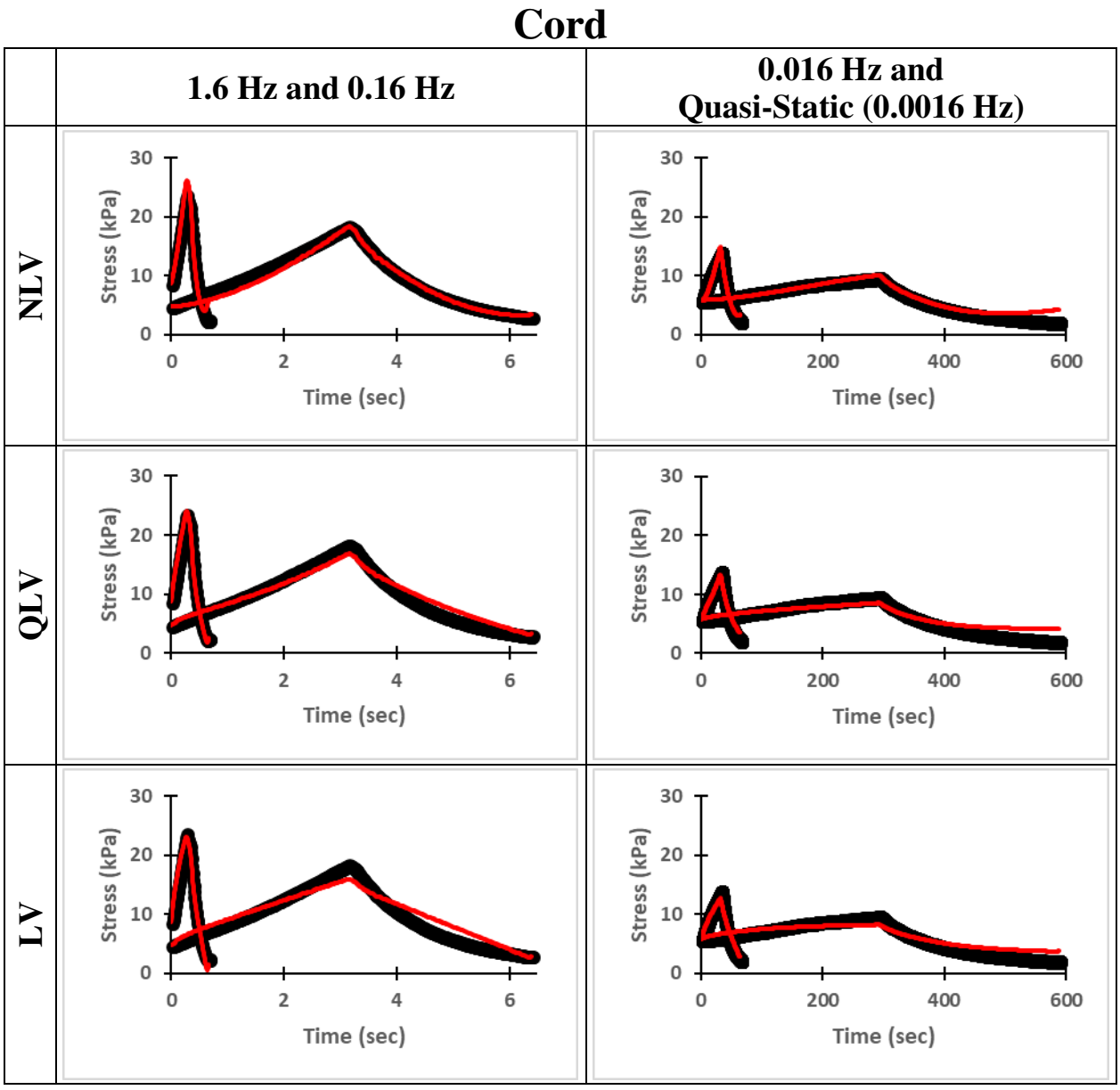

Figure C2: Representative fits of isolated cord condition data to all three viscoelastic formulations; for the cord condition, the fit RMSE values of the NLV formulation were significantly larger than those of the QLV formulation while the LV formulation values were not statistically different than the other two formulations. Although all four cycles were fit simultaneously, the curves have been separated to enable visibility of the faster tests.

PAC

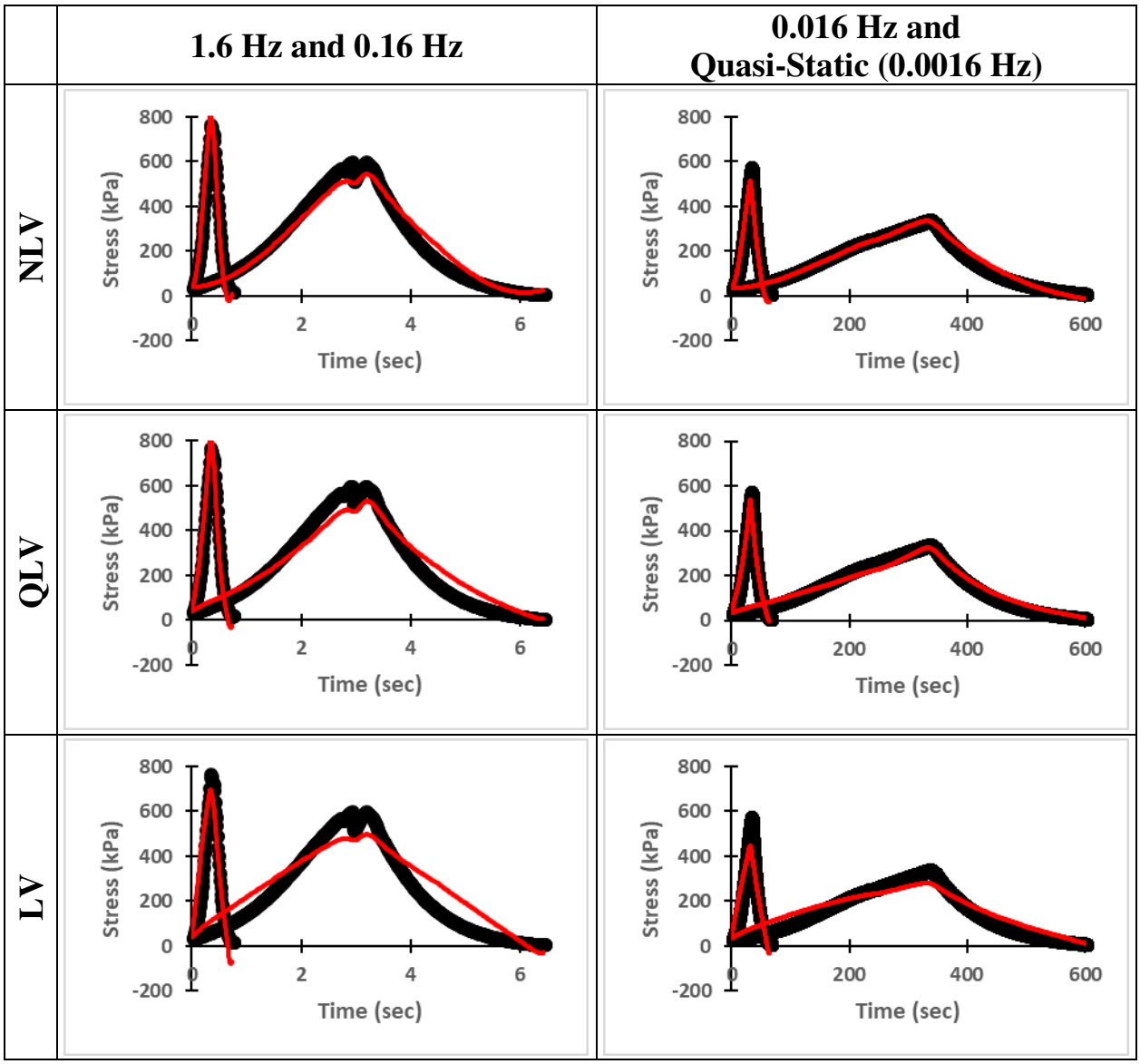

Figure C3: Representative fits of PAC condition data to all three viscoelastic formulations; for the PAC condition, the fit RMSE values of the LV formulation were significantly larger than those of the other two formulations. Although all four cycles were fit simultaneously, the curves have been separated to enable visibility of the faster tests; the reduction in stress seen in this 0.16 Hz test was due to a slight adjustment of the self-aligning grips and was also reflected in the strain data.

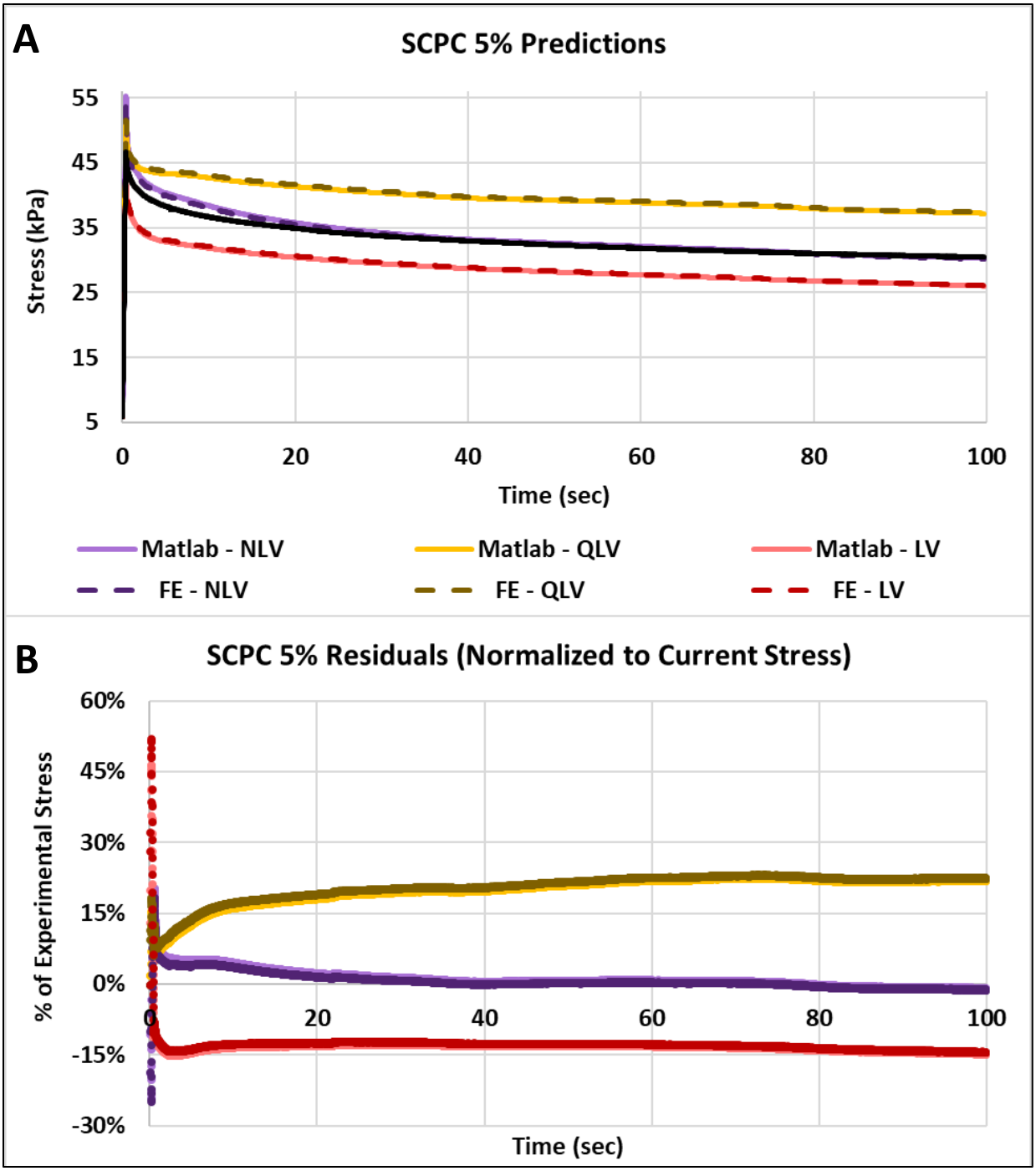

Figure C4: Predictions of the SCPC response to the 5% applied strain history (A) and the normalized residuals of each prediction (B). The long-term wRMSE of the NLV formulation prediction was lower than that of the LV and QLV formulations.

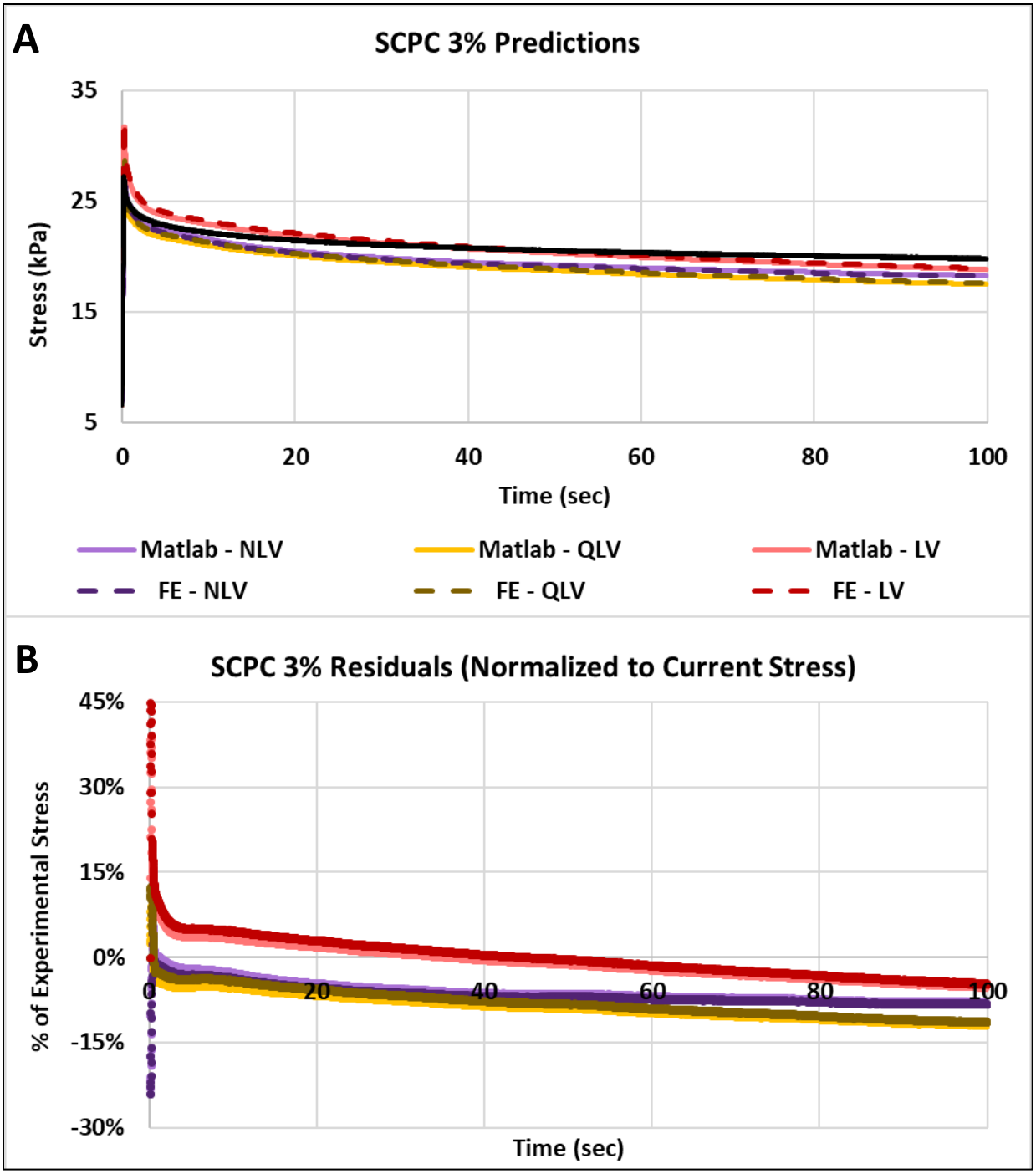

Figure C5: Predictions of the SCPC response to the 3% applied strain history (A) and the normalized residuals of each prediction (B). The long-term wRMSE of the LV formulation prediction was lower than that of the NLV and QLV formulations.

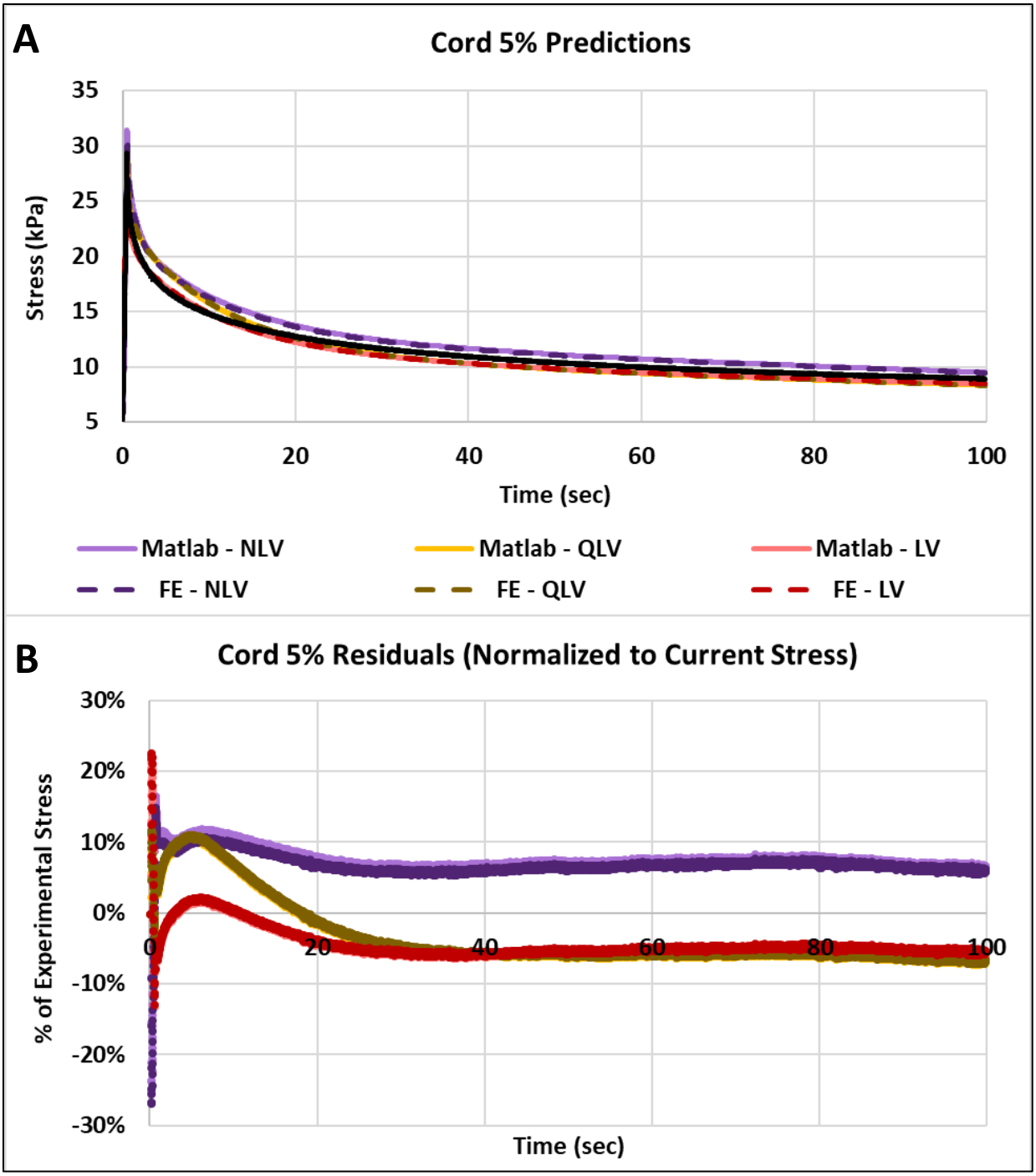

Figure C6: Predictions of the isolated cord response to the 5% applied strain history (A) and the normalized residuals of each prediction (B). The long-term wRMSE of the LV formulation prediction was lower than that of the QLV and NLV formulations.

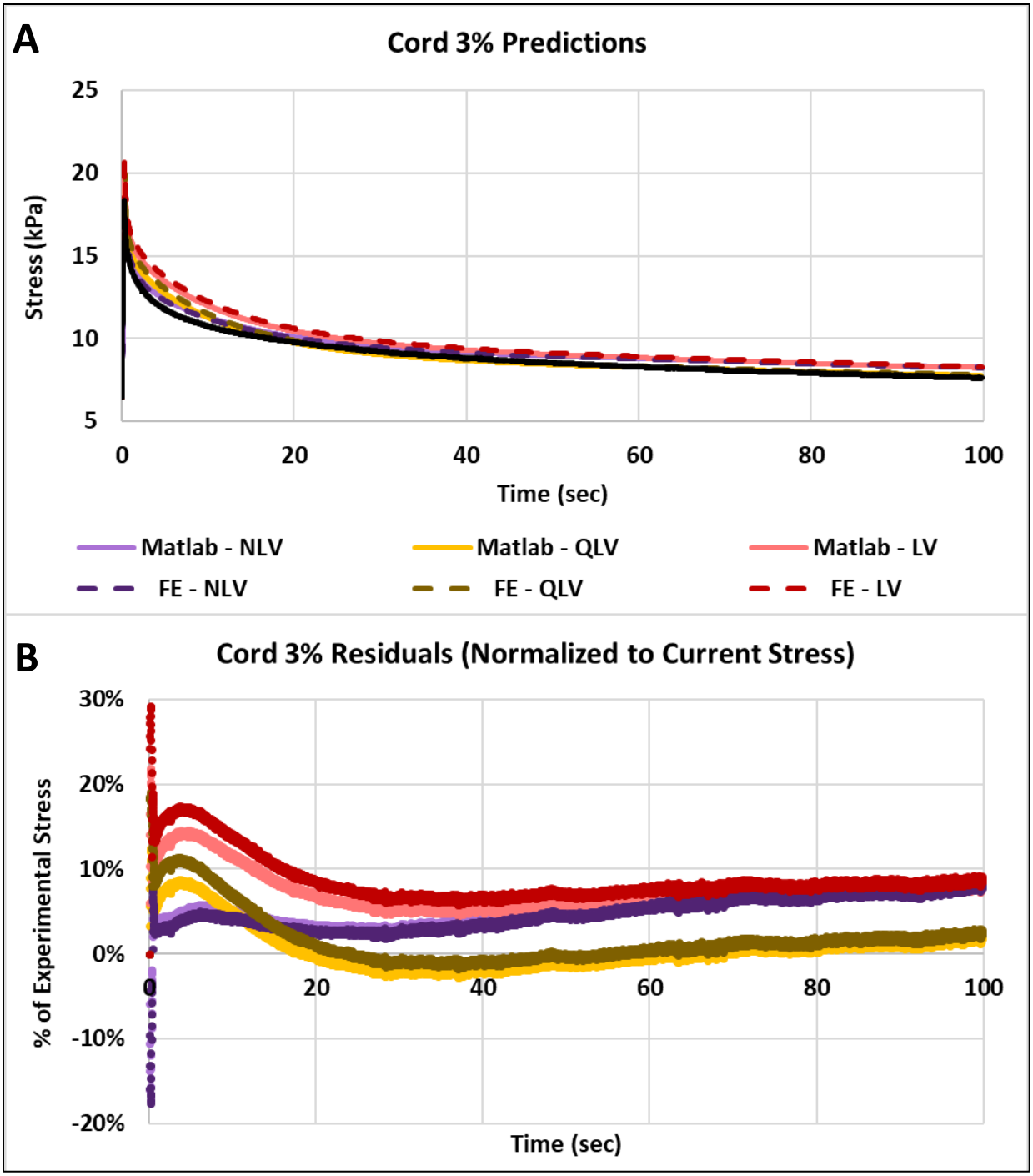

Figure C7: Predictions of the isolated cord response to the 3% applied strain history (A) and the normalized residuals of each prediction (B). The long-term wRMSE of the NLV formulation prediction was lower than that of the QLV and LV formulations.

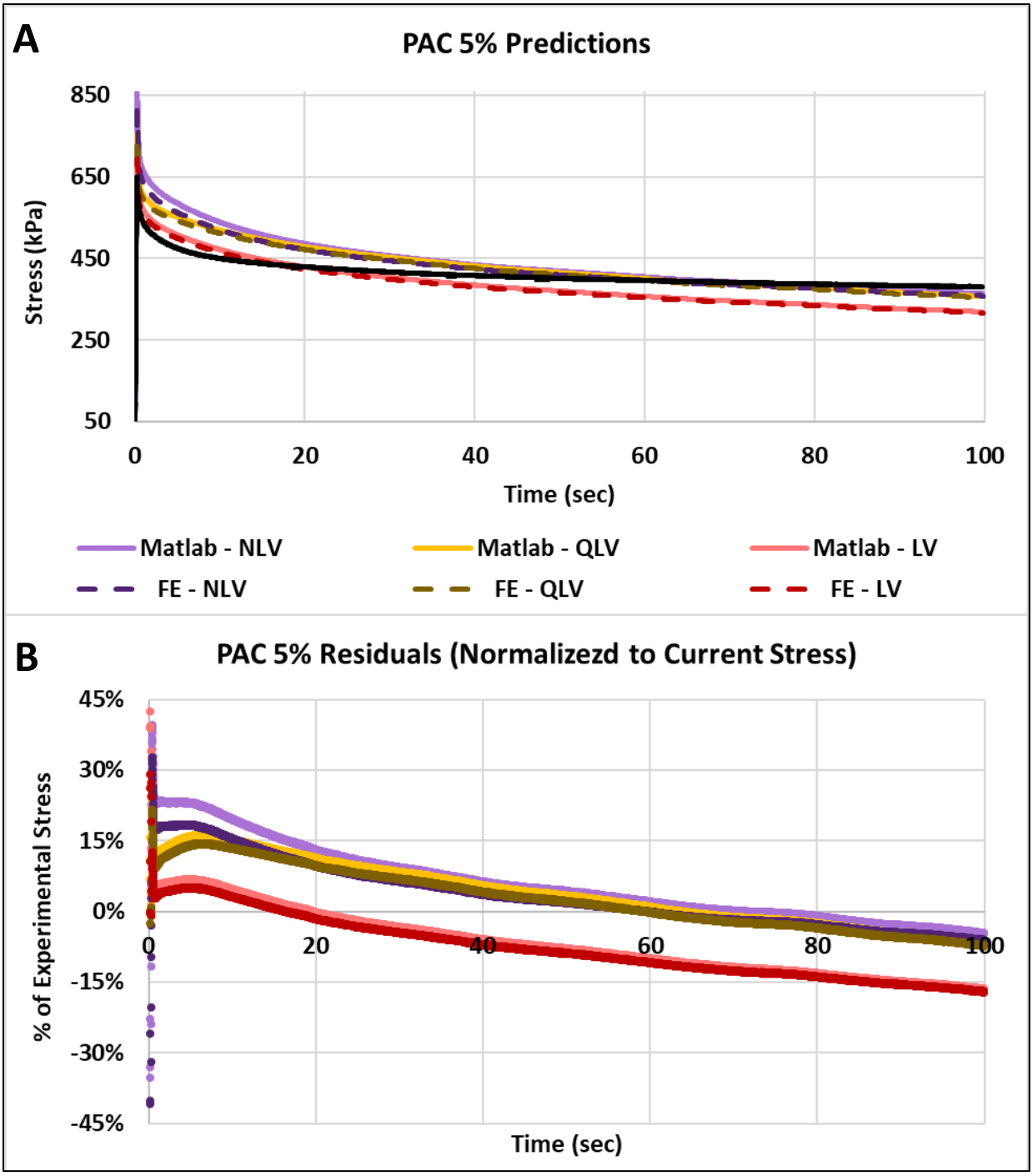

Figure C8: Predictions of the isolated PAC response to the 5% applied strain history (A) and the normalized residuals of each prediction (B). The long-term wRMSE of the LV formulation prediction was lower than that of the QLV and NLV formulations.

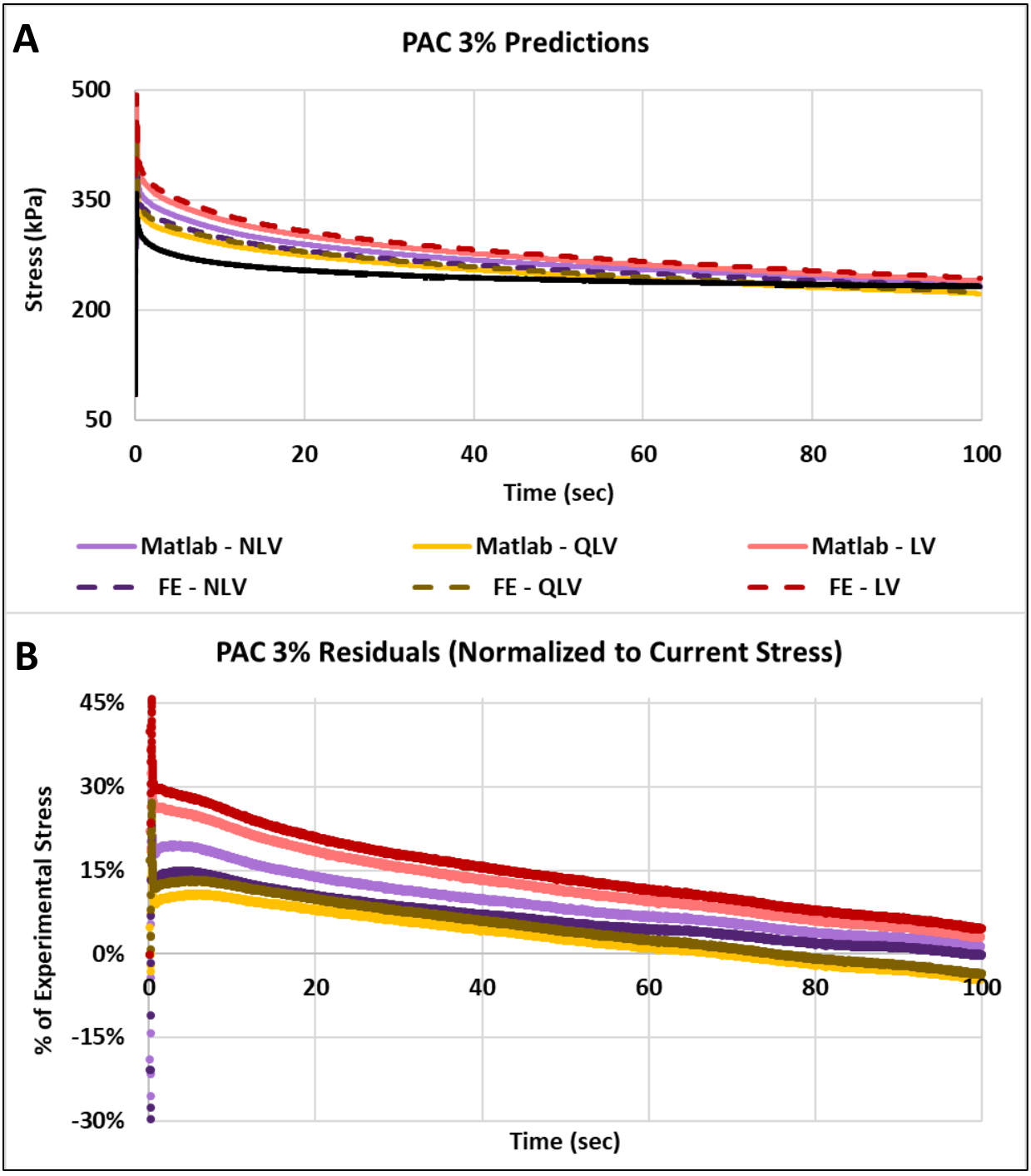

Figure C9: Predictions of the isolated PAC response to the 3% applied strain history (A) and the normalized residuals of each prediction (B). The long-term wRMSE of the QLV formulation prediction was lower than that of the NLV and LV formulations.